



**HAL**  
open science

# Theoretical study of a power generation unit based on the hybridization of a fuel cell stack and ultra capacitors

Marcos Garcia Arregui

## ► To cite this version:

Marcos Garcia Arregui. Theoretical study of a power generation unit based on the hybridization of a fuel cell stack and ultra capacitors: Application to the design of an aircraft emergency electrical network. Electric power. Institut National Polytechnique (Toulouse), 2007. English. NNT : 2007INPT040H . tel-04600200

**HAL Id: tel-04600200**

**<https://hal.science/tel-04600200>**

Submitted on 4 Jun 2024

**HAL** is a multi-disciplinary open access archive for the deposit and dissemination of scientific research documents, whether they are published or not. The documents may come from teaching and research institutions in France or abroad, or from public or private research centers.

L'archive ouverte pluridisciplinaire **HAL**, est destinée au dépôt et à la diffusion de documents scientifiques de niveau recherche, publiés ou non, émanant des établissements d'enseignement et de recherche français ou étrangers, des laboratoires publics ou privés.

# THÈSE

Présentée pour obtenir le titre de

DOCTORAT DE L'UNIVERSITE DE TOULOUSE

Delivré par

L'INSTITUT NATIONAL POLYTECHNIQUE DE TOULOUSE

Spécialité : Génie Electrique

par

**Marcos GARCIA ARREGUI**

Ingénieur de l'Universidad Pública de Navarra

---

## **Theoretical study of a power generation unit based on the hybridization of a fuel cell stack and ultracapacitors.**

**Application to the design of an aircraft emergency electrical network.**

Soutenue le 4 décembre 2007 devant le jury composé de :

MM.	HISSEL	Daniel	Président et rapporteur
	LE MOIGNE	Philippe	Rapporteur
	MARROYO	Luis	Examineur
	LANGLOIS	Olivier	Examineur
	SAVIN	Olivier	Examineur
	ASTIER	Stephan	Directeur de thèse
	TURPIN	Christophe	Co-encadrant

Thèse préparée au Laboratoire Plasma et Conversion d'Energie

UMR CNRS N° 5213



# Remerciements

Au terme de ces trois années passées au sein du LAPLACE, je suis très heureux de pouvoir exprimer mes remerciements à tous ceux qui ont contribué à l'aboutissement de ce travail de doctorat.

D'abord les membres du jury :

- Monsieur Daniel HISSEL, Professeur à l'université de Franche-Comté, pour m'avoir fait l'honneur de présider cette thèse et d'accepter la lourde tâche de rapporteur. Je le remercie également pour ses questions pertinentes ainsi que le grand intérêt qu'il a manifesté à l'égard de ce travail.
- Monsieur Philippe LE MOIGNE, Professeur à l'école Centrale de Lille, pour m'avoir fait l'honneur de rapporter sur ce travail. Je voudrais le remercier aussi pour son regard critique qui a enrichi les perspectives de ce travail de thèse.
- Monsieur Olivier SAVIN, Ingénieur au sein de DASSAULT pour sa rigueur, ses fructueux conseils et son regard critique qui m'ont permis de peaufiner mes travaux durant mes trois années de thèse, ainsi que sa sympathie.
- Monsieur Olivier LANGLOIS, Ingénieur docteur au sein d'AIRBUS et ancien collègue de bureau au LAPLACE, pour sa gentillesse et ses conseils toujours bénéfiques.
- Monsieur Luis MARROYO, Profesor de la Universidad Pública de NAvarra (UPNA). Muchas gracias por haber aceptado ser miembro del jurado y muchísimas gracias por haber aceptado mi beca erasmus hace ya más de cuatro años. Sin todo esto, esta tesis seguramente nunca hubiera sido escrita.
- Monsieur Stéphan ASTIER, Professeur à l'ENSEEIHHT et directeur de thèse. Grâce à ses qualités humaines, scientifiques et sa vaste culture générale il était fort agréable de travailler avec Stéphan. Merci beaucoup.
- Monsieur Christophe TURPIN, Chargé de recherche au CNRS et co-directeur de thèse, pour m'avoir encadré et dirigé pendant mes trois années de thèse, ainsi que pour son soutien inconditionnel pendant les mauvais moments. Je lui exprime toute ma gratitude pour la confiance et l'autonomie qu'il a pu m'accorder. Dans l'avenir, j'essaierai timidement d'imiter ses impressionnantes qualités scientifiques. Muchas gracias.

Il y a également certaines personnes du laboratoire que j'aimerais remercier :

Parmi les permanents je pense spécialement à : Xavier ROBOAM (chef du groupe), Bruno SARENI (merci pour l'opti), Stéphane CAUX, Guillaume FONTES, Jacques BENAOUN...

Un grand merci à Frederick GAILLY, grand buveur des bières et futur joueur du TEC, dont stage de master recherche j'ai eu le plaisir d'encadrer. Sans Fred je n'aurais réussi à finir la thèse dans le bon délai. *Eskerrick asko Fred !*

Et parmi les thésards, je me permets de vous présenter la *génération d'or* du LEEI :

- Bayram *Moro* TOUNSI. Amant inconditionnel de l'Espagne (sauf la Catalogne), des espagnoles (sauf les catalanes évidemment) et du CSS. Bayram nous a tous impressionné avec ses fortes connaissances de foot, tennis, danse, drague... Trois ans plus tard, il nous a encore une fois impressionné en nous annonçant qu'il avait fait une thèse et qu'il était prêt à la soutenir. Je pense également à toute la famille Tounsi et j'aimerais conclure en disant : *jia te azba l'étoile !*
- Marcus Alexandre Toward *Viadinho* da SOUSA. Malgré son sang brésilien, Marcus est un amoureux de la France. Les preuves de cet amour sont sa maîtrise de la langue française et les chants dédiés aux bleus lors du quart de final de la dernière coupe du monde (France 1 - Brésil 0). En ce moment, il prend du plaisir sur les plages ensoleillées et chaleureuses de Belgique. Je pense également très fort à la gentillesse de son adorable et magnifique copine : Shanna JACOBS.
- Mathieu *Le Gentil* COUDERC. Je suis assez fier d'être une des rares personnes qui a réussi à énerver Mathieu. Je lui souhaite tout le courage du monde pour ses derniers mois de rédaction.
- Bernardo COUGO. Amoureux des bons vins et fromages. Encore un autre brésilien, mais contrairement au Marcus, il sait danser la samba et jouer au *futbol*. Bernardo pourrait être un dur concurrent à Mathieu en termes de gentillesse.
- Ali *Logique Floue* Abdallah ALI. Prestigieux politicien et futur président du Djibouti. Exilé en ce moment dans le Royaume de Tarbes, il prépare ses troupes face à son imminent débarquement à Paris.
- Valentin COSTAN ou *monsieur brevet*. Délocalisé en ce moment sur les terres de Belfort. Il apportait sa sympathie et sa touche roumaine au sein du labo.
- Nicolas MARTINEZ. Plein de vécus et d'expériences avec ses 25 ans. On dirait que le temps ne passe pas pour lui. Il est le co-pilote de Mathieu dans le 4L trophy. Bon courage pour la rédaction !
- Christophe *Tomate* Conilh. Sympathique et pas du tout discret marmandais avec lequel on a bien bu ces dernières années. En ce moment il accompagne Valentin à Belfort.
- Sylvain GIRINON. Imbattable kendoka et joueur professionnel de World Of Warcraft. C'est lui qui s'est occupé de faire les diapos et les animations de ma présentation de thèse. En ce moment il essaie d'embobiner les thésards de première année pour remplir la garrafe d'eau à la cantine.

- No puedo olvidar a los hispanos del laboratorio. Entre Jesús LOPEZ (*tu tesis pa' cuando?*), Rafael DIEZ (*no me trates de usted, coño!*) y Ramiro DEL ALAMO (*coup d'abdo!*) han hecho más de la mitad de mi tesis. Desde estas líneas también quiero denunciar la degradación que ha sufrido lengua de Cervantes por parte de nuestros hermanos latinoamericanos.

Je ne pourrais oublier de citer dans ces quelques lignes Wojtek, Martin Blodt, Gian Luca, les 3 François (Pigache, Bonnet, Defaÿ), Jérôme Mavier, Adaõ, Mariam, Mehdi, Saghir... Mille excuses à ceux que j'aurais oubliés !

Cette génération a été caractérisée par les longues discussions à table à propos des IGBT cramés, thyristors et manipulations effectués la veille dans les bars de Toulouse.

Ces dernières années n'auraient pas été les mêmes sans la présence de certaines personnes extérieures au labo.

Je pense spécialement à :

- Mes coloks au 4 rue des Gallois : Mathieu et Vincent. Sacrée bande de babacools !
- Mes coloks à l'avenue de Muret : Elodie (*Ma montpelliéraine préférée*), Nico (*now in England !*), Gaëlle et ma charmante colok anglaise : Penny (*even if you didn't want to correct this brief report !*)
- Kiwi, Vinze et Priska !
- Al equipo español : Sebas, Luis, Marcos Vigo, Adriana, Alfonso, JuanPa, Saio, Abraham...
- Toulouse Electrogaz Club (TEC). Mon club de rugby. Rugby, bières et une ambiance très sympa m'ont accompagné tous les dimanches pendant les trois dernières saisons. Ensemble on a vécu la montée en promotion honneur et des lundis difficiles.
- A l'équipe de Saint Gaudens : Marjorie et Marlène.

Estas últimas líneas las reservo para mis padres y mi hermano. Sin ellos nada de esto hubiera sido posible. Os quiero.



*A mis padres y al pijo*





# **ABSTRACT**

The presented work deals with the design and conception of an electrical network from a fuel cell stack and its associated storage device. The framework of this project is an aeronautical and transport application.

Air pressurized fuel cell stacks need some auxiliary devices that permits a correct gas flow through the fuel cell stack. Due to the auxiliary devices, the fuel cell dynamics performances may be limited, and a power buffer is required to support power peaks. Furthermore, hybridization has a positive effect in the system size, and can lead to reduce the global system weight and volume. Ultracapacitors seem to be well adequate for this purpose.

Nevertheless, the introduction of a storage device in the electrical network opens a wide range of possible architectures. Indeed, due to the important voltage variations of the supercapacitor bank and the fuel cell stack, some power electronics interfaces may be placed in order to assure the electrical network requirements. Thus, the system behaviour varies according to the position of the power converters and the storage device in the electrical network. Therefore, the power converter conception, the retained electrical architecture characteristics and its associated control laws are studied in this work.

Due to the transport application, the system hydrogen consumption, volume, weight and cost are essential parameters, and become the key to choose one of the retained architectures. Furthermore, the system couplings and the important number of design variables makes impossible to design the system without the help of a software tool. Therefore, and in order to compare fairly all the proposed architectures, a multiobjective optimization tool is developed.

## **Keywords**

- Fuel cell stack
- Ultracapacitors
- Hybridization
- System sizing
- DC-DC converter
- Multiobjective optimization

## **RESUME**

Le travail présenté dans ce mémoire porte sur la conception d'un réseau électrique à base d'une pile à combustible et son organe de stockage associé. Le contexte de ce travail se place dans une application aéronautique.

Les piles à combustible à air comprimé ont besoin de certains dispositifs auxiliaires qui permettent la bonne diffusion des gaz à travers les canaux du stack. A cause de ces dispositifs auxiliaires, la dynamique globale du système est limitée, et une hybridation avec une source de puissance auxiliaire peut être nécessaire. En outre, l'hybridation a un impact positif sur la taille du système, et peut mener à la réduction du poids et du volume du système global. Les supercapacités semblent bien adaptées pour cette mission.

L'introduction d'un organe de stockage dans le réseau électrique permet un vaste nombre d'architectures possibles. En effet, les variations de tension de la pile et l'organe de stockage lors de son fonctionnement, imposent l'usage d'une interface d'électronique de puissance, permettant d'assurer le cahier des charges imposé par le réseau électrique. En conséquence, le comportement global du système dépend à la fois du positionnement des convertisseurs et des organes de stockage au sein du réseau électrique. La conception du convertisseur, le comportement électrique des architectures proposées et le contrôle du système global sont étudiés dans ce travail.

Etant donné que notre système est dédié à une application embarquée, le volume, le poids, le coût ainsi que la consommation d'hydrogène sont des paramètres clés pour le choix de l'une des architectures proposées. Cependant, le couplage du système et le nombre important des variables de conception rendent impossible un choix définitif basé juste sur le savoir faire de l'ingénieur d'études. Alors, un outil d'optimisation multicritère, permettant de comparer les architectures, doit être implémenté.

### **Mots-clés**

- Pile à combustible
- Supercapacités
- Hybridation
- Dimensionnement
- Convertisseur DC-DC
- Optimisation

# Contents

GENERAL INTRODUCTION.....	17
---------------------------	----

## CHAPTER I

CELINA PROJECT FRAMEWORK AND GENERIC SIZING METHODS.....	- 21 -
I.1 EUROPEAN UNION RESEARCH OBJECTIVES .....	- 22 -
<i>I.1.1 Hydrogen production and distribution.....</i>	- 22 -
<i>I.1.2 Hydrogen storage.....</i>	- 23 -
<i>I.1.3 Fuel cell basic research.....</i>	- 25 -
<i>I.1.4 Stationary and portable applications.....</i>	- 26 -
<i>I.1.5 Transport applications.....</i>	- 27 -
I.2 THE CELINA PROJECT.....	- 29 -
I.3 HYBRIDIZATION: POWER SHARING .....	- 32 -
<i>I.3.1 Definition of hybridization notions .....</i>	- 33 -
<i>I.3.2 Ideal hybridization.....</i>	- 33 -
<i>I.3.3 Hybridization with system losses. ....</i>	- 34 -
<i>I.3.4 Hybridization for the Airbus requirements. ....</i>	- 35 -
<i>I.3.5 Power sharing methods.....</i>	- 35 -
I.3.5.1 Frequential power sharing [Chapoulie].....	- 35 -
I.3.5.2 Band power sharing .....	- 38 -
I.3.5.3 Slope power sharing .....	- 39 -
I.4 GENERIC SIZING METHODS .....	- 41 -
<i>I.4.1 Fuel cell stack .....</i>	- 41 -
I.4.1.1 Generalities [Raissi] .....	- 41 -
I.4.1.2 Electrical model of a fuel cell stack .....	- 43 -
I.4.1.3 Stack size. Cell surface and cell number influence.....	- 44 -
I.4.1.4 Weight model of the fuel cell stack .....	- 46 -
I.4.1.5 Gas consumption. ....	- 49 -
I.4.1.6 Fuel cell stack sizing for a given mission power profile.....	- 51 -
<i>I.4.2 Ultracapacitors.....</i>	- 57 -
I.4.2.1 Ultracapacitors sizing .....	- 58 -
I.4.2.2 Ultracapacitor internal losses.....	- 63 -
I.4.2.3 Ragone plots [Christen] .....	- 65 -
I.5 CHAPTER CONCLUSION.....	- 69 -

## CHAPTER II

<b>ELECTRICAL ARCHITECTURE STUDY .....</b>	<b>- 71 -</b>
II.1 PRELIMINARY ANALYSIS OF ELECTRICAL ARCHITECTURES .....	- 72 -
II.1.1 Architecture with three power converters.....	- 72 -
II.1.2 Architecture with two power converters .....	- 72 -
II.1.3 Architecture with one power converter.....	- 74 -
II.1.4 Assessment of electrical architectures .....	- 76 -
II.2 ARCHITECTURES WITH TWO POWER CONVERTERS: PARALLEL CONNECTION .....	- 78 -
II.2.1 First sizing of this architecture. “Perfect system” .....	- 79 -
II.2.2 Effect of the losses .....	- 80 -
II.2.3 Methods to compensate for the system losses .....	- 81 -
II.2.3.1 Storage device voltage reference method .....	- 82 -
II.2.3.2 Estimator method .....	- 84 -
Capacitance estimation .....	- 86 -
II.2.4 Global sizing of a hybridized system .....	- 89 -
II.2.4.1 Sizing results with the storage device voltage reference method .....	- 90 -
II.2.4.2 Sizing results with the estimator method .....	- 94 -
II.2.5 Assessment of the proposed energy managements.....	- 96 -
II.3 ARCHITECTURE WITH ONE POWER CONVERTER: STORAGE DEVICE DIRECTLY CONNECTED TO THE FUEL CELL .....	- 97 -
II.3.1 Operation of a direct hybridization .....	- 97 -
II.3.2 Direct connection experimental results .....	- 99 -
II.3.3 System sizing procedure for a direct hybridization.....	- 101 -
II.3.4 Sizing and analysis of a ‘perfect’ direct hybridization .....	- 103 -
II.3.5 Loss effect on the behavior of a direct hybridization.....	- 106 -
II.3.5.1 Effect of the power converter losses.....	- 106 -
II.3.5.2 Effect of the ultracapacitor internal losses.....	- 107 -
II.3.6 Start-up of a direct hybridization.....	- 111 -
II.4 ARCHITECTURE WITH ONE POWER CONVERTER: STORAGE DEVICE DIRECTLY CONNECTED TO THE DC BUS.....	- 113 -
II.5 CHAPTER CONCLUSION .....	- 116 -

## CHAPTER III :

<b>POWER CONVERTER DESIGN .....</b>	<b>- 119 -</b>
III.1 POWER CONVERTER TOPOLOGIES PROPOSED FOR THE AIRBUS REQUIREMENTS .....	- 120 -
III.1.1 Insulated power converter topologies. ....	- 120 -
III.1.2 Non insulated power converter topologies .....	- 121 -
III.1.2.1 $\pm 270V$ Boost topology .....	- 122 -
III.1.2.2 $\pm 270V$ Buck topology .....	- 123 -
III.1.2.3 $\pm 270V$ Buck-Boost topology .....	- 123 -

III.1.2.4 Input filter .....	- 124 -
III.2 INTERLEAVING TECHNIQUE.....	- 125 -
III.2.1 General considerations .....	- 125 -
III.2.2 Output voltage dynamic response with interleaved converters .....	- 127 -
III.2.3 Interleaving technique disadvantages.....	- 128 -
III.3 POWER CONVERTER CONTROL.....	- 131 -
III.3.1 Buck-Boost converter .....	- 131 -
III.3.1.1 Buck-boost converter modeling .....	- 131 -
III.3.1.2 Buck-boost converter current loop.....	- 133 -
III.3.1.3 Buck-Boost converter voltage loop.....	- 134 -
III.3.1.4 Proposed Buck-Boost converter control validation.....	- 136 -
III.3.2 Boost converter control.....	- 136 -
III.3.2.1 Boost converter modeling .....	- 136 -
III.3.2.2 Boost converter current loop.....	- 138 -
III.3.2.3 Boost converter voltage loop .....	- 138 -
III.3.2.4 Proposed Boost converter control validation .....	- 139 -
III.3.3 Buck converter control.....	- 140 -
III.3.3.1 Buck converter modeling .....	- 140 -
III.3.3.2 Buck converter current loop.....	- 141 -
III.3.3.3 Buck converter voltage loop .....	- 142 -
III.3.3.4 Buck proposed control validation .....	- 143 -
III.3.4 Conclusions on the proposed control laws.....	- 143 -
III.3.5 Control of DC-DC Interleaved power converters .....	- 145 -
III.3.5.1 Discontinuous mode.....	- 146 -
III.3.5.2 Modification of the control law for the discontinuous mode.....	- 149 -
III.3.6 Behavior of the proposed power converters for the common mode voltage.....	- 153 -
III.3.6.1 Describing of the simulated power converters and the simulation conditions for the study of the common mode voltage.....	- 154 -
III.3.6.2 Common mode voltage behavior for the Boost converter with one branch .....	- 155 -
III.3.6.3 Common mode voltage behavior for the Boost converter with two interleaved branches .....	- 157 -
III.3.6.4 Common mode voltage behavior for the Boost converter with three interleaved branches .....	- 158 -
III.3.6.5 Conclusions about the common mode voltage study .....	- 159 -
III.4 POWER CONVERTER EFFICIENCY AND WEIGHT STUDY .....	- 161 -
III.4.1 Models of the losses within a power converter.....	- 161 -
III.4.2 Weight model.....	- 164 -
III.4.3 Library of components for power converters .....	- 166 -
III.4.4 Discussion about the sizing of interleaved power converters.....	- 166 -
III.4.5 Branch switching-off technique effect on the power converter efficiency .....	- 172 -
III.4.5.1 Effect on a 4-branch BOOST converter (Figure III. 77- a) .....	- 173 -
III.4.5.2 Effect on a 4-branch Buck converter (Figure III. 77- b).....	- 176 -
III.4.5.3 Effect on a 4-branch Buck-Boost converter (Figure III. 77- c) .....	- 178 -
III.4.5.4 Effect on a non-reverser 4-branch Buck-Boost converter (Figure III. 77 - c) .....	- 180 -

III.4.6 Evaluation of non insulated power converter topologies with interleaved branches for the AIRBUS requirements .....	- 182 -
III.4.6.1 Power converter topologies proposed for this evaluation.....	- 182 -
III.4.6.2 Evaluation of the Boost topology for the AIRBUS requirement.....	- 184 -
III.4.6.3 Evaluation of the Buck topology for the AIRBUS requirement.....	- 187 -
III.4.6.4 Evaluation of the Buck-Boost topology for the AIRBUS requirement.....	- 189 -
III.5 CONCLUSION OF CHAPTER III .....	- 193 -

## **CHAPTER IV :**

<b>OPTIMIZATION STUDY. ARCHITECTURE COMPARISONS .....</b>	<b>- 195 -</b>
IV.1 MULTI-OBJECTIVE OPTIMIZATION .....	- 197 -
IV.1.1 Optimization algorithms.....	- 197 -
IV.1.1.1 Deterministic methods .....	- 197 -
IV.1.1.2 Stochastic methods .....	- 198 -
IV.1.2 Pareto-optimal front.....	- 198 -
IV.1.3 Multi-objective Genetic Algorithms.....	- 199 -
IV.1.4 Description of the NSGA-II.....	- 200 -
IV.1.5 Design constraint handling in MOGAs .....	- 202 -
IV.2 THE OPTIMIZATION PROBLEM .....	- 204 -
IV.2.1 The design objectives.....	- 204 -
IV.2.2 The design variables.....	- 205 -
IV.2.3 The system constraints.....	- 207 -
IV.2.4 Complete optimization problem formulation.....	- 208 -
IV.2.5 Optimization process .....	- 208 -
IV.3 OPTIMIZATION RESULTS .....	- 210 -
IV.3.1 Architecture comparison .....	- 210 -
IV.3.2 Evolution of the design variables along the Pareto plot.....	- 211 -
IV.3.2.1 The architecture with the storage device connected to the DC bus.....	- 212 -
IV.3.2.2 The direct connection architecture.....	- 215 -
IV.3.2.3 The architecture with two parallel power converters .....	- 217 -
IV.3.3 System couplings.....	- 221 -
IV.3.4 Conclusions .....	- 223 -
IV.4 INFLUENCE OF THE MISSION DURATION .....	- 224 -
IV.5 EVOLUTION OF ULTRACAPACITOR PACK AND FUEL CELL VOLTAGES ALONG THE PARETO PLOT. -	227 -
IV.5.1 Evolution of the ultracapacitor pack voltage.....	- 227 -
IV.5.2 Evolution of the fuel cell voltage .....	- 228 -
IV.6 COMPARISON BETWEEN AIR-PRESSURIZED AND PURE OXYGEN FUEL CELLS .....	- 230 -
IV.6.1 Oxygen bottle mass estimation .....	- 230 -
IV.6.2 Optimization results.....	- 231 -
IV.7 COMPARISON BETWEEN PURE HYDROGEN AND REFORMATE FUEL CELLS. ....	- 232 -

IV.8 CONCLUSION OF THE CHAPTER IV .....	- 234 -
<b>GENERAL CONCLUSION AND PERSPECTIVES .....</b>	<b>- 237 -</b>
<b>BIBLIOGRAPHY .....</b>	<b>- 243 -</b>
<b>APPENDIX.....</b>	<b>- 253 -</b>
<i>APPENDIX I: CLASSICAL POWER CONVERTERS SIZING.....</i>	<i>- 255 -</i>
<i>APPENDIX II: SUPERCAPACITORS LIBRARY.....</i>	<i>- 259 -</i>
<i>APPENDIX III: IGBT AND DIODE LIBRARY.....</i>	<i>- 261 -</i>
<i>APPENDIX IV: INDUCTOR CORES LIBRARY AND SIZING PROCEDURE.....</i>	<i>- 263 -</i>
<i>APPENDIX V : RESUME EN FRANCAIS .....</i>	<i>- 267 -</i>





# General introduction

Fuel cells today are of special interest due to their high efficiency and low pollution features. Assuming the existence of a clean hydrogen production, fuel cells present a great number of advantages compared to traditional energy sources: high efficiency, particularly in the case of co-generation (heat and electricity), no noise, no green-house effect gas emissions... This explains why the European Union has decided to invest an important amount of money in fuel cells and hydrogen research projects.

The CELINA (fuel CELL application In a New configured Aircraft) project is a research project mostly funded by the EU, Airbus and Dassault Aviation, whose objective is to study (theoretically – no experiment) the possibilities and advantages of fuel cells in aeronautical applications. The main application studied is the emergency electrical DC network which must operate when the main electrical generation is lost (very critical situation!). About twenty companies and university research laboratories are involved in the CELINA project started on January 1, 2004.

This PhD is the heart of the work developed by the LAPLACE laboratory in the 2.4 task of the CELINA project. This task consists in the conception and design of the electrical architecture of the studied emergency electrical DC network, including the power electronic interface, that respects the aircraft makers' electrical networks requirements.

Most of the industrial demands (i.e. automotive industry) require that the energy source should be able to respond to more or less fast load changes and recover reversible energy (i.e. braking energy). Furthermore, hydrogen and pressured air fuel cell systems do not generally have the capacity to respond immediately to fast load changes due to the auxiliary device response time. Thus, the hybridization of the energy source (fuel cell) with a power source (batteries, ultracapacitors...) seems mandatory in this kind of systems.

The system hybridization opens a wide range of system design possibilities in terms of architectures and energy management. The fuel cell system designer will have to decide how to connect both sources, the number and the piloting strategy of power converters that will adapt the sources voltage to the electrical network requirements. The chosen strategy will have to be, of course, respectful with the electrical network requirements, and furthermore, the system volume, weight and cost will have to be minimized.

The aim of this PhD study is to analyze the operation mode of all the possible architectures and evaluate them in terms of weight and efficiency in order to do the correct choice and to design the power converter interface that will adapt the fuel cell stack supplied voltage to the electrical network requirements. Furthermore, a system sizing methodology and the power converter control laws must be established depending on the energy management.

This report is divided in 4 chapters.

In the first chapter, a brief state of art concerning the hydrogen technology is developed. Afterwards, the main EU hydrogen and fuel cells research projects are described. Then begins the description of the done work in our study.

As already explained previously, the proposed solution is to hybridize a fuel cell and a storage device. Batteries have not been considered in this PhD work, because previous Airbus studies have proved that ultracapacitors are better adapted to the case of the Airbus emergency electrical network. The “generic sizing methods” proposed to design the ultracapacitor pack and the fuel cell stack are here developed in details. They are called “generic sizing methods” because these methods do not have to take into account, at this step, the system coupling, and they can be only applied if the source is directly connected to a load, and if there is no interaction with another source. Nevertheless, these methods are necessary to size each source. The coupling between both sources is developed in the following chapter 2.

The second chapter analyzes all the possible electrical connection architectures for this hybrid system. After careful reflections, it is possible to reject the most complicated architectures due to their bad efficiencies and high weight. Nevertheless, three architectures remain in competition after this first selection step. These three architectures are then developed along the chapter.

The three retained architectures do not present the same characteristics which are described here in details. In some of them, it is not possible to control the DC bus voltage. Another architectures need to modify their control laws and add an energy management control loop in order to compensate power converter and ultracapacitors internal losses. In other cases, there is no need to implement an energy strategy thanks to the original characteristics of the connection.

Nevertheless, the three architectures present a common point. It is not possible to size the electrical devices just by applying the generic sizing methods presented in chapter 1. This is due to the system couplings that are not considered in the generic sizing methods. In order to solve this problem, an iterative sizing method is proposed in this chapter.

Airbus requirements impose one  $\pm 270$  volts DC electrical network and an unique fuel cell stack to limit the fluidic complexity. Thus, an original power electronics interface was proposed in order to adapt the fuel cell supplied voltage to the electrical network requirements. It consists in associating in series or in parallel (for the source side) boost and/or buck converter legs and in differential mode (for the load mode). The more interesting combination is the parallel one. The conception and design of the proposed power converter solution is developed in chapter three.

The third chapter could be divided in two main parts. Due to the important power values, and in order to reduce the final converter weight, interleaving techniques are applied to parallel elementary converters branches. This makes difficult the power converter control because the power converter can

easily reach the non continuous operating mode where the power converter transfer function becomes non linear. In order to solve this problem, a “branch switching off” technique is proposed. Furthermore, the power converter common mode voltage rejection capacity must be evaluated due to the asymmetry of the proposed power converter solution. The second part of this chapter deals with the weight and efficiency estimations of the proposed converters.

Finally, the fourth and last chapter explains the developed global system optimization tool. Indeed, due to the system complexity, it seems almost impossible to evaluate and compare, in a satisfactory way, the three proposed architectures. The proposed optimization tool is able to find the optimal configuration of each architecture. A multi-objective optimization was implemented in order to evaluate and compare in terms of weight, volume, efficiency and cost the three retained architectures. This optimization tool is not just a decision tool, it also permits to better understand the system behaviour and helps to fix, for future applications, some design variables such as the fuel cell current density, fuel cell minimal voltage, ultracapacitors maximal voltage...and even technological choices such as ultracapacitors technology, number of parallel interleaved branches...



## *Chapter I*

# **CELINA project framework and generic sizing methods**

---

**N**owadays, human being energy consumption has fully increased. Furthermore, fossilized combustible reserves risk to be exhausted in some years, and the instable political situation in some of the main petrol and fossilized combustible producing countries led to a significant price rise in last years. On the other hand, though the effort of some governments to control the CO<sub>2</sub> emissions and the greenhouse effect, the reality is that the earth pollution is quickly increasing. Therefore, the human beings have to find new environmental friendly energy sources that can be obtained not only in some determined countries and easy to be stored, transported and distributed. Furthermore, the new energy source must be easy to adapt into the usual energy consumption forms: electrical, mechanical, chemical...

Hydrogen seems to be well adapted to the previous requirements. Hydrogen can be cleanly produced thanks to water electrolysis, furthermore hydrogen has already been transported for over seventy years and in last years a new energy converter is becoming popular: fuel cells. Indeed, fuel cells can transform hydrogen into electricity with zero emission characteristics.

Hydrogen qualities have not gone unnoticed for the European Union that in recent years has multiplied by six the budget for hydrogen research projects. **Janez Potočnik** Commissioner for Science and Research affirms in [EU]: *“The European Commission believes that sustainable energy systems are fundamental to our objective for sustainable development. Sustainable energy systems require the right balance of appropriate policies with appropriate, well-targeted research and technology development. This research must cover conventional and innovative energy production and conversion technologies, including obviously Hydrogen and Fuel Cells.”*

The EU has established five research axes concerning fuel cells and hydrogen: hydrogen production, hydrogen storage, fuel cells basic research, stationary and portable applications and transport applications. In the next lines the five axes will be explained in further details, and a brief state of art and EU objectives for each topic are developed [EU].

## I.1 European Union research objectives

The European Union had decided to focus his hydrogen research objectives in five different axes:

### I.1.1 Hydrogen production and distribution

The deployment of processes and facilities that will be able to supply the required quantities of hydrogen is a key issue in the successful transition to a more hydrogen based energy economy. The way that hydrogen will be produced and distributed should contribute to the security of energy supply and the protection of the environment, as well as being economically competitive. Approximately 600 billion Nm<sup>3</sup> of hydrogen is produced every year through well established commercial processes for the hydro-cracking of oil, the production of ammonia and hydrogenation of edible fats, 95% of which is captive (consumed on-site). Significant progress is needed for hydrogen to become a widely available “consumer fuel” which meets the previously mentioned energetic, environmental and production cost constraints. A key attraction of hydrogen as an energy vector is that it can be produced from a variety of sources including renewable, nuclear and fossil sources. The production of hydrogen today is mainly performed by steam reforming, partial oxidation of gaseous or liquid fuels or the gasification of coal. Electrolysis is used when a small amount of pure hydrogen is required at a specific site. The purification of hydrogen rich gases is an important step in improving the quality of hydrogen produced, depending on eventual use. Certain fuel types require very high purity hydrogen. Distribution of hydrogen is done through pipelines, or using trucks carrying hydrogen in high pressure gas cylinders or cryogenic tanks. The latter involves an energy-intensive liquefaction step, though the energy required just to compress gaseous hydrogen is itself significant. In the short- to-medium term, the lack of readily available non-fossil sources means that the bulk of hydrogen produced will come from fossil fuels, firstly without carbon capture and sequestration (CCS), and then with CCS in the medium term. The long term goal is to produce hydrogen from indigenous carbon-free and carbon-lean energy sources. Some of the long-term pathways for the production of hydrogen that are being currently investigated in the EU research projects on Hydrogen production are:

- Thermochemical processes that use high temperature heat from nuclear or concentrated solar technologies to split water into hydrogen and oxygen
- Photo-electrolysis or photo-catalytic water splitting, which is a combination of photovoltaic cells and in situ electrolysis
- New, advanced electrolysers (based on PEM or SOFC technology) with expected higher efficiency than the conventional alkaline electrolysis
- Bio-photolysis and photo-fermentation processes that use sun light and biological processes to produce hydrogen (upstream research)

- Dark fermentation biological processes that produce hydrogen in the absence of light
- Hydrogen from biomass by thermo-chemical routes via syngas generation. There is a plethora of technical issues to be addressed to develop and optimize the hydrogen production and distribution processes depending on the primary source of energy, the scale of each application and the planned use.



**Figure I. 1: Electrolyser prototype elaborated in the GENHYPEM project.**

## I.1.2 Hydrogen storage

Effective hydrogen storage is a key for the transition to a more hydrogen-based energy economy. The challenge is especially demanding for on-board storage for road vehicles.

A number of novel storage techniques are being investigated to complement the currently available methods where hydrogen is stored in gaseous (up to a pressure of 350 bars) or liquid form (cryogenic temperatures).

- For the case of **gaseous storage**, current technology is around five times less energy dense than gasoline or diesel fuels – that is to say, storing hydrogen uses five times the space per unit energy. So, there is a need for ever increasing pressures, and the current aim is for 700 bars in fibre-reinforced composite tanks, which would give acceptable road vehicle autonomy. High-strength fibres need to be developed and liners made impermeable to hydrogen. Composite structures made in this way are not cheap, with complex, time-intensive laminating processes – so there is a need for cheaper methods, with an emphasis on recyclable materials. Safety and certification issues are paramount. Lastly, it is



important to standardise peripheral equipment such as safety sensors, fuel station flow meters, and 700 bar dispensers and nozzles for rapid refuelling.

- **Liquid storage**, even if currently providing the highest energy density, has high energy penalties associated with liquefying and storing hydrogen in liquid form (boil-off). The efficiency of hydrogen liquefaction can be improved through magnetic refrigeration or other processes and at the same time needs to be scaled-down for localised application. New lightweight and low volume tanks need to be developed with novel insulating material, while tanks should incorporate safe methods for handling boil-off.
- Hydrogen can also be stored through **solid storage**, where the hydrogen is chemically absorbed into in metal hydrides or chemical hydrides or physisorbed in porous materials (e.g. carbon structures). This technique is suitable for portable, stationary and potentially transports applications. However, such technology is very much in the laboratory stage, with much still to be learned about the basic science of the materials involved. Current solid storage systems are based on AB<sub>2</sub> or AB<sub>5</sub> metal hydrides and low temperature chemical hydrides (such as sodium alanate) but are limited to system energy densities (weight of hydrogen relative to that of the tank) ranging from 0.6% to 1.5%. To increase the energy density, the cyclability (>1500 cycles) and the operating temperature range, a number of issues related to governing bond strength, kinetics, absorption, desorption, degradation and heat management need to be addressed. New materials with low heat of formation must be identified and new theoretical and experimental techniques must be developed, supported by computational tools. Emphasis must be placed on safety and certification issues, and on optimising filling procedures, which can generate a build-up of heat in the tank.
- Sodium borohydride is also used in experimental fuel cell systems as a means of storing hydrogen. As a fuel it is less flammable and less volatile than gasoline but more corrosive. It is relatively environmentally friendly because it will quickly degrade into inert salts when released into the environment. The hydrogen is generated for a fuel cell by catalytic decomposition of the aqueous borohydride solution:

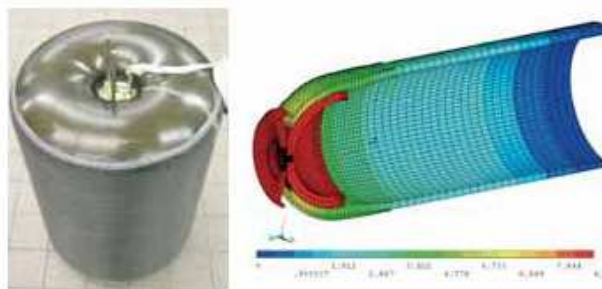


**Figure I. 2: Hydrogen storage tank designed for an automotive application in the StorHy project.**

### **I.1.3 Fuel cell basic research**

Fuel cells offer a significant advantage over traditional combustion-based thermal energy conversion, in that they provide efficiencies of electrical power supply in the range of 35 to 55%, whilst causing very low levels of pollutant emission. Fuel cells can in principle be built in a wide range of power ratings, from a few mW to several MW, and can be used in a wide variety of applications, from miniaturised portable power (effectively substituting the battery in portable electronic devices) through transport (as a zero-emission propulsion system) to power generation in a variety of sizes (from domestic combined heat and power systems, through to full size power stations and quad- generation). They offer advantages of weight compared with batteries, and instantaneous refuelling, similar to combustion engines.

Electrochemical energy conversion involves complex developments of materials: due to the close link between electricity flow and corrosion processes, morphological changes, building of resistive layers and exhaustion of catalytically active components, material development for enhanced lifetimes becomes the major challenge in fuel cell basic research and development. In portable applications this means a lifetime of a few thousand hours, in mobile applications of around 5 000 hours and in stationary installations around 40 000 hours and more. This implies allowable degradation rates from steady-state operation of some percent per 1000 hours of operation down to 0.25% and less for power generation.

At the same time, the topics of low-cost materials and processing have to be additionally tackled in order to achieve acceptable market costs. The reconciliation of high-performance materials with low degradation and low-cost targets is an extremely challenging issue.

Fuel cells today have to further evolve from laboratory prototypes into rugged, robust units that can cope with mechanical as well as electrochemical ‘stress’ and be operated at will with as little restrictions as possible whilst offering value for money and being a desirable product for the general customer. No matter what fuel cell type is considered, the issue of ageing and ruggedness in everyday operation is of major concern. If cost reduction is one main driver in bringing fuel cells to the market,

long lifetime and robust and reliable operation are the issues to be addressed to ensure quality and suitability as consumer product.

The projects supported by the EU address long-term issues within the whole range of fuel cell types, with a focus on the **high temperature technologies** (mainly Solid Oxide, **SOFC**) and **low temperature technologies** (mainly Polymer Electrolyte, **PEFC**) types where Europe has significant strength but there is need for such basic research. Issues of long-term reliability, low degradation and ruggedness also apply to the small portable types and to the Molten Carbonate (MCFC) -based devices as well as to any other fuel cell type.

### **I.1.4 Stationary and portable applications**

This category of research covers a very wide range of fuel cell sizes. At the smallest end of the market, fuel cells have the potential to replace battery power for portable equipment, from laptops to small electric wheelchairs; and to provide clean, quiet portable power in place of engine-powered generator sets.

Portable fuel cell applications are expected to be the first to market, because some of these applications will command a price premium for the cleanliness, quietness or extended operating range of the fuel cell.

Stationary fuel cell applications, for domestic or commercial power demands, have the potential to offer increased efficiency compared to conventional technology, as well as being compatible with renewable fuels, such as fuel from biomass. Stationary fuel cells are often used in Combined Heat and Power (CHP) configuration, taking advantage of their high cooling need. Such uses can range from domestic heating boilers which generate “free” electricity, to larger industrial plant, usually using natural gas as a fuel.

The aim of research, into stationary and portable fuel cell applications, is to deliver high efficiency, low cost and high durability materials for the fuel cell stack and the balance of plant components. EU research aims cover the main technological challenges which need to be overcome to ensure widespread use of portable and stationary fuel cell applications.

- **Cost** – Cost reduction is required to ensure fuel cell technology becomes competitive with conventional technologies via new materials development, low-cost, high-volume manufacture and (in the case of PEFC) minimising the use of precious metals in the stack. The cost of fuel processors is currently high due to its operating temperature requiring high temperature precious metal materials.
- **Durability and Reliability** – Increased durability is required to ensure full life operation for the demanding requirements of both portable and stationary applications. Durability requirements of fuel cell stacks must include tolerance to impurities such as CO<sub>2</sub>, sulphur

and ammonia, in addition to mechanical durability, which is required to be > 40000 hours for stationary applications and “maintenance free for life” for smaller portable units.

- **Packaging** – Packaging and weight are critical especially for portable applications for ease of use. This includes both the fuel cell stack and the balance of plant components. Component miniaturisation for portable applications will be required. This will include miniaturisation of small scale fuel processing, micro-compressors, fuel storage and distribution.
- **Thermal, Air and Water Management** – Thermal management process includes heating, cooling and steam generation, which requires advances in heat exchange systems. Water management techniques to address humidification requirements and to maintain the water balance are required, especially in miniature portable applications where externalised humidity is unacceptable.

### **I.1.5 Transport applications**

Energy efficient, very low polluting and greenhouse-gas-neutral transport are key objectives of European transport and energy policies. Transport propulsion research is addressing this need at every level, from advanced conventional technologies such as clean and efficient internal combustion (piston and turbine engines) and hybrid road vehicles, to long term solutions compatible with a transition away from fossil fuel dependence. Hydrogen is a favoured transport energy vector for the future, as it can be produced by multiple means, and used in efficient fuel cells as well as in combustion engines.

Cost is a key challenge in the transport sector, in terms of both purchase and operation. Both the fuel cell and hydrogen storage could be more than ten times more expensive than their conventional counterparts if introduced today. But there are other challenges, including robustness of the product in the hands of the public, training of maintenance technicians, and satisfying authorities and users that the technology is safe.

The aim of the current EU research program is to develop and validate the technology for market conditions expected for 2020. Transport applications will have to meet criteria on performance, cost targets, safety and durability. The accompanying (hydrogen) supply and refuelling infrastructure will have to be in place.

Transportation projects focussing on Hydrogen and Fuel Cells within EU research programs cover a variety of these topics, including key prime mover technologies, peripheral systems, critical components, training and education. Many of these technologies are subsequently seen in demonstration projects.

A large part of the UE objectives are dedicated to transport applications focuses on the development of hydrogen-fuelled surface transport, with the aim to validate performance under real

world conditions, including hydrogen supply infrastructures, in subsequent demonstration projects. However, research for aircraft and shipping applications is also emerging. The objective is that Hydrogen and Fuel Cell road vehicles will meet challenging performance, durability, safety and cost targets by 2015, anticipating mass-market rollout in 2020.

Technical developments on critical components will often target road applications, whose market requirements are the most technically and economically challenging; however, road applications are of great long-term policy relevance for the EU and receive the highest level of investment by the respective industries.

It is expected that lead applications will spin-off benefits to other (transport) applications without any important additional component developments. System integration activities and clearly defined industrial targets (system performance targets) are of prime importance to make sure every application fulfils its own needs; cost reduction will remain a prime target in any future work.

It is in this research topic where the CELINA project is placed. In next paragraphs the CELINA project will be explained in further details.

## I.2 The CELINA project

Aircraft maker estimations show that aircraft electrical power consumptions will highly increase in next years [Langlois2]. Therefore, new high efficiency and environmental friendly electrical energy sources must be investigated. Fuel cells seem to be candidates for this purpose. Furthermore, other non European aircraft companies have already been interested in fuel cell possibilities in aeronautical applications [Dagett], [Friend].

The abstract of the CELINA project description of work [DOW] defines the objectives of the project as follows: *“For the next aircraft generation the pneumatic and hydraulic systems will be replaced step-by-step by electrical systems. The goal for the future is to find a highly efficient primary electric power source. Fuel cell systems have the potential to be a highly efficient system with a significantly reduction of fuel consumption and noise and gaseous emissions. As a drop in possibility the fuel cell application as emergency power supply will be investigated. A feasibility study will be carried out to clarify in which operational scenarios like stand by, continuously running or power storage the fuel cell system is able to work. The technical focus of the project is therefore the investigation of the technical capabilities of an existing fuel cell system under special aircraft operation conditions and the identification of the needs for an airworthy design. Investigations of the behaviour and limiting conditions of the fuel cell system in terms of different system parameters such as performance output, thermal management, mass flow, cooling and air supply will be carried out. For these investigations dynamic simulation models of a fuel cell stack and a kerosene reformer will be used and verified by tests as far as possible. The scientific approach is the investigation of the operational behaviour of the complete fuel cell system including kerosene reformer, fuel cell stack, air supply and all subsystems based on simulation models in terms of aircraft environment operational conditions, aircraft load conditions, thermal management, mass flow, performance, air supply and cooling. A study works out the differences between the current fuel cell systems and an airworthy design and describes the technical steps, which have to be done to develop an airworthy fuel cell power system. Another main focus is the development of all relevant safety and certification requirements for the fuel cell system. A preliminary safety assessment for a fuel cell system on board of an aircraft will be carried out. A further essential task is the integration trade-off of the fuel cell system into the aircraft environment with investigating of integration strategies and concepts.”*

AIRBUS and DASSAULT requirements have forced to choose a Proton Exchange Membrane (PEM) fuel cell technology, and due to space reasons, the number of fuel cell stacks is limited to one. In other words, **all the required power will have to be supplied with only one fuel cell stack.** AIRBUS and DASSAULT have chosen the total electrical generation failure as the most constraint mission. Thus, this mission will be used as the sizing mission (Figure I. 3).

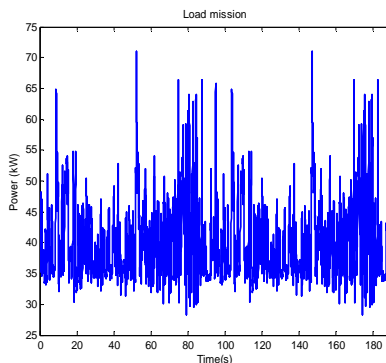


Figure I. 3: Airbus emergency mission power profile.

This PhD study is basically focused in the design of the aircraft electrical network. The three main goals of the PhD could be defined as follows:

- **Electrical architectures to connect a fuel cell system into an aircraft electrical network.**

The fuel cell system must be able to supply all the load power, included peaks power, with high electrical quality. Nevertheless, a fuel cell system needs auxiliary devices such as hydraulic pumps, compressors...for a correct operation. Auxiliary devices limit the fuel cell system dynamics response, and thus the hybridization of the fuel cell with an external energy source, such as ultracapacitors and batteries, seems mandatory. Furthermore, previous works have proved that hybridization can lead to system weight [Langlois] and/or fuel consumption [Markel] reduction

Hybridization introduces a variety of different architectures that have to be analyzed, and that means the global electrical system control analysis and the system efficiency and weight estimation.

The study of the electrical architectures will be analyzed in chapter II.

- **Design and simulation of Power Conversion (DC/DC converters).**

Due to the fuel cell stack supplied voltage characteristics, a conditioning interface must be placed between the fuel cell and the electrical network. **Furthermore, the difficulty is increased because the chosen electrical network is a  $\pm 270$  volts and AIRBUS requirements limit to only one stack as energy source (no modularity is possible with the stacks!).** Obviously the maximum possible efficiency is highly desired and in order to achieve these goals the modularity of the power converters has to be considered.

The power converter design will fully detailed in § chapter III.

- **Global system optimization.**

In transportable applications the system volume and weight acquire an extremely importance. Therefore, fuel consumption (hydrogen in this case) and global system cost must be minimized. Thus,

all the proposed solutions must be evaluated in terms of weight, volume, cost (if possible) and fuel consumption in order to make possible a final architecture choice.

The global system optimization problem is treated in § chapter IV.

Figure I. 4 summarizes the objectives of this PhD study. Indeed, Figure I. 4 shows the most general possible electrical architecture for the fuel cell system. Up to three power converters can be connected in order to adapt the fuel cell and the storage devices to the DC electrical network requirements. Nevertheless, it must be noticed that the final system must respect the electrical network requirements, and furthermore, it must be optimized in terms of weight, volume and cost. Not all the possible architectures will lead to the same results.

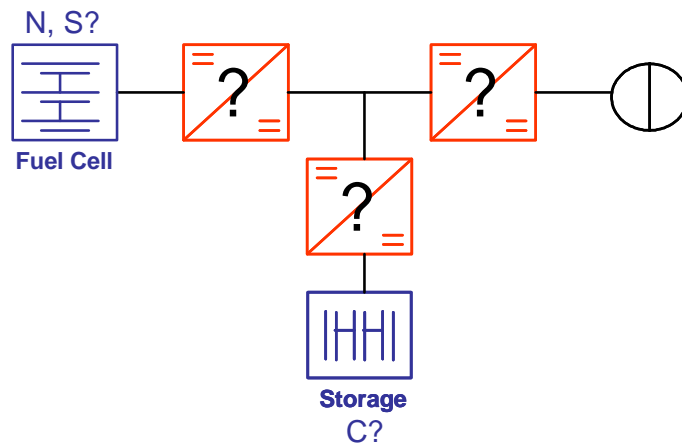


**Figure I. 4: Challenge for the CELINA project system design.**

Furthermore, the global system must be sized. In other words, the cell number  $N$ , the cell surface  $S$  and the capacitance  $C$  of the storage device must be identified.



### I.3 Hybridization: power sharing

Transport application mission power profiles are usually composed by permanent and transitory loads. Permanent loads are the loads that consume the same amount of power during the whole mission, independently from the pilot control actions. These kinds of load in an aeronautical application are: aircraft pressure conditioning systems, air-conditioning, electronics equipment power supply... On the other hand, transitory loads are the loads that are due to the pilot control actions. Transitory power load duration will be only a few seconds. Thus, the mission power profile will be formed by a permanent load and a succession of different transitory loads due to the pilot maneuvers.

In the Airbus mission example power profile in Figure I. 5, 40 kW constant power must be supplied (mean power). Therefore, a succession of transitory loads increases the maximal power consumption up to 70 kW that makes a difference of 30 kW between the maximal power consumption and the mean power consumption.

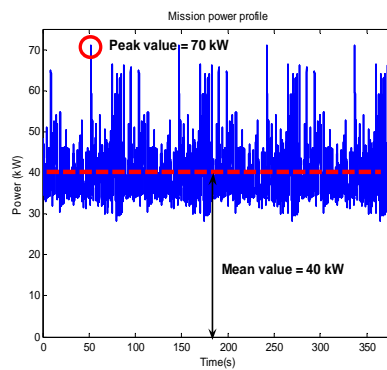


**Figure I. 5: Mission power profile. Source Airbus F.**

Therefore, it seems that sizing a fuel cell stack in order to supply 70 kW only for a few seconds is not the best strategy. If an OverSizing Rate  $OVSR$  is defined:

$$OVSR = \frac{\max(\text{Power}) - \text{mean}(\text{Power})}{\max(\text{Power})} = \frac{70e3 - 40e3}{70e3} = 0.42 \quad \text{E I.1}$$

The  $OVSR$  gives an idea about the energy source oversizing. An  $OVSR$  value close to zero means that the power availability of the energy source is well used. The energy source will supply its nominal (and sized) power during the majority of the mission. In the other side, an  $OSVR$  value close to one means that the nominal (and sized) fuel cell power is only used occasionally. Thus, in the Airbus application example, it is possible to say that the energy source (the fuel cell) is far away from an optimized use. Langlois has already proved that hybridization can lead to system weight and volume reduction [**Langlois**].

However, this is not the only reason that proves the need of hybridization. In the CELINA project, the proposed energy source is an air-compressed fuel cell. Air-compressed fuel cells need auxiliary devices like hydraulic pumps, compressors... that will permit correct hydrogen air supplying. Moreover, it was initially foreseen that hydrogen could be supplied through a kerosene reformer.

Air supplying auxiliary devices and kerosene reformers present more or less poor dynamics response. That means that for an important power load steps, the air-pressurized fuel cell will not be able to supply power, or the auxiliaries will create important power demands to response the load power steps. In the first case, this is not tolerated because the load power must always be guaranteed, and the second case presents poor system efficiency.

Therefore, hybridization seems mandatory in the case of the CELINA project.

### I.3.1 Definition of hybridization notions

In the next lines some notions will be often used. Therefore, we propose to define all of them.

- **Source hybridization:** for a given mission power profile and for  $n$  sources, the source hybridization proposes to share the load power between all the sources. The hybridization can be done in parallel and/or in series, depending on the sources connection. The power sharing between sources can be obtained by applying the methods proposed in § I.3.5
- **Energy source:** for a given mission, the sources that supply a mean power greater than zero ( $\text{mean}(P_s) > 0$ ) are called energy sources. In the CELINA project, the fuel cell stack is the energy source.
- **Power source:** for a given mission, the sources that supply a mean power equal to zero ( $\text{mean}(P_s) = 0$ ) are called power sources. In the CELINA project, the storage devices are the energy sources.
- **Direct hybridization:** the hybridization is called direct hybridization if the sources are connected directly (without any power electronics interface). There are no freedom degrees in this kind of hybridization. The power sharing is obtained thank to the sources sizing. Further details in § II.3
- **Indirect hybridization:** the hybridization is called indirect hybridization if the sources are connected through a power electronics interface.

### I.3.2 Ideal hybridization

In all cases, the sum of the energy and power sources must be equal to the load power. Thus:

$$P_{Esource} + P_{Psource} = P_{Load} \quad \text{E I.2}$$

Furthermore, the supplied power can be divided in two components: the mean value and the alternative value.

$$P = \langle P \rangle + \tilde{P} \quad \text{E I.3}$$

Applying the definitions in § I.3.1:

$$P_{Esource\ moy} = \frac{1}{T} \int_0^T P_{Esource} dt \quad \text{E I.4}$$

$$\langle P_{Psource} \rangle = \frac{1}{T} \int_0^T P_{Psource} dt = 0$$

With  $T$  the mission duration.

Thus the load power can be written as:

$$\langle P_{Esource} \rangle + \tilde{P}_{Esource} + \tilde{P}_{Psource} = \langle P_{Load} \rangle + \tilde{P}_{Load} \quad \text{E I.5}$$

Assuming a total filtering  $\Leftrightarrow \tilde{P}_{Esource} = 0$ . This leads to:

$$\langle P_{Esource} \rangle + \tilde{P}_{Psource} = P_{Load} \quad \text{E I.6}$$

According to expression E I.6 the energy source (fuel cell) supplies the load mean power and the power source (storage device) supplies the load alternative power (assuming a total load power filtering and an ideal system).

### I.3.3 Hybridization with system losses.

In the previous section no system losses were considered. In this case the power source mean value is not equal to zero.

$$\langle P_{Psource} \rangle = \frac{1}{T} \int_0^T P_{Psource} dt = losses \quad \text{E I.7}$$

**However, there is no sense to size a power source that should face the losses during the whole mission. Therefore, an energy management strategy must be implemented in the system control.** The aim of the energy management loop is to force the energy source to compensate the power source losses. Nevertheless, the losses compensation action must be respectful with the energy source dynamics. This will be further explained in § II.2.3

The power distribution, in this case, is equal to:

$$\langle P_{Esourc} \rangle + \tilde{P}_{Psourc} + losses = \langle P_{Load} \rangle + \tilde{P}_{Load} \quad \text{E I.8}$$

with:

$$\begin{aligned} \langle P_{Esourc} \rangle &= \langle P_{Load} \rangle + \langle P_{Psourc} \rangle = \langle P_{Load} \rangle + losses \\ \tilde{P}_{Psourc} &= \tilde{P}_{Load} \end{aligned} \quad \text{E I.9}$$

### I.3.4 Hybridization for the Airbus requirements.

Thus, in the Airbus case, a possible solution in order to avoid energy source oversizing is the hybridization with a power source. The power source would be in charge, roughly speaking, to supply the power peaks and the energy source would supply the power mean value. Thus, the size, weight and volume of the energy source will be reduced. The final weight of a hybridized system (energy + power source) will be lower than a system with a full power sized system.

Furthermore, power sharing must be respectful with the fuel cell system limitation dynamics. The assigned fuel cell power cannot present faster dynamics variations than the auxiliary devices and reformer fastest dynamics. Faster dynamics will have to be obligatorily supplied by the power source.

There are several storage devices that can be candidates to be the power source: ultracapacitors, lithium-ion batteries, nickel-cadmium batteries... **An internal study of Airbus France [Langlois] has proved that ultracapacitors seem to be the best adapted storage devices for the Airbus case.**

[Burke],[Candusso] are successful examples of the hybridization of a fuel cell with power sources.

### I.3.5 Power sharing methods

There are different possibilities to set out the power sharing between the energy source and the power sources. Several different power sharing methods are proposed in the following lines:

#### I.3.5.1 Frequential power sharing [Chapoulie]

The frequency power sharing principle is explained in Figure I. 6. The energy source will supply an almost constant power (it will depend on the hybridization rate). During power peaks, the fuel cell will supply mean power and the load requirements will be completed by the power source. In the case that the load power is lower than the energy source power, the fuel cell extra power will be used to recharge the power source.

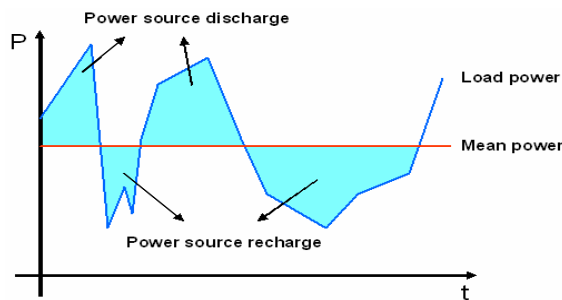


Figure I. 6: Frequential power hybridization principle.

The proposed method to obtain a correct power sharing is a load profile Fourier frequency analysis (FFT). Thus, the power mission profile is submitted to a frequency analysis and its harmonic decomposition can be obtained. **Then, a filtering frequency has to be chosen. This frequency will fix the frequency that will separate the frequencies given by the energy source and the power source.** Roughly speaking it can be said that the power source will supply the load high frequencies and the energy source will supply the lower frequencies. In all cases, it must be verified that the chosen filtering frequency is lower than the auxiliaries and reformer fastest mode ( $f < f_{aux}$ ). After this operation, the signal reconstruction can be done, and the fuel cell supplied and storage devices powers can be obtained. Figure I. 7 represents the power sharing method.

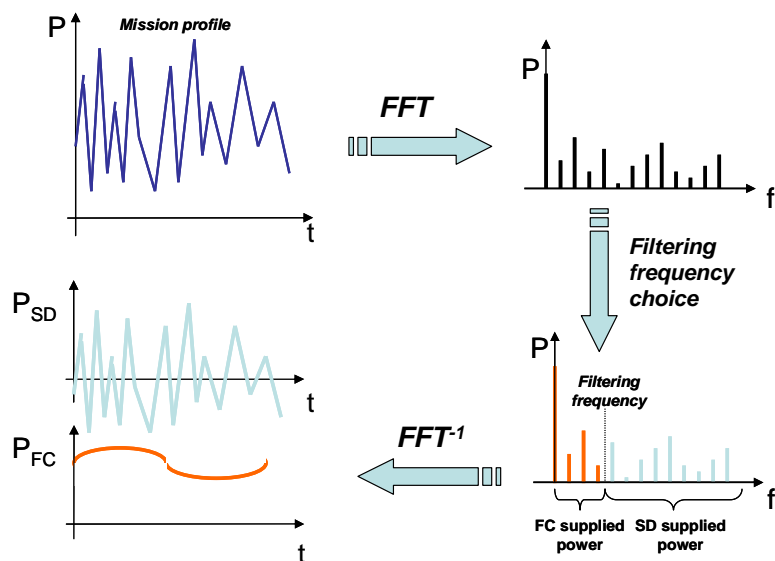


Figure I. 7: FFT analysis power sharing method.

In Figure I. 8 the frequential hybridization results are presented applied to the Airbus power profile. The filter frequency was 50 mHz.

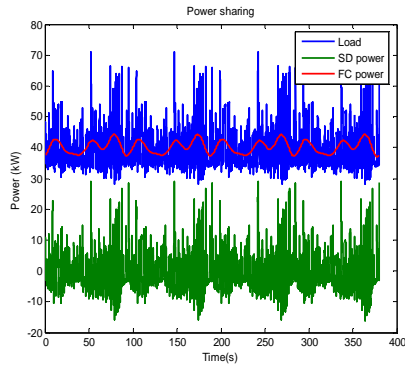


Figure I. 8: Obtained power sharing.

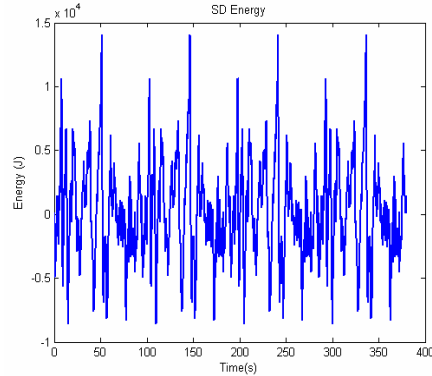


Figure I. 9: Storage device energy evolution.

The main advantage of the frequency power sharing method is that, independently of the chosen filtering frequency, the mean power supplied by the power source is always equal to zero (perfect hybridization).

Indeed, this can be easily proved thanks to the Fourier series definition.

Given a function  $f$  of real argument  $t$ ,  $f: \mathbf{R} \rightarrow \mathbf{C}$ , where  $f(t)$  is piecewise smooth and continuous, periodic with period  $T$ , and square-integrable over the interval from  $t_1$  to  $t_2$  of length  $T$ , that is,

$$\int_{t_1}^{t_2} |f(t)|^2 dt < \infty \quad \text{E I.10}$$

Where  $T = t_2 - t_1$  is the period and  $t_1$  and  $t_2$  are integration bounds.

The Fourier series expansion of  $f$  is:

$$f(t) = \frac{1}{2} a_0 + \sum_{n=1}^{\infty} [a_n \cos(\omega_n t) + b_n \sin(\omega_n t)] \quad \text{E I.11}$$

where, for any non-negative integer  $n$ ,  $\omega_n = n \frac{2\pi}{T}$  is the  $n$ th harmonic (in radians) of the function

$f$ ,  $a_n = \frac{2}{T} \int_{t_1}^{t_2} f(t) \cos(\omega_n t)$  are the even Fourier coefficients of  $f$  and  $b_n = \frac{2}{T} \int_{t_1}^{t_2} f(t) \sin(\omega_n t)$  are the odd

Fourier coefficients of  $f$ .

Thus, if the  $f$  function is the load mission profile and assuming that the power source supplies the highest harmonics, the power source supplied power will be composed by a series of sine and cosine waveforms. Therefore, the power source mean value is equal to zero because the mean value of a sine or a cosine is zero.

### I.3.5.2 Band power sharing

Another strategy to share power between sources is to use the power source as a power complement to the energy source from a maximal power limit  $P_{max}$ . In other words, the fuel cell will supply all the mission power if the load power is under maximal power limit  $P_{max}$ . If the load power is over  $P_{max}$ , the fuel cell will supply power up to  $P_{max}$  and the power source will assume the extra power. This strategy is inspired in the works of Büchi [Büchi].

Nevertheless, if there is a maximal power limit, the power source cannot be recharged, because there is no “negative” power flow. Thus, a minimal power limit  $P_{min}$  must be also defined. If the mission power profile is under this value, the fuel cell will supply a constant  $P_{min}$  power. The extra power will be used to recharge the power source. Figure I. 10 presents this power sharing method.

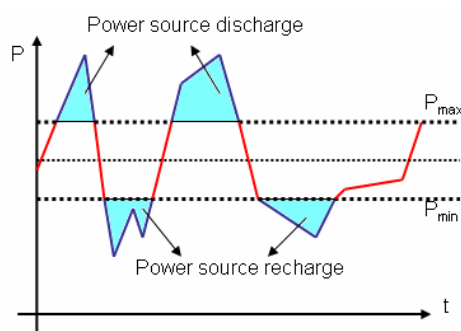


Figure I. 10: Power complement power sharing.

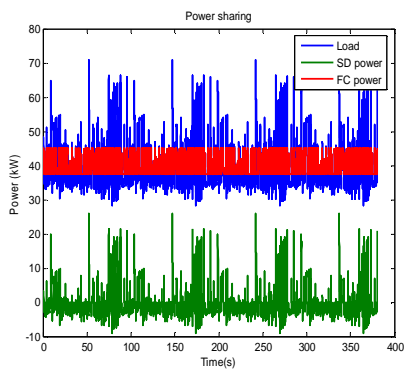


Figure I. 11: Obtained power sharing.

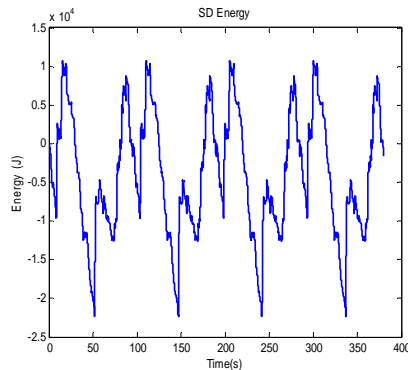


Figure I. 12: Storage device energy evolution.

Figure I. 11 shows the obtained power sharing with a  $P_{max}$  of 45 kW. It can be observed that the power supplied by the fuel cell never exceeds this amount of power.

This power sharing method seems to be well adapted to pure hydrogen and pure oxygen fuel cells. Indeed, pure hydrogen pure oxygen fuel cells do not have (or at least they are less limited) dynamics limitations due to auxiliaries, and thus, it is possible to supply power with higher dynamics. In this case, the hybridization aim is just to reduce the global system weight. Nevertheless, it also

could be possible to apply this method to an air-pressurized fuel cell in the case of smooth power profiles.

Nevertheless, one of the main drawbacks of this power sharing method is to determine the minimal power  $P_{min}$  that makes the power source mean value equal or almost equal to zero. Indeed, the minimal power  $P_{min}$  is the degree of freedom that permits to obtain a storage device whose mean power is equal to zero. Apparently, it seems that no literal law exists to fix this value (nevertheless, the time dedicated to the study of this case was limited). Indeed, the minimal power value depends on the studied power profile. In this case,  $P_{min}$  was obtained after a numerical sweeping of different values and the value that minimized the power source mean power was retained. In this case  $P_{min}$  was fixed at 37.5 kW.

### I.3.5.3 Slope power sharing

Some fuel cell makers use to express the fuel cell stack dynamics limitations in terms of power response slope. For positive load steps, fuel cells makers usually fix the maximal power slope that can be achieved. Nevertheless, there are no limitations for negative load steps, and the fuel cell can response instantaneously. This can be easily explained because the fuel cell stack has enough gas supply in order to face negative load steps, which is not the case with positive steps where the fuel cell system must wait for the auxiliaries' response.

In all cases, maximal fuel cell power  $P_{max}$  should be fixed in order to limit the maximal power supplied by the fuel cell. The power sharing could be defined as in Figure I. 13 [Dang bang]:

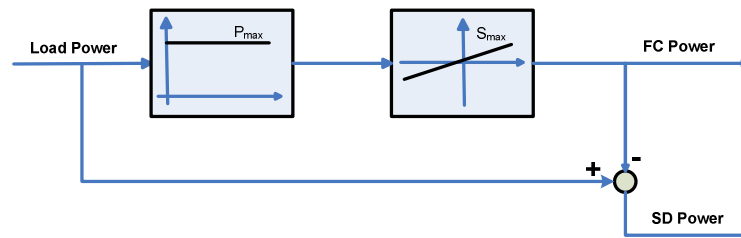


Figure I. 13: Slope power sharing.

As it was the case with the band power sharing, the main drawback with this kind of power sharing is once again to obtain a storage device whose mean power is equal to zero. In this case, only the positive slope limitation is imposed, and thus, the negative slope limit is the degree of freedom that permits to obtain a storage device mean power equal or almost equal to zero. Nevertheless, it seems that there is no literal law to identify the negative slope limit that leads to a storage device mean power equal to zero. Similarly to the band power sharing case, this value is determined after a numerical sweeping. Figure I. 14 shows the obtained power sharing for an 800 W/s slope limitation. The negative slope limit was 592 W/s.



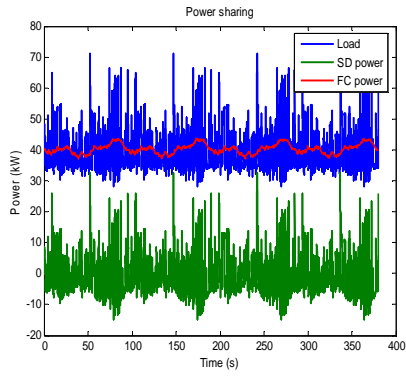


Figure I. 14: Obtained power sharing.

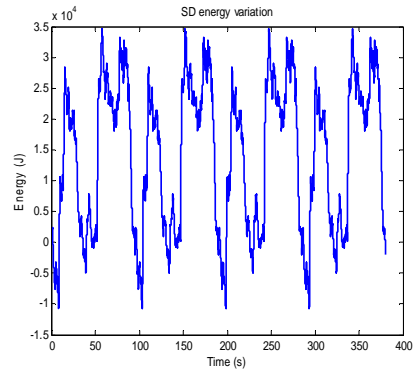


Figure I. 15: Storage device energy evolution.

Figure I. 9, Figure I. 11, Figure I. 12 and Figure I. 15 show the storage device energy evolution through the time. It can be observed that the storage device use is totally different according to the chosen power sharing strategy.

## I.4 Generic sizing methods

As explained in previous paragraphs, the final system is composed by two different energy sources: the fuel cell as main energy source, and ultracapacitors as power sources. In the following lines, the two devices and their associated generic sizing methods are presented. **They are called “generic sizing methods” because they do not take into account the existent coupling in the final system.** In other words, the generic methods size the devices individually and in order to obtain a device capable to supply power for a given power profile if there are no other devices interacting in the same system.

### I.4.1 Fuel cell stack

#### I.4.1.1 Generalities [Raissi]

A fuel cell is an electrochemical energy conversion device. It produces electricity from external supplies of fuel (on the anode side) and oxidant (on the cathode side). These react in the presence of an electrolyte. Generally, the reactants flow in and reaction products flow out while the electrolyte remains in the cell. Fuel cells can operate virtually continuously as long as the necessary flows are maintained.

Many combinations of fuel and oxidant are possible. A hydrogen cell uses hydrogen as fuel and oxygen as oxidant. Other fuels include hydrocarbons and alcohols. Other oxidants include air, chlorine and chlorine dioxide. According to the electrolyte, it is possible to classify fuel cells as in Table I. 1

Comparison of Fuel Cell Technologies

Fuel Cell Type	Common Electrolyte	Operating Temperature	System Output	Efficiency Electrical	Applications	Advantages	Disadvantages
Polymer Electrolyte Membrane (PEM)*	Solid organic polymer poly-perfluorosulfonic acid	50 - 100°C 122 - 212°F	<1kW – 250kW	53-58% (transportation)  25-35% (stationary)	•Backup power •Portable power •Small distributed generation •Transportation	•Solid electrolyte reduces corrosion & electrolyte management problems •Low temperature •Quick start-up	•Requires expensive catalysts •High sensitivity to fuel impurities •Low temperature waste heat •Waste heat temperature not suitable for combined heat and power (CHP)
Alkaline (AFC)	Aqueous solution of potassium hydroxide soaked in a matrix	90 - 100°C 194 - 212°F	10kW – 100kW	60%	•Military •Space	•Cathode reaction faster in alkaline electrolyte, higher performance	•Expensive removal of CO <sub>2</sub> from fuel and air streams required (CO <sub>2</sub> degrades the electrolyte)
Phosphoric Acid (PAFC)	Liquid phosphoric acid soaked in a matrix	150 - 200°C 302 - 392°F	50kW – 1MW (250kW module typical)	32-38%	•Distributed generation	•Higher overall efficiency with CHP •Increased tolerance to impurities in hydrogen	•Requires expensive platinum catalysts •Low current and power •Large size/weight
Molten Carbonate (MCFC)	Liquid solution of lithium, sodium, and/or potassium carbonates, soaked in a matrix	600 - 700°C 1112 - 1292°F	<1kW – 1MW (250kW module typical)	45-47%	•Electric utility •Large distributed generation	•High efficiency •Fuel flexibility •Can use a variety of catalysts •Suitable for CHP	•High temperature speeds corrosion and breakdown of cell components •Complex electrolyte management •Slow start-up
Solid Oxide (SOFC)	Solid zirconium oxide to which a small amount of Ytria is added	650 - 1000°C 1202 - 1832°F	5kW – 3MW	35-43%	•Auxiliary power •Electric utility •Large distributed generation	•High efficiency •Fuel flexibility •Can use a variety of catalysts •Solid electrolyte reduces electrolyte management problems •Suitable for CHP •Hybrid/GT cycle	•High temperature enhances corrosion and breakdown of cell components •Slow start-up •Brittleness of ceramic electrolyte with thermal cycling

Table I. 1: Different fuel cell technologies. Source [EEERE].

In the CELINA project the retained type of fuel cell is the Proton Exchange Membrane fuel cell (PEM). In a PEM fuel cell, a proton-conducting polymer membrane (the electrolyte) separates the anode and cathode sides. The PEM fuel cell operates at low temperatures (< 80 °C) that makes possible a quick start-up. Furthermore, solid electrolyte reduces corrosion and electrolyte management problems. In the other hand, PEM fuel cells use expensive platinum catalysts and they are high sensitive to fuel impurities. Low temperature fuel cells produce low heat energy and make co-generation no suitable. Nevertheless, the rapid start-up characteristics and the actual state of art of PEM fuel cells have been the main cause to choose this kind of technology.

In PEM fuel cells, on the anode side, hydrogen diffuses to the anode catalyst layer where it is later dissociated into protons and electrons. The protons are conducted through the membrane to the cathode, but the electrons are forced to travel in an external circuit (supplying power) because the membrane is electrically insulating. On the cathode catalyst layer, oxygen molecules react with the electrons (which have travelled through the external circuit) and protons to create water. In this example, the waste products are water vapour and/or liquid water and heat.

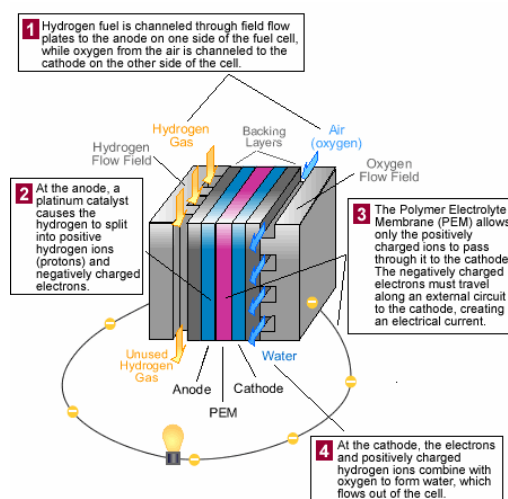
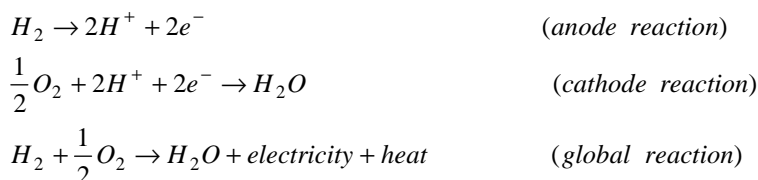


Figure I. 16: Proton Exchange Membrane fuel cell. Source [EU]

The PEM fuel cell reactions are:



Fuel cell can present higher efficiency ratios than traditional combustion energy sources (i. e. combustion engines), as they are not limited by the maximal Carnot cycle efficiency, because they do not operate with a thermal cycle. At times, this is misrepresented when fuel cells are stated to be exempt from the laws of thermodynamics. Instead, it can be described that the "limitations imposed by the second law of thermodynamics on the operation of fuel cells are much less severe than the

limitations imposed on conventional energy conversion systems". Consequently, they can have very high efficiencies in converting chemical energy to electrical energy, especially when they are operated at low power density, and using pure hydrogen and oxygen as reactants.

However, in the CELINA case, an air pressured PEM fuel cell is studied. Losses due to the air supply system must also be taken into account. This refers to the pressurization of the air and adding moisture to it. This reduces the efficiency significantly and brings it near to the efficiency of a compression ignition engine. Furthermore fuel cells have lower efficiencies at higher loads. It is also important to take losses due to production, transportation, and storage into account.

The efficiency of a fuel cell is very dependent on the current density through the fuel cell: as a general rule, the more current drawn, the lower the efficiency.

Fuel cells can be sized differently to supply the same amount of power. Different combinations of fuel cells surface and number of connected serial cells will lead to same power fuel cell stacks. This will be farther analyzed in § I.4.1.3.

#### I.4.1.2 Electrical model of a fuel cell stack.

A single fuel cell is modelled according to the models proposed by Kim and Dicks [Kim], [Dicks].

$$V_{cell} = E^0 - \frac{R}{S} I - A \ln \left( \frac{I + i_n S}{i_0 S} \right) \quad \text{E I. 12}$$

- $E^0$  is a constant determined thanks to experimental measures (Attention: it is not the theoretical voltage or the open circuit voltage).
- $\frac{R}{S} I$  models the ohmic and the lineal term of the diffusion losses. They depend lineally on the current value. Other literature authors [Fontes] models the diffusion losses with a logarithmical term. Nevertheless, if the limit current is much greater than the operation current, it is possible to linearize this term.
- $A \ln \left( I + \frac{i_n}{i_s} \right)$  models the activation voltage drop ("overvoltages" for the electrochemical engineers). It translates in a simplified way the chemical reaction kinetics laws for both electrodes.

The voltage of a cell is typically inferior to 1 volt. In order to create an enough voltage level, the cells are stacked and electrically associated in series to form a fuel cell stack. Assuming a perfect voltage distribution between the stack cells, a fuel cell stack can be modelled as follows:

$$V_{STACK} = N \left( E^0 - \frac{R}{S} I - A \ln \left( \frac{I + i_n S}{i_0 S} \right) \right) \quad \text{E I.13}$$

with  $N$  equal to the stack cell number.

Thus, a fuel cell is intrinsically modular. Two degrees of freedom can be exploited: the cell surface  $S$  which fixes the current of the fuel cell stack and the number of elementary cells stacked in series  $N$  which fixes the voltage of the fuel cell stack. Naturally there are limits for these two degrees of freedom: to date, one speaks about  $800 \text{ cm}^2$  for the maximum surface and about 400 cells stacked in series at best [Ballard], [Hydrogenics]. So a fuel cell naturally delivers its electric power in the shape of a low voltage and a high current.

The current/density voltage and the current density/power plots of a 50 kW maximal power fuel cell are presented in Figure I. 17 and Figure I. 18. The stack is composed by 374 elemental stacked cells and a cell surface of  $272 \text{ cm}^2$ .

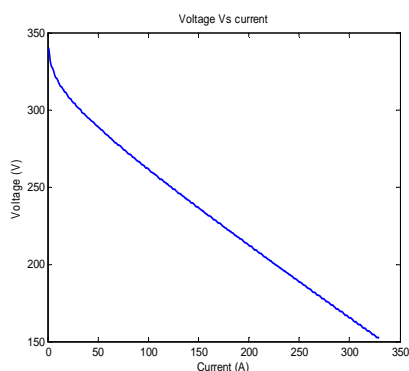


Figure I. 17: Current density with voltage.

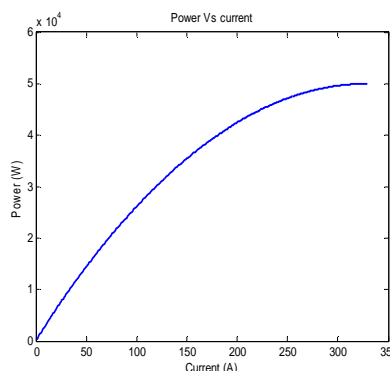


Figure I. 18: Current density with power.

However some considerations have to be done. The fuel cell maximal power is 50 kW, but according to CELINA consortium references, **the fuel cell current density  $J$  should be limited to  $0.8 \text{ A/cm}^2$** . That means that the **real usable power** of the previous fuel cell is reduced to 40 kW approximately.

#### I.4.1.3 Stack size. Cell surface and cell number influence

Cell number and cell surface can be differently combined to obtain the same maximal power value for a fuel cell stack. Fuel cell stack with “big surface” needs lower cell number to obtain the desired power. In the other side, fuel cell stack with small surface needs a bigger amount of cells to reach the desired power.

This is proved in Figure I. 19 and Figure I. 20, where different combinations of cell surface and cell number are considered for a 50 kW stack. However, the response of these stacks in terms of current and weight will not be identical for the same load. Indeed, high cell surface sized stacks will

supply higher current and lower voltage values than the low surface sized fuel cell stack and vice versa.

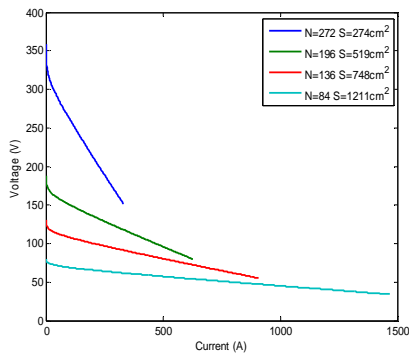


Figure I. 19: 50kW stacks current with voltage.

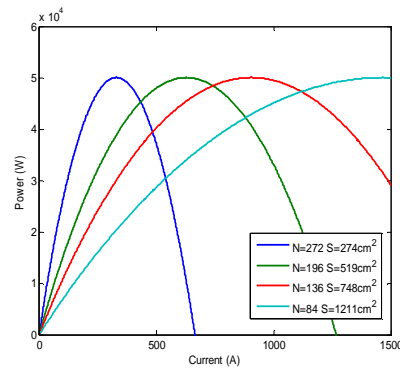


Figure I. 20: 50 kW stacks Current with power.

Nevertheless same power sized fuel cell stacks have the same current density/power plot, as it is shown in Figure I. 21. This means that for the same load power, all the fuel cell stacks supply power with the same current density.

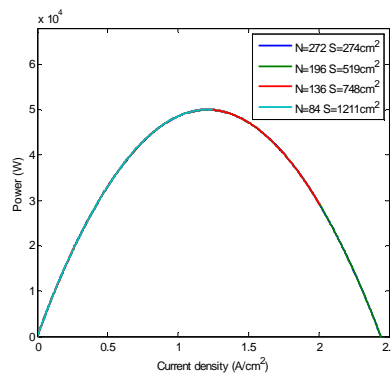


Figure I. 21: 50 kW stacks current density with power.

The power of a fuel cell stack could be defined as follows:

$$P_{STACK} = I_{FC} N \left( E^0 - \frac{R}{S} I_{FC} - A \ln \left( \frac{I_{FC} + i_n S}{i_0 S} \right) \right) \quad \text{E I.14}$$

The fuel cell current value  $I_{FC}$  will depend on the cell number and the cell surface (even if the stacks supply the same power). Thus, it is also possible to write E I.14 in function of the maximal current density. This leads to:

$$P_{STACK} = J_{FC} S N \left( E^0 - \frac{R}{S} J_{FC} S - A \ln \left( \frac{J_{FC} S + i_n S}{i_0 S} \right) \right) \quad \text{E I.15}$$

Simplifying, we obtain:

$$P_{STACK} = J_{FC} S N G \quad \text{with} \quad G = \left( E^0 - R J_{FC} - A \ln \left( \frac{J_{FC} + i_n}{i_0} \right) \right) \quad \text{E I.16}$$

Thus, if two stacks are sized to supply the same power:

$$P_{STACK} = J_{FC} S_1 N_1 G = J_{FC} S_2 N_2 G \quad \text{E I.17}$$

The  $G$  term is identical for both stacks, because, as it was proved in Figure I. 21, same power sized stacks operate with the same current density values. Thus,

$$S_1 N_1 = S_2 N_2 \quad \text{E I.18}$$

And assuming that both stacks are made with the same bipolar plate width, we can find between the volumes of the fuel cell stacks:

$$Vol_1 = Vol_2 \quad \text{E I.19}$$

Thus, for a given power, the volume is unchanged whatever cell number and cell surface.

Figure I. 22 presents the different cell number and cell surface couples that leads to the same fuel cell stack sizing. Isopower bars are plotted in kW. Furthermore it is possible to confirm the parabolic law shown in E I.17.

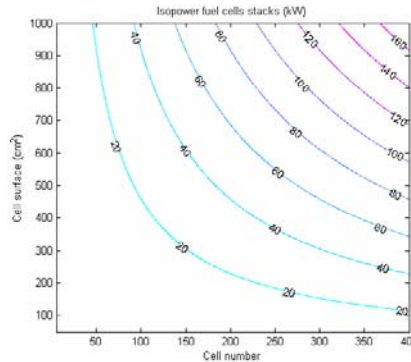


**Figure I. 22: Isopower fuel cell stacks (in kW) with cell number and cell surface ( $J=0.8A/cm^2$ ).**

#### I.4.1.4 Weight model of the fuel cell stack

Due to the transportation application of the CELINA project, the fuel cell stack weight becomes a crucial issue for the system design. We, thus, had to develop a generic calculation in order to estimate the fuel cell stack mass. The difficulty of this work is that a mass estimation is ever strongly linked to the implemented technology. Two choices were possible:

To consider roughly the current and future ( $\approx 1\text{kg/kW}$ ) in order to estimate very simply the fuel cell stack mass.

To calculate the weight in details and in a modular and generic way.

The second possibility was chosen, and we were confronted to the problem of the technology knowledge. A lot of choices are possible for material and architectures (fluidic, thermal, electrical...) to design a fuel cell stack. In order to avoid any confidentiality difficulty in the CELINA consortium, we choose to start from a published study carried out in the UK by Davies [Davies] (even if some data of this study are unfortunately confidential). This work was developed for the company Advances Power Sources APS Ltd. The choice of this study is due to the good performances obtained by Davies.

Davies succeeded in developing a compact and lightweight 14-cell air-pressurized PEM stack, using carbon bipolar plates. An electrical power output of 1.47 kW was achieved at 0.7 V/cell. The obtained power density was 1.1 kW/kg and volumetric density was 1.7 kW/l. Both results were achieved at high efficiency and high gas utilization rates, which are function of the overall design, and in particular of the APS Ltd gas channel design in the bipolar plate (unfortunately confidential!).

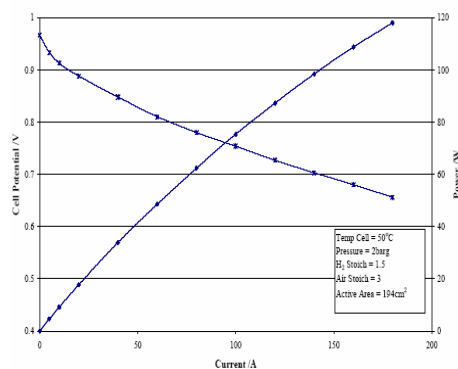


**Figure I. 23: Fuel cell voltage. Source: [Davies]**

From a previous study was deduced that a 1.1 mm bipolar plate could be used, however, and in order to provide a safety margin and to ensure lower gas permeability, a slightly thicker plate of 1.35 mm was adopted.

In order to implement the 14-cell fuel cell stack, a total of 20 plates were required. This includes all gas distribution plates as well as those needed to provide water cooling. Ideally, at a fixed current, the voltage of each individual cell within the stack should be the same. However, there are a number of reasons why this is not the same. These include inconsistencies in channel geometry, pressure and temperature. To control the temperature across the stack, a number of cooling plates were included every fourth cell. This modular approach introduces a temperature profile over the four-cell repeat module.



The fuel cell stack weight model should be modular. That means that this model can estimate the fuel cell stack weight for any cell number and cell surface. The total stack volume and weight will be the sum of the bipolar plate  $bp$ , end plate  $ep$  and cooling plate  $cp$  weights and volumes.

$$W_{FCstack} = W_{bp} + W_{ep} + W_{cp} \quad \text{E I.20}$$

$$V_{FCstack} = V_{bp} + V_{ep} + V_{cp} \quad \text{E I.21}$$

### **Bipolar plates.**

We assume that the bipolar plates are in carbon with  $\rho_{bp}$  density and with  $w$  width. Nevertheless, the bipolar plates are curved with gas channels which supply the electrodes. A  $\delta_{bp}$  coefficient was introduced to take into account the presence of the gas channels in the bipolar plates. Furthermore, the bipolar plate must be bigger than the active cell surface in order to give a physical support to gas channels and stack structural devices. In order to take into account real bipolar plate surface, an increase surface coefficient  $\beta_{bp}$  is introduced.

A cell number  $N$  and cell surface  $S$  fuel cell stack is modelled as follows:

$$W_{bp} = (N + 1) S w_{bp} \beta_{bp} \delta_{bp} \rho_{bp} \quad \text{E I.22}$$

And the bipolar plates volume is given by:

$$V_{bp} = (N + 1) S w_{bp} \beta_{bp} \quad \text{E I.23}$$

### **End plates.**

We assume that the end plates containing the input and output ports for gases and water were machined from stainless steel with  $\rho_{ep}$  density. In this case, the end plates real surface is given by multiplying the active surface by a coefficient  $\beta_{ep}$  that in this case is bigger than in bipolar plates. Furthermore the end plates width it is not constant and depends on the stack length. The end plate width law has been achieved to fit the Davies results. Thus, the connecting plates weight and volume expressions are given in E I.24 and E I.25.

$$W_{ep} = 2 S ( 0.0236 N + 0.0701 ) \rho_{ep} \beta_{ep} \quad \text{E I.24}$$

$$V_{ep} = 2 S ( 0.0236 N + 0.0701 ) \beta_{ep} \quad \text{E I.25}$$

## Cooling plates

Cooling plates are added in order to equilibrate elementary cell temperature across the fuel cell stack. One cooling cell will be placed for 4 elementary cells. Unfortunately, any specification is given about cooling cells in the article. Thus, in the proposed model, it has been assumed that cooling cells have the same characteristics as bipolar plates.

$$W_{ep} = N_{ep} S w_{ep} \beta_{ep} \delta_{ep} \rho_{ep} \quad \text{E I.26}$$

$$V_{ep} = N_{ep} S w_{ep} \beta_{ep} \quad \text{E I.27}$$

The model parameters are:

S =	variable	$\rho_{bp} =$	1.86 gr/cm <sup>3</sup>
N =	variable	$\rho_{ep} =$	2.7 gr/cm <sup>3</sup>
$w_{bp} =$	1.1 mm	$\rho_{cp} =$	1.86 gr/cm <sup>3</sup>
$w_{ep} =$	0.0236 N+0.0701 mm	$\delta_{bp} =$	1/3
$w_{cp} =$	1.1 mm	$\delta_{ep} =$	1
$\beta_{bp} =$	1.1	$\delta_{cp} =$	1/2
$\beta_{ep} =$	1.1	$\beta_{cp} =$	1.2

### I.4.1.5 Gas consumption.

The fuel cell must be capable to supply the load power profile. Thus, a hydrogen flow has to be supplied to the fuel cell anode in order to guarantee the power supply.

Assuming that all gases that arrive to the fuel cell anode is consumed (that means a perfect faradic efficiency and no over stoichiometry), the gas consumption is given by:

$$n_{H_2} = \frac{N}{2F} \int_0^t I_{FC} dt \quad \text{E I.28}$$

$$n_{O_2} = \frac{N}{4F} \int_0^t I_{FC} dt \quad \text{E I.29}$$

with:

$n_{H_2}$ :	Hydrogen consumption (moles)
$n_{O_2}$ :	Oxygen consumption (moles)
N:	Elementary cells number
F:	Faraday constant = 96485 (F/mol)
$I_{FC}$ :	Fuel cell current (A)

The gases consumption depends on the cell number, and in the fuel cell supplied current. Nevertheless, in expressions E I.28 and E I.29 it is not easy to appreciate the cell surface and cell number influence on the hydrogen consumption. As it has been already explained (§ I.4.1.3), the chosen surface and elementary cells number impose the fuel cell response type, and thus, the fuel cell supplied current  $I_{FC}$ . Thanks to expression E I.15 it is possible to write the stack power as:

$$P_{STACK} = I_{FC} N G \quad \text{with} \quad G = \left( E^0 - R J_{FC} - A \ln \left( \frac{J_{FC} + i_n}{i_0} \right) \right) \quad \text{E I.30}$$

Thus, the power supplied by the fuel cell stack is equal to:

$$I_{FC} = \frac{P_{STACK}}{N G} \quad \text{E I.31}$$

Considering constant power consumption, E I.28 leads to:

$$n_{H_2} = N \frac{I_{FC}}{F} t \quad \text{E I.32}$$

Inserting E I.31 in E I.32:

$$n_{H_2} = \frac{N P_{STACK}}{N 2 F G} t = \frac{P_{STACK}}{2 F \left( E^0 - R J_{FC} - A \ln \left( \frac{J_{FC} + i_n}{i_0} \right) \right)} t \quad \text{E I.33}$$

**Expression E I.33 proves that hydrogen consumption is independent of the cell number and the cell surface. Indeed, the only parameter that influences on hydrogen consumption is the fuel cell current density  $J_{FC}$**  (it should be noticed that the impact of the fuel cell auxiliary devices on the gas consumption has not been considered). Therefore, that means that for equal power sized fuel cells (fuel cell stacks that respect relation E I.18, the hydrogen consumption is exactly the same. Nevertheless, for different size stacks (in other words, stacks that not respect E I.18), hydrogen consumption is not the same because these stacks do not supply the same power with the same current density  $J_{FC}$ . Same conclusions can be obtained with the oxygen consumption.

E I.33 proves the existent relation between the hydrogen consumption and the fuel cell size. Nevertheless, in next lines it will be confirmed graphically expression E I.33.

Figure I. 24 and Figure I. 25 show the current/voltage and the current/power curves for different stack surface values, but for the same cell number ( $N= 200$ ). Looking in details Figure I. 25 it is possible to observe that for the same load (50kW in this example), bigger surfaces supply power with lower current, and thus with less hydrogen consumption according to expression E I.28.

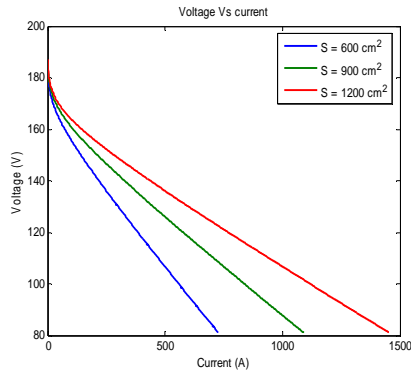


Figure I. 24: Voltage vs current.

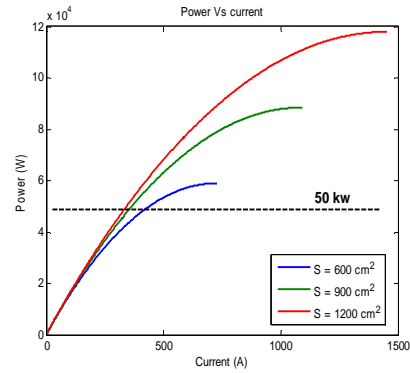


Figure I. 25: Power vs current.

In a similar way it is possible to analyze the elementary stacked cell number. Therefore, Figure I. 26 and Figure I. 27 show the three fuel cell stacks with the same surface ( $S = 100 \text{ cm}^2$ ), but different cell numbers. In this case, bigger cell number stacks supply power with lower current values. Nevertheless, in this case this current value reduction can be reduced because the hydrogen consumption expression E I.28 depends also on the cell number.

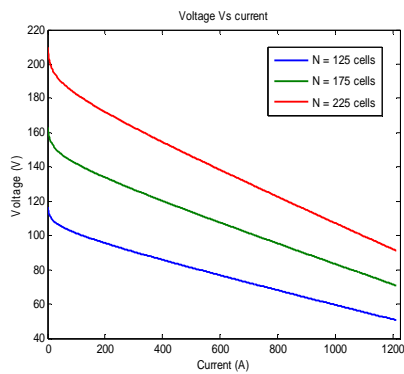


Figure I. 26: Voltage vs current.

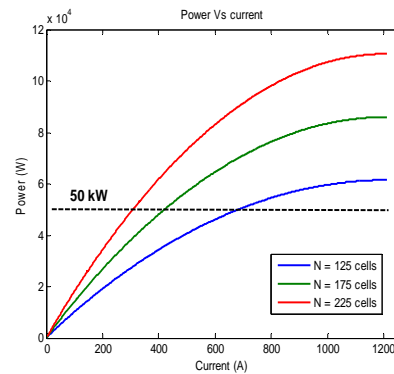


Figure I. 27: Power vs current.

#### I.4.1.6 Fuel cell stack sizing for a given mission power profile

In previous lines it has been explained that many possibilities exist to size a fuel cell stack that can accomplish a given mission. Same power fuel cell stacks can be sized in order to obtain a given voltage or current response of the fuel cell. Furthermore it is also possible to oversize the fuel cell in order to reduce the hydrogen consumption even if it is penalizing in terms of weight and volume.

Nevertheless fuel cells deliver output voltages with more or less high variations that in some cases can be up to 50 per cent of the open circuit voltage. Therefore, in most cases the use of a power electronics interface seems mandatory. DC-DC power converters adapt the fuel cell voltage to the desired DC bus voltage.

Power converters are sized to handle power with limited and well defined operation conditions. That means that they are made to operate on a range of given current and voltage. Power converter semiconductors and inductor cores are chosen according the defined range of voltage and current. Thus, if during the mission, fuel cell delivered current and/or voltage exceed the extreme values of the involved range, the power converter risks to be seriously damaged or even broken down. Therefore, it seems almost mandatory that fuel cell stack sizing method will assure that extreme conditions will not be exceeded during the whole mission.

In power converters case, extreme conditions take place at the mission maximal power point. At this moment, the maximum expected power value flows through the power converter and furthermore, the fuel cell delivers its minimal voltage value and its maximal current value. Thus, it can be interesting that the proposed sizing method will guarantee a minimal voltage value  $V_{FC}$  during the whole mission. **Therefore, the mission minimal voltage value  $V_{FC}$  is one of the chosen criteria in order to size the fuel cell stack. This criterion is fixed by the system designer.**

On the other hand, a recommended maximal current density value will ever exist for a fuel cell stacks. For higher current densities than this maximal value, several problems can indeed occur: flooding (too much water produced), thermal runaway (too much losses to evacuate), operation point instability...The maximal fuel cell current density value depends on the implemented technology, the supplied gasses (pure oxygen or ambient air), the chosen cooling and the operation conditions.

Furthermore, as it has been already explained in §I.4.1.5, the current density value is one of the parameters that fix the hydrogen consumption, or what it is the same, the parameter that fixes the fuel cell working point in the polarization curve. Low current density values reduce the hydrogen consumption and high values increase consumption. Nevertheless, the aim is to develop a sizing method that permits to design a fuel cell stack freely and not in an imposed operation point, as it could be the classical 0.7 volts per elementary cell. **Thus, the sizing method has to guarantee that during the whole mission the fuel cell current density will never exceed a given value  $J_{FC\ max}$  imposed by the system designer.**

To summarize, the proposed fuel cell stack sizing procedure will take into account two criteria that must be respected during the mission. In order to respect the usual optimization vocabulary, the sizing criteria will receive the name of design variables in §chapter IV. Due to the previously explained reasons, the chosen criteria and/or design variables are:

- The fuel cell stack must respect a pre-determined minimal voltage value  $V_{FC\ min}$  during the whole mission. The fuel cell voltage must never drop under this value.
- The fuel cell stack must always operate under a known maximal current density value  $J_{FC\ max}$  during the whole mission. The fuel cell current density must never exceed this value.

Once the two sizing criteria are known and/or imposed, it is possible to size the fuel cell stack as follows.

### Sizing procedure

From the fuel cell mission power profile, and with the desired fuel cell stack minimal voltage, it is possible to determine the maximal fuel cell current value.

$$I_{FC \max} = \frac{\max(\text{mission power})}{V_{FC \min}} \quad \text{E I.34}$$

The fuel cell stack must operate always under a pre-determined density current value  $J_{FC \max}$ . This will always arrive at the mission maximal power point or, in other words, the maximal fuel cell current  $I_{FC \max}$ . The maximal fuel cell current leads us to calculate the cell surface.

$$S = \frac{I_{FC \max}}{J_{FC \max}} \quad \text{E I.35}$$

The cells number can be calculated thanks to the fuel cell stack voltage expression E I.13 evaluated with the fuel cell maximal current  $I_{FC \max}$ . At this point, the fuel cell supplies the minimal authorized voltage  $V_{FC \min}$ . Thus, it is possible to calculate the cell number:

$$N = \frac{V_{FC \min}}{\left( E^0 - \frac{R}{S} I_{FC \max} - A \ln \left( \frac{I_{FC \max} + i_n S}{i_0 S} + 1 \right) \right)} \quad \text{E I.36}$$

At this step, the fuel cell is already sized. Though, two different operation points for the fuel cell are possible. Indeed, it is possible that the two chosen sizing criteria ( $V_{FC \min}$  and  $J_{FC \max}$ ) lead us to an operation point too close to the fuel cell maximal power (point number 1 in Figure I. 28). This would not be a valid solution. Indeed, the blue area in Figure I. 28 defines a not Valid Operation Area (VOA). Usually fuel cell makers advise not to operate close to the fuel cell maximal power point. On the other hand, if the sizing criteria lead to a fuel cell operation point in the VOA (point number 2 in Figure I. 28), the fuel cell stack size can be considered correct.

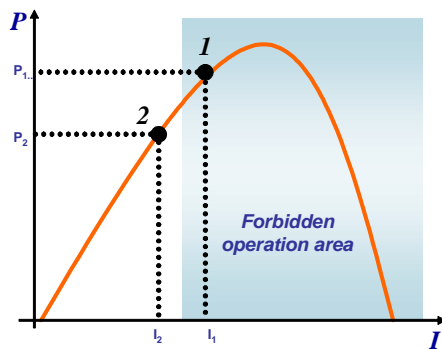


Figure I. 28: Possible operation point.

The stack cell number or the stack cell surface size (or even both of them) will have to be increased if the previous sizing has led us to an operation point like in case number 1 in Figure I. 28. Therefore, expression E I.14 can be used.

Finally, the proposed method could be schematically represented as follows:

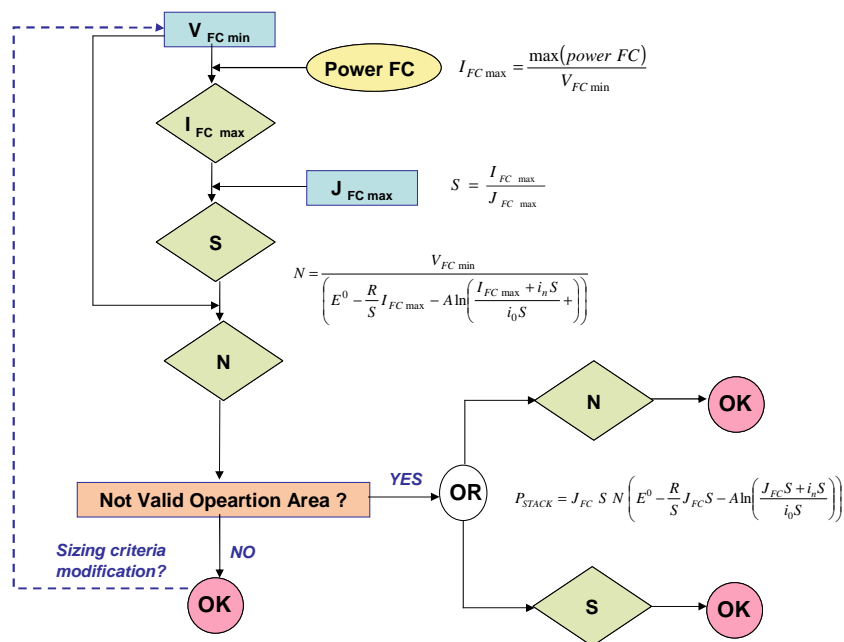


Figure I. 29: Proposed fuel cell stack sizing method.

The VOA should be defined according the fuel cell maker advice. In the CELINA project, all the fuel cells that operate with current densities higher than 0.8 A/cm<sup>2</sup> are considered not valid solutions.

In order to validate the proposed method an example is proposed. The mission power profile is presented in Figure I. 30. The fixed criteria are:

- Fuel cell stack minimal voltage value  $V_{FC \min} = 100 \text{ V}$
- Fuel cell stack maximal current density value  $I_{FC \max} = 0.8 \text{ A/cm}^2$

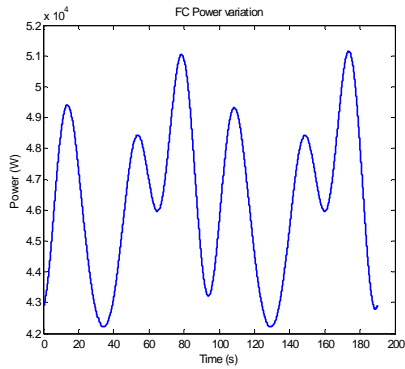


Figure I. 30: FC mission power profile (Exemple).

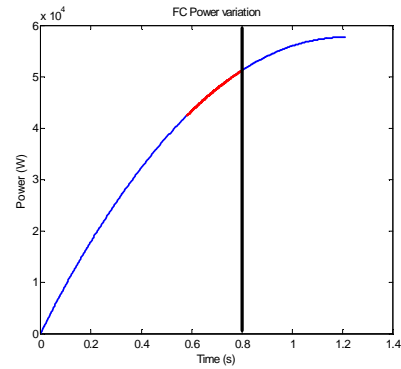


Figure I. 31: Sized Fuel cell. Operation points (red)

In Figure I. 31 and in Figure I. 32 is observed that the sizing criteria are respected. The current density maximal value never exceeds  $0.8 \text{ A/cm}^2$  and the minimal voltage value is never below 100 Volts.

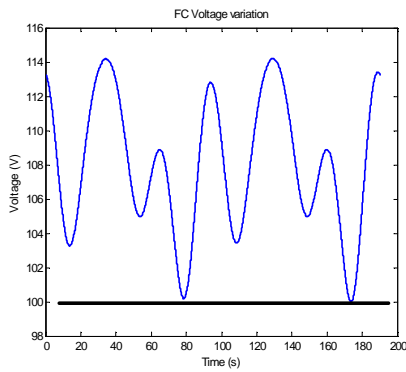


Figure I. 32: Fuel cell voltage.

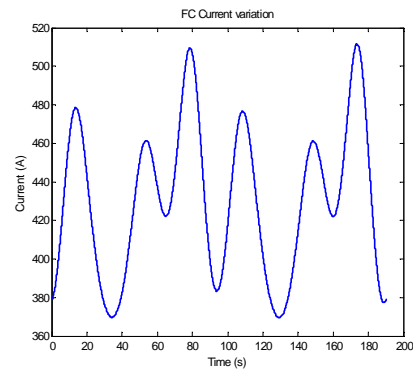


Figure I. 33: Fuel cell current.

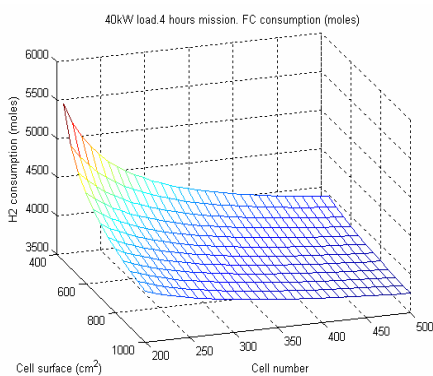


Figure I. 34: Hydrogen consumption.

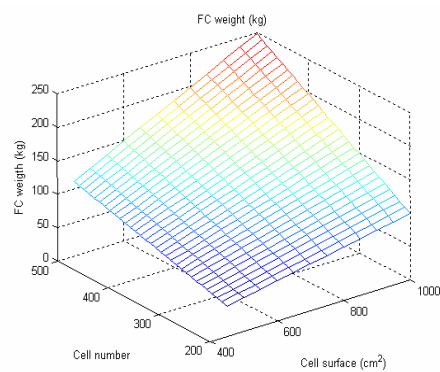


Figure I. 35: FC stack weight.

Though, the choice of the optimized sizing criteria is not an easy task. Figure I. 34 shows the hydrogen consumption for a 40 kW DC load and 4 hours mission versus the cells number and the cell surface. It is possible to observe that “big” stacks leads to lower hydrogen consumptions. This can be easily explained because “big” fuel cells supply the mission power at lower current density. However,



“big” fuel cells are obviously heavier, as it is shown in Figure I. 35. Thus, consumption and weight criteria are conflicting objectives. Therefore, the design of the fuel cell system and the choice of the optimized design variables become a complex issue. This will be further explained in next chapters.

### I.4.2 Ultracapacitors

An ultracapacitor, also known as a double-layer capacitor, polarizes an electrolytic solution to store energy electrostatically. Though it is an electrochemical device, no chemical reactions are involved in its energy storage mechanism. This mechanism is highly reversible, and allows the ultracapacitor to be charged and discharged hundreds of thousands of times.

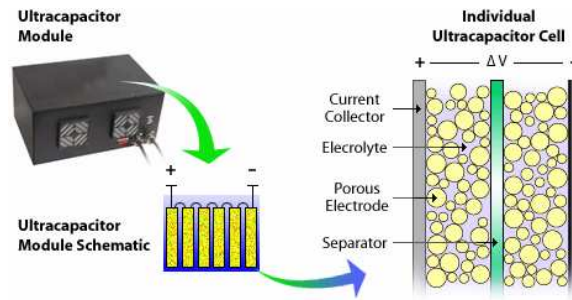


Figure I. 36: Ultracapacitor cell.

An ultracapacitor can be viewed as two non reactive porous plates, or collectors, suspended within an electrolyte, with a voltage potential applied across the collectors. A separator between the two electrodes prevents the charge from moving between the two electrodes. Contrarily to standard capacitors, there is no dielectrical layer in the electrolyte.

The amount of energy stored is very large compared to a standard capacitor because of the double layer phenomenon due to the absence of the dielectric layer in the electrolyte. Furthermore, the enormous surface area created by the porous carbon electrodes and the small charge separation (10 angstroms) created by the separator increases even more the ultracapacitors capacitance. However, it stores a much smaller amount of energy than does a battery. Since the rates of charge and discharge are only determined by its physical properties, the ultracapacitor can release energy much faster (with more power) than a battery that relies on slow chemical reactions.

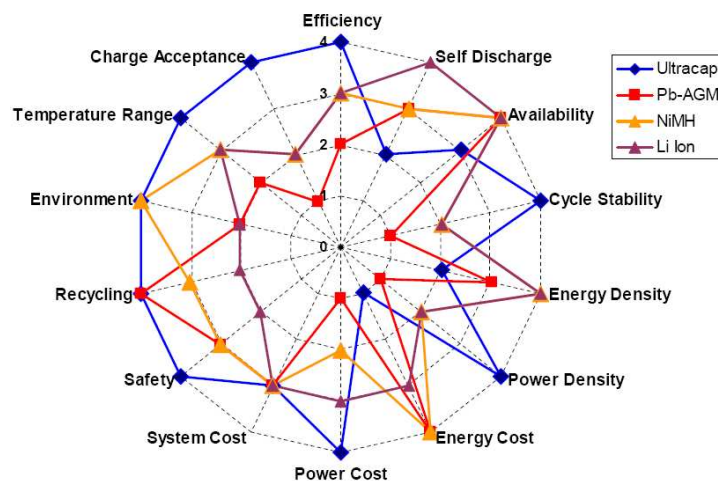


Figure I. 37: UC and batteries comparison. Source: Maxwell.

### I.4.2.1 Ultracapacitors sizing

There are two conditions that must be considered in order to determine the size of a storage device: the energy sizing and the power sizing. Indeed, the power ultracapacitor must be able to store the needed energy to face the mission, and must be able to supply this energy within the load power requirements.

As it was the case with fuel cells, ultracapacitors will be sized from a load power profile (Figure I. 38) and some pre-established sizing criteria.

#### Energy sizing

The ultracapacitor mission power profile determines the time evolution of the power that must be supplied by the ultracapacitors [Roasto]. This power can be positive (supplied power) or negative (recovered power). A power profile involves an energy time evolution that must be stored in the ultracapacitor pack. The energy variation (Figure I. 39) can be easily calculated with expression E I.37

$$E_{UC} = \int P_{UC} dt \tag{E I.37}$$

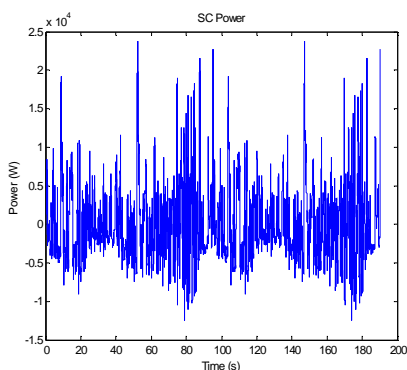


Figure I. 38: Random generated UC mission power profile.

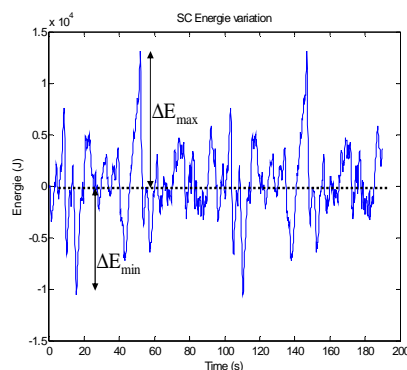


Figure I. 39: UC energy variation.

Energy variation leads to calculate the necessary energy that has to be stored in the ultracapacitor pack. The energy variation will present a maximal and minimal value point. These two points are going to define the total energy variation  $\Delta E$ . This value represents the total energy that has to be stored in the storage device.

$$\Delta E = \max(E) - \min(E) \tag{E I.38}$$

The Ultracapacitor voltage value  $V$  is an image of the stored energy and/or the State Of Charge (SOC) of the ultracapacitor pack. The energy stored in a  $C$  capacitance of one ultracapacitor pack is equal to:

$$E = \frac{1}{2} CV^2 \quad \text{E I.39}$$

The Ultracapacitor voltage cannot vary without any limit. An ultracapacitor cell can withstand a maximal cell voltage value between  $V_{UC\ cell\ max}$  2.5 or 2.7 V depending on the technological choice. Thus, the maximal voltage value that can be withstood by an ultracapacitor pack  $V_{UC\ max}$  is the maximal cell voltage  $V_{UC\ cell\ max}$  multiplied by the number of series stacked ultracapacitor cells  $n_s$ . ( $V_{UC\ max} = V_{UC\ cell\ max} \cdot n_s$ ). Furthermore, the maximal cell voltage must never be exceeded; otherwise there is a high risk to cause irreversible damages to the ultracapacitors that could even lead to the ultracapacitors explosion! **Therefore, the sizing method must guarantee that a chosen maximal ultracapacitors pack voltage  $V_{UC\ max}$  will never be exceeded during the whole mission.**

However, not all the stored energy in the ultracapacitor pack can be used. The ultracapacitor discharge under 50 % of the ultracapacitor maximal voltage presents bad efficiency [Barrade]. Indeed, due to ultracapacitor internal losses, a maximal discharge ratio can be achieved if the discharge efficiency must be greater than a given efficiency [Barrade]. Furthermore, if an eventual power converter interface is implemented in order to adapt the ultracapacitor supplied power to the load requirements, **the ultracapacitor discharge ratio must be limited in order to guarantee a minimal voltage for the correct operation of the power converter.** Thus, the ultracapacitor maximal discharge ratio  $d_{max}$ , or in other words, the minimal voltage must be limited. **Therefore, the discharge ratio can be considered as an ultracapacitor sizing criterion.** The discharge ratio  $d_{max}$  can be defined as follows:

$$d_{max} = \frac{V_{UC\ min}}{V_{UC\ max}} 100 \quad \text{E I.40}$$

Thus the sizing criteria for the ultracapacitors pack will be:

- The ultracapacitor discharge ratio  $d_{max}$ . The ultracapacitor discharge must not be under this value during the whole mission.
- The maximal ultracapacitor pack voltage  $V_{UC\ max}$ . The ultracapacitor pack voltage must not exceed this value during the whole mission.

Both sizing criteria are fixed by the system designer.

$\Delta E$  can be written as:

$$\Delta E = \max(E) - \min(E) = \frac{1}{2} C (V_{UC\ max}^2 - d_{max}^2 V_{UC\ max}^2) \quad \text{E I.41}$$

If the ultracapacitor mission initial state of charge  $V_0$  is taken into account, the previous expression can be written as:

$$E_{\max} = \frac{1}{2}CV_0^2 + \Delta E_{\max} = \frac{1}{2}CV_{UC \max}^2 \tag{E I.42}$$

$$E_{\min} = \frac{1}{2}CV_0^2 + \Delta E_{\min} = \frac{1}{2}Cd_{\max}^2 V_{UC \max}^2$$

Thus, the total capacitance value and the initial state of charge are:

$$C = 2 \frac{E_{\max} + E_{\min}}{d_{\max}^2 V_{UC \max}^2 + V_{UC \max}^2} \tag{E I.43}$$

$$V_0 = \frac{\sqrt{(E_{\max} - E_{\min})(E_{\max}d_{\max}^2 V_{UC \max}^2 - E_{\min}V_{UC \max}^2)}}{4(E_{\max} - E_{\min})} \tag{E I.44}$$

In order to illustrate the sizing method, an application example is given with the mission profile in Figure I. 38.

Sizing criteria		Sizing results	
$V_{UC \max}$ (V)	$d_{\max}$ (%)	$C$ (F)	$V_0$ (V)
80	50	9.32	62.17

**Table I. 2: Application example. Sizing criteria and sizing results of an UC pack.**

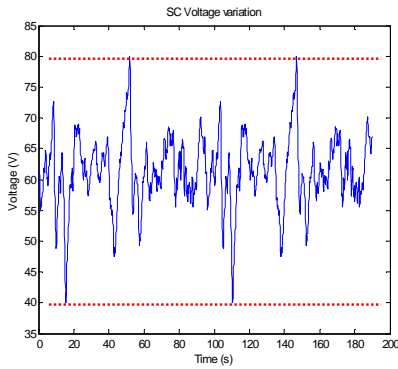


Figure I. 40: UC voltage variation.

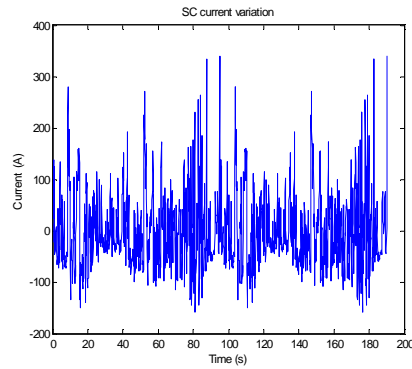


Figure I. 41: UC current variation.

The simulation results are presented in Figure I. 40 and in Figure I. 41. The sizing criteria are always respected during the whole mission profile as it can be confirmed in Figure I. 40. The ultracapacitor pack voltage evolution never exceeds the maximal authorized value  $V_{UC \max}$  and the pack discharge is never higher than 50 % of the maximal authorized ultracapacitor charge. The voltage evolution must stay between the two red lines (Figure I. 40). Nevertheless, this method does not take into account the ultracapacitor internal losses. The way to treat ultracapacitor internal losses and the

influence of losses on the pack sizing will depend on the chosen architecture. Further details will be given in next chapter (§ II.2.4) and in §I.4.2.2.

Once the ultracapacitor pack capacitance is determined, the number of elementary ultracapacitors that must be stacked in series can be easily obtained.

An ultracapacitors cell can withstand a given maximal voltage  $V_{UC\ cell\ max}$ . This value is usually between 2.5 or 2.7 V. Thus, in order to withstand the maximal ultracapacitor pack desired maximal voltage  $V_{UC\ max}$ , several elementary ultracapacitors must be connected in series. The number of elementary stacked cells  $n_s$  is given by:

$$n_s = \frac{V_{UC\ max}}{V_{UC\ cell\ max}} \quad \text{E I.45}$$

The series association of  $n_s$  elementary ultracapacitors leads to an ultracapacitor pack with lower capacitance than a single ultracapacitor  $C_{cell}$ . Thus, the capacitance of the serial connected cells is:

$$C_s = \frac{C_{cell}}{n_s} \quad \text{E I.46}$$

The series connected cell capacitance  $C_s$  has to be bigger than the calculated capacitance  $C$ . If the capacitance is lower, the number of parallel branches will have to be increased. This number is given by

$$n_p = \frac{C}{C_s} \quad \text{E I.47}$$

Thus, the total number of an elementary ultracapacitors is:

$$n_t = n_p \cdot n_s \quad \text{E I.48}$$

## Power sizing

In the previous paragraph, an ultracapacitor pack has been sized according to the energy needs for the mission. However, the power needs and the energy availability were not considered. Ultracapacitor discharge capability is proportional to the load current demands.

Usually the ultracapacitor makers fix a maximal current  $I_{UC\ cell\ max}$ . This value must not be exceeded. Thus, it must be verified that the previous sized ultracapacitor pack respect the maximal current during the whole mission.

Therefore, if the maximal mission current  $I_{UC\ max}$  is bigger than the recommended current  $I_{UC\ cell\ max}$  multiplied by the number of parallel branches  $n_p$  (we assume an homogenous current sharing between the ultracapacitor branches), the number of parallel branches  $n_p$  must be modified.

The new  $n_p^*$  will be equal to:

$$\text{If } I_{UC\ max} > I_{UC\ cell\ max} n_p \Rightarrow n_p^* = \frac{I_{UC\ max}}{I_{UC\ cell\ max}} \quad \text{E I.49}$$

Obviously, if the number of parallel branches has to be modified, the total ultracapacitor pack capacitance is modified. Nevertheless, the capacitance modification does not cause any problems because the global pack capacitance is increased and the sizing criteria will always be respected. This oversizing is imposed by technological limits.

The maximal current  $I_{UC\ cell\ max}$  that is usually defined in the datasheets is the short circuit current. It is impossible to obtain a higher current. Maximal current corresponds to an internal dissipation of the initially stocked energy in the ultracapacitor. Thus, if the ultracapacitor manages to dissipate this energy, the short circuit test will not be destructive and the ultracapacitor will recover its initial properties. However, if this maximal current is reached periodically and the ultracapacitor pack is not well cooled, there will exist an ultracapacitor degradation process. This is due to alterations in the electrolyte (decomposition phenomena, electrolysis and gas emissions). The ultracapacitor becomes less capacitive and more resistive. Thus, this shows the importance of a good cooling.

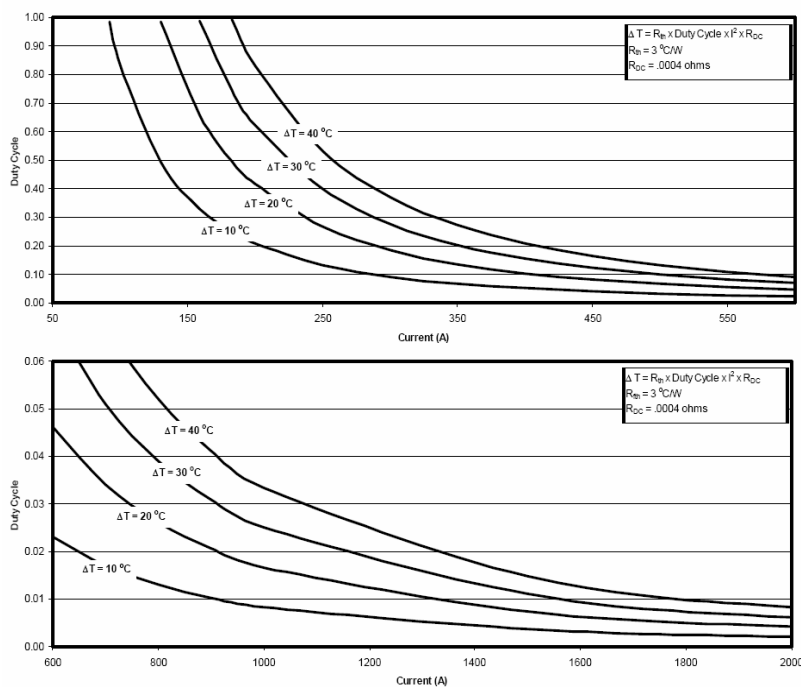


Figure I. 42: Ultracapacitor heating with current and duty cycle SC. Source: Maxwell.

Therefore, the main constraint about the charge and discharge process is a thermal constraint. This constraint must be respected in order to assure the recommended cycle number and the life time of the ultracapacitor. In order to analyze this phenomenon, ultracapacitor makers use to provide curves like the ones presented in Figure I. 42. These curves define in function of the discharge current value and the duty cycle the ultracapacitor heating. The duty cycle is defined as the existent time between a charge phase and two consecutive discharge phases. The main problem of these curves is that data are given for a full ultracapacitor discharge, which never occurs. However, these curves permit to have an idea about the thermal constraints admissible by the ultracapacitor [Barrade2].

### I.4.2.2 Ultracapacitor internal losses

Generally, ultracapacitor terminals are connected to the electrical circuit trough a couple of current collectors. Collectors are usually made of aluminium. The quality of the connection between the collector and the electrode defines the maximal specific power of the ultracapacitor (specific power refers to the ability of an ultracapacitor to quickly deliver power).

Furthermore, a separator is needed in order to facilitate the electrolyte ions path. The separator must guarantee electronic insulation between the two electrodes which are impregnated with the electrolyte. Usually, the separator is a porous insulating membrane, and generally is made of polyethylene and polypropylene.

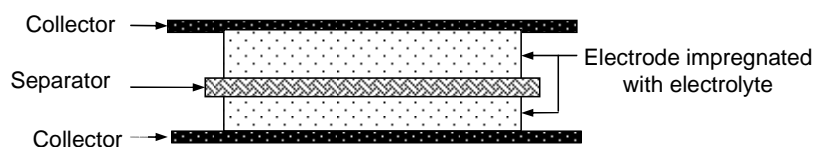


Figure I. 43: Ultracapacitors cell.

Thus, it is possible to say that the current collector and the separator are the devices that define the ultracapacitor losses. Indeed, an elementary ultracapacitor can be modelled as a capacitor with a series resistor (this assumes that other phenomena such as self-discharge, relaxation...are neglected). The series resistor models losses in the current collector and the separator. The model is presented in Figure I. 44. The resistance is given in ultracapacitor datasheets and its value varies between 0.4 mΩ and 4 mΩ depending on the chosen technology and power range.

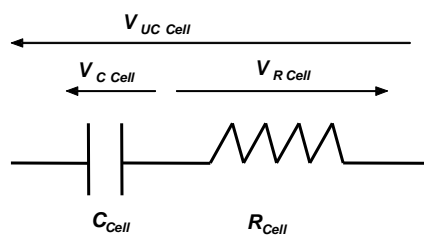


Figure I. 44: Real ultracapacitor cell model.



Loss effect modifies the previously calculated ultracapacitors voltage response. Indeed, the recovered energy will be lower than the initially expected. On the other hand, the supplied energy will be higher than initially expected because internal losses must also be supplied. The dissipated energy due to the internal losses is equal to:

$$W_{losses} = \frac{n_s}{n_p} \int_0^t R_{cell} I_{UC}^2 dt \quad \text{E I.50}$$

The previously proposed ultracapacitor pack sizing method does not take into account internal losses. Expression E I.50 shows that dissipated energy depends on the current supplied or absorbed by the ultracapacitor pack, the resistance and the mission duration. The mission duration can be really long (several hours) and the dissipated energy can become huge. Thus, it is senseless to size an ultracapacitor pack that is going to face the internal losses (the ultracapacitors capacitance would become huge!). Therefore, it is the main energy source (the fuel cell) that should compensate this energy. Thus, an energy management loop must be implemented in the global system control. Nevertheless, energy management loop affects the ultracapacitor final sizing, but this will be fully explained in § II.2.3

### Limitations in the ultracapacitor discharge ratio [Barrade].

Ultracapacitor internal losses limit the ultracapacitor discharge ratio. The equation that models  $n_s$  series stacked ultracapacitors voltage is:

$$V_{UC} = n_s V_{C\ cell} - n_s R_{Cell} \cdot I_{UC} \quad \text{E I.51}$$

Assuming a constant power discharge  $P_L$ , it is possible to write:

$$n_s R_{Cell} \cdot I_{UC}^2 - n_s V_{C\ cell} I_{UC} + P_L = 0 \quad \text{E I.52}$$

with  $P_L$  the load power and  $I_{UC}$  the current supplied by the ultracapacitor pack.

The solution to equation E I.52 is given by:

$$I_{UC} = \frac{1}{2R_{Cell}} V_{C\ cell} \pm \frac{1}{2R_{Cell}} \sqrt{\Delta} \quad \text{with} \quad \Delta = V_{C\ cell}^2 - 4 \frac{R_{Cell} P_L}{n_s} \quad \text{E I.53}$$

The two possible solutions for  $I_{UC}$  are real if  $\Delta$  is positive. This is the case with:

$$V_{C\ cell} \geq 2 \sqrt{\frac{R_{Cell} P_L}{n_s}} \quad \text{E I.54}$$

That leads to:

$$V_{C\ cell\ min} = 2\sqrt{\frac{R_{Cell}P_L}{n_s}} \quad \text{E I.55}$$

The variation range of the voltage  $V_C$  across one single ultracapacitor has to be limited in order to satisfy the equation E I.55. This is a new limitation on the minimum voltage that can be obtained during the discharge of the component. This can be seen considering again the definition of the voltage discharge ration  $d_{max}$ . Thus the maximal discharge ratio will be:

$$d_{max} = \frac{V_{UC\ cell\ min}}{V_{UC\ cell\ max}} 100 = 200\sqrt{\frac{R_{Cell}P_L}{n_s V_{UC\ cell\ max}^2}} \quad \text{E I.56}$$

As a consequence, the useable energy  $E_u$  of an ultracapacitor pack is then only a part of the total stored energy. The useable energy is limited by this condition:

$$E_u = n_s \frac{1}{2} C V_{UC\ cell\ max}^2 \left( 1 - 4 \frac{R_{Cell}P_L}{n_s V_{UC\ cell\ max}^2} \right) \quad \text{E I.57}$$

Thanks to equation E I.57, it is possible to re-formulate the power sizing requirements presented in the previous lines. The maximal power supplied by a given ultracapacitor is:

$$P_{max} \leq \frac{1}{4} \frac{n_s V_{UC\ cell\ min}^2}{R_{Cell}} \quad \text{E I.58}$$

Thus, the maximal resistance of an elementary ultracapacitor should be:

$$R_{Cell\ max} \leq \frac{1}{4} \frac{n_s V_{UC\ min}^2}{P_{max}} \quad \text{E I.59}$$

According to previous expressions, the discharge ratio cannot be arbitrarily determined due to the discharge ratio limitations shown in E I.56. Therefore, this constraint must be respected.

### I.4.2.3 Ragone plots [Christen]

As it has been explained in the previous section, ultracapacitors cannot be fully discharged. Internal losses will limit the power-energy operating points. Thus, not all possible combinations in the power-energy plane (Ragone plot) are permitted.

The Ragone plot is a graphical tool that permits to verify the sizing of an ultracapacitor pack. Ragone plot is a graphical representation of the power-energy operation points in the power-energy

plane. The Ragone plot establishes a Valid Operating Area (VOA). If the ultracapacitor mission power-energy evolution exceeds the VOA, the ultracapacitor pack sizing is not possible. On the other hand, if the VOA is much greater than the mission power-energy evolution, that means that, the ultracapacitor pack is oversized.

Equation E I.60 describes an ultracapacitor pack behaviour according to the elementary ultracapacitor model presented in Figure I. 36.

$$V_{UC} = V_C - R_{UC} \cdot I_{UC} \quad \text{E I.60}$$

with:

$$C = C_{cell} \frac{n_p}{n_s} \quad \text{E I.61}$$

$$R_{UC} = R_{cell} \frac{n_s}{n_p} \quad \text{E I.62}$$

$$V_C = n_s V_{UC\ cell} \quad \text{E I.63}$$

The limit energy-power plane (Ragone plot) traces the ultracapacitors real stored energy  $W_c^*$  versus the ultracapacitors supplied power.

The ultracapacitor real stored energy  $W_c^*$  will be:

$$W_c^* = \frac{1}{2} \cdot C \cdot V_C^2 \quad \text{E I.64}$$

The ultracapacitor pack voltage and the power evolution are:

$$V_{SC} = V_C - R_{SC} \cdot I_{SC} \quad \text{E I.65}$$

$$P_{UC} = V_{UC} \cdot I_{UC}$$

From the last three expressions, it is possible to write the ultracapacitors real stored energy in function of the supplied current and power. In order to obtain coherent results, the real stored energy should be higher that the value obtained in E I.66.

$$W_c^* > \left( \frac{1}{2} \cdot \frac{C}{I_{UC}^2} \right) \cdot P_{UC}^2 + (R_{UC} \cdot C) \cdot P_{UC} + \left( \frac{1}{2} \cdot R_{UC}^2 \cdot C \cdot I_{UC}^2 \right) \quad \text{E I.66}$$

The plot of the ultracapacitor pack real stored energy in function of the supplied power and current is a parabola (violet curve in Figure I. 45) whose minimal point is tangent to the power axes for a power of  $R_{SC} \cdot I_{SC}^2$ . That means that for a fully discharged ultracapacitor pack, the supplied power must be higher than this value to begin the ultracapacitor charge. This is phenomena is due to the ultracapacitor internal losses.

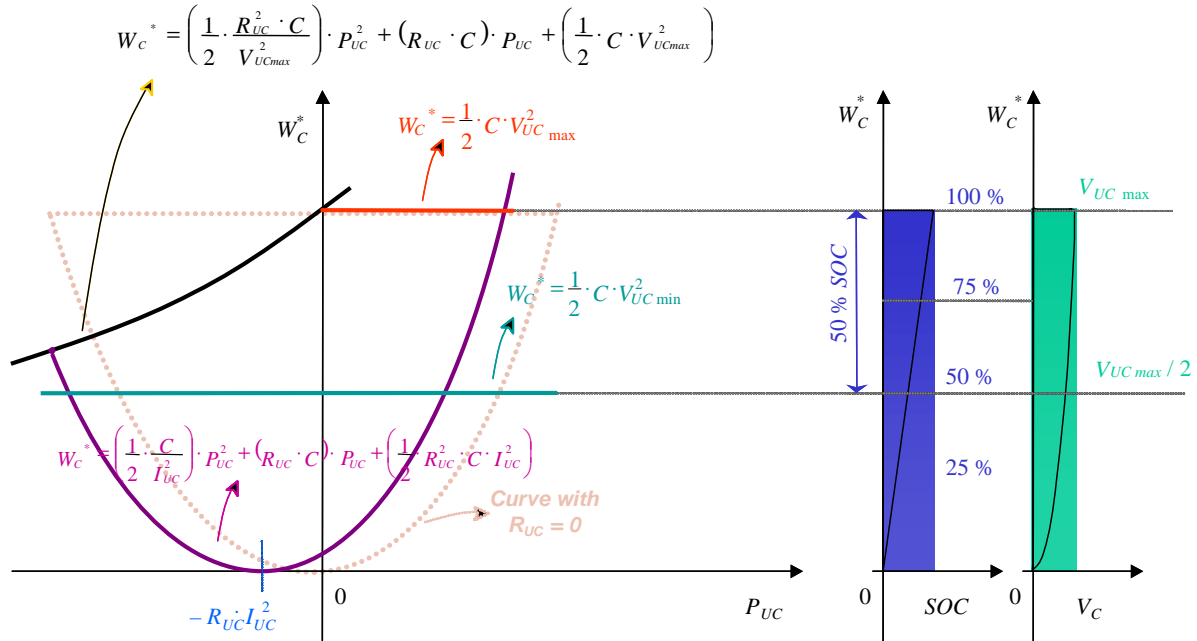


Figure I. 45: SC Ragone plot area. Source: Langlois

Nevertheless, relation E I.66 is not the only relation that must be respected in the power-energy plane. As it has been already explained, the ultracapacitor pack cannot exceed a sizing maximal voltage value  $V_{Cmax}$ . The ultracapacitor discharge ratio is also limited. Thus, these limits can be expressed in a mathematical way by the following expressions:

$$W_C^* < \frac{1}{2} \cdot C \cdot V_{UCmax}^2 \tag{E I.67}$$

$$W_C^* > \frac{1}{2} \cdot C \cdot d \cdot V_{UCmax}^2 = \frac{1}{2} \cdot C \cdot V_{UCmin}^2$$

These two limit conditions are represented in Figure I. 45 by the red and green lines respectively.

However there will be another voltage limitation during the ultracapacitor pack charge. During ultracapacitors charge phase, the voltage drop in the series resistor is positive and can lead to exceed the maximal ultracapacitors voltage value  $V_{UCmax}$ . This phenomenon is more important with high current and power values.

It is also possible to express mathematically the dependence of the real stored energy in function of the maximal tolerated voltage and power. This condition is represented in yellow in Figure I. 45. The mathematical expression of the limit condition is:

$$W_C^* < \left( \frac{1}{2} \cdot \frac{R_{UC}^2 \cdot C}{V_{UCmax}^2} \right) \cdot P_{UC}^2 + (R_{UC} \cdot C) \cdot P_{UC} + \left( \frac{1}{2} \cdot C \cdot V_{UCmax}^2 \right) \tag{E I.68}$$

In conclusion it can be said that the set of all these limit conditions must be respected during the whole mission. The ultracapacitor mission power-energy evolution must be restricted to the permitted area. If the evolution leaves the permitted area, the sizing will be erroneous.

One of the utilities of the Ragone plots is that they permit to verify the ultracapacitor pack sizing.

For example, the mission power profile presented in Figure I. 38 is treated with a ultracapacitors pack with the following characteristics.

Sizing criteria		SC characteristics	
$V_{SCmax} (V)$	$d (%)$	$C (F)$	$V_o (V)$
80	50	9.32	62.17

**Table I. 3: SC sizing criteria and sizing results.**

As it can be observed in Figure I. 46, the ultracapacitor voltage evolution respects the sizing criteria. Furthermore, the voltage evolution fits perfectly the voltage limits. In other words, all the permitted voltage variation area is used.

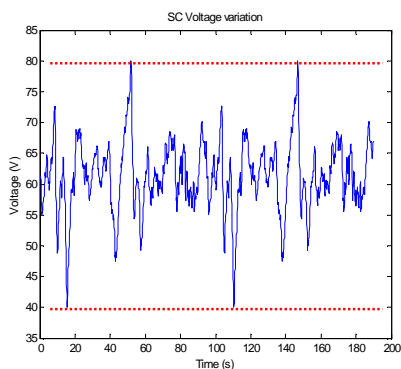


Figure I. 46: UC voltage variation. (Correct sizing)

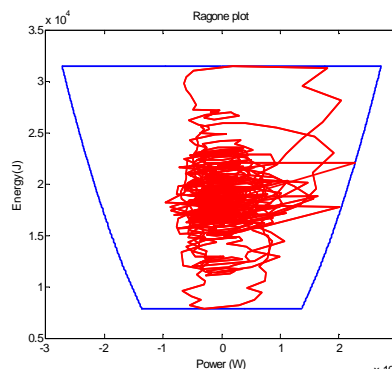


Figure I. 47: Ragone plot. (Correct sizing).

The ultracapacitor VOA is reflected in the ultracapacitor Ragone plot in Figure I. 47. The limit area is plotted in blue and the ultracapacitor power-energy evolution in red. It can be observed that the power-energy uses all the permitted area. The red plot is tangent to the limit area in the maxima energy value, minimal energy value and in the maximal current value (lateral). That means that this would be the minimal size for the ultracapacitor pack. The ultracapacitors cannot be smaller for the

proposed mission. A smaller ultracapacitor pack would cause that the ultracapacitor power-energy evolution would leave the permitted area.

The same power profile has been simulated with an oversized ultracapacitor pack. Table I. 4 shows the pack characteristics.

Sizing criteria		SC characteristics	
$V_{SC\ max}$ (V)	$d$ (%)	$C$ (F)	$V_o$ (V)
80	50	20	61

**Table I. 4: Oversized sizing.**

In this case, it can be observed that the voltage evolution respects the sizing criteria (Figure I. 48). However, the voltage variation is not perfectly fitted to the maximal and minimal voltage values. The Ragone plot shows that it has not been made the best use of the permitted operation area.

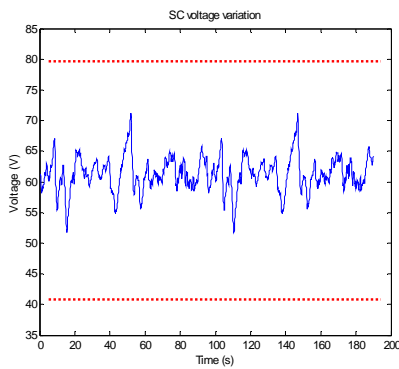


Figure I. 48: UC voltage variation. (Over sizing).

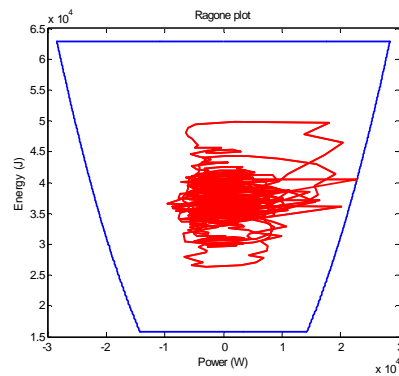


Figure I. 49: Ragone plot. (Over sizing).

Notice that in both Ragone plots the yellow line or the parabola corresponding to  $W_C^* < \left( \frac{1}{2} \cdot \frac{R_{UC}^2 \cdot C}{V_{UCmax}^2} \right) \cdot P_{UC}^2 + (R_{UC} \cdot C) \cdot P_{UC} + \left( \frac{1}{2} \cdot C \cdot V_{UCmax}^2 \right)$  is horizontal. This is due because a non significant resistor value has been considered ( $\approx 0$ ). In § II.2.2 the influence of the internal losses will be fully explained.

## I.5 Chapter conclusion

In this chapter, the CELINA project was introduced. The CELINA project aim is to design a power generation unit based on a fuel cell system. Nevertheless, due to the fuel cell dynamics limitations and in order to obtain a lightweight system, hybridization between the fuel cell and an ultracapacitor pack is proposed. Here, the fuel cell is considered as an energy source and the ultracapacitor pack is considered as a power source.

Afterwards, the generic sizing methods for both sources were presented. In both cases, the generic sizing methods are conceived in order to respect some sizing criteria: minimal fuel cell voltage, maximal fuel cell current density, maximal ultracapacitor discharge ratio and/or maximal ultracapacitor voltage.

Nevertheless, the proposed sizing methods do not take into account the system imperfections (UC internal losses, converter power losses...) and the system couplings (energy management loop, direct couplings...). Therefore, these methods cannot be directly applied in order to size the global system because the sizing criteria will not be respected, as it will be shown in the next chapter (that is why these methods are called generic).

Thus, in the next chapter, a global sizing method will be proposed. Furthermore, we will try to analyze the main objective of this work: the system electrical architecture study.

## *Chapter II*

# Electrical Architecture Study

---

**I**n this chapter, the possible architectures for the future DC bus emergency electrical network are analyzed. The system should be lightweight, should not take up a big volume and should be reliable. Furthermore, good efficiency is highly desired.

As it was explained in the previous chapter, due to the poor dynamic performances of the fuel cell system, a power buffer is required in order to support power peaks and important load variations. This power buffer can be based on a battery pack or an ultracapacitor pack. However, in this work only ultracapacitors will be considered. Thus, the emergency electrical network will be composed of a fuel cell stack, an ultracapacitor pack and several power converters that assure the DC bus electrical requirements and handle the power flowing through the system.

Many architectures are possible offering different degrees of freedom for energy management. Several methods were proposed to connect an ultracapacitor pack with a fuel cells stack in [**Drolia**], [**Santi**] and [**Neergard**]. In the case of the CELINA project, the proposed architectures are developed in the following lines.



## II.1 Preliminary analysis of electrical architectures

### II.1.1 Architecture with three power converters

Figure II. 1 shows the most general and complete configuration of the system. The fuel cell and the storage devices are connected through several power converters to an internal DC bus. An intermediate converter between the internal DC bus and the  $\pm 270\text{V}$  DC bus is placed in order to adapt the voltage levels.

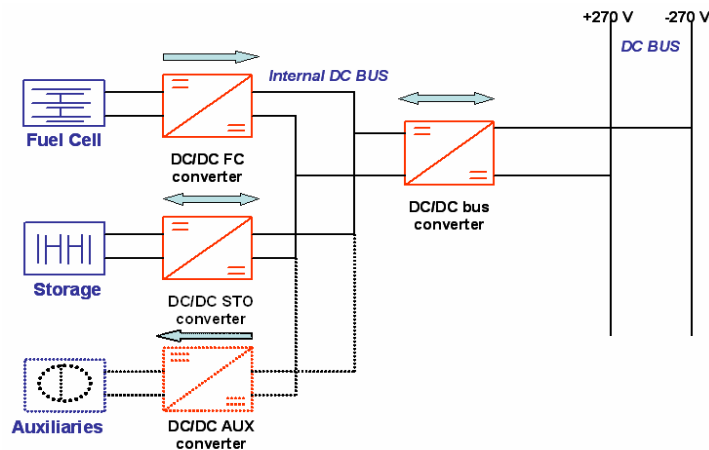


Figure II. 1: Architecture with three power converters. Internal DC bus. Solution A

This architecture permits a rich energy management in the system. In this case, the voltage booster function is achieved in two different stages: that will facilitate the power converter design and an intermediate booster transformer may be saved. Nevertheless, the presence of three power converters generates extra losses and reduces system reliability because the power is handled twice. The intermediate power converter (“the DC bus converter”) handles the whole power. Roughly speaking, it is possible to say that the fuel cell converter handles the mean power and the storage converter handles the transient power. In all cases, the storage converter must be bidirectional. Thus, the whole power is handled once by the intermediate power converter and once again by the fuel cell converter (mean) and the storage device converter (transient). Furthermore, the use of three power converters will highly increase the weight of the system. These are the main reasons why the number of power converters should be reduced.

### II.1.2 Architecture with two power converters

It is possible to obtain a structure with only two power converters achieving the electrical network requirements. Three cases can be distinguished according to the position of the power converters.

### *The fuel cell converter is removed*

As shown in Figure II. 2, a structure with two converters is obtained if the fuel cell converter is removed. The system variables can be perfectly controlled. The DC bus converter will guarantee the DC bus voltage requirements. The bidirectional storage converter is used to obtain the desired power sharing.

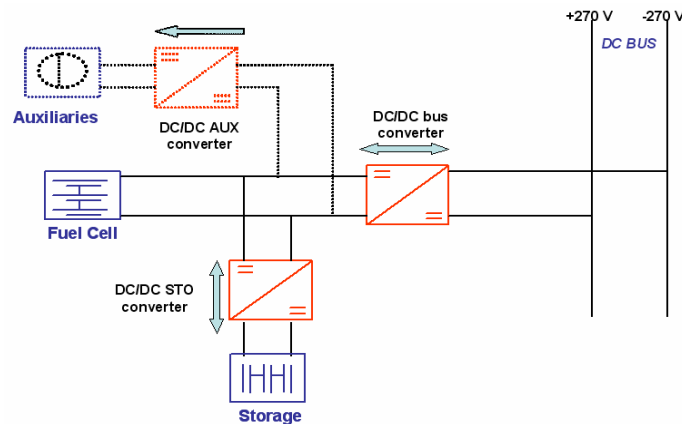


**Figure II. 2: Architecture with two power converters. System without the FC converter. Solution B**

This architecture is a priori more reliable than the architecture with three converters. Losses are also decreased. Nevertheless, load power is handled more than once. The DC bus power converter handles the whole power. Furthermore, the transient power is handled once again by the storage converter.

### *The storage converter is removed*

Similar characteristics are obtained if the storage device converter is retired as shown in Figure II. 3. Reliability and system losses are improved. Nevertheless, the load power is handled more than one time too. As in the previous case, the DC bus power converter handles the whole load power. And in this case, the fuel cell converter handles once again all the mean power.

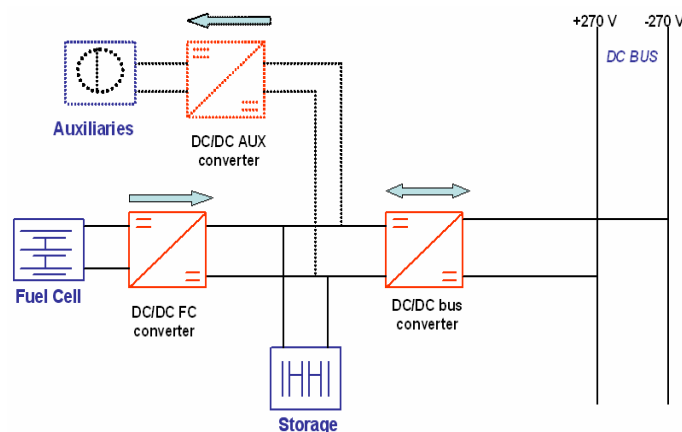


**Figure II. 3: Architecture with two power converters. System without the storage converter. Solution C**

***The DC bus converter is removed.***

This solution (Figure II. 4) keeps the advantages of previous solutions compared to the architecture with three converters. The main advantage is that the whole load power is only handled once. The mean power will be handled by the FC converter and the transient power will pass through the bidirectional storage device converter.

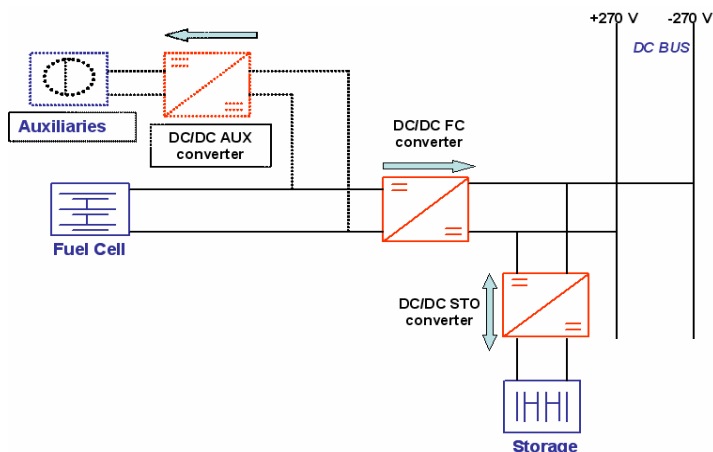


**Figure II. 4: System without the DC bus converter. Solution D**

Therefore, **this solution seems more advantageous compared to the other architectures with two converters. Thus, it will be studied in further details in § II.2.**

**II.1.3 Architecture with one power converter**

In this case, there is no need to have any bidirectional power converter. According to the storage device position, it is possible to distinguish the two following architectures.

***Storage device directly connected to the DC bus.***

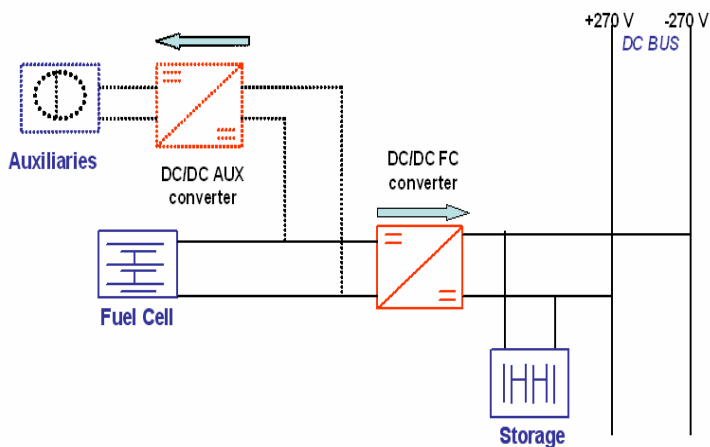


**Figure II. 5: Architecture with one power converter. Storage device directly connected to the DC bus. Solution E**

Figure II. 5 presents a very classical architecture, where the storage device is directly connected to the DC bus. This architecture increases system reliability. Only the mean power is handled by the power converter. Therefore, in this case, the losses are minimized.

Nevertheless, in this case, the storage device fixes the DC bus voltage. Indeed, the power converter does not control the DC bus voltage and it must be piloted in current. Therefore, the DC bus voltage varies with the state of charge of the storage device.

In the ultracapacitor case, the DC bus voltage is more and less fluctuant depending on the ultracapacitor size. Then, small variations mean higher cost for a given stored energy.

Anyway, ultracapacitors are low voltage energy buffers. Thus, in order to reach high DC bus voltage values, a big number of elementary cells must be stacked in series. Therefore, storage device can become huge depending on the application, the electrical network requirements and the DC bus voltage. This architecture is fully developed in § II.4.

### *Storage device directly connected to the fuel cell*

In this case, the energy buffer is on the low voltage side (fuel cell side) (Figure II. 6). This architecture presents a direct coupling between the fuel cell and the storage device. Their dynamic responses are coupled making the global system sizing a difficult issue. Furthermore, in this solution, the power converter has to handle the whole load power (mean and transient power) and this leads to a heavier power converter than in the previous case. The DC bus is perfectly controlled thanks to the power converter control. This architecture is fully developed in § II.3.

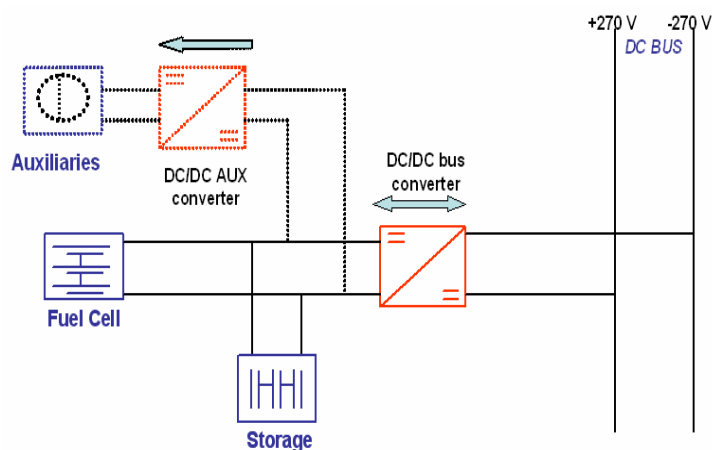


**Figure II. 6: Architecture with one converter. Direct coupling of both electrical sources. Solution F**

### II.1.4 Assessment of electrical architectures

The previous analysis has rejected the architecture with three power converters for the CELINA project. This architecture (solution A) is indeed heavier and less reliable than the other proposed architectures.

For the architectures with two converters, solutions B and C present the same advantages than solution D. But, for B and C, the power is handled more than once and therefore system losses are higher. Thus, solutions B and C can be rejected after the preliminary study achieved in these lines.

Solution D presents two power converters. Its weight seems to be higher than for a solution with one converter. However, solution D leads to the best use of the storage device; therefore, the storage device weight can be minimized in this architecture. Solution E handles only the mean power and thus the power converter is lower than in solution F. Nevertheless, solution F presents the storage device in the low voltage side of system.

To summarize, at this level of the study, this is difficult to choose between architectures D, E and F. Therefore, in the following of this chapter, these three architectures will be deeply studied and the global system sizing will be further developed.

All the architectures will have to face the Airbus mission power profile presented in Figure II. 7. **The aim of this chapter is to analyze the electrical behavior of each architecture. In the chapter IV, an optimization study is developed in order to compare objectively in terms of weight and efficiency the three proposed architectures (solutions D, E and F).**

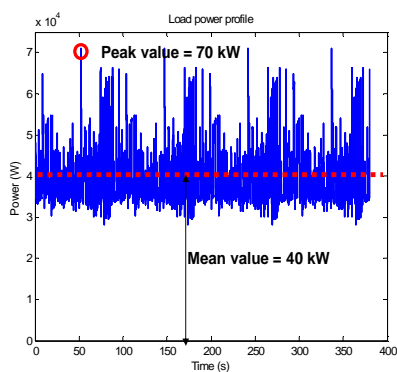


Figure II. 7: Airbus sizing mission power profile.

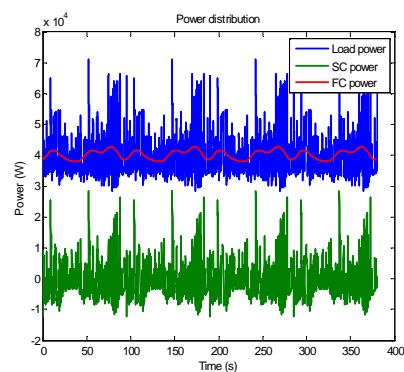


Figure II. 8: Desired power sharing.

**In order to illustrate the electrical architectures, the following assumptions are done:**

As explained in the chapter I, the sizing methods for the fuel cell and the storage devices need sizing power profiles. Therefore, the mission power profile must be submitted to one of the power sharing methods proposed in § I.3.5. Thus, an arbitrary power sharing between the fuel cell and the storage device has to be defined according to the

“tendencies” that are the most often imposed by the fuel cell system (dynamics limitation, advices from the fuel cell maker...). In order to compare **objectively** all the architectures, the chosen power sharing for all the architectures is based on a frequency power sharing tuned to 0.05 Hz. Therefore, the desired power sharing should be similar to the one shown in Figure II. 8.

However, the system is not perfect. The power converter and the storage devices add losses to the load consumptions. For the following architecture analysis, the fuel cell stack and the ultracapacitor pack are modeled as in § I.4.1.2 and in § I.4.2.2. The considered converter for this first architecture analysis is one classical Boost converter as the one presented in Figure II. 9. The chosen output voltage is 540V (it should be noticed that this converter do not achieve Airbus DC bus requirements, but it will be valid for a first approach in order to study the proposed architectures). The power converter model is fully explained in § III.4

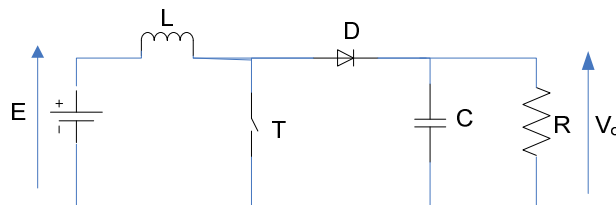


**Figure II. 9: Boost converter scheme.**

The power converter losses depend on the voltage supplied by the fuel cell and the power flowing through the power converter. Thus, surfaces that cartography the power converter efficiency in function of these two parameters can be plotted as the one shown in Figure II. 10. These efficiency cartography plots are fully explained in § III.4

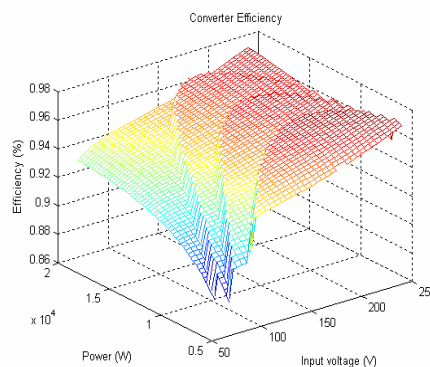


**Figure II. 10: Power converter efficiency according to the input voltage and the load power.**

Finally, the **auxiliaries' consumption** will be modeled with a consumption of **20% of the total fuel cell supplied power.**

## II.2 Architectures with two power converters: parallel connection

The main advantages of this solution are that the power is only handled once, the good use of ultracapacitor discharge capacity and the total control of the DC bus voltage. Furthermore, and roughly speaking, the mean power is handled by the fuel cell converter and the transient power flows through the storage device converter. This architecture is presented in Figure II. 11.

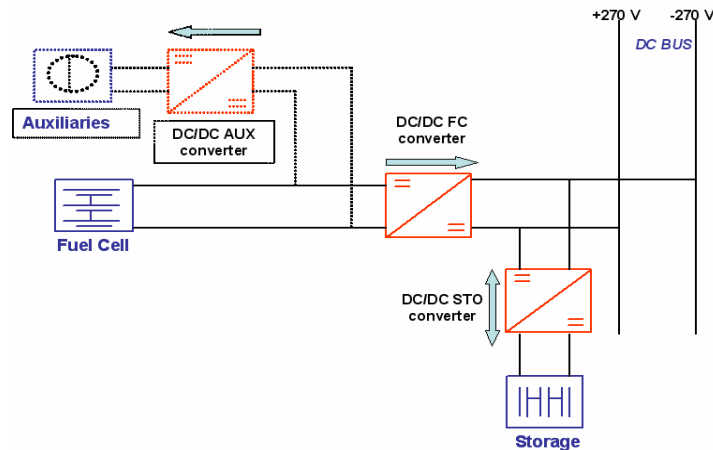


**Figure II. 11: Parallel connection architecture.**

This architecture and the desired power sharing can be easily implemented with one low-pass or high-pass filter. Nevertheless, different power converters piloting strategies can be adopted.

Assuming that the power converter controls are based on a cascade of two imbricated control loops (actually, it is the chosen option in chapter III), and according to the fundamental association rules in power electronics, it can be said that only one converter can impose the bus voltage and the rest of power converters (even if more power converters are associated to the same DC bus) must impose the current.

Therefore, two different control strategies can be implemented:

- In Figure II. 12, the fuel cell power converter is piloted in voltage (= this converter imposes the DC bus voltage) and the storage device converter is piloted in current (= this converter imposes the current). The fuel cell power converter presents two control loops: the internal loop controls the current through the boost inductor, and the external loop controls the DC bus voltage. On the other hand, the storage device converter is just controlled by one current loop that controls the current supplied by the storage devices. Power sharing is done thanks to a high-pass filter that will create the reference current for the storage device power converter.

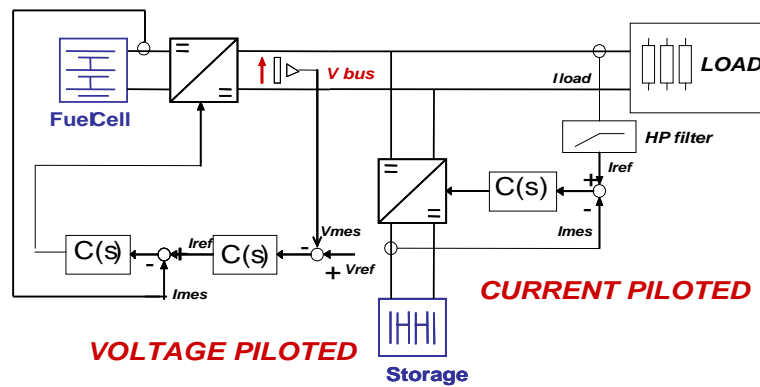


Figure II. 12: Control strategy with the DC voltage imposed by the fuel cell converter.

- In Figure II. 13, the roles of the power converters are permuted. The storage device converter is piloted in voltage (= this converter imposes the DC bus voltage) and the fuel cell converter is piloted in current (= this converter imposes the current). In this case, a low-pass filter is needed.

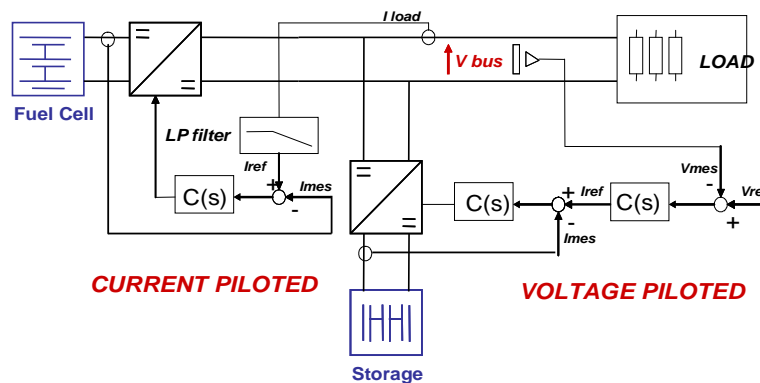


Figure II. 13: Control strategy with the DC voltage imposed by the storage device.

The two proposed system control strategies can operate correctly. Nevertheless, it seems that piloting the DC bus with the fuel cell converter is the most logical solution. Indeed, the fuel cell is the main energy source, and therefore, the fuel cell is in charge to supply, roughly speaking, the mean power. Thus, if a default occurs in the storage device branch and the system control is configured like in Figure II. 12, the fuel cell can still assure the DC bus voltage at a reduced power. On the other hand, if the system is controlled like in Figure II. 13, the DC bus voltage is not assured in case of storage device branch default. If these commentaries can be reversed if a default occurs in the fuel cell branch, the operation in degraded conditions will be possible but very limited for its duration.

### II.2.1 First sizing of this architecture. “Perfect system”

Assuming a “perfect system” (no losses within the power converters and the storage device), the system sizing can be done applying the generic sizing methods explained in § I.4.1.6 and § I.4.2.1.



Global sizing criteria must be defined in order to apply generic methods. Some sizing criteria (design variables) were chosen arbitrarily in order to illustrate one application example:

- FC minimal voltage (V) = 100
- UC maximal voltage (V) = 80
- UC maximal discharge (%) = 50
- Cut-off frequency (Hz) = 0.05
- Fuel cell max current density (A/cm<sup>2</sup>) = 0.5
- Switching frequency (Hz) = 20.000
- Number of parallel converter branches = 4

The results of the “perfect system” are shown in Table II. 1.

FC Surface (cm <sup>2</sup> )	FC cell number	C (F)	V <sub>o</sub> (V)
627.7	154	9.83	61.16

Table II. 1: "Perfect system" sizing results.

**It must be considered that these sizing criteria (and all the other sizing criteria in this chapter) were arbitrarily chosen, and thus, they are not optimized.**

In Figure II. 14 and in Figure II. 15, the simulations of the "perfect system" are shown. It can be noticed that the sizing criteria are respected. The fuel cell voltage never falls below 100V. On the other hand, the ultracapacitor voltage varies between the tolerated margins.

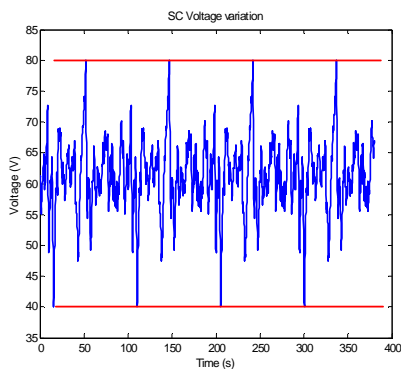


Figure II. 14: UC voltage time evolution.

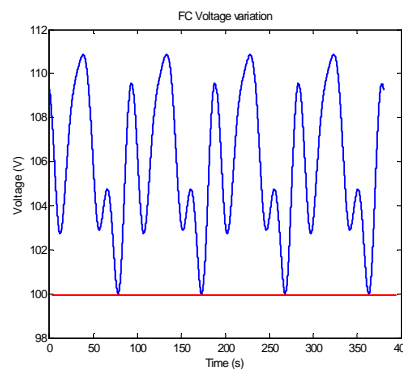


Figure II. 15: FC voltage time evolution.

### II.2.2 Effect of the losses

The above simulation does not take into account the storage device internal losses and the power converter losses.

If the system is piloted just like in Figure II. 12, the ultracapacitor internal losses and the power converter losses will cause the total discharge of the storage device as illustrated in Figure II. 16. Even

if the ultracapacitor pack is pre-charged up to its maximal tolerated voltage value, the pack will be totally discharged. Indeed, the ultracapacitor pack was sized for supplying the desired power sharing, but the sizing did not take into account the ultracapacitor internal losses and the storage device power converter losses.

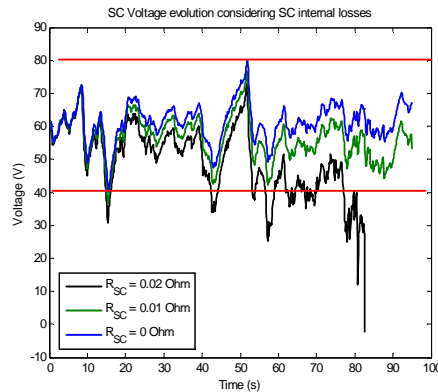


**Figure II. 16: Ultracapacitor total discharge due to their internal losses.**

Obviously the ultracapacitor pack cannot be sized for assuming all the mission losses. If the mission would be infinite, an infinite ultracapacitor bank would be needed to supply the desired power sharing and its associated losses. Thus, the fuel cell will have to supply the energy to compensate the losses and recharge the storage device (§ I.3.3). However, the fuel cell cannot supply the losses instantaneously, because important power peaks could be then created in the fuel cell. Therefore, an energy management respecting the fuel cell dynamics must be implemented in the global system control. In other words, the energy management action must take into account the tolerated fuel cell dynamics.

This last affirmation is quite interesting, because it confirms that losses will not be compensated immediately. Consequently the storage device must supply the losses and the transient load power for a given period of time, before being re-charged later. Thus, the ultracapacitor pack must be lightly oversized, compared to the results in Table II. 1, in order to face losses for the given period (the compensation action of losses is not instantaneous!). This means that the power profiles of the fuel cell and storage devices will be modified by the energy management action as it will be shown in the next paragraphs.

### II.2.3 Methods to compensate for the system losses

Two different methods are proposed in this development. The first one is based on the storage device voltage. Indeed, this voltage rightly represents the state of charge of some particular storage devices (ultracapacitors, Lithium-ion batteries...). This property can be used in order to create an energy management loop in the global system control.



The main difficulty of this method is the determination of the values of the proportional corrector and of the reference voltage. The next simulation results illustrate the influence of these parameters. The simulations are made with the previous UC sizing (the first sizing that does not consider the storage device internal losses and the power converter losses). Figure II. 19 presents the simulation results for the ultracapacitor pack responses to different reference voltages and different proportional correctors. Thanks to the compensation loop of system losses, the ultracapacitor tank is no longer discharged in some cases.

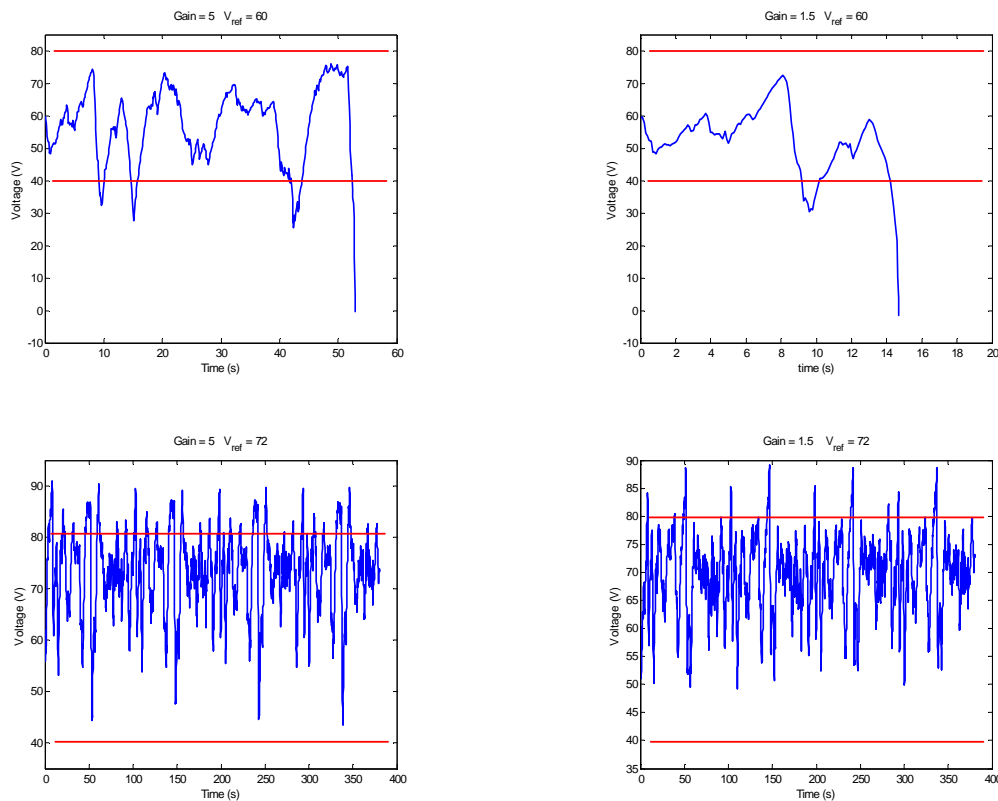


**Figure II. 19: UC voltage time evolution. Simulations with the compensation loop of system losses. (Proportional corrector + filter).**

These simulation results prove the importance of the choice of the values for the reference voltage and the corrector gain. In the two first figures (voltage reference = 60V), the voltage reference seems to be too small, and the storage device voltage falls to 0V (full discharge). In the other figures (voltage reference = 70V), the voltage reference the system seems to be better, but the limits (in red) used for the storage device sizing are not respected.

The sizing voltage criteria are not respected here because the compensation action modifies the initial ultracapacitor power profile, while the ultracapacitor sizing methods are based on the power profile. **Thus, the sizing method must take into account the compensation action.**

### II.2.3.2 Estimator method

In order to avoid the main drawbacks of the previous method based on the storage device voltage reference, the “estimator method” is proposed. The estimator method is based on the spirit of a “counter of losses”. The “counter” will count the losses in the storage device branch. Afterwards, it is the fuel cell that compensates for these losses. Nevertheless, the losses cannot be compensated instantaneously because important power peaks could be then created in the fuel cell and/or the energy management loop would not be respectful with the fuel cell system dynamics.

Thus the following strategy is proposed:

A period of time is arbitrarily chosen. The losses are estimated in real time during this period of time. The mean value of the losses can be also estimated for the given period. Afterwards, and during the next period, the fuel cell restores the mean value of the losses. To resume, the strategy consists in restoring the losses, produced in one period, in the next period as summarized in Figure II. 20. The step between the different periods is limited by a slope limiter.

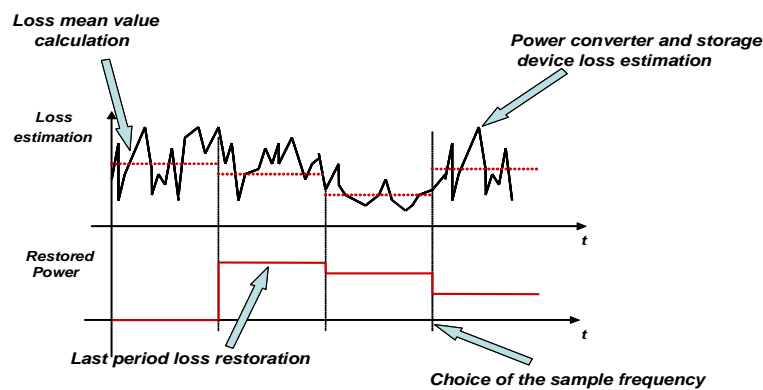


Figure II. 20: Estimator method strategy.

Once the losses are estimated, a new current reference for the fuel cell power converter is calculated. This modifies the original power sharing and will compensate for the losses. The dynamics of the compensation loop is limited thanks to a slope limiter. The compensation loop is drawn in Figure II. 21.

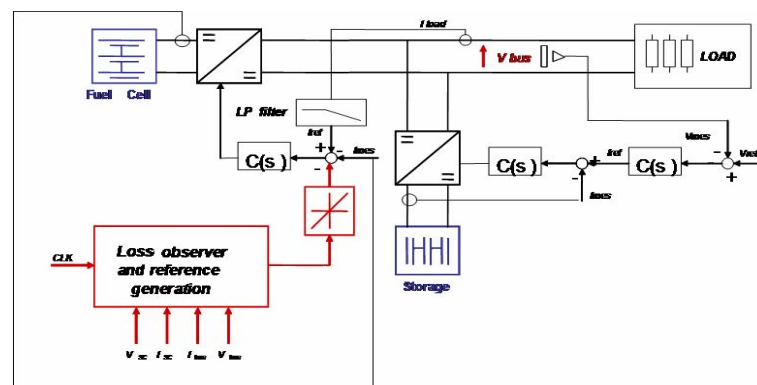


Figure II. 21: Estimator method compensation loop.

### Loss estimation

First of all, the losses in the storage device branch must be estimated. Concerning the storage device power converter, they can be calculated in a theoretical way (see chapter III) or in real time, just by subtraction of the output power to the input power of the power converter (though, this can also become a complicated issue and difficult to implement).

The internal losses of the storage device are much more complicated to calculate. In this study, only the ultracapacitor case is considered. Nevertheless, the principle of the method can be applied to all storage devices just by adapting the storage device model. The ultracapacitor internal losses can be estimated as proposed in Figure II. 22.

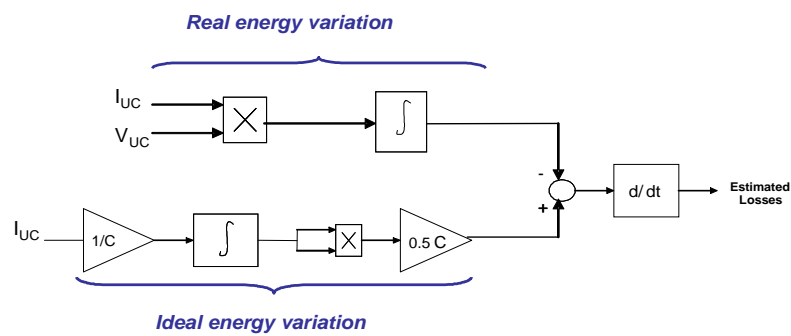


Figure II. 22: Estimator of the ultracapacitor losses.

The principle of the ultracapacitor loss estimator resides in a comparison between the real energy supplied by the storage device and the ideal energy variation (calculated assuming no losses) throughout the mission. The difference between both calculated energies gives the losses in terms of energy. Then, the derivative gives the losses in terms of lost power.

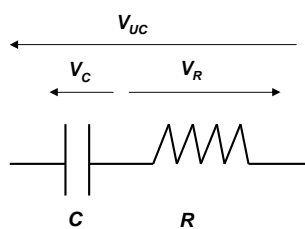


Figure II. 23: Ultracapacitor pack model.

According to the ultracapacitor pack model defined in Figure II. 23, the real energy supplied by the storage device or the “real energy variation” can be easily calculated because energy is the integral of the power supplied by the ultracapacitor pack:

$$E_{real} = \int P_{UC} dt = \int V_{UC} I_{UC} dt = \tag{E II.1}$$

The ideal energy variation is an image of the ideal voltage  $V_C$  ( $R=0$ ) given by:

$$V_C = \frac{1}{C} \int I_{UC} dt \tag{E II.2}$$

Then,

$$E_{ideal} = \int \frac{1}{2} C V_C^2 dt = \int \frac{1}{2} C \left( \frac{1}{C} \int I_{UC} dt \right)^2 dt \tag{E II.3}$$

So the derivative of the difference between these two energies will enable us to calculate the ultracapacitor internal losses by:

$$W_{internal\_loss} = \frac{d}{dt} (E_{real} - E_{ideal}) \tag{E II.4}$$

The simulation results in Figure II. 24 and in Figure II. 25 validate the operation principle of the loss estimator. The losses are well estimated with a small delay as usually with estimators and observers (It is not possible to predict something that it has not happened yet!).

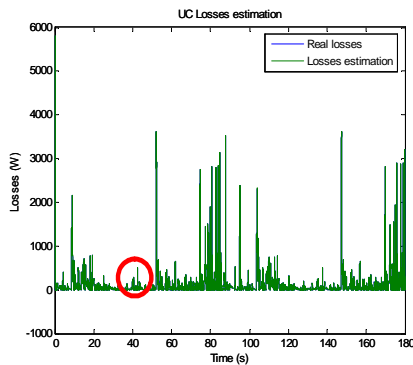


**Figure II. 24: UC Real losses and estimated losses.**

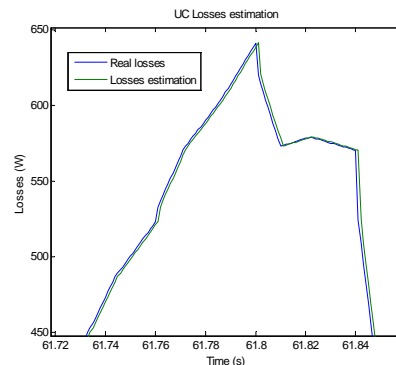


**Figure II. 25: Real and estimated losses. (zoom).**

**One of the limitations of this method is that the exact capacitance must be known** in order to calculate the ideal energy variation. This is an important drawback because the capacitance is never exactly well known and can evolve (heating, ageing...) with the time. Indeed, the ultracapacitor capacitance depends on the temperature, and thus the exact capacitance must be also estimated.

### Capacitance estimation

There is no need to estimate the ultracapacitor capacitance in real time because the capacitance does not vary instantaneously. Therefore, the ultracapacitor capacitance value can be checked periodically. With this purpose, it is enough to compare the ultracapacitor voltage and current evolution between two different periods of time as explained in Figure II. 26.

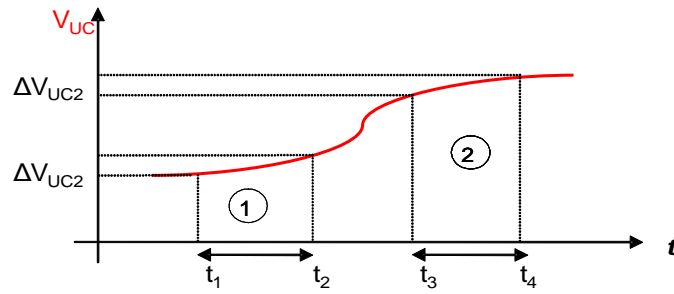


**Figure II. 26: UC voltage time evolution. Capacitance estimation.**

The equations that model the ultracapacitor pack behavior and based on the model presented in Figure II. 25 are:

$$\begin{aligned}\Delta V_{UC1} &= \Delta V_{C1} - \Delta I_{UC1} R \\ \Delta V_{UC2} &= \Delta V_{C2} - \Delta I_{UC2} R\end{aligned}\quad \mathbf{E II. 5}$$

The ultracapacitor pack internal voltage value  $V_C$  is:

$$\begin{aligned}\Delta V_{C1} &= \frac{1}{C} \int_{t_1}^{t_2} I_{UC1} dt \\ \Delta V_{C2} &= \frac{1}{C} \int_{t_3}^{t_4} I_{UC2} dt\end{aligned}\quad \mathbf{E II.6}$$

Comparing both periods of time:

$$C = \frac{\Delta I_{UC1} \Delta V_{UC1} - \Delta I_{UC2} \Delta V_{UC2}}{\Delta I_{UC2} \Delta V_{C1} - \Delta I_{UC1} \Delta V_{C2}}\quad \mathbf{E II.7}$$

Expression E II.7 permits to calculate the ultracapacitor capacitance just by comparing the ultracapacitor pack current and voltage variations between two different periods of time.

In order to validate this approach, two different simulations were made.

In Figure II. 27, the global system is simulated by keeping constant (=10.65F) the ultracapacitor pack capacitance. The committed error for the capacitance estimation is not significant.



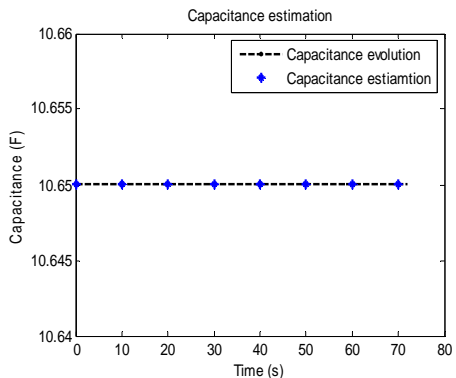


**Figure II. 27: Capacitance estimation. (The capacitance is kept constant during the simulation).**

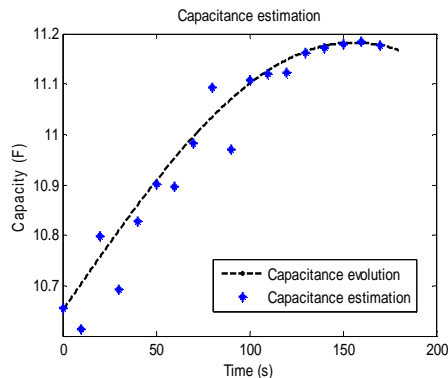


**Figure II. 28: Capacitance estimation. (A time variation is imposed to the capacitance during the simulation).**

In Figure II. 28, the ultracapacitor pack capacitance was artificially changed during time. The imposed capacitance evolution is shown in black, and the estimated capacitances are the blue points. The simulated capacitance variation is a 5% evolution of the rated capacitance (10.65F) in 180 seconds. The maximal error is 0.09923F, which is less than 1% of the total estimated capacitance. Thus, the estimation method is able to follow some time variations of the capacitance.

However, the estimation method precision is a function of the sample time in the real implemented system or the simulation step size in the simulation results. Small sample times logically lead to better capacitance estimations.

One important drawback is the practical implementation of this method. Indeed, the neglected phenomena in the ultracapacitor (self-discharge, relaxation...) can become more important than initially expected. Therefore, more complicated models should be used [Belhachemin], [Zubieta]. In all cases, a large number of calculations must be implemented in the system calculator. Due to this drawback, **an experimental validation seems necessary for future works.**

Nevertheless, as it is the case of the voltage reference method (Figure II. 19), this method does not operate correctly if the sizing in Table II. 1 is directly used. Therefore, **a global system sizing that takes into account the energy management must be implemented.** This will be detailed in the next section.

This method was applied to the ultracapacitor case. Though, it can be applied to other storage devices. The main drawback is to obtain a good model of the storage device. [Do] and [Colson] propose models of the state of charge and model parameter identification techniques of other storage devices such as Lithium-ion batteries.

## II.2.4 Global sizing of a hybridized system

In the previous lines, two different loss compensation methods were proposed. Both methods can be efficient, but simulation results showed that the sizing criteria were not fully respected or even not respected at all, if the system sizing proposed in Table II. 1. was directly used. Indeed, the energy management loop modifies the initially desired power profiles.

**In order to obtain a sizing method that respects the sizing criteria and considers the energy management loop, an iterative method is proposed.**

We assume that the initial arbitrary power distribution and the sizing criteria (ultracapacitor voltage limits, minimal fuel cell voltage, cut-off frequency...) were chosen. This permits a first global sizing as summarized in Table II. 1. The storage device and the fuel cell being sized, the global system can be now simulated with the energy management loop. As explained, the maximal and minimal voltages desired for the storage device will not be probably respected. Thus, this initial sizing is not correct.

Nevertheless, it is possible to recover, from these last simulation results, new power profiles supplied by the fuel cell and the storage device. These new power profiles are closer to the correct power profiles because they take into account the loss compensation loop. These new storage device and fuel cell power profiles will permit a new system global sizing. This process can be repeated until the sizing criteria are respected. Finally, the method will converge into a solution that respects the sizing criteria. Figure II. 29 describes the proposed iterative sizing method. It should be noticed that the iterative proposed method is applied independently of the chosen loss compensation strategy.

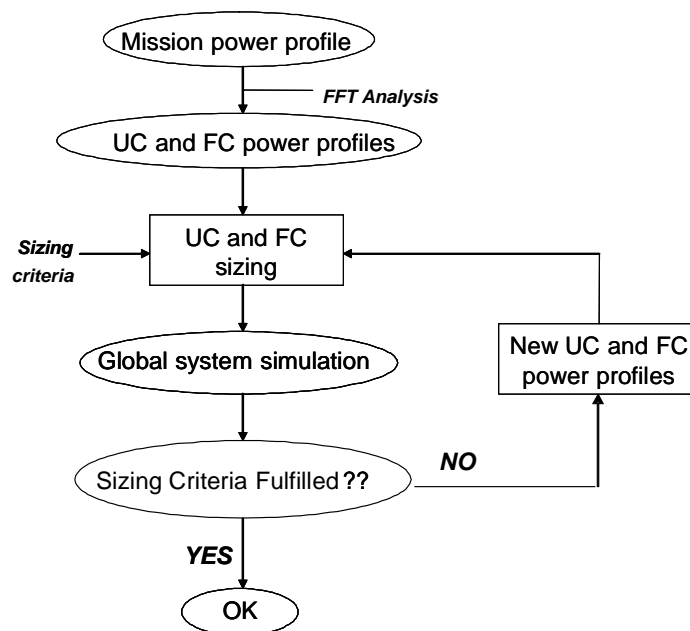


Figure II. 29: Proposed iterative sizing method.

In the next lines, the global sizing method is applied to the two proposed energy management strategies.

### II.2.4.1 Sizing results with the storage device voltage reference method

The previous new sizing method provides the following results for the voltage reference and corrector values proposed arbitrarily in §II.2.3.1:

V reference	Gain	C (F)	Vo (V)
60	5	17.3	80
60	1.5	45	80
72	5	22.11	40.7
72	1.5	18.1	46.4

**Table II. 2: Proposed iterative sizing method results.**

Table II. 2 proves the big influence of the energy management method. An inappropriate compensation action can carry a really important system oversizing (up to 50% bigger storage devices!!!).

In Figure II. 30 are shown the simulation results with the new sizing values:

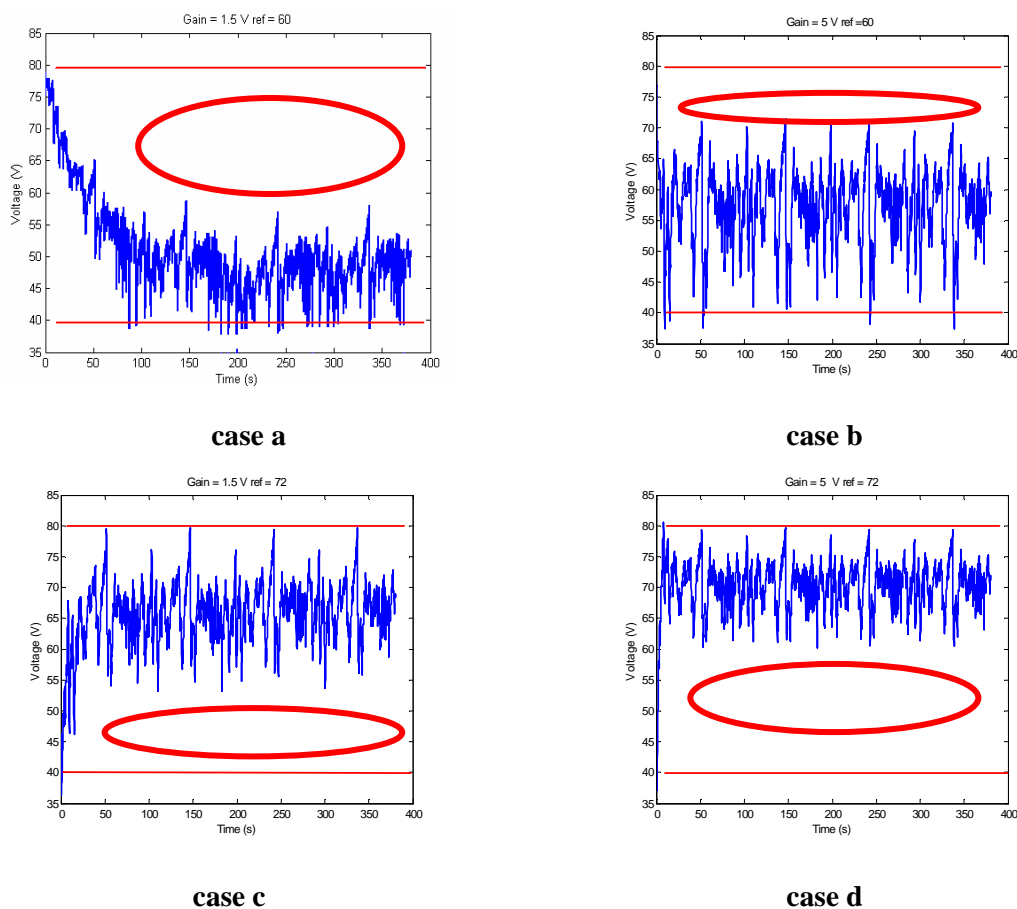


**Figure II. 30: UC voltage time evolution.**

The new sizing respects the storage device sizing criteria (voltage limits) as seen in Figure II. 30. It also shows the big influence of the compensation loop in a graphical way.

In the cases a and b of Figure II. 30, the region close to 80V is only used during the first seconds of the mission. In the cases c and d of Figure II. 30, the region close to 40V is only used during the first seconds. The fact that all the ultracapacitor capacity is not used all along the mission will cause an oversizing of the storage device.

### Remarks:

In some other cases, the iterative sizing method can find ultracapacitor voltage time evolution like the one presented in Figure II. 31.

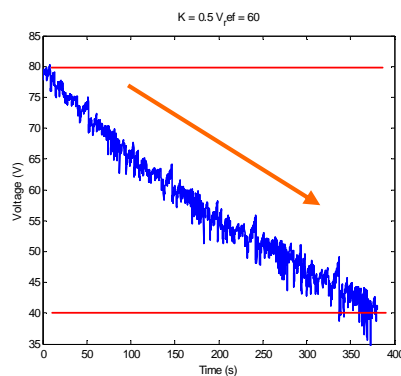


**Figure II. 31: Not valid sized solution.**

In this case, even if the sizing criteria are respected, it is quite easy to imagine that the ultracapacitor pack would be discharged if the mission profile was longer (red arrow). Thus, these kinds of solutions found by the iterative sizing method are automatically rejected.

These simulation results demonstrate the difficulty to choose the right values for the voltage reference and the corrector gain. Therefore, **only an optimization will enable to choose the two values for the voltage reference and the corrector gain that will minimize the ultracapacitor pack size.** Table II. 3 gives an example when the compensation loop is well optimized.

V reference	Gain	C (F)	Vo (V)
68	3	12.1	47.5

**Table II. 3: Sizing results after compensation loop optimization.**

The sizing results of Table II. 3 lead to the ultracapacitor voltage time evolution drawn in Figure II. 32.

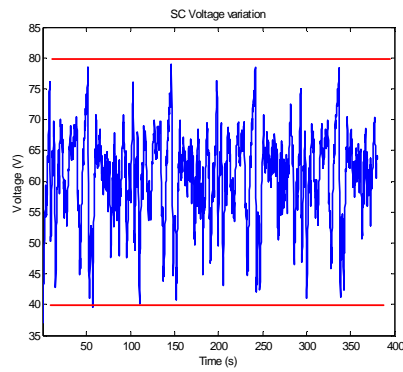


**Figure II. 32: UC voltage time evolution after compensation loop optimization.**

These results prove the big influence of the parameters of the loss compensation loop, and how they can contribute to reduce (or to increase if badly chosen!) the size of the storage device. The simulation results in Figure II. 32 illustrate that it is possible to obtain a good use of ultracapacitor storage capacity (all the ultracapacitor storage capacity is used over the mission) with an optimized compensation loop. Figure II. 33 presents the influence of the voltage reference and the corrector sizing on the ultracapacitor pack capacitance sizing.

However the aim of the project is to minimize the whole system mass, and not only the storage device. Therefore, a global system optimization study must be achieved. This study is fully detailed in the chapter IV.

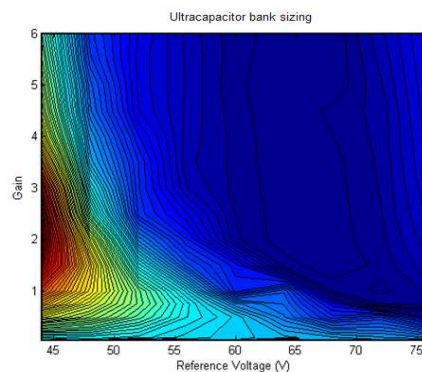


**Figure II. 33: Influence of the compensation loop on the sized capacitance.**

The finally obtained power sharing for the optimized compensation loop ( $\text{Gain} = 3$ ,  $V_{\text{ref}} = 68\text{V}$ ), including the compensation loop action, the losses within the power converter and the ultracapacitor pack, and considering an auxiliaries' consumption of 20 % of the total power supplied by the fuel cell, is presented in Figure II. 34. The mean power supplied by the fuel cell is finally around 50kW because of losses and auxiliaries' consumption. However, the harmonic content of the fuel cell power seems also to have increased compared to the initial fuel cell power in Figure II. 8.

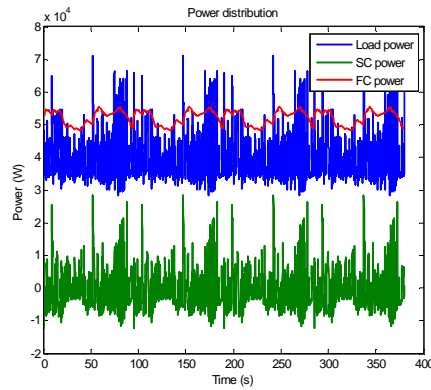


**Figure II. 34: Final obtained power sharing (storage device voltage reference method).**

In order to compare the desired and the finally obtained fuel cell powers, both curves are plotted in Figure II. 35. Nevertheless, as these curves do not present the same mean value (auxiliaries consumption is not taken into account in Figure II. 8), they were plotted subtracting the mean value of each curve. This explains why the mean value of each plotted curve is equal to zero.

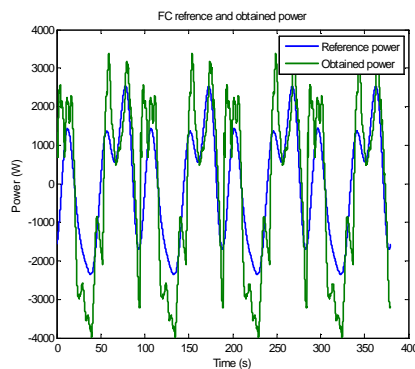


**Figure II. 35: Comparison of the desired and finally obtained fuel cell powers.**

This plot confirms that the harmonic content of the finally obtained fuel cell power increased. This is due to the system losses and the compensation loop action. The extra power due to the loss compensation action is plotted in Figure II. 36.

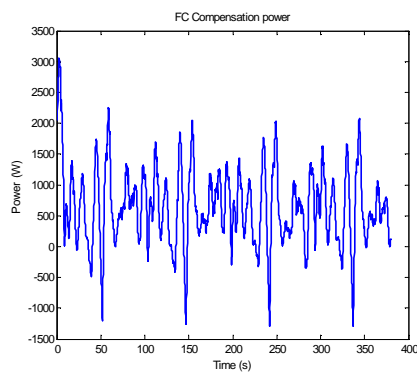


**Figure II. 36: Extra power due to the loss compensation action.**

### II.2.4.2 Sizing results with the estimator method

Next results present the iterative sizing method applied to an energy management method implementing a loss estimator.

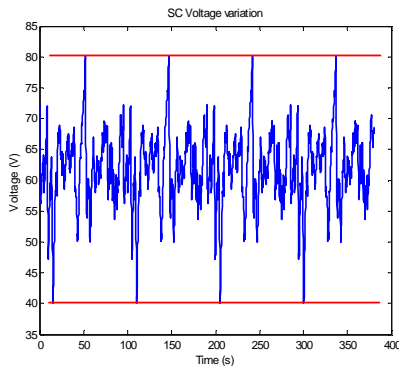


Figure II. 37: UC voltage evolution.

Sample time = 5 sec

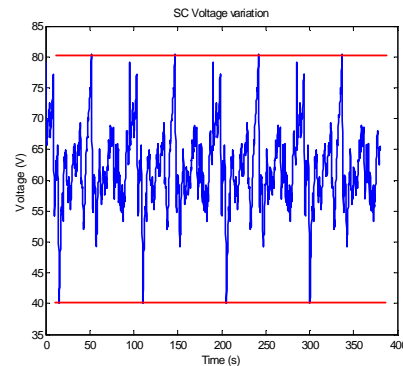


Figure II. 38: UC voltage evolution.

Sample time = 20 sec

The simulation results of the estimator method are presented in Figure II. 37 and in Figure II. 38. Two different sample time (= time during the losses are estimated) were chosen. The good use of the ultracapacitor charge-discharge capability is clear in both cases. This can be explained because the fuel cell just restores losses and does not modify significantly the storage device mission power profile.

Different sizing results of this estimator method are presented in Table II. 4.

Sample time (s)	C (F)	V <sub>0</sub> (V)
5	11.7	66.1
10	12.5	70
15	13.5	72.8
20	14.3	73.9

Table II. 4: Estimator method sizing results according several sample times.

As expected, the longer the sample time is, the more the capacitance is big (the storage device will remain a longer time without receiving energy to compensate the losses). **If the capacitance size is compared to the one obtained in the storage device voltage reference method, it is possible to conclude that both methods lead to similar values. Nevertheless, it seems that the estimator method leads automatically to a good use of the ultracapacitor discharge capacity, independently of the chosen sample time.**

The final power sharing for a sample time of 5 seconds is given in Figure II. 39.

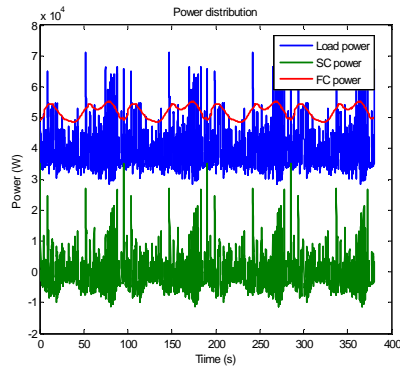


**Figure II. 39: Finally obtained power sharing with the estimator method.**

And similarly to the storage device voltage reference method, the comparison between the final and the desired powers can be observed in Figure II. 40.

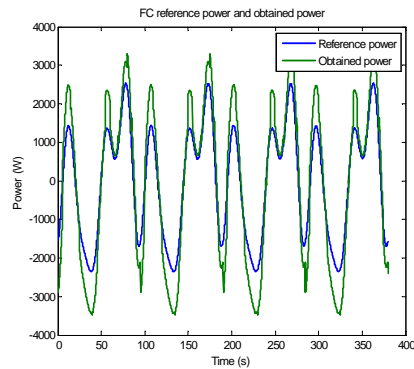


**Figure II. 40: Comparison of the desired and finally obtained fuel cell powers.**

In this case, the harmonic content of the fuel cell supplied power also increased compared to the initially desired. Nevertheless, the fuel cell power seems to have a smaller content of non desired harmonics. The extra power due to the loss compensation action is plotted in Figure II. 41.

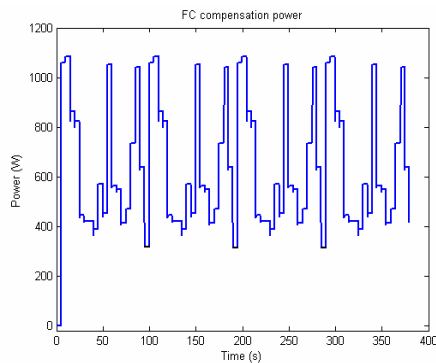


**Figure II. 41: Extra power due to the loss compensation action.**



### **II.2.5 Assessment of the proposed energy managements**

The main advantage of the storage device voltage reference method is its simplicity. Indeed, the compensation loop can be easily implemented by just comparing the storage device voltage with a reference value. There is no important computation cost and this method was already tested and validated with simple power profiles [Raël].

Nevertheless, the main drawback of this method is the determination of the voltage reference and the corrector gain.

On the other hand, the estimator method is based on a model of the storage device more and less complicated. Thus, the implementation of the loss estimator can become difficult in terms of computation cost. Furthermore this technique has never been validated experimentally and the concrete implementation can become extremely complex.

Nevertheless, the main advantage of the estimator method is that it can be applied to any type of storage devices (even if the storage device voltage is not an image of the state of charge). The only need is a good model of the storage device.

## II.3 Architecture with one power converter: storage device directly connected to the fuel cell.

### II.3.1 Operation of a direct hybridization

In this case, the system energy source is based on the direct coupling of the fuel cell with a storage device. In this original association, the fuel cell and the storage device share the same voltage (Figure II. 42). **In transient state, the storage device imposes the voltage to the fuel cell stack. In response, the fuel cell imposes current. But it always the fuel cell that imposes the operating point in steady state according to the load power demand.**

In transient state, if the load power demand is higher than the power supplied by the fuel cell, the storage device delivers the additional power necessary to satisfy the load power demand. On the other hand, if the power supplied by the fuel cell is higher than the load power demand, the storage device is recharged.

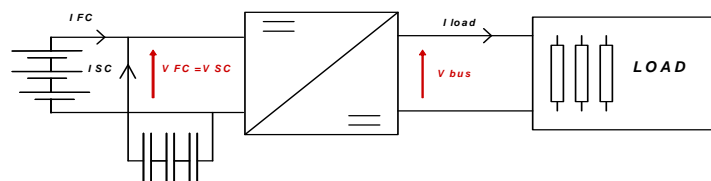


Figure II. 42: Direct connection.

The equation that models a direct connection is:

$$I_{FC} + I_{UC} = I_{Load} \quad \text{E II.8}$$

This leads to:

$$I_{FC} + C_{UC} \frac{dV_{UC}}{dt} = I_{Load} \quad \text{E II.9}$$

Thus, in steady state,  $I_{FC} = I_{Load}$  because  $(I_{UC})_{ss} = \left( C_{UC} \frac{dV_{UC}}{dt} \right)_{ss} = 0 \quad \text{E II.10}$

In transient state, the dynamic behavior of each source in direct connection is given in Figure II. 43 [García2].

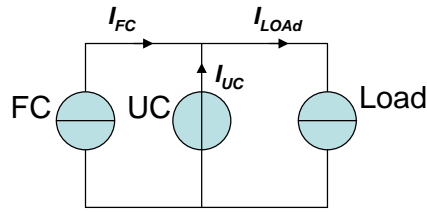


Figure II. 43: Dynamic behavior in transient state in a direct connection

As already explained, the ultracapacitors seems to be well adapted to Airbus requirements. Thus, in this manuscript, only the ultracapacitor case will be analyzed. Nevertheless, similar works were achieved in the laboratory Laplace by [Zugasti] considering a lithium-ion battery and a fuel cell.

From Figure II. 44 to Figure II. 47, the system responses to a 4 kW load power step are presented. In the first column, the ultracapacitor pack value is fixed to 52 F and, in the second column to 26 F [García].

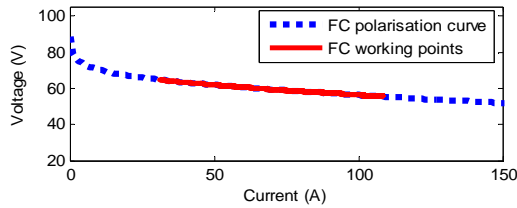


Figure II. 44: Fuel cell operating points. (C= 52 F).

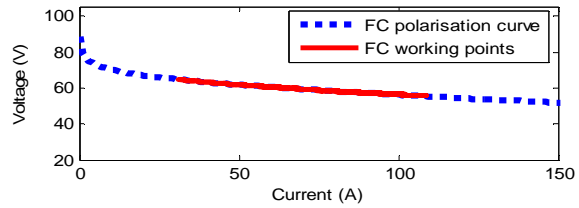


Figure II. 45: Fuel cell operating points. (C= 26 F).

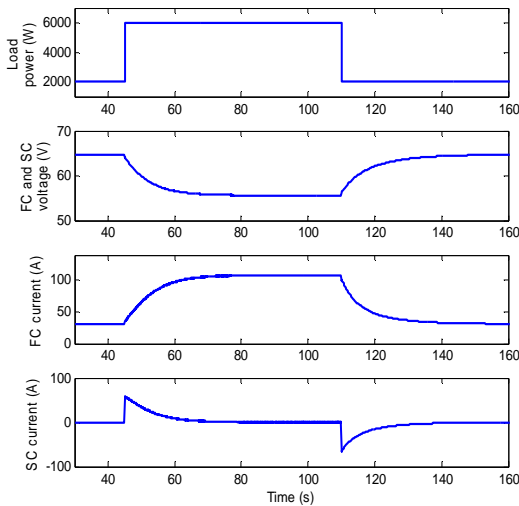


Figure II. 46: FC and UC responses to a 4kW load step. (C=52F).

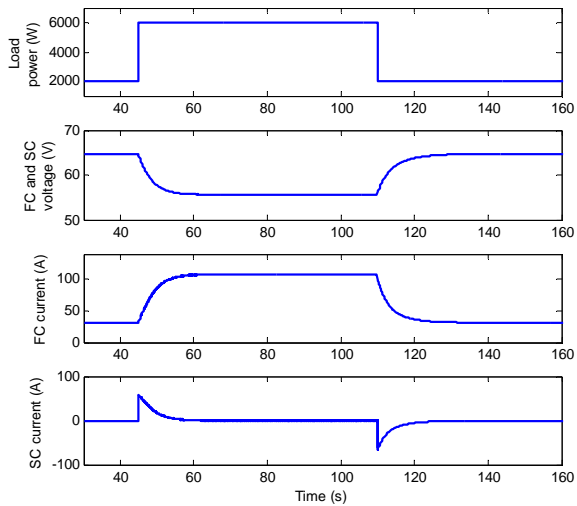


Figure II. 47: FC and UC responses to a 4kW load step. (C=26F).

Before the load step, as the voltage is stabilized, the fuel cell supplies a constant power. In steady state, the ultracapacitors supply no power.

When a positive load step occurs, the ultracapacitors immediately supply the power peak protecting the fuel cell against the power step. This is due to the fact that the ultracapacitors offer naturally a behavior of a “voltage source” (= their voltage cannot vary instantaneously). As long as there is no variation of the ultracapacitor voltage, there is no variation of the fuel cell power. But the ultracapacitor pack is not a perfect “voltage source”: thus the ultracapacitors discharge more or less during the power peak generating a variation of their voltage. Thus, if the ultracapacitor voltage decreases, the power supplied by the fuel cell increases. The voltage variation will stop, in this example, once the fuel will supply the whole load power (= the steady state is reached).

For a negative load step, the commentaries on the system behavior are similar. The only difference is that, in this case, the ultracapacitors will absorb a part of the current supplied by the fuel cell in transient state.

As it can be appreciated in the previous figures, the time necessary for the fuel cell to reach the steady state depends on the ultracapacitor pack capacitance. Smaller ultracapacitor packs lead to smaller response times. This is an important property of the system: **the ultracapacitor pack capacitance will fix the capability of the system to filter the load power and to avoid too rapid variations of the fuel cell power.**

The main advantages of this architecture are:

- There is only one power converter that treats the load power.
- There is no need to implement an energy management control loop contrarily to all the other proposed topologies. Indeed, the proposed architecture is able to “self-manage” the energy flowing through the system. Especially, the storage device losses are compensated naturally.

On the other hand, this architecture seems to lead to a worse use of the ultracapacitors, and consequently to bigger storage devices.

### II.3.2 Direct connection experimental results

Simulation results show that, *a priori*, the direct connection between a fuel cell and ultracapacitors should present no drawback. Nevertheless, it is difficult to find any reference in the literature that validates this original approach. Therefore, a small power scale experimental set-up was developed [Gailly].

The aim of this experimental validation is to reproduce and to validate the results previously obtained by simulation, and to detect if there is any phenomenon that is not taken into account with the proposed model.

The experimental set-up is made of:

- A PAXITECH fuel cell delivering typically under 1V and a maximal current to 5A. This fuel cell is used in “dead mode” on the hydrogen side (= no circulation of hydrogen). This means that the provided hydrogen is fully consumed on the reaction sites. The fuel cell directly “breathes” oxygen from the ambient air (“breathing PEM fuel cell”); therefore, the operation pressure is limited the atmospheric pressure. The hydrogen supplying comes from a 2 bars and 250ml hydrogen tank. The tank is connected to the fuel cell through two valves and a pressure reducer that regulates the hydrogen pressure to 1 bar. The pressure variation between both electrodes has to be very limited in order not to damage the fuel cell membrane. The thermal management and the management of water produced by the chemical reaction are assured by the fuel cell itself. There is no water exhaust pipe.
- The tested ultracapacitor is a 2.5V, 10F (PANASONIC).
- The experimental set-up is completed with two standard voltage sources and an “active load” (Figure II. 50).

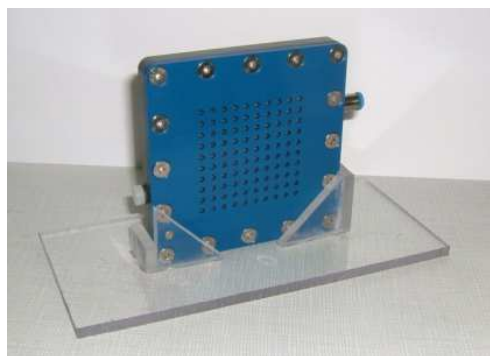


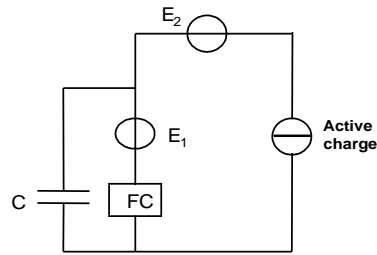
Figure II. 48: Tested air-breathing PEM fuel cell  
(PAXITECH)



Figure II. 49: Tested 10F ultracapacitor  
(PANASONIC)

The experimental set-up is a little more complex than expected, but this does not disturb the operation principle of the association fuel cell/ ultracapacitor. The aim of the active load is to impose/simulate a given load current. In order to assure a correct operation of this active load (a minimal voltage at its terminals is required for its good operation), a voltage source  $E_2$  is connected in series with the ultracapacitor and fuel cell association. A second voltage source  $E_1$  is used in order to adapt the values of the ultracapacitor voltage and the fuel cell voltage in order to exploit the ultracapacitor in conditions close to its nominal performances (2.5V). Indeed, the voltage supplied by the fuel cell varies from 0.5V to a maximum value of 1V.

Of course, in real applications, both added voltage sources will be removed.



**Figure II. 50: Experimental set-up.**

The experimental results for several load steps are plotted in Figure II. 51

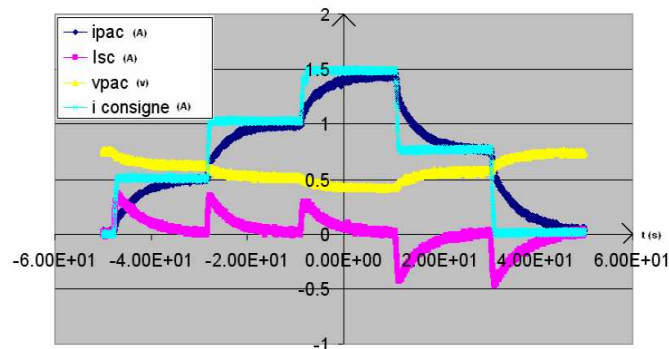


**Figure II. 51: Experimental results for several load steps.**

The system operates correctly. The light blue curve is the load current. It can be observed that the ultracapacitor absorbs the power peak at the beginning of any positive the load step. After any positive load step, the ultracapacitor is discharging and the fuel cell current rises up to the load current. At this moment, the fuel cell reaches the steady state and supplies all the load power. The system behavior is similar for negative load steps. The only difference is that, in this case, the ultracapacitor absorbs a part of the current supplied by the fuel cell in transient state.

### II.3.3 System sizing procedure for a direct hybridization

Similar to the case of the architecture with two parallel power converters, a power sharing strategy must be chosen. In order to compare objectively all the architectures, the same arbitrarily chosen power sharing is maintained and presented in Figure II. 52 (0.05Hz cut-off frequency).

**Remark: the desired power sharing does not take into account the auxiliaries consumption.**

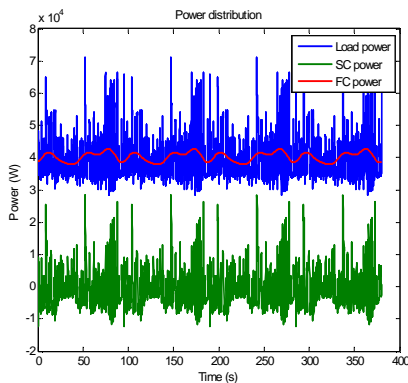


Figure II. 52: Desired power sharing.

In the architecture with two parallel power converters, a total independence between both energy sources (fuel cell stack and ultracapacitor pack) existed. All the desired power distributions were achieved, with a small harmonic re-injection due to the energy management control loop action (§II.2.4.1 and §II.2.4.2).

On the other hand, in the case of the direct connection, a direct coupling between the fuel cell and the ultracapacitor pack does not permit to obtain any desired power sharing. The generic sizing method, explained in the chapter I, can be directly applied to the fuel cell sizing. But some new considerations must be taken into account concerning the ultracapacitor pack sizing.

In order to size the system, the fuel cell stack must be sized before sizing the ultracapacitor pack.

The maximal voltage to be withstood by the ultracapacitor pack is the same as the fuel cell maximal voltage (= the open circuit voltage). The ultracapacitor maximal voltage permits to determine the number of ultracapacitor cells that must be connected in series. Figure II. 53 summarizes the different sizing parameters.

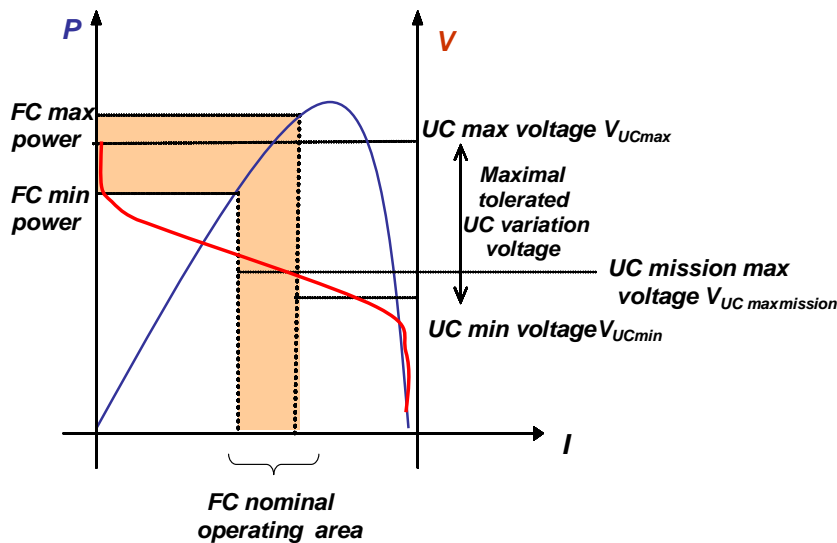


Figure II. 53: FC and UC sizing parameters. Graphical representation.

Thus, the number of series ultracapacitor cells is given by:

$$n_s = \frac{V_{UC\max}}{V_{UCcell\max}} \quad \text{E II.11}$$

Once in steady-state (after the start-up sequence), the fuel cell voltage varies in a determined range depending on the initial and arbitrary power distribution (pink zone in Figure II. 53). This zone represents all the steady state operation points desired for the fuel cell during the mission. The maximal and the minimal voltages of the fuel cell during the mission can be determined thanks to the required maximal and minimal powers. Thus, during this phase, the ultracapacitor voltage should only vary between these two values. In this case, this is this voltage variation that will determine the capacitance and not the variation between the maximal and the minimal tolerated values by the ultracapacitor as in the generic case presented in § I.4.2.1. This leads to:

$$\Delta E = \max(E) - \min(E) = \frac{1}{2} C (V_{UC\max}^2 - V_{UC\min}^2) = \frac{1}{2} C (V_{UC\max\ mission}^2 - V_{UC\min}^2) \quad \text{E II.12}$$

$$\begin{aligned} E_{\max} &= \frac{1}{2} C V_0^2 + \Delta E_{\max} = \frac{1}{2} C V_{UC\max\ mission}^2 \\ E_{\min} &= \frac{1}{2} C V_0^2 + \Delta E_{\min} = \frac{1}{2} C V_{UC\min}^2 \end{aligned} \quad \text{E II.13}$$

**Nevertheless, and as it was the case for the architecture with two parallel power converters, an iterative sizing method must be implemented in order to respect the sizing criteria (§ II.2.4).** Indeed, in this case, even if there is no energy management loop that modifies the chosen power sharing, **the desired power sharing may not be achieved because the system presents a direct coupling.** Therefore, the obtained results will not respect the sizing criteria and the global system sizing method must be necessarily iterative. The finally obtained power sharing will be analyzed in the next paragraphs. The iterative method is fully identical to the proposed method in the previous part (Figure II. 29).

### II.3.4 Sizing and analysis of a ‘perfect’ direct hybridization

In the previous paragraph, it was said that this kind of architecture does not need to implement a special energy management loop. However, and in order to better understand the behavior of this architecture, a first simulation considering a ‘perfect’ system (no losses within the storage device and the power converters) will be analyzed. **However, be careful because the fuel cell is never considered as perfect in our work!**



The arbitrarily chosen criteria are:

- FC minimal voltage (V) = 100
- UC maximal voltage (V) = 80
- Cut-off frequency (Hz) = 0.05
- Fuel cell max current density (A/cm<sup>2</sup>) = 0.5
- Switching frequency (Hz) = 20.000
- Number of parallel converter branches = 4

The sizing results for the previous sizing criteria and for the previous profile are show in Table II.

5

FC Surface (cm <sup>2</sup> )	FC Cell number	C (F)	V <sub>o</sub> (V)
1224.5	154	55.6	103

**Table II. 5: ‘Perfect’ direct hybridization sizing results.**

The simulation results for the just previously sized “perfect system” are presented in Figure II. 54 and Figure II. 55. The sizing criterion concerning the fuel cell minimal voltage is respected all over the mission. It can also be observed that the ultracapacitor pack absorbs the high frequency harmonics of the load current as expected. In the other hand, the fuel cell, roughly speaking, supplies the low frequency harmonics of the load current.

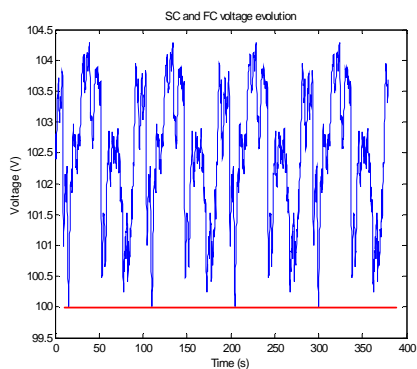


Figure II. 54: FC and UC voltage time evolution (both voltages are equal).

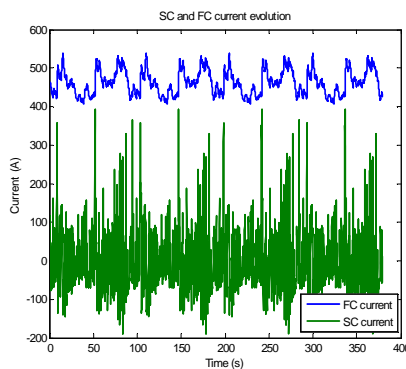
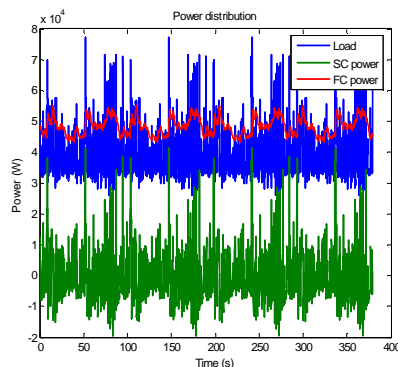


Figure II. 55: FC and UC current time evolution.

However, looking at Figure II. 56, it is obvious that the initially desired power sharing is not achieved. As already explained, this is due to the direct coupling between the fuel cell and the ultracapacitor pack.



**Figure II. 56: Final obtained sharing for the “perfect system”.**

In order to evaluate the final obtained power sharing, the desired and the obtained fuel cell powers are plotted in Figure II. 57. It should be noticed that the mean fuel cell power is close to 50 kW. This is due to the auxiliaries consumption. These curves are compared to the one obtained by filtering the load power through a first order low-pass filter. This filter was tuned to the initially desired filtering frequency (0.05Hz). Let us underline that the mean powers were subtracted in these curves to better visualize the filtering effect.

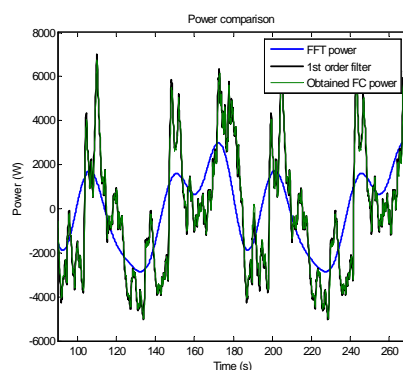


**Figure II. 57: Comparison between the desired (perfect FFT), obtained and first order filter power delivered by the fuel cell.**

The fuel cell power finally obtained is very close to the one obtained after a filtering by a first order low-pass. This can be explained as follows: **the equivalent capacitor of the ultracapacitor pack and the fuel cell membrane resistor constitute a first order filter (RC circuit) when connected in parallel** (Let us recall that the ultracapacitor internal losses have not been considered yet).

**In conclusion, even a ‘perfect’ direct hybridization does not permit to obtain all the desired power sharing. Actually, the final sharing can only tend towards this desired sharing.** In fact, the best power filtering effect that this ‘perfect’ direct hybridization can propose is like a ‘1st order’ response. Moreover and unfortunately, the system filtering capacity can even be diminished due to the system losses (ultracapacitor pack and power converter) as it will be analyzed in the following lines.

### II.3.5 Loss effect on the behavior of a direct hybridization

The introduced system losses are losses within the power converter and the ultracapacitor pack. Both losses are modeled like in the previous cases.

Nevertheless, both losses affect differently the system.

#### II.3.5.1 Effect of the power converter losses

The power converter losses do not have a special effect on the system. They just modify the load power profile and they must be considered as an extra load.

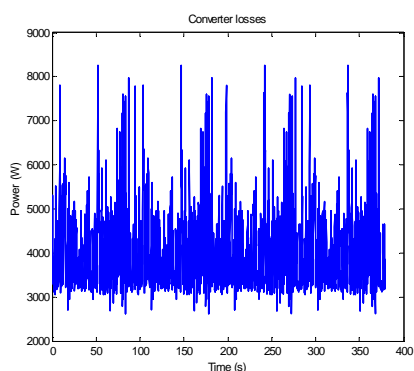


Figure II. 58: Power converter losses.

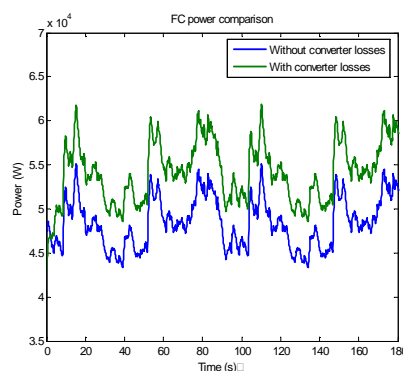


Figure II. 59: Time evolution of the power supplied by the fuel cell (with and without considering the power converter losses).

**The power converter losses do practically not modify the filtering effect of the direct hybridization** as illustrated in Figure II. 59. The ultracapacitor pack continues to supply, roughly speaking, the fluctuant power (including the fluctuant power due to the power converter losses) and the fuel cell continues to supply the mean power (including the mean power due to the power converter losses). No new power harmonics seem to be added to the fuel cell power.

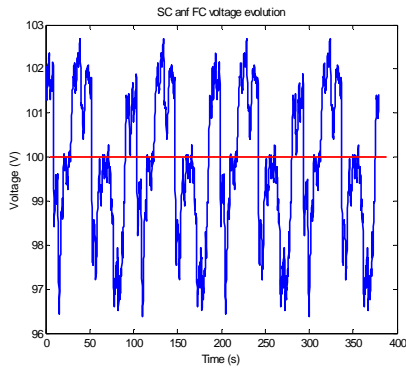


Figure II. 60: UC and FC voltage time Evolution.  
(Previous sizing - Table II. 5).

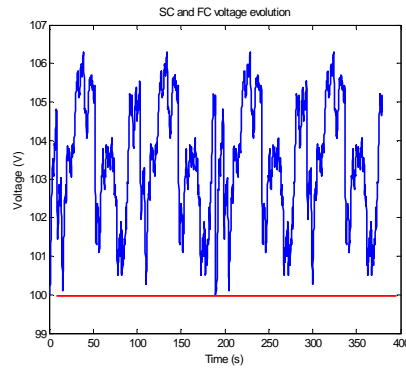


Figure II. 61: UC and FC voltage time evolution.  
(After a fuel cell re-sizing – Table II. 6).

Nevertheless, the fuel cell minimal voltage will be under the desired value as shown in Figure II. 60 if the previous sizing (Table II. 5) is kept. The reason is the power converters losses were not considered as an extra load and were not added to the mission load profile. If necessary, the fuel cell can be re-sized increasing the cell number and/or the stack surface, and the fuel cell mission minimal voltage value will be respected (Figure II. 61).

The sizing results after considering the power converter losses are:

FC Surface (cm <sup>2</sup> )	FC Cell number	C (F)	V <sub>o</sub> (V)
1301	154	55.6	103

**Table II. 6: Direct hybridization sizing results considering the power converter losses.**

In this case, the only parameter that was modified is the fuel cell surface. A bigger surface will reduce the fuel cell internal losses and will permit to increase the fuel cell voltage response. In this case the fuel cell surface was increased of almost 70cm<sup>2</sup>.

### II.3.5.2 Effect of the ultracapacitor internal losses

The ultracapacitor internal losses have a different effect from the power converter losses.

In this case, the fuel cell mean power is *a priori* not modified. And there is no need to do an eventual fuel cell re-sizing.

However the system power filtering capacity is deteriorated. Voltage peaks, and consequently power peaks, appear at the terminals of the fuel cell. Figure II. 62 and Figure II. 63 compare the system response considering and not considering the ultracapacitor internal losses.

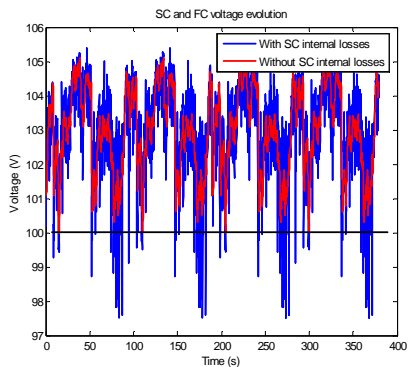


Figure II. 62: Voltage time evolution. Ultracapacitor internal loss effect.

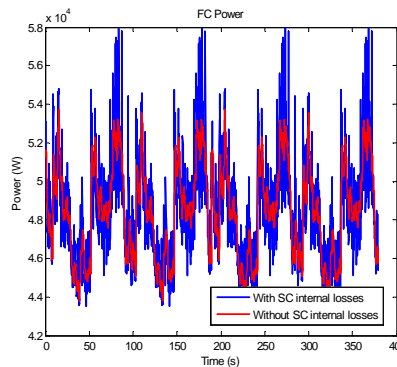


Figure II. 63: FC power time evolution. Ultracapacitor internal loss effect.

The ultracapacitor internal resistor can be seen as a source of perturbations for the fuel cell. Indeed, at each load step, this ultracapacitor internal resistor generate more or less important voltage peak at the terminals of the parallel association of both components (fuel cell and ultracapacitor pack). And the fuel cell internal resistance “translates” these voltage peaks into more or less current peaks within the fuel cell.

In others words, **the ultracapacitor pack branch resistance increases by considering its internal losses. The filtering offered by this branch is thus worse when a load step occurs. The fuel cell is then less protected against power peaks when a load step occurs.**

**REMARKS: Role of the fuel cell double layer capacitor when a load step occurs**

Figure II. 64 shows the equivalent circuit of the fuel cell and the ultracapacitor pack when a load step occurs. Assuming they are too slow, the diffusion phenomena are here neglected.

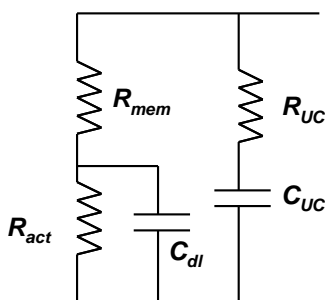


Figure II. 64: Equivalent circuit of the direct hybridization when a load step occurs. (Diffusion phenomena neglected).

Due to the double layer capacitor within the fuel cell, the load current will be divided instantaneously between the fuel cell and the ultra capacitor like a current divider:

$$(I_{FC})_{I=step} = \frac{R_{UC}}{R_{mem} + R_{UC}} I_{Load}$$

E II.14

$$(I_{UC})_{I=step} = \frac{R_{mem}}{R_{mem} + R_{UC}} I_{Load}$$

That means that the fuel cell is rapid enough to react when a load step occurs because of its double layer capacitor. At this instant, the fuel cell dynamics is not limited by the fluidics (air compressor...): the double layer capacitor, which is an electrostatic phenomenon, can deliver instantaneously the required current (the oxidation-reduction reaction does not intervene at this instant!). Naturally, its capacitance is limited and the current peak should be afterwards assumed by the oxidation-reduction reaction.

Thus, **in a direct hybridization, it is not possible to completely protect the fuel cell from quick current variations when load steps occur because of the double layer phenomenon.** Anyway, **this effect could be limited if  $R_{UC} \ll R_{mem}$ .** This statement should be considered in the system sizing.

### **First solution to limit the power peak when a load step occurs: the modification of the ultracapacitor pack realization**

The ultracapacitor internal loss effect can be minimized if the ultracapacitor resistance is decreased and/or if the storage device is divided in several parallel branches to decrease the current seen by each branch. Both strategies lead to a rise of the ultracapacitor pack weight.

$$C = C_{cell} \frac{n_p}{n_s}$$

E II.15

$$R_{UC} = R_{cell} \frac{n_s}{n_p}$$

This leads to a rise of the global capacitance that will increase the filtering effect of the direct connection (the global pack capacitance value is increased) and will reduce the perturbations caused by the ultracapacitor pack resistor. This fact can be appreciated in the simulation results in Figure II. 65. Nevertheless, increasing the parallel branches leads to a weight rise.

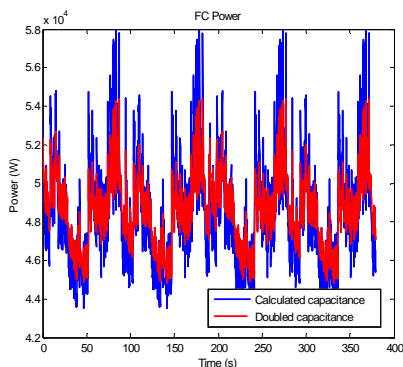


Figure II. 65: FC Power time evolution. (in blue: with the UC sized capacitance; in red: with a doubled capacitance).

**Second solution to limit the power peak when a load step occurs: the increase of the minimal fuel cell voltage**

Another degree of freedom to limit the power peaks at each load step effectively is the minimal fuel cell voltage admitted during the mission. This possibility sure is less obvious than both previous strategies.

For identical powers, if the minimal fuel cell voltage is increased, the currents flowing through the fuel cell and ultracapacitor association are reduced. Thus, the perturbations caused by the internal ultracapacitor resistor are also reduced (the voltage drop at the terminals of the ultracapacitor resistor is dependent on the ultracapacitor current). Therefore, the fuel cell power peaks are lower as proved in Figure II. 66.

But, the ultracapacitor internal resistance also increases with the minimal fuel cell voltage. Increasing the fuel cell operating voltage can become even worse in terms of power harmonic injection into the association.

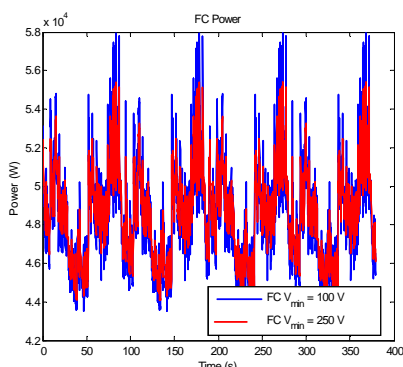
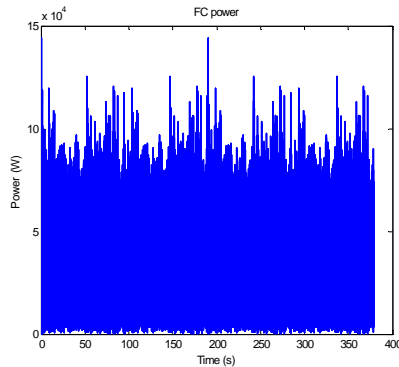


Figure II. 66: FC power time evolution for different minimal fuel cell voltages.

Thus, **one of the main problems of this architecture is the level of harmonics injected due to the ultracapacitor internal losses.** Indeed, it is possible that non expected harmonics become so high

that the solution becomes unacceptable as illustrated in Figure II. 67. **A maximal distortion rate must be fixed, and all solutions that exceed this rate must be automatically rejected.** This maximal distortion rate should be fixed in agreement with the fuel cell maker. After a simulation study, we noticed that this kind of solutions were usual with fuel designed with low current density values ( $J_{FC\ max} < 1.5\ A/cm^2$ ) in the CELINA project conditions.



**Figure II. 67: FC power time evolution ( $V_{FC\ min} = 60\ V$  ;  $J_{FC\ max} = 0.1\ A/cm^2$ ). Unacceptable solution.**

### **Conclusions of this paragraph:**

The problem of the power peaks at each load step is directly linked to the ultracapacitor pack and the chosen ultracapacitor technology. It is possible to obtain low equivalent series resistances. Thus, **this kind of architecture can be used in the CELINA project if a careful design is considered.** Therefore, in order to avoid this case, the fuel cell current density  $J_{FC}$  must be higher than  $0.2\ A/cm^2$ .

### **II.3.6 Start-up of a direct hybridization**

Until now, the system has only been considered in steady state. The start-up phase of this kind of architecture is a task more delicate than in the case of the architecture with two parallel converters. Indeed, both electrical sources sharing the same voltage, an eventual high voltage difference between the ultracapacitor and the fuel cell, at the time of starting the association, can lead to a high short circuit current.

Therefore, before the system start-up, the ultracapacitor pack must be pre-charged to the fuel cell open circuit voltage. A storage device pre-charge system must be implemented. This system should not be too much complicated and too heavy: indeed it is only used once before the system start-up. A small converter or even a resistor associated to a contactor will permit to pre-charge the ultracapacitor pack.

During the first seconds of the mission, the ultracapacitor pack must logically supply all the mission power because their voltage (which is equal to the fuel cell open circuit voltage at  $t=0$ ) can not vary rapidly by principle. The power filtering operates since the beginning as the ultracapacitor pack is well pre-charged. Consequently, the ultracapacitor pack must withstand the whole mission current for



several seconds. This must be considered for the ultracapacitor pack sizing. The system start-up phase simulation is illustrated in Figure II. 68 and Figure II. 69.

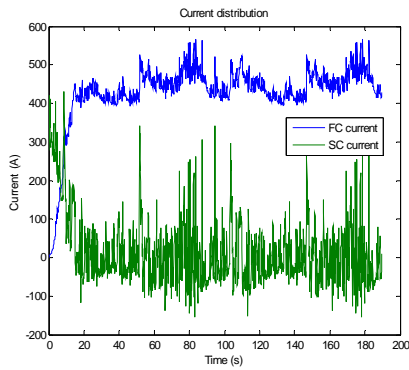


Figure II. 68: FC and UC currents during the start-up.

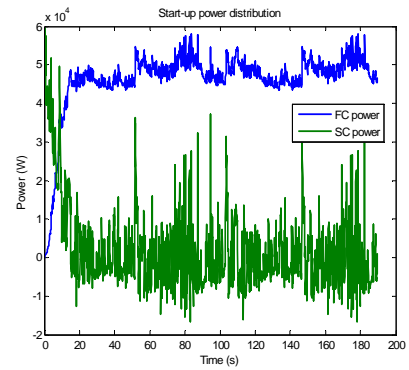


Figure II. 69: FC and UC powers during the start-up.

However, during the start-up phase, there is a negative current risk which can damage the fuel cell if the ultracapacitor bank is not exactly pre-charged up to the fuel cell open circuit voltage. In order to avoid any risk, a protection diode must be implemented despite the global efficiency penalization.



details.

The main difference is that, in this case, the ultracapacitor pack discharge ratio cannot be established freely. Indeed, the ultracapacitor pack fixes the DC bus voltage, and so all the voltage variations in the DC bus are not permitted. The DC bus voltage must vary between the specified authorized margins for the DC bus in the electrical network requirements. Usually, this margin is very small compared to the DC bus voltage nominal.

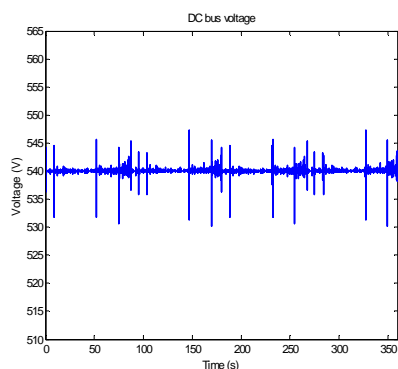


Figure II. 71: Controlled DC bus. Architecture with two parallel power converters.

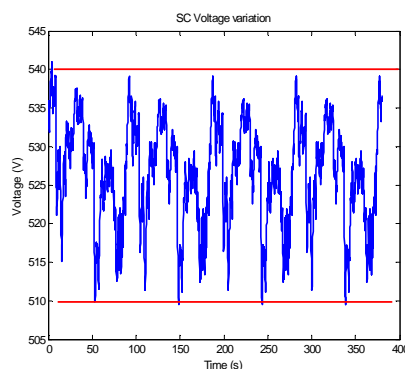


Figure II. 72: Not controlled DC bus. UC directly connected to the DC bus.

Figure II. 71 and Figure II. 72 compare the quality of the electrical network DC bus for both cases: the architecture with two parallel power converters and the architecture with one converter and the storage device directly connected to the DC bus. Figure II. 71 shows a very well controlled DC bus voltage: the electrical network quality is optimal. On the other hand, Figure II. 72 shows a non controlled DC bus voltage: the DC bus voltage varies freely between the authorized margins (30V in this case). Nevertheless, in this second case, if there is a default in the storage device or if the losses are not adequately compensated, the electrical network voltage could fall below the authorized margins.

Furthermore, in the case of High Voltage Direct Current (HVDC) electrical networks, the voltage that must be withstood by the ultracapacitor pack can become really important (over 500V). A large quantity of elementary ultracapacitor cells must be then connected in series.

It *a priori* seems that the size, weight and volume of the ultracapacitor pack can become really important compared to the previous cases. Nevertheless, there is only one power converter, and furthermore, only the mean power transits through this power converter. This leads to reduce the power converter weight.

The ultracapacitor pack size is also fully dependent on the maximal authorized ultracapacitor discharge. The smaller the authorized discharge is, the more the capacitance is big. Figure II. 73 shows

the evolution of the ultracapacitor size with the authorized minimal DC bus voltage. The maximal voltage considered for the DC bus is 540V.

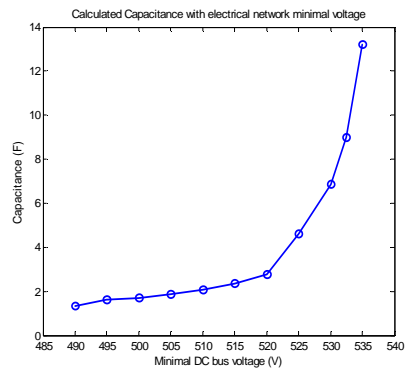


**Figure II. 73: Calculated capacitance with the authorized minimal DC bus voltage.**

This previous figure shows that, if large DC bus voltage variations should be avoided, large ultracapacitor pack capacitance should be placed as energy buffers. For a voltage ripple between 50V and 20V, the ultracapacitor pack capacitances are quite similar. Nevertheless, if the authorized voltage ripple is lower, the ultracapacitor size increases rapidly.

## II.5 Chapter conclusion

In this chapter all the possible architectures were analyzed. Some of them can be rejected after a preliminary study. On the other hand, three of them seem to be well adapted to the CELINA project requirements and were deeply studied. The retained architectures are:

### 1) The architecture with two parallel power converters

This architecture permits a perfect control of the DC bus voltage and the electrical network. Furthermore, the ultracapacitor discharge ratio can be established freely, and thus, this architecture leads to the most lightweight storage devices. On the other hand, the main drawbacks of this architecture are the system loss management and the power converter weight.

One of the main difficulties of this architecture is to compensate for the system losses (power converter and ultracapacitor internal losses). Two different strategies were proposed to compensate for them.

The first one is based on the voltage value of the storage device. This strategy consists in comparing the storage device voltage with a reference value so as to modify the power converter current reference. The main advantage of this strategy is its simplicity. However, this strategy cannot be applied to any storage device because the storage device voltage must be an image of the state of charge.

The other proposed strategy is based on an estimate of the losses. The lost power is estimated, and the fuel cell power reference is then modified in order to supply the estimated losses. This strategy can be implemented for all the types of the storage devices. Nevertheless, the main disadvantage of this strategy is its complexity and its great number of sensors.

Finally, it should be underlined, that both compensation methods will modify the original and arbitrarily chosen power sharing, and thus, an iterative sizing method was proposed in order to respect the desired sizing criteria.

### 2) The architecture with one power converter and a direct connection of the storage device with the fuel cell

This architecture also permits a perfect control of the DC bus voltage. Furthermore, this architecture makes it possible to remove one power converter. A priori, the system efficiency should be higher because the number of power converters is decreased.

The main characteristic of this architecture is that both electrical sources (fuel cell and the storage device) share the same voltage. Therefore, any desired power sharing cannot be achieved. The best filtering effect that could be obtained is similar to a 1<sup>st</sup> order low-pass filter. On the other hand, this architecture does not need to implement any specific energy management loop for the power converter

control. This architecture “self-manages” the system losses. Nevertheless, the system losses still affect this architecture but differently.

The power converter losses must be considered as an extra load. Thus, the power converter losses should be added to the load mission power profile. On the other hand, the ultracapacitor internal losses affect the filtering capacity of the system. Indeed, new harmonics are injected into the fuel cell power. This issue must be carefully considered for the system design and the ultracapacitor technological choice.

### **3) The architecture with one power converter and a direct connection of the storage device to the DC bus**

This architecture presents a priori the best efficiency because only the load mean power transits through the power converter. This leads to an important reduction of the power converter weight. On the other hand, the main disadvantages of this architecture are the bad use of the ultracapacitor pack and the fact that the DC bus voltage is not controlled.

This architecture is quite similar to the architecture with two parallel power converters, and the same loss compensation control loop could be adopted. Finally, an iterative sizing method, that takes into account the energy management loop, should be implemented.

#### **Which architecture should be chosen?**

The architecture 2 (direct connection) could be rejected due to the power harmonics injected into the fuel cell. The architecture 3 (storage device connected to the DC bus) could be rejected because the DC bus is not controlled. Anyway, if the electrical network requirements allow these behaviors, the choice should be done strictly in terms of weight, efficiency and volume.

But to evaluate the three architectures in terms of weight, volume and efficiency and to compare them objectively are complex issues. Indeed, in the three cases, some arbitrary sizing criteria must be fixed. These sizing criteria determine the operation point of the fuel cell, the storage device, the power converter weight... that lead to a calculation of the global system weight and efficiency. Thus, if the sizing criteria are arbitrarily chosen, it is possible that the system is not optimized in terms of weight and volume. Furthermore, the number of sizing criteria can be too high and makes impossible to optimize the system with a simple sweeping of parameters. Thus, a system global optimization tool must be implemented. The three optimized architectures could be then compared.

A global system optimization tool and a comparison of the three architectures will be achieved in the chapter IV.



## Chapter III :

# Power Converter Design

---

Fuel cells present large output voltage variations: the supplied voltage can indeed vary up to 50 per cent between the maximal power point and the open circuit point. Thus, in order to obtain a controlled DC bus electrical network, it seems mandatory to place a power converter between the fuel cell stack and the DC bus.

Many different types of DC-DC power converters are proposed in literature. The choice is huge. It is possible to find insulated DC-DC converters [Lefevre] [Wang] [Wetzel] [Sickel] and/or soft switching structures [Li], [Shoyama], [Wei], [Yao]. However, due to the aeronautical constraints, the power converter structure has to be reliable, lightweight and with high efficiency.

Furthermore, **AIRBUS DC electrical network requirements impose to obtain a  $\pm 270\text{V}$  DC bus starting from just one fuel cell stack. In all cases, the negative pole of the fuel cell stack must be connected to the airplane ground. The power which will be handled by the power converter is approximately 40 kW. The fuel cell current ripple should not be higher than 10 per cent of the fuel cell nominal current.** Airbus requirements are schematically represented in *Figure III. 1*.

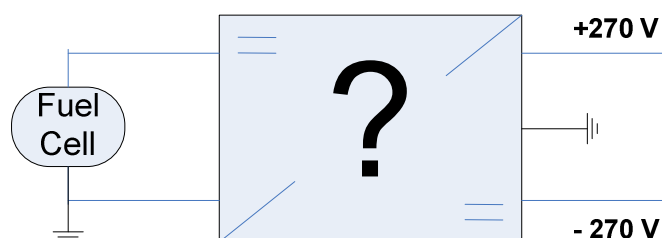


**Figure III. 1: Power converter requirements.**

As it has been explained in § I.4.1 a fuel cell stack is sized by determining the stack cell surface  $S$  and the cell number  $N$ . The cell number will determine the maximal fuel cell voltage value  $V_{FCmax}$ . Furthermore, the proposed sizing method in § II.2.4 guarantees a minimal fuel cell voltage  $V_{FCmin}$



during the whole mission. Therefore, according to these two values, it is possible to define the type of power converter structure. Figure III. 2 represent schematically all these possibilities.

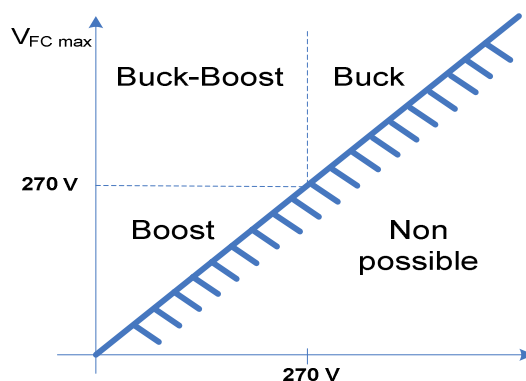


**Figure III. 2: Power converter structure possibilities according to the FC voltage**

$V_{FCmax}$  must be superior or equal to  $V_{FCmin}$ : the lower half part of the diagram thus is non applicable. If  $V_{Fmax}$  and  $V_{FCmin}$  are higher than 270V, a buck structure should be proposed. On the other hand, if both values are lower than 270V, the retained solution should be a boost structure. It is also possible that  $V_{FCmax}$  would be higher than 270V and  $V_{FCmin}$  would be lower than 270V: in that case, a buck-boost structure should be proposed.

In this chapter, the fuel cell will be seen as a voltage source to simplify.

## III.1 Power converter topologies proposed for the AIRBUS requirements

### III.1.1 Insulated power converter topologies.

Insulated structures present an intermediate magnetic circuit that insulates the input source (fuel cell and/or storage device) from the DC bus. Usually the magnetic circuit is a transformer. There are two different types of insulated DC-DC power converters: asymmetric and symmetric.

The Flyback converter and the Forward converter are classical asymmetric power converters. In these converters, the transformer is used asymmetrically and an additional demagnetization circuit is needed. The transformer operation point only evolves in one quarter of the B and H plan. Therefore, asymmetric DC-DC converters present lower efficiency than symmetric converters [Ferrieux].

The Push-pull converters are the classical examples of symmetric power converters. In this case, the transformer is used in the whole B and H plan. Therefore, this type of insulated power converters leads to a better use of the magnetic circuit.

There are two different types of Push-Pull converters: the current-fed push-pull converter and the voltage-fed push-pull converter. The current-fed Push-Pull converter is a structure fed in current (= presence of an input inductor) and it is naturally a boost structure (the output voltage is higher than the

input one), even without the transformer effect. In the other hand, the voltage-fed Push-Pull converter is a structure fed in voltage (= no input inductor) and it is naturally a buck structure (the output voltage is lower than the input one) without the transformer effect. A comparison between these two structures is shown in Table III. 1.

	Current-fed Push-pull converter	Voltage-fed Push-pull converter
Transfer function	$k \frac{1}{1-\alpha}$	$2.\alpha.k$
Operation conditions	$\alpha > 0.5$	$\alpha < 0.5$
Maximal switch voltage	$\frac{V_{FC}}{1-\alpha}$	$2.V_{FC}$

**Table III. 1: Comparison between current-fed and voltage-fed Push-Pull converters.**

Push pull converters satisfying the AIRBUS requirements are shown in Figure III. 3 and in Figure III. 4. The high frequency transformer has two secondary windings in order to produce, via two rectifier bridges, the two required DC voltage levels. Thanks to the insulation provided by the transformer, it is possible to obtain two different ground points that can be linked without danger: the negative pole of the fuel cell and the capacitive mid-point at the converter output.

These solutions being judged *a priori* luxurious, it was decided to not develop them in details. They are roughly evaluated by THALES AES, one of our partners in the CELINA project.

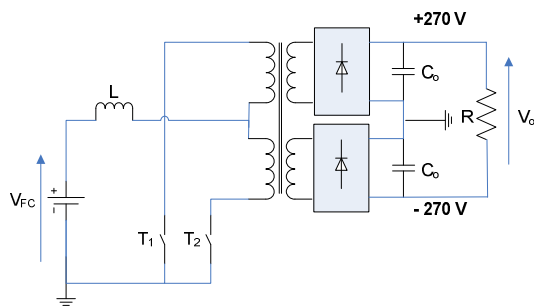


**Figure III. 3: Proposed current-fed Push-Pull converter adapted to the Airbus requirements.**

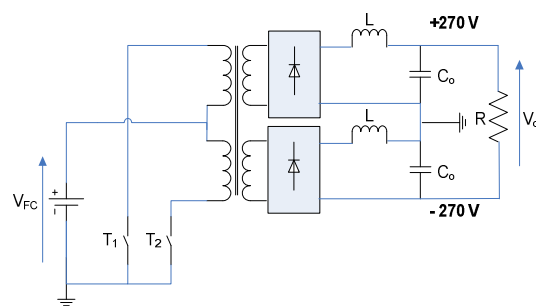


**Figure III. 4: Proposed voltage-fed Push-Pull converter adapted to the Airbus requirements.**

### III.1.2 Non insulated power converter topologies

Traditional and classical non insulated power converters cannot be directly used for this application. The solution necessarily is the combination of different elementary power converters.

**Moreover, let us recall that any solution has to assure that the fuel cell negative pole is connected to the airplane ground.**

In this study, we propose to achieve the AIRBUS requirements by associating classical DC-DC power converters, the Boost converter or the Buck converter, with a classical Buck-Boost converter. This last one will make possible to obtain the -270V DC bus. Anyway, these structures cannot work in all the identified cases in Figure III. 2.

Sizing details for all the elementary power converters are given in § Appendix I.

### III.1.2.1 ±270V Boost topology

The proposed converter in Figure III. 5 can only operate in the boost area of Figure III. 2. This means that the maximal fuel cell mission voltage  $V_{FCmax}$  and the minimal mission voltage  $V_{FCmin}$  will always be lower than 270V.

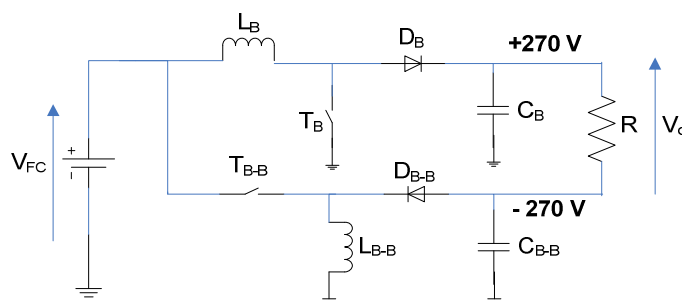


**Figure III. 5: ±270V Boost topology. Parallel association.**

The topology is composed of a Boost converter connected in parallel with a Buck-Boost converter. The Boost converter will boost the fuel cell supplied voltage up to +270V. On the other hand, the Buck-Boost converter will also boost the fuel cell voltage (in absolute value!). But in this case, and thanks to the polarity inversion characteristics of the converter, it will be boosted up to -270V.

The half of the handled power will transit through the Boost converter and the other half will transit through the Buck-Boost converter. This is one of the main reasons to prefer a parallel connection to a serial connection shown in Figure III. 6. In this last case, the whole power will transit through the Boost converter and the half of the handled power will transit once again through the Buck-Boost converter. Therefore, the serial association will present lower efficiency that the parallel association.

In the following, only the parallel association is retained because of its higher efficiency.

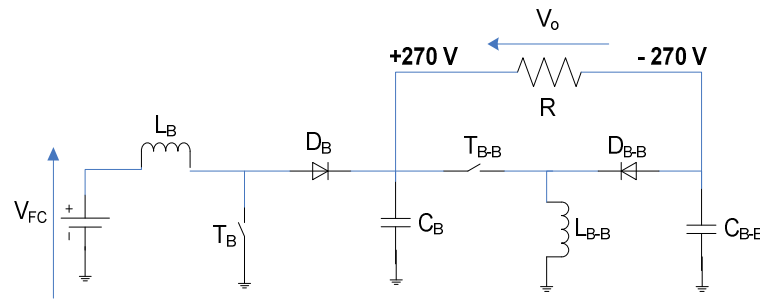


**Figure III. 6: ±270V Boost topology. Serial association.**

Both associations will present an important common mode output voltage due to the asymmetry of the global structure. Nevertheless, this value will be higher in the serial association because the Buck-Boost converter input voltage is fixed by the Boost converter. This means that both converters will not have the same input voltage source. Thus, both converters output voltage will be more different and will create a higher common mode output voltage. This will be further detailed in § III.3.6.1.

### III.1.2.2 ±270V Buck topology

The proposed converter in Figure III. 7 can only operate in the buck area of Figure III. 2. This means that the maximal fuel cell mission voltage  $V_{FCmax}$  and the minimal mission voltage  $V_{FCmin}$  will always be higher than 270V.

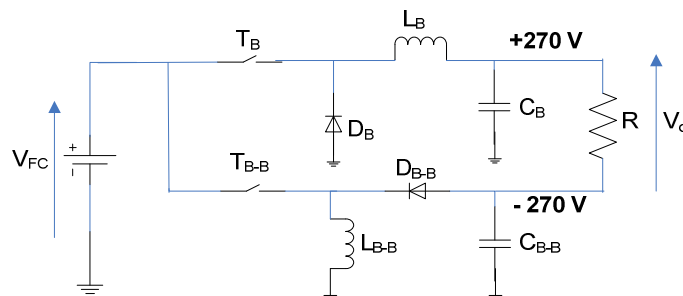


**Figure III. 7: ±270V Buck topology. Parallel association.**

The topology is composed of two buck-boost converters connected in parallel. A classical Buck converter will decrease the fuel cell voltage value down to +270V. On the other hand, similarly to the previous Boost case, a Buck-Boost converter will fix the -270V DC bus. However, in this case, the Buck-Boost will operate in its buck mode. The handled power will be equally shared between both converters.

### III.1.2.3 ±270V Buck-Boost topology

Figure III. 8 shows the proposed topology for the buck-boost area of Figure III. 2. That means that the maximal fuel cell mission voltage  $V_{FCmax}$  is higher than 270V and the minimal mission voltage  $V_{FCmin}$  is lower than 270V.

This topology could work in all areas in Figure III. 2. Nevertheless, it will present, *a priori*, lower efficiency than previous cases because the number of silicon switches has increased.

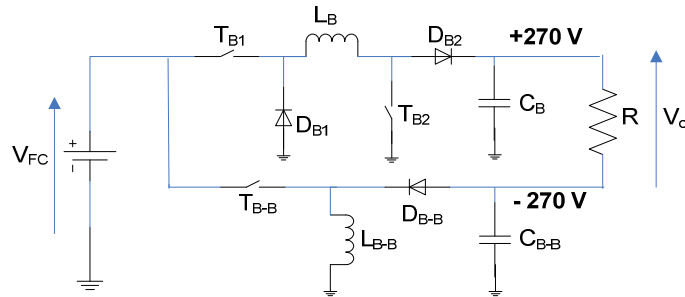


**Figure III. 8 :** ±270V Buck-Boost topology. Parallel association.

The -270V DC bus will be generated by a classical Buck-Boost converter which naturally delivers an output voltage with a polarity reversed compared to the input voltage. A Buck-Boost converter, which does not reverse the polarity of the output voltage compared to the input voltage, will generate the 270V DC bus. This power converter is in fact a serial association of classical buck and boost converters which share respectively their output filtering inductor (for the buck converter) and input inductor (for the boost converter). Sizing details are given in § Appendix I.

### III.1.2.4 Input filter

All the non insulated proposed power converters are based on the association of traditional DC-DC converters (Boost, Buck and Buck-Boost). Buck and Buck-Boost converters do not present naturally an input current filtering device such as a capacitor or an inductor, that protects the fuel cell against the necessary current harmonics produced when the power converter is operating. Therefore, a filtering stage should be placed between the fuel cell and the power converter. **[Dang Bang]** proposes and sizes a LC filter stage. The non insulated power converter topology and the associated input filter stage are presented in Figure III. 9

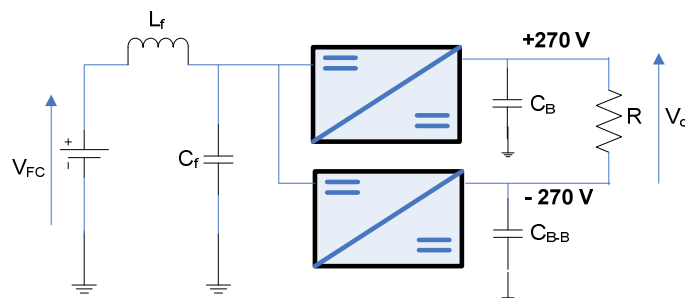


**Figure III. 9:** Input filter and non insulated power converters.

In the following of this chapter, weight and efficiency calculations do not take into account the input filter stage. However, we will see that the interleaving techniques, developed in the next paragraph can help to reduce the input filter sizing, and even to limit it to only one capacitor.

## III.2 Interleaving technique

### III.2.1 General considerations

Due to the required high power (close to 50kW), it is not currently possible to create a power converter that can handle the whole power and can achieve high efficiencies. The current through the inductor will be huge and copper and iron losses will be highly increased. Furthermore, it seems that technology limits nowadays exist to make high current inductors (over 500A) (interview of french inductor societies).

Therefore, usually several elementary power converters are connected in parallel (interleaved converters) in order to share the power to be handled. Figure III. 10 shows, as example, a three elementary Boost power converter connected in parallel for the input and the output. In this case, each branch will handle one third of the load power. Some other authors have also studied the interleaving technique possibilities with coupled [Costan] [Lee] and regular inductors [Brett] [Destraz] [Rufer] [Lai]

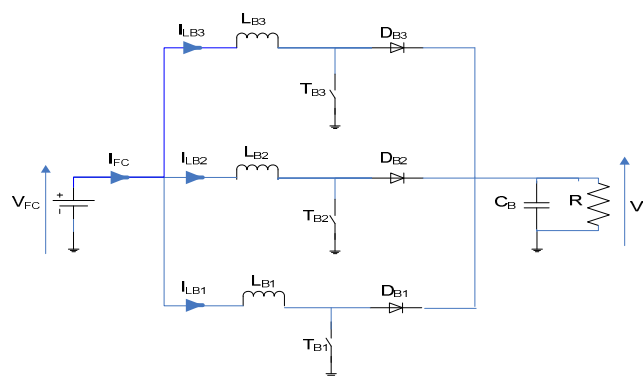


Figure III. 10: Three interleaved Boost converters.

In the following lines, the case of interleaved classical Boost converters will be treated; nevertheless, the same analysis can be similarly applied to the other classical converters.

Firstly, let us recall the inductance expression in the case of only one Boost converter (E III. 1):

$$L_{BOOST} = \frac{\alpha V_{FC}}{f_s \Delta i_{FC}} \quad \text{E III. 1}$$

The fuel cell current ripple (= the inductor ripple in this case) depends on the voltage  $V_{FC}$  supplied by the fuel cell, the switching frequency  $f_s$  of the silicon switches, and the duty cycle  $\alpha$  of the silicon switches ( $\alpha$  = conduction duration/ switching period  $T_s$ ).

Secondly, let us consider the case of interleaved Boost converters. If all inductor are sized with the value calculated in E III. 1 and if each silicon switches PWM modulation is  $360^\circ/n$  degrees shifted

(with  $n$  the number of interleaved branches). In this case, it is possible to reduce the fuel cell current ripple. Figure III. 11 shows the fuel cell current ripple in function of the duty cycle and the interleaved branch number. Under these assumptions, the fuel cell current ripple clearly decreases with the number of interleaved converters.

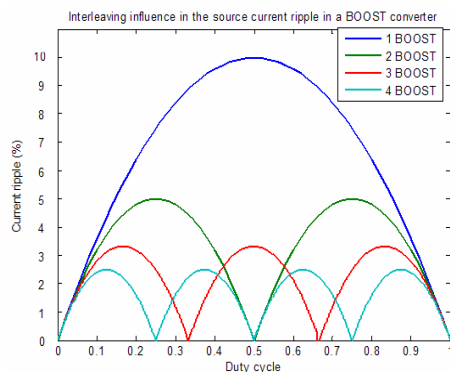


**Figure III. 11: Fuel cell current ripple in function of the duty cycle and the number of interleaved branches.**

Nevertheless, our main aim is **to limit the fuel cell current ripple to 10% of the fuel cell nominal current**. On the other hand, the current ripple in each branch in parallel can be *a priori* increased if losses remain limited. Therefore, this means that the branch inductance can be reduced if the interleaving technique is applied correctly by accepting the rise of the branch current ripple.

Expression E III. 2 gives the inductance **to obtain the desired fuel cell current ripple**:

$$L_n = \frac{\alpha V_{\min FC}}{f_s \Delta i_{FC} n} \tag{E III. 2}$$

The inductance can be strongly reduced with the number of interleaved branches. Figure III. 12 shows the obtained current ripple if inductors are sized like in E III. 2. The maximal fuel cell current ripple remains limited to 10%.

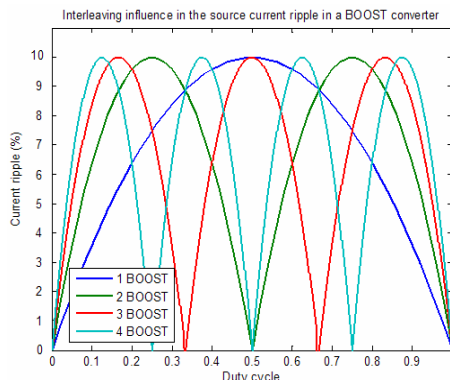


**Figure III. 12: Fuel cell current ripple in function of the duty cycle and the number of interleaved branches  $n$  by assuming an inductance variable with  $n$ .**

The previous proposed inductance sizing will permit to reduce the inductance  $L$  if the number of interleaved branches is increased. But how will the global inductor weight and volume be affected?

Inductor stored energy is an image of the global inductor weight and volume. It can be calculated thanks to the well-known formula  $\frac{1}{2}LI^2$ . Figure III. 13 plots the inductor stored energy in function of the input current ripple.

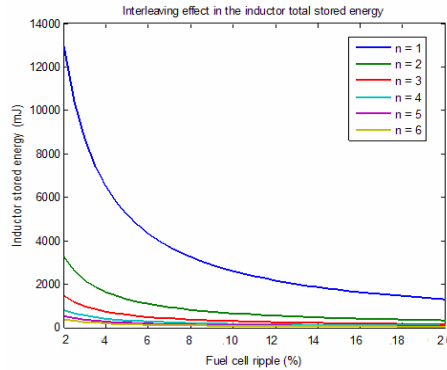


**Figure III. 13: Inductor stored energy in function of the fuel cell current ripple.**

As it can be observed in Figure III. 13, inductor stored energy, and thus inductor weight and volume, is greatly reduced with two, three and four interleaved branches. However, if the number of interleaved branches increases further, the gain in terms of stored energy is less important.

Nevertheless, the influence of the number of interleaved converters in terms of weight and efficiency remains difficult to be evaluated easily, because the efficiency and weight of the power converter depends on losses produced by silicon switches and inductors. Indeed, if the number of interleaved branches increases, the current flowing through silicon switches and inductors will be reduced; this will permit to change the range of the silicon switches and of the inductor cores; the power converter losses will be modified with this range change. Estimating the gain in terms of efficiency and weight needs a more complete study that will be achieved in § III.4.

The fuel cell current ripple reduction can be explained because the input apparent switching frequency is multiplied by the number of parallelized converters  $n$ . A similar effect is obtained for the output capacitor  $C_o$  due to the rise of the output apparent frequency. Expression E III. 3 gives the capacitance  $C_o$  to obtain the desired output voltage ripple.

$$C_o = \frac{\alpha I_{load}}{f_s \Delta v_o n} \quad \text{E III. 3}$$

### III.2.2 Output voltage dynamic response with interleaved converters

In order to evaluate the interleaving effect on the converter dynamics, the behavior of a 20kW Boost converter, not regulated (open loop), was simulated face to a 10kW load step. Simulation results



are presented in Figure III. 14. It can be observed that the power converter response time to reach the steady state strongly decreases with the rise of parallel branch number. Nevertheless, the output voltage overvoltage was not increased. All the simulated converters in fact present the same maximal overshoot.

The same power converters were simulated face an output voltage reference step. In this case, the output voltage reference was increased from 270V up to 340V. Figure III. 15 shows the simulation results. As in previous case, the more the number of branches increases, the more the response time decreases; the overvoltage remains the same in all cases.

Thus, it is possible to say that the interleaving technique will improve the power converter response time without increasing transitory overshoots. This can be explained because interleaved converters present smaller inductances and capacitances and because the apparent switching frequency is increased.

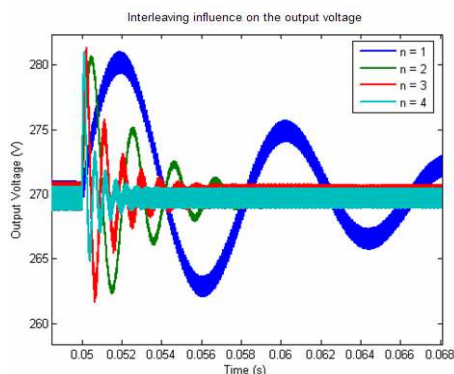


**Figure III. 14: Response of open loop interleaved Boost converters for a load step**

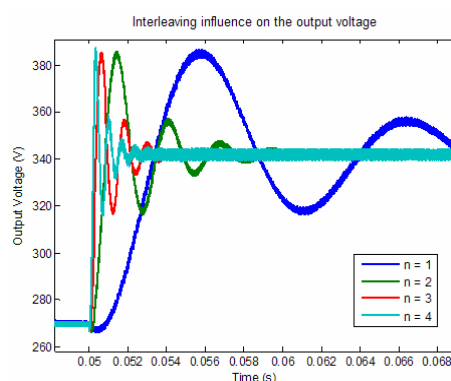


**Figure III. 15: Response of open loop interleaved Boost converters for a reference voltage step**

### III.2.3 Interleaving technique disadvantages.

The major drawback of interleaved power converters is the branch current ripple rise. Indeed, if the branch inductance is reduced, the branch current ripple will logically increase. This branch ripple rise causes two main drawbacks:

- Losses produced by silicon power switches and iron losses within the inductors depend on the current ripple. If the current ripple is extremely increased, conduction losses within the silicon switches will increase. Silicon switch conduction losses and inductor iron losses are respectively given by expressions E III. 4. and E III. 5.

$$W_{conduction} = \alpha I_{Ln} V_{ce0} + \left( \alpha I_{Ln}^2 + \alpha \frac{\Delta I_{Ln}^2}{12} \right) R_d \tag{E III. 4}$$

$$W_{iron} = f_s^{1.46} \Delta B^2 \tag{E III. 5}$$

The power converter efficiency will be studied in § III.4.

- If the branch current ripple is highly increased, it is possible to reach non continuous conduction mode for the power converter. In that mode, each elementary DC-DC power converter does not present the same transfer function as in continuous mode. Therefore, the power converter control can become a complicated issue. The control of interleaved power converters will be farther detailed in § III.3.5.

In some cases, the amount of power required by the load is small enough to be transferred with duration smaller than the whole switching period. In this case, the current through the inductor falls to zero during a part of the switching period. This operation mode is called discontinuous. Although slight, the difference between the continuous and discontinuous modes has a strong effect on the output voltage equation [Ferriux].

The static behavior of a 20kW and 270V output voltage Boost converter can be observed in Figure III. 16. This figure plots the input voltage variation in function of the output current for a fixed duty cycle. It can be observed that power converter response is totally different in the continuous and discontinuous modes.

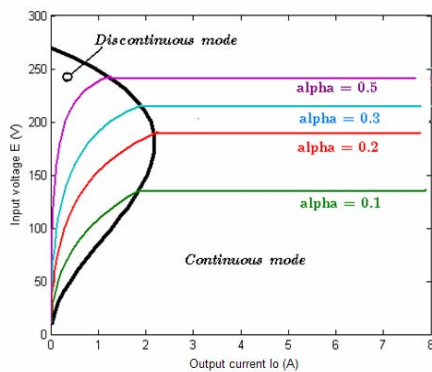


**Figure III. 16: Border between the continuous and discontinuous modes.**

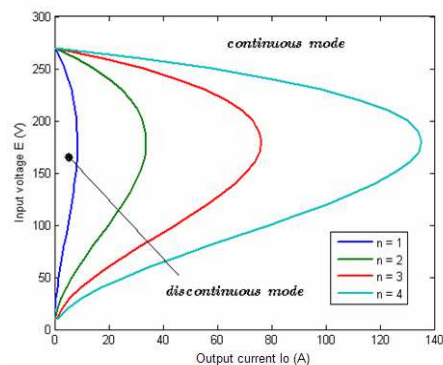


**Figure III. 17: Evolution of the border between the continuous and discontinuous modes with the number of interleaved branches.**

Remark: Usual representations plot the normalized current with the normalized voltage, but this kind of plots do not let to see the evolution of the border between continuous and discontinuous modes with the number of parallel branches.

The border between discontinuous and continuous modes is reached when the inductor current falls to zero exactly at the end of the switching cycle (black line in Figure III. 16).

If the continuous and discontinuous mode border is plotted for several numbers of interleaved Boost converters (Figure III. 17), it can be observed that the discontinuous mode area will increase with the number of parallel branches. **That means that it is easy to reach the discontinuous mode with interleaved converters, if inductors are sized like in E III. 2.**

Furthermore, as observable in Figure III. 17, discontinuous conduction mode can be reached even at nominal power (that corresponds to an output current of 74 A). Thus, it can be senseless to size a small inductor, if the power converter is going to operate in discontinuous mode at nominal power. Therefore, in these cases, the sized inductor will be the minimal inductor that guarantees the continuous mode working mode. Expression E III. 6 gives the proposed inductor sizing methodology:

$$L_n = \max \left[ \frac{\alpha V_{\min FC}}{f_s \Delta i_{FCn}}, \frac{\alpha(1-\alpha)^2 V_0 n}{2f_s P} \right] \quad \text{E III. 6}$$

The inductance value will be the maximum between the obtained value that guarantees the desired maximal fuel cell current ripple and the value that guarantees the continuous conduction mode.

## III.3 Power converter control

All proposed converters are an association of elementary power converters: Buck converter, Boost converter and Buck-Boost converter. Even the current-fed and voltage-fed Push-Pull converters are variants of elementary power converters (respectively of the Boost converter and of the Buck converter). Therefore, the control loops which will be studied in this part can be rather easily applied to the evocated insulated power converters. In future paragraphs, the proposed control loops for elementary power converters will be detailed.

Literature offers a huge variety of control laws in order to pilot classical power converters: sliding mode [Olm] [Giral] [Bilanovic], predictive[Babu] [Ren], fuzzy logic [Faucher]...

In our study, we chose a confirmed control structure based on the works of [Sanchis], [Sanchis2], [Flumian]: the cascade structure (a rapid current loop imbricated into a slow voltage loop) with complete compensations of non linearities (to assure the robustness face to load and input voltage variations). Switching signal for the silicon switches will be obtained after two cascaded control loops and finally through a classical constant frequency PWM modulation. One of the main advantages of this kind of modulation is the simplicity to implement the correct phase-shift for each parallelized branch in comparison with other usual control techniques such as sliding mode or hysteresis, for which, if there is no control modification, the switching frequency is not constant.

### III.3.1 Buck-Boost converter

#### III.3.1.1 Buck-boost converter modeling

The Buck-boost converter (Figure III. 18) is a DC-DC converter that can offer an output voltage higher or lower than the input voltage. The output voltage is adjustable via the duty cycle of the silicon switch T:

$$\frac{V_o}{E} = \frac{\alpha}{1-\alpha} \quad \text{where } 0 < \alpha < 1 \quad \text{E III.7}$$

As already expressed, the polarity sign of the output voltage is opposed to the input voltage one. Moreover, one drawback of this converter is that the switch does not have a terminal connected to the ground. This complicates its necessary driving circuitry which has to be insulated.

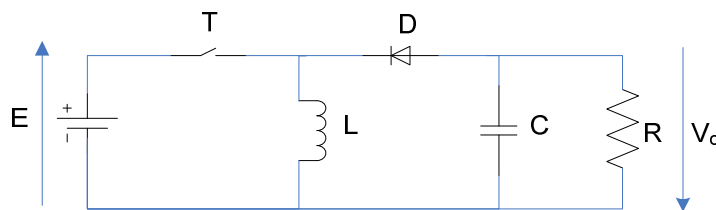


**Figure III. 18: Buck-Boost converter.**

The power converter analysis is done considering a constant input voltage  $E$ . The inductor and capacitor internal resistors are not considered. According to the state of the switch  $T$ , it is possible to find two different working sequences:

- The switch  $T$  is closed (= it conducts):  $t_{on}$

During this sequence, the switch  $T$  is conducting and the diode  $D$  is open. The inductor  $L$  is storing the energy supplied by the voltage source. The capacitor  $C$  is supplying load power. The equations that model the power converter behavior during this sequence are:

$$v_L = L \frac{di_L}{dt} = E \tag{E III.8}$$

$$i_C = -C \frac{dv_O}{dt} = i_O = \frac{v_O}{R} \Rightarrow C \frac{dv_O}{dt} = -\frac{v_O}{R} \tag{E III.9}$$

- The switch  $T$  is open (= it does not conduct):  $t_{off}$

In this sequence, the energy previously stored in the inductor  $L$  is transferred to the output capacitor  $C$  and the load. The diode  $D$  is conducting and the silicon switch  $T$  is open. The equations that model the power converter behavior during this sequence are:

$$v_L = L \frac{di_L}{dt} = -v_o \tag{E III.10}$$

$$i_C = -C \frac{dv_O}{dt} = i_O - i_L = \frac{v_O}{R} - i_L \Rightarrow C \frac{dv_O}{dt} = i_L - \frac{v_O}{R} \tag{E III.11}$$

If we define  $M$  as the state of the switch  $T$  ( $M=1 \Leftrightarrow T$  ON ;  $M=0 \Leftrightarrow T$  OFF), and thanks to expressions E III.10, E III.11, E III.8 and E III.9 , it is possible to find expressions E III.12 and E III.13 that model the time variations of the state variables:

$$L \frac{di_L}{dt} = M \cdot E - (1-M) \cdot v_o \tag{E III.12}$$

$$C \frac{dv_o}{dt} = (1-M) \cdot i_L - \frac{v_o}{R} \quad \text{E III.13}$$

Considering the duty cycle  $\alpha$  it is possible to transform E III.12 and E III.13 into an average model, that can reproduce the average time variations of the state variables.

$$L \frac{di_L}{dt} = \alpha \cdot E - (1-\alpha) \cdot v_o \quad \text{E III.14}$$

$$C \frac{dv_o}{dt} = (1-\alpha) \cdot i_L - \frac{v_o}{R} \quad \text{E III.15}$$

### III.3.1.2 Buck-boost converter current loop

The current loop guarantees limited variations of the current flowing through the inductor during important load variations. This will protect the power converter components from overvoltages and not desired high current values.

The inductor is characterized by expressions E III.16 and E III.17:

$$v_L = L \frac{di_L}{dt} \quad \text{E III.16}$$

$$v_L = \alpha E - (1-\alpha)v_o \quad \text{E III.17}$$

The second equation derives from the average model. It must be considered that the output voltage  $v_o$  is a state variable. Thus, starting from E III.16 and E III.17 and by applying the Laplace transformation, an inductor current model is obtained:

$$I_L(s) = \frac{1}{Ls} V_L = \frac{1}{Ls} [E\alpha(s) - V_o(1-\alpha(s))] = \frac{1}{Ls} [(E + V_o)\alpha(s) - V_o(s)] \quad \text{E III.18}$$

From E III.18, the expression that gives the inductor current in function of the duty cycle is:

$$I_L = \frac{\alpha(E + V_o) - V_o}{Ls} \quad \text{E III.19}$$

The inductor current loop is deduced from the inductor current modeled in equation E III.19, and shown in Figure III. 19.

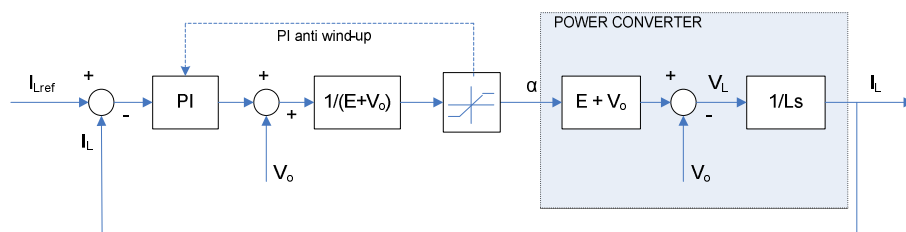


**Figure III. 19 : Inductor current control loop**

We chose to compensate all non linearities to be robust face to load and input voltage variations [Sanchis]. The following system transfer function is obtained:

$$I_L(s) = K_i \frac{T_i \cdot s + 1}{T_i \cdot s} \cdot \frac{1}{L \cdot s} \tag{E III.20}$$

The employed corrector is a proportional-integral whose parameter identification was classically achieved. The desired corrector margin phase  $m_\phi$  is  $45^\circ$  and the controller bandwidth  $\omega_{bw}$  should be ten times lower than the switching frequency. The PI corrector parameters are given in E III.21 and E III.22 [Flumian].

$$T_i = \frac{\tan(m_{\phi_i})}{\omega_{bwi}} \tag{E III.21}$$

$$K_i = \frac{L T_i \omega_{bwi}^2}{\sqrt{1 + (T_i \omega_{bwi})^2}} \tag{E III.22}$$

The current loop reference is given by the slower voltage loop detailed in the following paragraph.

### III.3.1.3 Buck-Boost converter voltage loop

The output voltage loop was designed following a similar strategy to the current loop. The relations between inductor current and capacitor voltage are as follows:

$$i_C = C \frac{dv_o}{dt} \tag{E III.23}$$

$$i_C = (1 - \alpha)i_L - i_o = (1 - \alpha)i_L - \frac{v_o}{R} \tag{E III.24}$$

The second equation derives from the average model. As it has been previously done in the current loop, the transfer function characterizing the output voltage is given by:

$$V_o(s) = \frac{1}{C} I_c(s) = \frac{1}{C} [I_L(1 - \alpha(s)) - I_o(s)] \quad \text{E III.25}$$

From previous equations, a useful expression, that will help to design the output voltage control loop, can be obtained:

$$I_L(s) = \frac{I_c(s) + I_o(s)}{1 - \alpha} \quad \text{E III.26}$$

Considering the Buck-Boost continuous mode transfer function, the previous equation could be written:

$$I_L(s) = \frac{[I_c(s) + I_o(s)] [E(s) + V_o(s)]}{E(s)} \quad \text{E III.27}$$

The final output voltage control loop is shown in Figure III. 20.

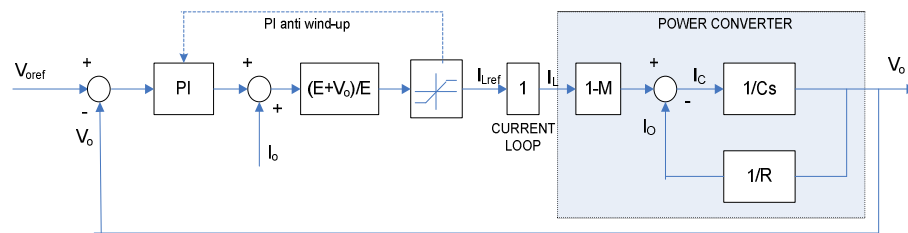


**Figure III. 20: Output voltage control loop.**

The control loop proposes to compensate all non linearities to obtain the following transfer function:

$$V_o(s) = K_v \frac{T_v \cdot s + 1}{T_v \cdot s} \cdot \frac{1}{C \cdot s} \quad \text{E III.28}$$

The desired corrector margin phase is  $45^\circ$  and the controller bandwidth should be one hundred times lower than the switching frequency. The PI corrector parameters are given in E III.29 and E III.30 [Flumian].

$$T_v = \frac{\tan(m_{\phi_v})}{\omega_{bw_v}} \quad \text{E III.29}$$

$$K_v = \frac{CT_v \omega_{bw_v}^2}{\sqrt{1 + (T_v \omega_{bw_v})^2}} \quad \text{E III.30}$$



### III.3.1.4 Proposed Buck-Boost converter control validation

In order to validate the two proposed control loops, a 20kW Buck-Boost converter was submitted to the load profile drawn in Figure III. 21. The simulated Buck-Boost converter requirements were:

$$P = 20 \text{ kW}$$

$$f_s = 20 \text{ kHz}$$

$$E = 135 \text{ V}$$

$$V_o = - 270 \text{ V}$$

$$\Delta i = 150 \text{ A}$$

$$\Delta V_o = 2 \text{ V}$$

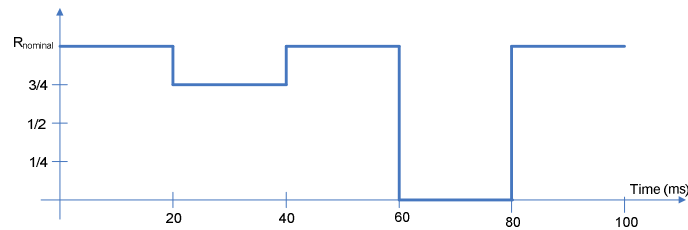


Figure III. 21: Simulated load profile.

Simulation results in Figure III. 22 and Figure III. 23 illustrate the good dynamic behavior of the proposed control for the Buck-boost converter.

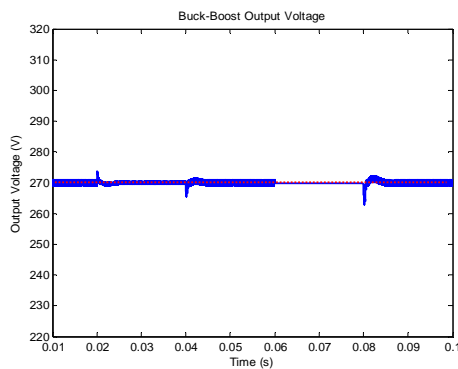


Figure III. 22: Buck-Boost output voltage

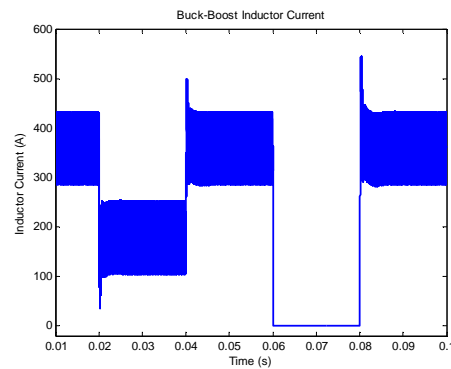


Figure III. 23: Buck-Boost inductor current.

### III.3.2 Boost converter control

#### III.3.2.1 Boost converter modeling

A boost converter (Figure III. 24) (or step-up converter) is a DC-DC power converter which offers an DC output voltage higher than its DC input voltage. The output voltage is adjustable via the duty cycle of the silicon switch T:

$$\frac{V_o}{E} = \frac{1}{1-\alpha} \quad \text{where } 0 < \alpha < 1 \tag{E III.31}$$

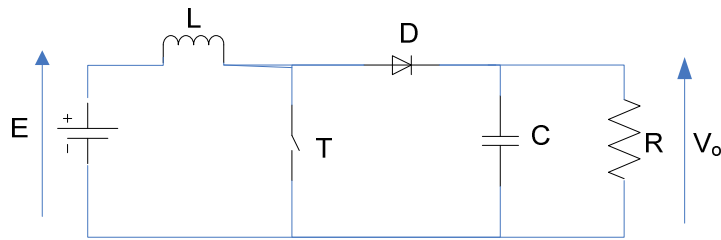


**Figure III. 24: Boost converter.**

As the Buck-Boost converter, the Boost converter is a non linear converter. Thus, the proposed control is going to be obtained in a similar way as for the Buck-Boost converter.

The power converter analysis is done considering a constant input voltage  $E$ . The inductor and capacitor internal resistors are not considered. According to the state of the switch  $T$ , it is possible to find two different working sequences:

- The switch  $T$  is closed (= it conducts):  $t_{on}$

The switch  $T$  is conducting, resulting in an increase of the inductor current. The capacitor is feeding the load and is keeping constant the output voltage. The equations that model the power converter behavior during this sequence are:

$$v_L = L \frac{di_L}{dt} = E \quad \text{E III.32}$$

$$i_C = C \frac{dv_o}{dt} = i_o \Rightarrow C \frac{dv_o}{dt} = \frac{v_o}{R} \quad \text{E III.33}$$

- The switch  $T$  is open (= it does not conduct):  $t_{off}$

The switch is open and the only path offered to the inductor current is through the diode  $D$ , the capacitor  $C$  and the load  $R$ . This results in transferring the energy stored in the inductor during the previous sequence into the capacitor. The equations that model the power converter behavior during this sequence are:

$$v_L = L \frac{di_L}{dt} = E - v_o \quad \text{E III.34}$$

$$i_o = i_L - C \frac{dv_o}{dt} = \frac{v_o}{R} \Rightarrow C \frac{dv_o}{dt} = i_L - \frac{v_o}{R} \quad \text{E III.35}$$

If  $M$  is defined as the state of the switch ( $M=1 \Leftrightarrow T$  ON ;  $M=0 \Leftrightarrow T$  OFF), and thanks to expressions E III.32, E III.33, E III.34 and E III.35, it is possible to find expressions E III.36 and E III.37 that model the time variations of the state variables:

$$L \frac{di_L}{dt} = E - (1 - M) \cdot v_o \tag{E III.36}$$

$$C \frac{dv_o}{dt} = (1 - M) \cdot i_L - \frac{v_o}{R} \tag{E III.37}$$

Considering the duty cycle  $\alpha$ , it is possible to transform E III.36 and E III.37 into an average model, that can reproduce the average time variations of the state variables:

$$L \frac{di_L}{dt} = E - (1 - \alpha) \cdot v_o \tag{E III.38}$$

$$C \frac{dv_o}{dt} = (1 - \alpha) \cdot i_L - \frac{v_o}{R} \tag{E III.39}$$

### III.3.2.2 Boost converter current loop

In the same way as for the Buck-boost converter, starting from these two equations

$$v_L = L \frac{di_L}{dt} \tag{E III.40}$$

$$v_L = E - (1 - \alpha)v_o \tag{E III.41}$$

it can be obtained the following final equation and the current loop in Figure III. 25:

$$I_L = \frac{E - V_o(1 - \alpha)}{L s} \tag{E III.42}$$

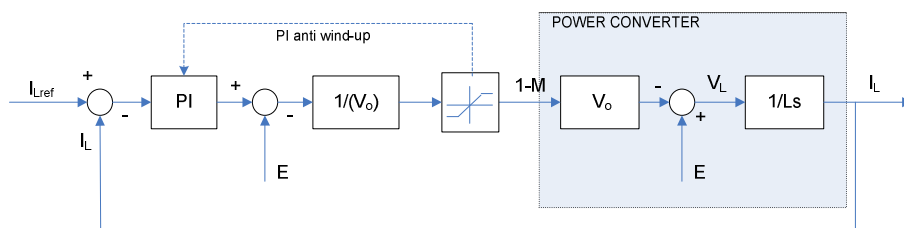


Figure III. 25: Boost current control loop.

The proportional-integral corrector is designed in the same way as the Buck-boost converter [Flumian].

### III.3.2.3 Boost converter voltage loop

Similarly, starting from these two equations

$$i_C = C \frac{dv_O}{dt} \quad \text{E III.43}$$

$$i_C = (1-\alpha)i_L - i_O = (1-\alpha)i_L - \frac{v_O}{R} \quad \text{E III.44}$$

and using the transfer function of the Boost converter, it can be obtained the following results:

$$I_L(s) = \frac{I_C(s) + I_O(s)}{1-\alpha} \quad \text{E III.45}$$

$$I_L(s) = \frac{V_O(s) [I_C(s) + I_O(s)]}{E(s)} \quad \text{E III.46}$$

The proposed output voltage control loop is shown in Figure III. 26.

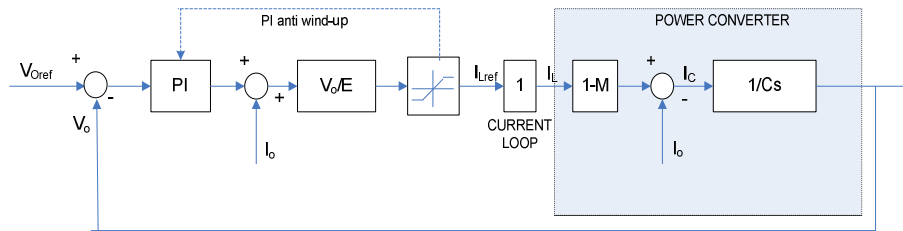


**Figure III. 26: Output voltage control loop.**

The proportional-integral corrector is designed in the same way as the Buck-boost converter [Flumian].

### III.3.2.4 Proposed Boost converter control validation

In order to validate the two proposed control loops, a 20kW Boost converter was submitted to the load profile drawn in Figure III. 21. The simulated Boost converter requirements were:

$$P = 20 \text{ kW}$$

$$f_s = 20 \text{ kHz}$$

$$E = 70 \text{ V}$$

$$V_o = 270 \text{ V}$$

$$\Delta i = 10 \%$$

$$\Delta V_o = 2 \text{ V}$$

Simulation results in Figure III. 27 and Figure III. 28 illustrate the good dynamic behavior of the proposed control for the Boost converter.

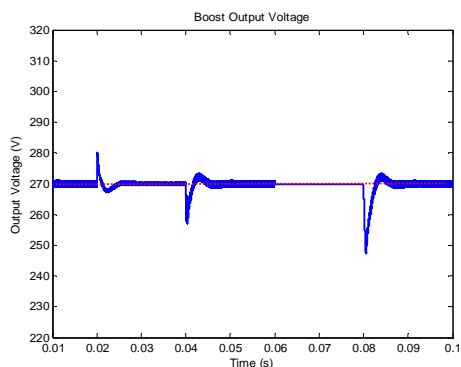


Figure III. 27: Boost output voltage

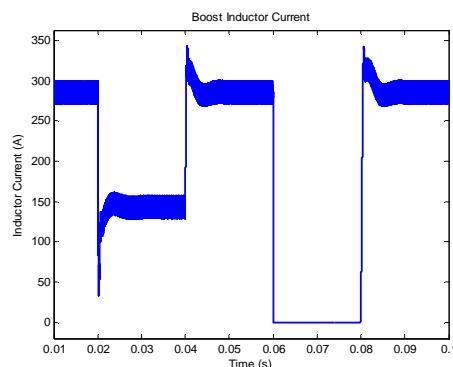


Figure III. 28: Boost inductor current.

### III.3.3 Buck converter control

#### III.3.3.1 Buck converter modeling

A buck converter (Figure III. 29) is a step-down DC/DC converter. That means that it offers an output voltage magnitude that is lower than the input voltage. The output voltage is adjustable via the duty cycle of the silicon switch  $T$ :

$$\frac{V_o}{E} = \alpha \quad \text{where } 0 < \alpha < 1 \tag{E III.47}$$

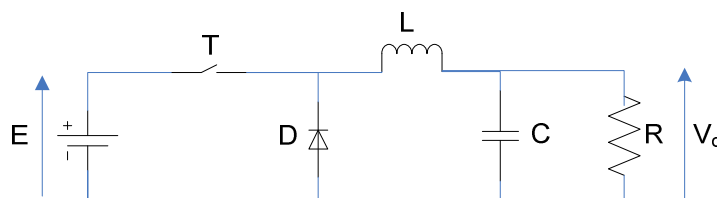


Figure III. 29: Buck converter.

As for both previous cases, the proposed control loop is a cascade structure: a rapid current loop imbricated into a slow voltage loop.

The power converter analysis is done considering a constant input voltage  $E$ . The inductor and capacitor internal resistors are not considered. According to the state of the switch  $T$ , it is possible to find two different working sequences:

- The switch  $T$  is closed (= it conducts):  $t_{on}$

During this sequence, the switch is conducting and the diode is open. The inductor voltage is  $V_L = E - v_o$ . The current through the inductor rises linearly. As the diode is reverse-biased by the voltage source  $E$ , no current flows through it. Thus, the inductor is storing the energy supplied by the voltage source. The capacitor is feeding the output load. The equations that model the power converter behavior during this sequence are:

$$v_L = L \frac{di_L}{dt} = E - v_o \quad \text{E III.48}$$

$$i_C = C \frac{dv_o}{dt} \Rightarrow C \frac{dv_o}{dt} = i_L - i_o = i_L - \frac{v_o}{R} \quad \text{E III.49}$$

□ The switch  $T$  is open (= it does not conduct):  $t_{\text{off}}$

In this sequence, the inductor stored energy is transferred to the output capacitor. The diode is forward biased. The inductor voltage is  $V_L = -V_o$  (by neglecting the diode drop). Thus, the current  $i_L$  decreases. The equations that model the power converter behavior during this sequence are:

$$v_L = L \frac{di_L}{dt} = -v_o \quad \text{E III.50}$$

$$i_C = C \frac{dv_o}{dt} \Rightarrow C \frac{dv_o}{dt} = i_L - i_o = i_L - \frac{v_o}{R} \quad \text{E III.51}$$

If we define  $M$  as the state of the switch ( $M=1 \Leftrightarrow T \text{ ON}$  ;  $M=0 \Leftrightarrow T \text{ OFF}$ ), and thanks to E III.48, E III.49, E III.50 and E III.51, it is possible to find expressions E III.52 and E III.53 that model the time variations of the state variables:

$$L \frac{di_L}{dt} = M \cdot E + (2M - 1) \cdot v_o \quad \text{E III.52}$$

$$C \frac{dv_o}{dt} = i_L - \frac{v_o}{R} \quad \text{E III.53}$$

Considering the duty cycle  $\alpha$ , it is possible to transform E III.52 and E III.53 into an average model, that can reproduce the time average variations of the state variables:

$$L \frac{di_L}{dt} = \alpha \cdot E + (2\alpha - 1) \cdot v_o \quad \text{E III.54}$$

$$C \frac{dv_o}{dt} = i_L - \frac{v_o}{R} \quad \text{E III.55}$$

### III.3.3.2 Buck converter current loop

In the same way as for the Buck-boost converter, starting from these two equations

$$v_L = L \frac{di_L}{dt} \quad \text{E III.56}$$

$$v_L = \alpha \cdot E + (2\alpha - 1) \cdot v_o \tag{E III.57}$$

it can be obtained the following final equation and the current loop in Figure III.30:

$$I_L = [(E + 2V_o)\alpha - V_o] \frac{1}{Ls} \tag{E III.58}$$

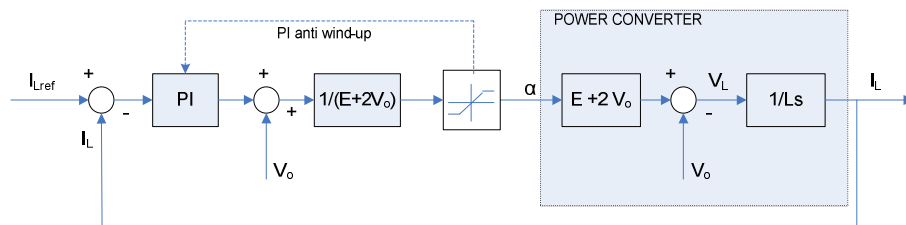


Figure III. 30: Buck inductor current control loop

The proportional-integral corrector is designed in the same way as the Buck-boost converter.

### III.3.3.3 Buck converter voltage loop

Similarly, starting from these two equations:

$$i_C = C \frac{dv_o}{dt} \tag{E III.59}$$

$$i_C = i_L - \frac{v_o}{R} \tag{E III.60}$$

it can be obtained the following results:

$$V_o = (I_L - I_o) \frac{1}{Cs} \tag{E III.61}$$

$$I_L(s) = I_C(s) + I_o(s) \tag{E III.62}$$

The proposed output voltage control loop is shown in Figure III. 31.

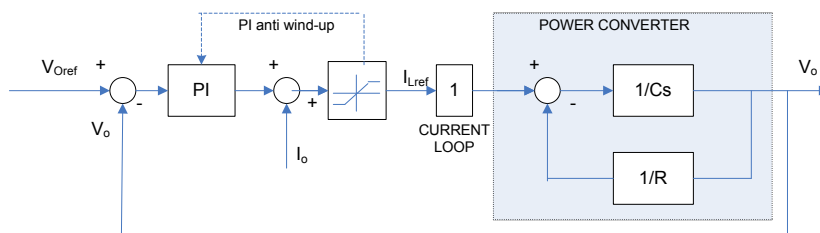


Figure III. 31: Buck voltage control loop.

The proportional-integral corrector is designed in the same way as the Buck-boost converter [Pablo].

### III.3.3.4 Buck proposed control validation

In order to validate the two proposed control loops, a 20kW Boost converter was submitted to the load profile drawn in Figure III. 21. The simulated Buck converter requirements were:

- P = 20 kW
- $f_s = 20$  kHz
- E = 400 V
- $V_o = 270$  V
- $\Delta i = 20$  %
- $\Delta V_o = 2$  V

Simulation results in Figure III.32 and Figure III.33 illustrate the good dynamic behavior of the proposed control for the Boost converter.

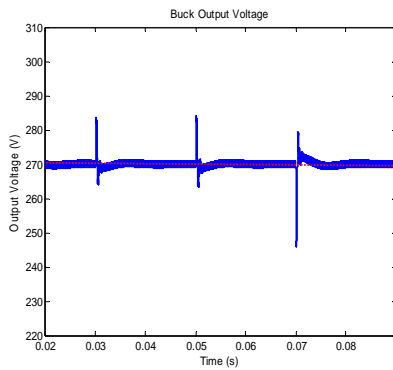


Figure III. 32: Buck output voltage

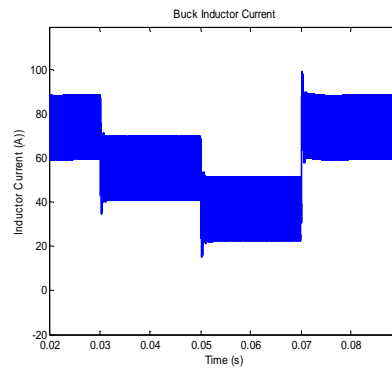


Figure III. 33: Buck inductor current.

### III.3.4 Conclusions on the proposed control laws

All the control laws proposed for the three previous power converters were obtained by compensating all non linearities in order to obtain two cascade control loops, each one composed of a PI corrector and responding to a first order transfer function. The control scheme is presented in Figure III. 34.

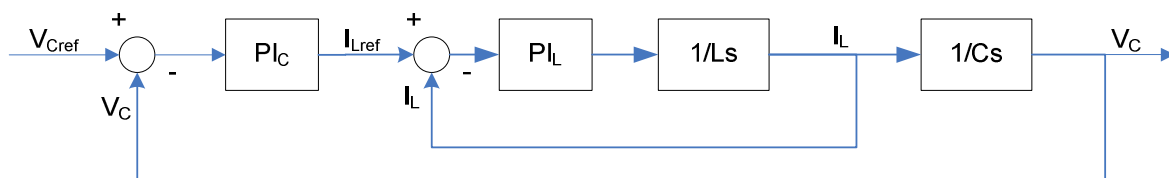


Figure III. 34: Proposed control loop structure for the three power converter

The internal control loop will depend in all cases on the inductance and the external loop on the capacitance. Thus, it is possible to affirm that, if the three proposed converters are sized with similar



inductances and capacitances, all of them will present similar output voltage characteristics face to load and input voltage variations. This point will be important to satisfy the airbus requirements concerning the output voltage common mode rejection. This study will be further developed in § III.3.6.1.

Obviously, in order to obtain similar voltage response, both classical converter capacitors (the two bus capacitors) must have the same capacitance value. Thus, it is the highest capacitance of the two classical converters which determines the two DC bus capacitor value.

### III.3.5 Control of DC-DC Interleaved power converters

The aim of power converter control laws is to control the output voltage behavior (while also controlling inductor current behavior).

In the case of interleaved DC-DC converters, only one output voltage control loop is required because all the branch outputs are connected in parallel. Nevertheless, the control law must also guarantee a balanced current sharing between all the interleaved branches. A branch current overcharge will lead to worse efficiency operating points. And if this current overcharge becomes important, it is possible that it will damage or even break down the branch.

For a correct interleaved operation mode, the PWM modulation must be shifted of  $k/n$  degrees, with  $k$  the number of the branch (by assuming that an order for the branches was chosen) and  $n$  the total number of branches. Moreover, the current reference created by the voltage loop must be equally shared between all the branches. Thus, the current reference must be divided by the total number of branches.

Two different methods can be applied in order to calculate the duty cycle  $\alpha$  and switching orders of the silicon switches. In Figure III. 35., the proposed method presents just one current loop. A reference duty cycle is calculated from one reference branch. The same duty cycle is applied to the other branches after a correctly shifted PWM modulation.

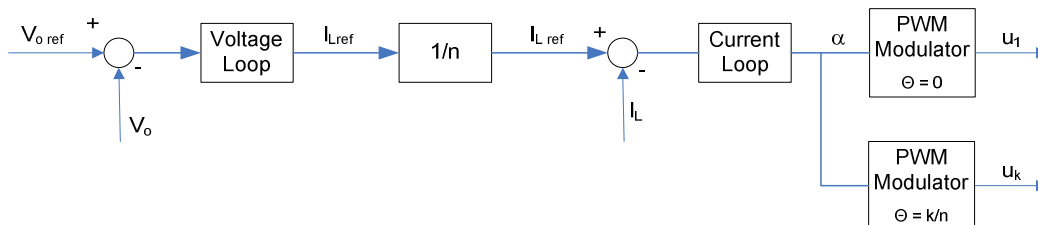


Figure III. 35: Interleaved converter control with one current control loop.

On the other hand, Figure III. 36 proposes a control structure with  $n$  current control loops. The inductor current reference coming from the output voltage control loop is treated separately for all the branches. Thus, the power converter control will have to calculate  $n$  different duty cycles.

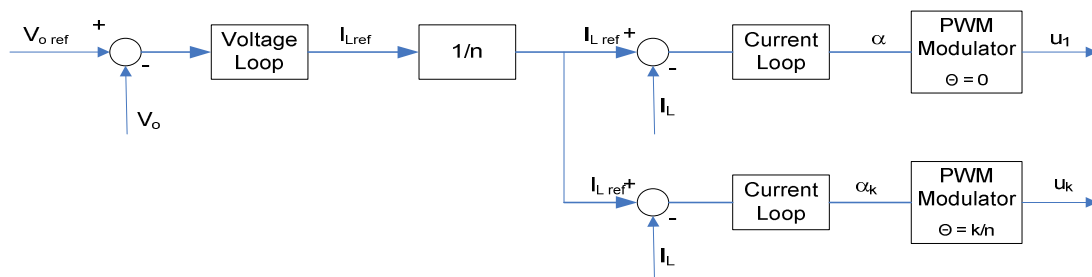


Figure III. 36: Interleaved converter control with  $n$  current control loops.

Each control structure presents advantages and disadvantages.

The one current control loop method will economize sensors and will be easier to implement. However, this method can only work if losses are similar in all branches. Furthermore, if the reference branch breaks down, the whole converter will be out of control.

The  $n$  current control loop method presents the opposite characteristics. The number of current sensors is increased and the control system implementation becomes more difficult. On the other hand, the current is controlled through the whole converter. A disparity of branch losses will not be prejudicial, and in default case, it is possible to continue supplying power with a reduced value.

### III.3.5.1 Discontinuous mode

As already explained in §III.2, interleaving technique can reduce inductances and capacitances. Nevertheless, the branch current ripple will increase with the number of parallel branches, making it possible easily to reach the discontinuous mode for the power converter.

The control loops proposed in § III.3.1, III.3.2 and III.3.3. are based on continuous mode models. Nevertheless, it has been already explained (§III.2.3) that the transfer functions of power converters are not equal in continuous and discontinuous modes. That means that in discontinuous mode cases, proposed control loops are based on erratic models.

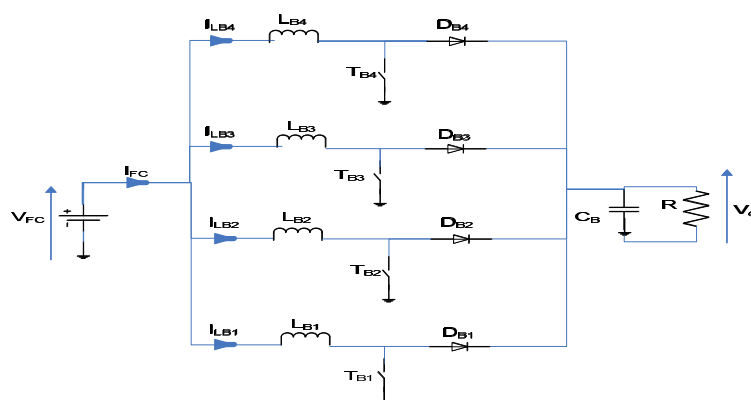


**Figure III. 37: Four interleaved boost converters.**

Thus, in order to evaluate the consequences of these errors, the power converter drawn in Figure III. 37 is going to be simulated. Two load profiles (Figure III. 38 and Figure III. 39) will be simulated; they are formed by several load steps that will force the converter to operate in discontinuous mode. In this paragraph, only the Boost case will be illustrated, but the same conclusions can be obtained for the three previous power converters.

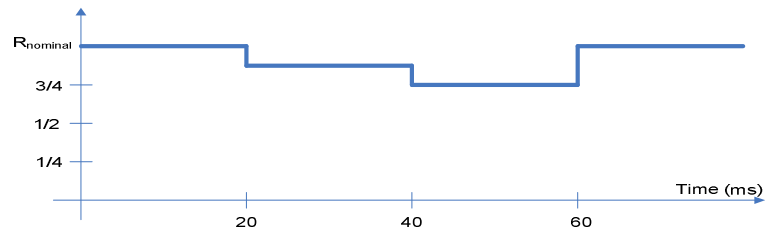


**Figure III. 38: Load profile 1.**

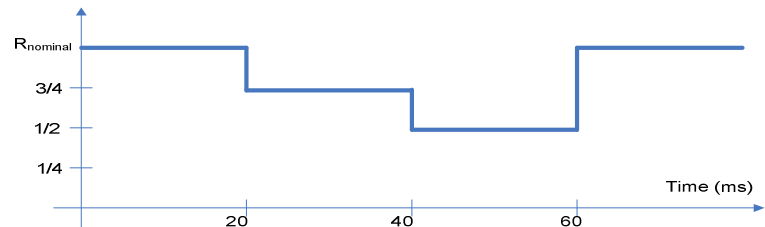


**Figure III. 39: Load profile 2.**

Boost converter requirements are:

$$P = 20 \text{ kW}$$

$$f_s = 10 \text{ kHz}$$

$$E = 110 \text{ V}$$

$$V_o = 270 \text{ V}$$

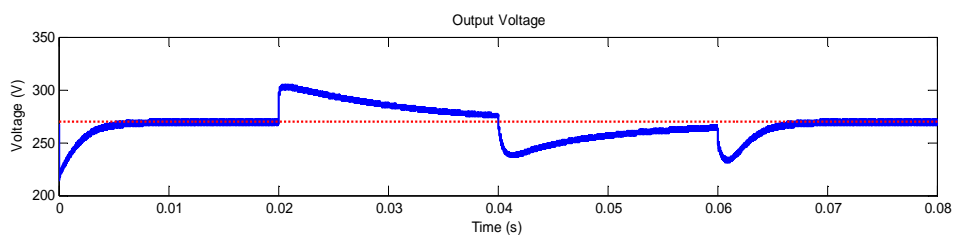
$$\Delta i_{FC} = 20 \text{ A}$$

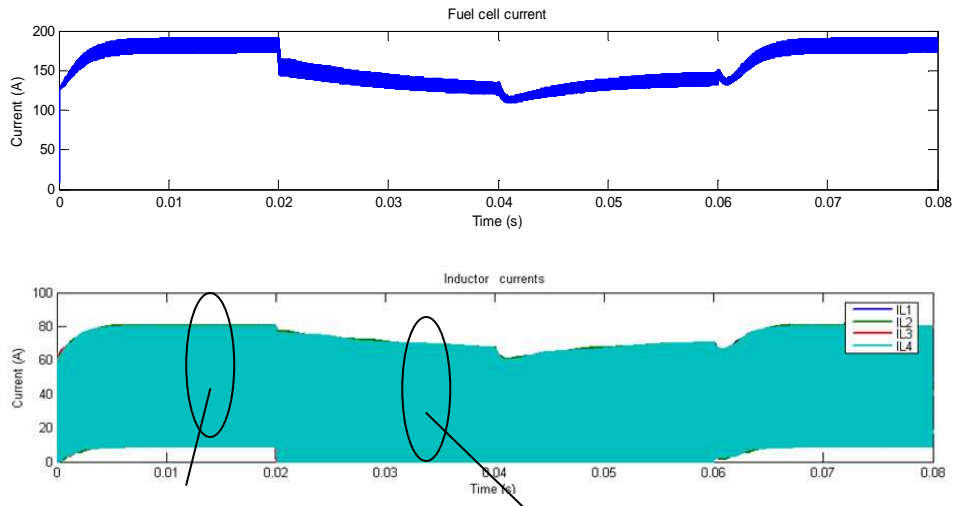
$$\Delta V_o = 2 \text{ V}$$

Both profiles are similar, but the second will force the simulated power converter to operate in more aggressive discontinuous mode.

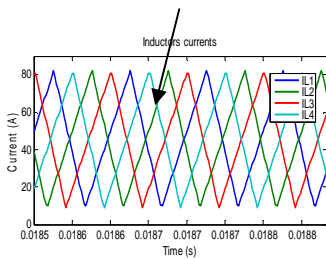
The simulation results are given in Figure III. 40 for the load profile 1. After a good start-up phase (from zero to nominal load), the output voltage does not present good dynamics face to load steps. Overt Voltages due to load step variations are important and the system response time is not at all satisfactory.

The fuel cell current seems to be well filtered. But having a look at the current flowing through the inductors, it is possible to observe that, after the first load step, the converter is operating in the discontinuous mode. Indeed, the inductors are fully discharged before the end of the switching period, as it is shown in Figure III. 42. After the second load step, the power converter is still operating in the discontinuous mode. Thus, not satisfactory output voltage characteristics are obtained due to load steps forcing the converter to operate in the discontinuous mode.

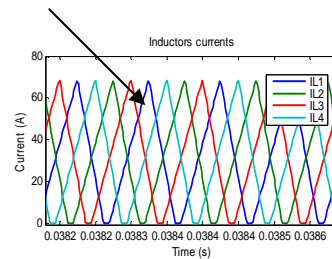




**Figure III. 40: Simulation results for 4 interleaved Boost converters with the load profile 1.**

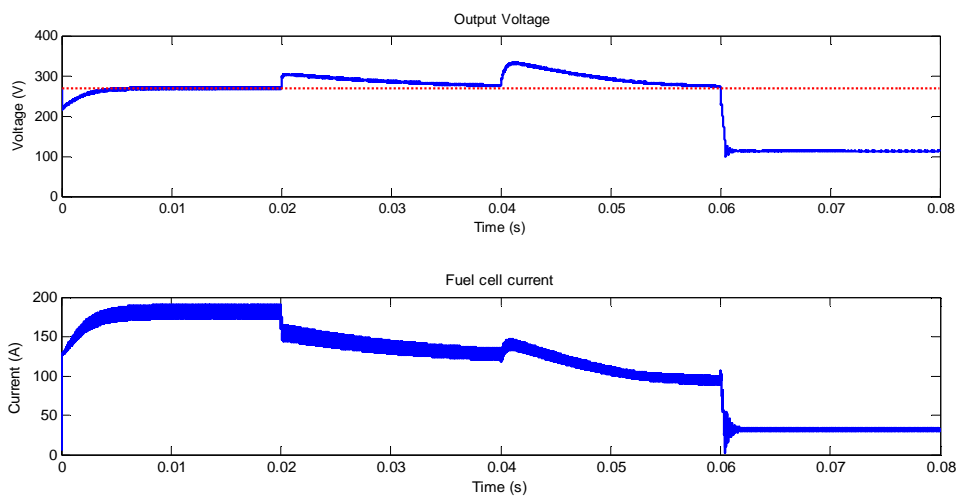


**Figure III. 41: Continuous operating mode**



**Figure III. 42: Discontinuous operating mode**

The simulation results are given in Figure III. 43 for the load profile 2. This simulation shows that output voltage dynamics becomes worse for the second load step. The control of the power converter cannot even be recovered at the last load step (the one which should bring the power converter into a continuous mode operation point).



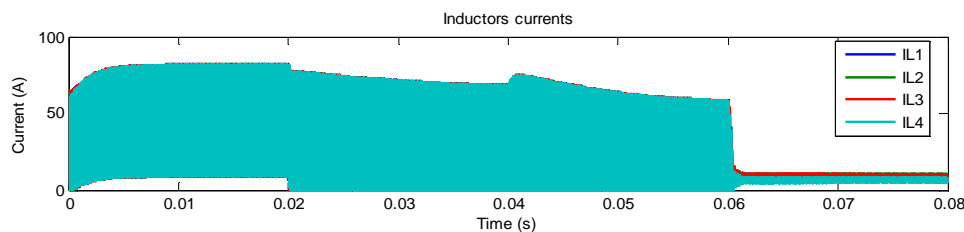


**Figure III. 43: Simulation results for 4 interleaved Boost converters with the load profile 2.**

In conclusion, the proposed control cannot be directly applied to interleaved converters if the load profile forces the converter to operate in an “aggressive” discontinuous mode. It would be interesting for further works, to determine the limit where the power converter control is lost.

### III.3.5.2 Modification of the control law for the discontinuous mode

In order to solve this problem there are two traditional solutions: to implement saturable inductors and/or increase the switching frequency of the silicon switches.

Saturable inductors are inductors whose inductance increases when the current increases. The inductance depends on the current. This kind of inductors is onerous and rather delicate to design. Few applications a priori implemented this solution.

Another option is to increase the switching frequency of the silicon switches at loads that force the converter to operate in the discontinuous mode. The current ripple is then decreased in the same proportions as the switching frequency. The main drawback of this solution is that increasing the switching frequency will lead to a switching and inductor iron losses rise. Furthermore, even high load values can lead the converter to operate in the discontinuous mode ( $3/4 R_n$  in our example), thus, the increase of the switching frequency at low load values causes worse efficiency for the power converter.

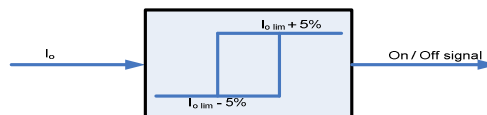
Therefore, we propose another solution to solve this problem. The idea consists in **switching off** some branches in order to avoid reaching the discontinuous mode. Indeed, as soon as the load current decreases, each interleaved converter will reach easily the discontinuous mode due to an important branch current ripple.

Concretely, the proposed strategy consists in imposing a current reference equal to 0A to the branches that we want to switch off, in order to increase the current through the other branches. This action will avoid reaching the discontinuous mode. Of course, there will not be any current through the switched-off branches.

Expression E III.63 gives the output current limit value that makes the converter reach the discontinuous conduction mode in function of the active branches  $n_{active}$ . This current value will be called the continuous conduction limit output current.

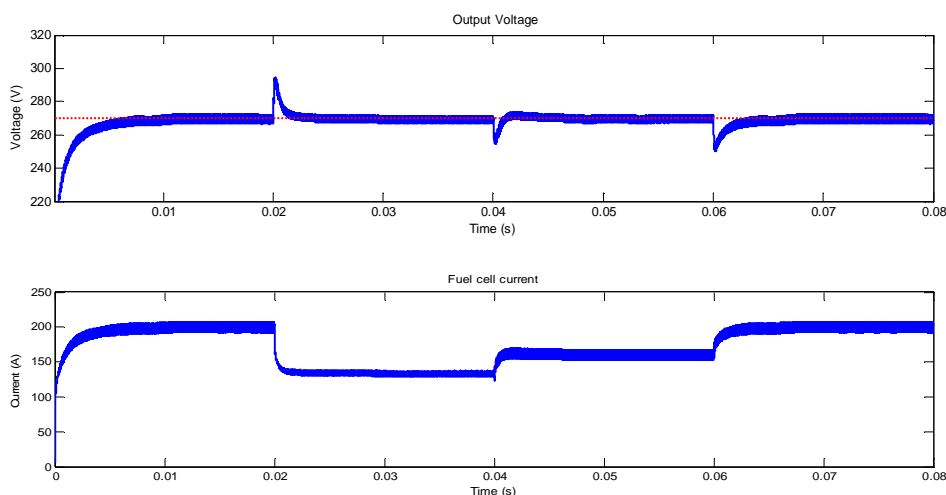
$$(I_{O \text{ lim}})_{\text{active}} = n_{\text{active}} \frac{\alpha(1-\alpha)^2 V_o}{2 f_s L} \quad \text{E III.63}$$

If the output current value passes through an hysteresis centered on the continuous conduction limit output current, it is possible to obtain the ON/OFF signal that will switch on or switch off the branches.



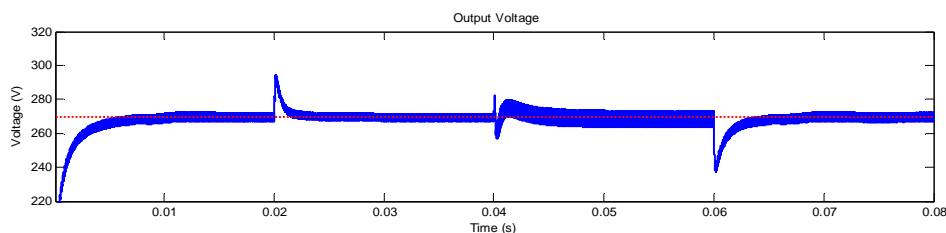
**Figure III. 44: Hysteresis to switch on or switch off the branches**

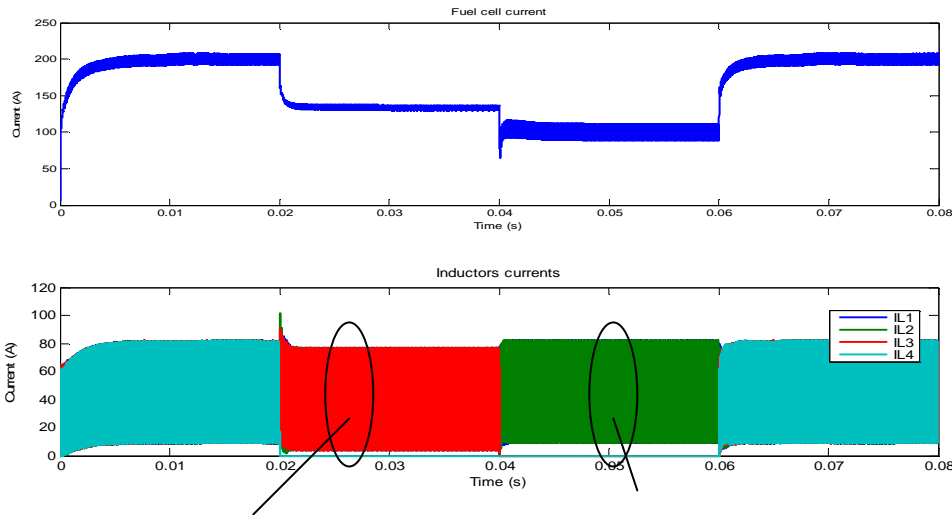
In Figure III. 45 are shown the simulation results for the load profile 1 (Figure III. 38). The dynamic response of the power converter has been fully improved.



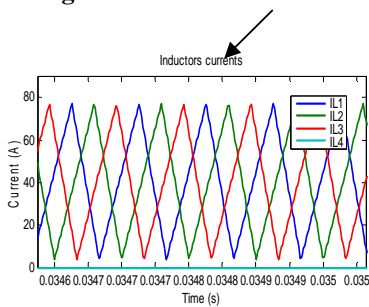
**Figure III. 45: Simulation results for the load profile 1. One branch switched off.**

Figure III. 46 shows the simulation results for the load profile 2 (Figure III. 39). In this case, the dynamic response of the power converter is excellent too. And the control of the power converter can be recovered at the last load step. One branch has been switched off during the first load step; a second branch has been switched off for the second load step. Both branches have been switched on with the last load step.





**Figure III. 46: Simulation results for the load profile 2. One or two branches switched off.**



**Figure III. 47: Continuous operating mode**

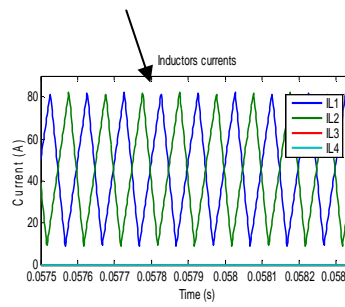


**Figure III. 48: Discontinuous operating mode**

Nevertheless, it is possible to observe in Figure III. 46 that the inductor current ripple and the output voltage ripple have increased and exceed lightly the permitted limits. Indeed, this will be the prize to pay for using this “switching off branches” strategy. This ripple rise can be easily explained because the interleaved power converter has been initially designed to operate with four branches and not with two. Nevertheless, it seems that the input LC filter could easily filter the extra current ripple.

One possible solution to this problem is to consider all the operating possibilities (that means the lowest and highest output power values and its associated number of active branches), and to size the power converter inductors and capacitors with the obtained maximal values.

Figure III. 49 shows the chart of the active branches according to the input voltage and the load power. Even at the nominal power (20 kW in our example), it is possible to find operating points where the power converter should operate with just three active branches. This can be easily explained because the sizing of all the inductors was achieved just considering current ripple criteria. In consequence, the continuous mode was not guaranteed at any operation point.



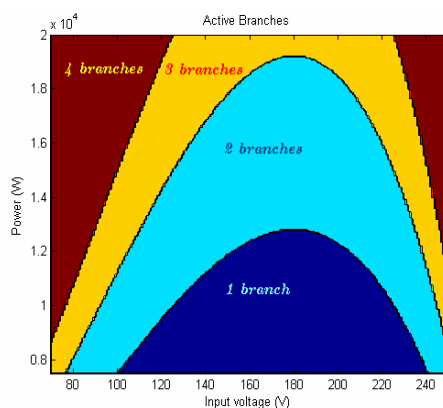


**Figure III. 49: Chart of the active branches according to the input voltage and the load power for the simulated 20kW power converter. (Inductor sizing based on current ripple criteria)**

If the sizing of all the inductors was achieved considering continuous mode criteria (that means to guarantee the continuous mode at any input voltage for the nominal power), the chart of the active branches is the one presented in Figure III. 50.

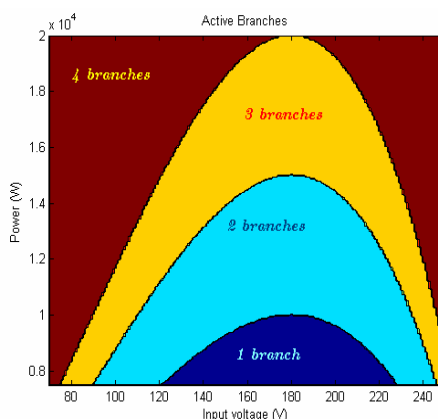


**Figure III. 50: Chart of the active branches according to the input voltage and the load power for the simulated 20kW power converter. (Inductor sizing based on continuous mode criteria).**

In this last case, the sizing based on continuous mode criteria leads to bigger inductances; that will be translated in terms of weight and volume by heavier and bigger inductors. Therefore, **the inductor sizing will be a compromise between the chosen continuous mode area and the input current ripple. Moreover, it must be considered individually for each application.**

### III.3.6 Behavior of the proposed power converters for the common mode voltage

One of the most important AIRBUS criteria in order to choose the power converter topology is the quality of the electrical network, specially the reduction of the DC bus common mode voltage. Indeed, high DC bus common mode voltages will induce important leakage currents through the parasitic capacitors to the aircraft ground. The leakage current induced by the DC bus common mode voltage must be reduced as much as possible.

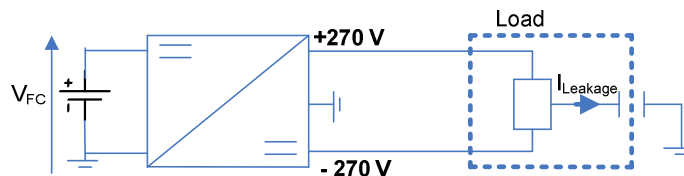


Figure III. 51: Common mode problem

The aim of this section is to analyze the capability of the proposed power converters in § III.1.2 to reject the DC bus common mode voltage.

The common mode voltage expression is given in E III.64:

$$V_{CM} = \frac{1}{2}(V_{+270} - V_{-270}) \quad \text{E III.64}$$

As it has been explained in § III.1, there are two different types of power converters that can carry out the AIRBUS requirements: the insulated and the non insulated power converters.

Insulated power converters delivering a  $\pm 270\text{V}$  DC bus are obtained thanks to an extra secondary winding into the high frequency transformer core of the classical Push-Pull topology. If both secondary windings are considered as being identical, **it is possible to consider insulated topologies as symmetric power converters**. Thus, and always by considering identical secondary windings, the output voltage will be distributed equally between the two transformers. There is no need to control separately each DC pole and there is only one duty cycle to calculate.

Nevertheless, **the proposed non insulated power converters can be considered as asymmetric power converters**. Indeed, the  $\pm 270\text{Volts}$  DC bus is obtained from an association of classical but different DC-DC power converters. One Buck-Boost converter will create the  $-270\text{V}$  pole and another converter (depending on the input voltage) will create the  $+270\text{V}$  pole. Each classical converter has to be controlled separately in order to assure the stability of the global  $\pm 270\text{V}$  DC bus. There will be two different duty cycles to control. Therefore, the power converter dynamics will depend on the load variations.

In order to test the common mode rejection for the proposed non insulated power converters, these power converters are going to be submitted by simulation to a series of load steps. The chosen input voltage is 70V in order to simulate a high current low voltage scenario which usually generates problem. The nominal power is 40kW. The input current ripple is limited to 10% and the output voltage ripple to 2V. The chosen switching frequency is 10 kHz.

**III.3.6.1 Describing of the simulated power converters and the simulation conditions for the study of the common mode voltage.**

As explained in § III.2, the interleaving technique will be used in order to reduce the converter weight and volume and improve the converter efficiency. It was said in § III.2.2 that the interleaved power converters are faster and present lower response times. Nevertheless, the interleaving effect has to be tested for the common mode voltage.

Regarding the simulated input voltage (70V), the asymmetric power converter that will be here simulated was presented in Figure III. 5. In order to evaluate the interleaving technique effect on the common mode rejection, the power converter will be simulated with just one, two and three interleaved branches as shown in Figure III. 52.

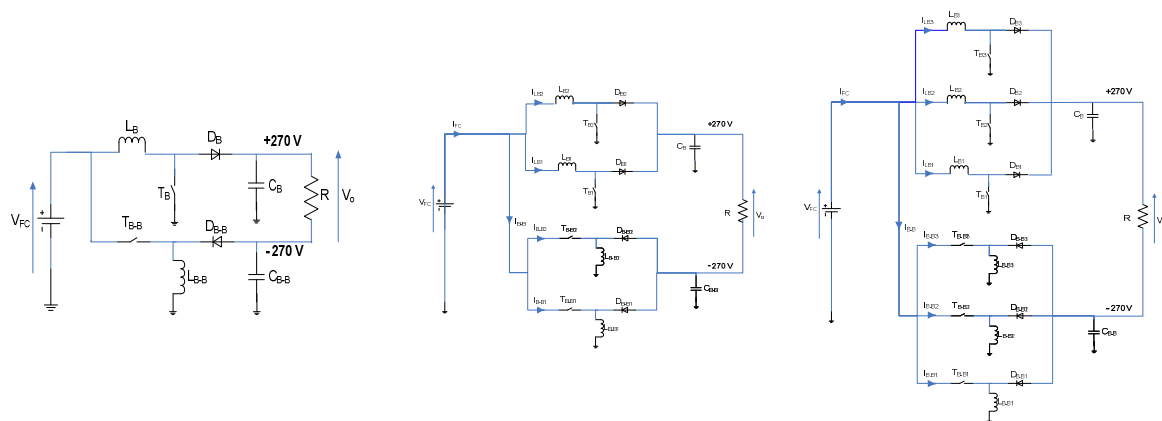


**Figure III. 52: Simulated Boost converters for the common mode voltage problem.**

Looking at the Airbus power profile in Figure I. 3, it is possible to observe that the load variations have a shape of slopes. Thus, in order to simulate a load profile representative of the required mission power profile within reasonable simulation durations (to avoid huge simulations), the load profile drawn in Figure III. 53 will be submitted to the power converter. This power profile represents a 50 % load variation with slopes lasting 50 ms.

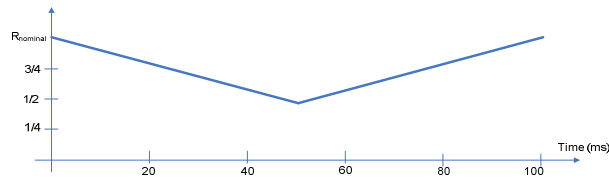


**Figure III. 53: Simulated SLOPE load profile for the common mode voltage problem.**

Furthermore, the three simulated power converters (Figure III. 52) will be submitted to a more aggressive and not expected step load profile (Figure III. 54). In this case, a series of load steps are submitted to the power converters. The bigger load step will be a load step from the nominal load to a no load operating point and vice versa.

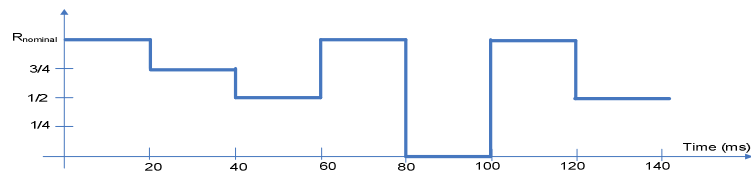


**Figure III. 54: Simulated STEP load profile for the common mode voltage problem.**

### III.3.6.2 Common mode voltage behavior for the Boost converter with one branch

The simulated output voltages for the STEP load profile are shown in Figure III. 55. The +270V pole and the -270V pole do not evaluate equally with load steps.

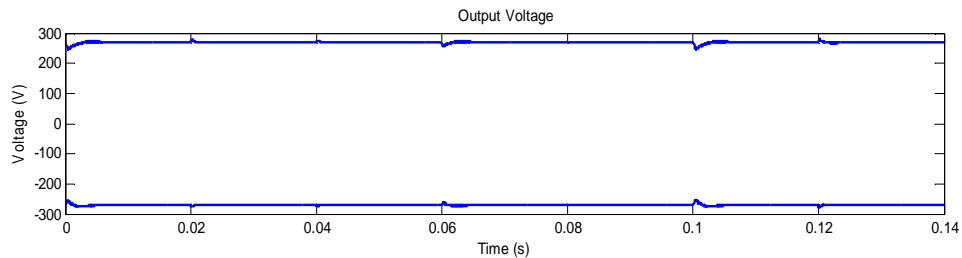


**Figure III. 55: Time evolution of the one-branch power converter output voltages.**

In order to better visualize the two voltages, the absolute value of the -270V pole is plotted with the +270V pole in Figure III. 56. In the same figure, the common mode voltage  $V_{CM}$  was plotted too.

As predicted, both poles do not have the same dynamic response for the load steps. Indeed, the “Buck-Boost converter part” of the global power converter seems to have lower response times than the “Boost converter part”. Concerning the voltage overshoots after the load steps, the “Boost converter part” seems to be better than the “Buck-Boost converter part”

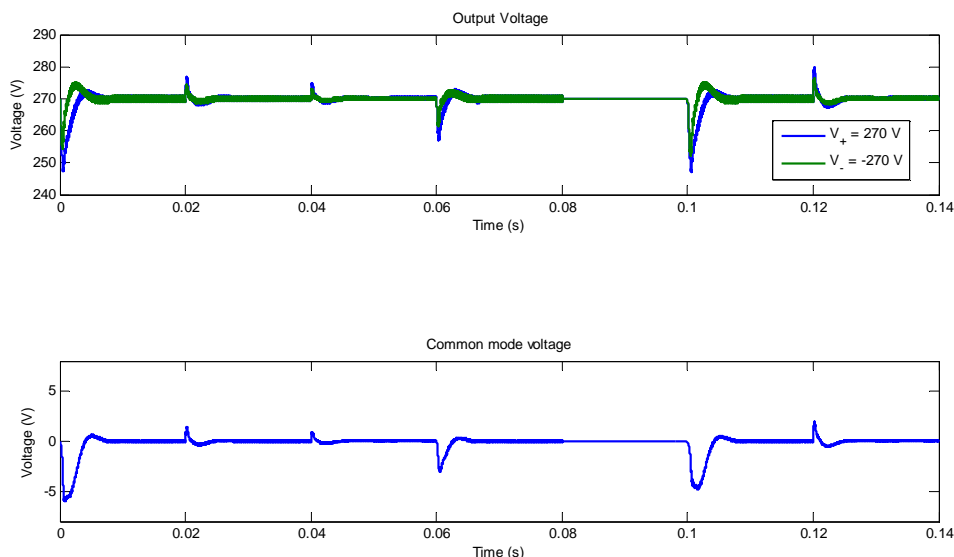


**Figure III. 56: Time evolution of common mode and output voltages (STEP load profile).**

From these simulation results, it is possible to come to interesting conclusions. In steady state, the common mode voltage is not significant. But during the load steps, the common mode voltage varies. The common mode voltage increases with the magnitude of the load steps; during the zero to nominal load step, the common mode voltage reaches its higher value. Nevertheless, a variation of 5V for the common mode voltage only represents 1% of the global DC bus voltage value. This good result is obtained because the control loops of both power converter parts were implemented following the same compensation method of non linearities, leading finally to both similar transfer functions as it was explained in § III.3.4.

In the next figures, the simulation results for the SLOPE load profile are presented.

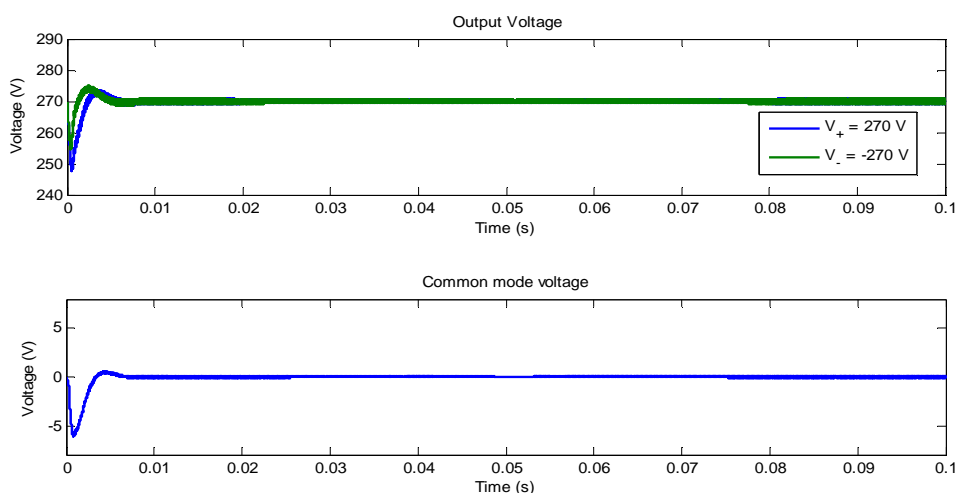


**Figure III. 57: Time evolution of common mode and output voltages (SLOPE load profile).**

The start-up phase is similar to the STEP load profile. During this phase, the common mode voltage reaches its more important value. Nevertheless, during the rest of the SLOPE load profile, the common voltage is not significant, even when the slope change occurs.

### III.3.6.3 Common mode voltage behavior for the Boost converter with two interleaved branches

The simulation results for the STEP load profile are presented in the next figures:

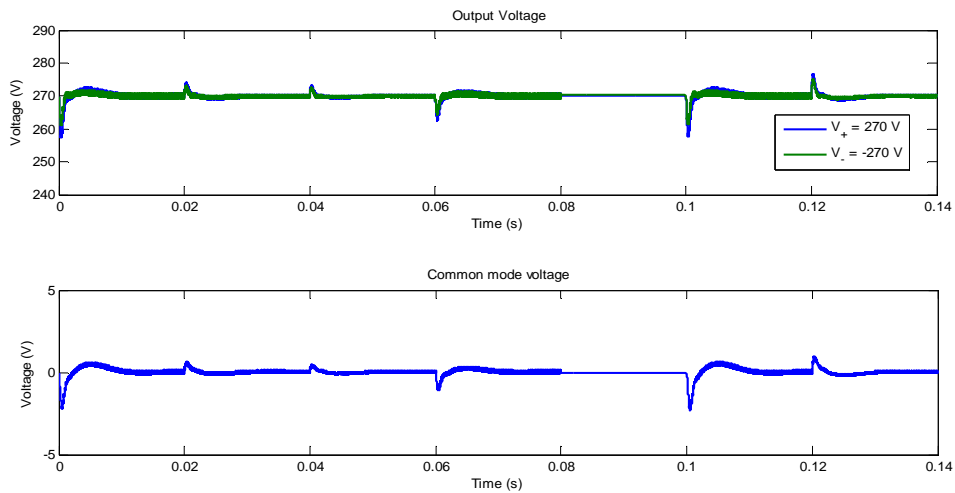


**Figure III. 58: Time evolution of common mode and output voltages (STEP load profile).**

As already explained, the interleaving technique reduces the system response time: the dynamic responses will be better because the capacitances and inductances were reduced. Thus, a faster response time implies a common mode voltage reduction, even in the start-up phase, as it can be observed in simulation results.

Similar conclusions can be drawn for simulation results of the SLOPE load profile: common mode reduction for the start-up phase and not significant common mode during the rest of the profile, including the slope change.

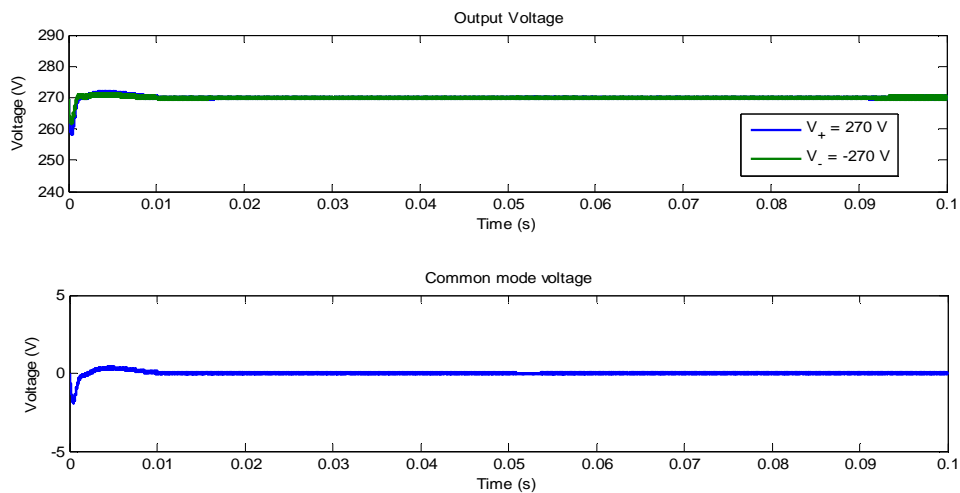


**Figure III. 59: Time evolution of common mode and output voltages (SLOPE load profile).**

### III.3.6.4 Common mode voltage behavior for the Boost converter with three interleaved branches

According to the observed performances for the power converter with two interleaved branches, the common mode voltage should be reduced in the case of the power converter with three interleaved branches. The simulation results, in Figure III. 60, show that, for the start-up phase and for the 25% load step, the common mode voltage was indeed reduced.

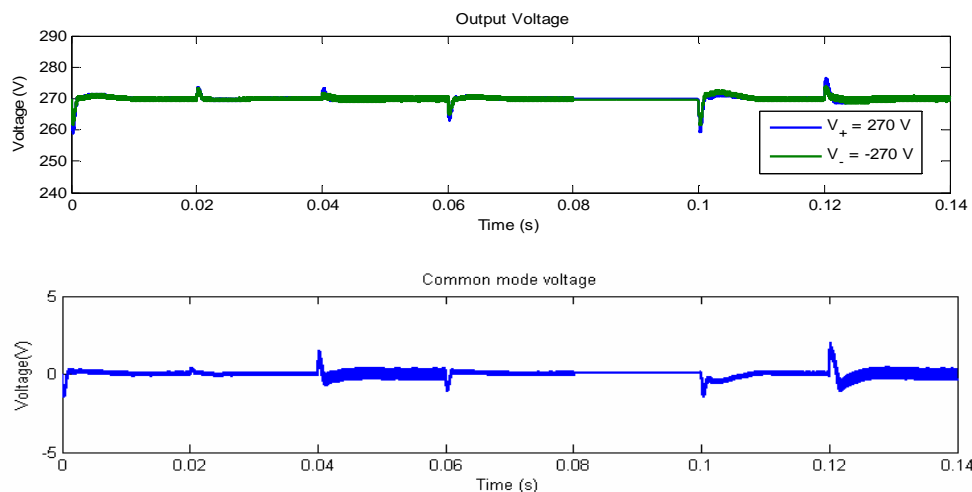


**Figure III. 60: Time evolution of common mode and output voltages (STEP load profile).**

Nevertheless, when the load is reduced of 50% of the nominal load, the dynamic response of the power converter becomes worse. Furthermore, during the steady state following the 50% load step, the common mode voltage presents a higher voltage ripple than initially expected.

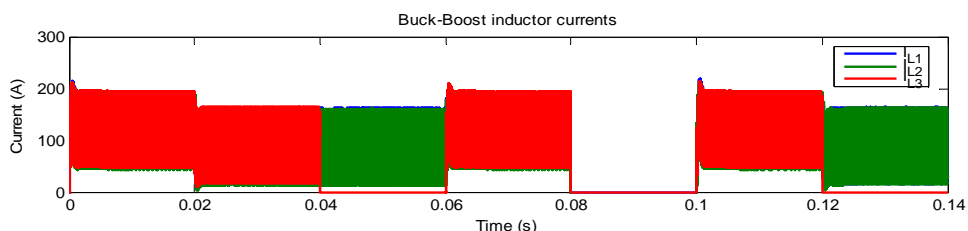


**Figure III. 61: Inductor currents of the “Buck-boost converter part”.**

The common mode voltage ripple rise and worse dynamic response can be easily explained by having a look at the inductor currents of “Buck-Boost converter part”. Indeed, the Buck-Boost converter has reached the discontinuous mode. Thus, one branch has been switched off generating a light rise of the Buck-Boost converter output voltage ripple; this rise itself generating a light common mode voltage rise in steady state.

Let us now observe the impact of the switching-off of a branch on the common mode voltage with the SLOPE load profile. Simulation results are presented in Figure III. 62.

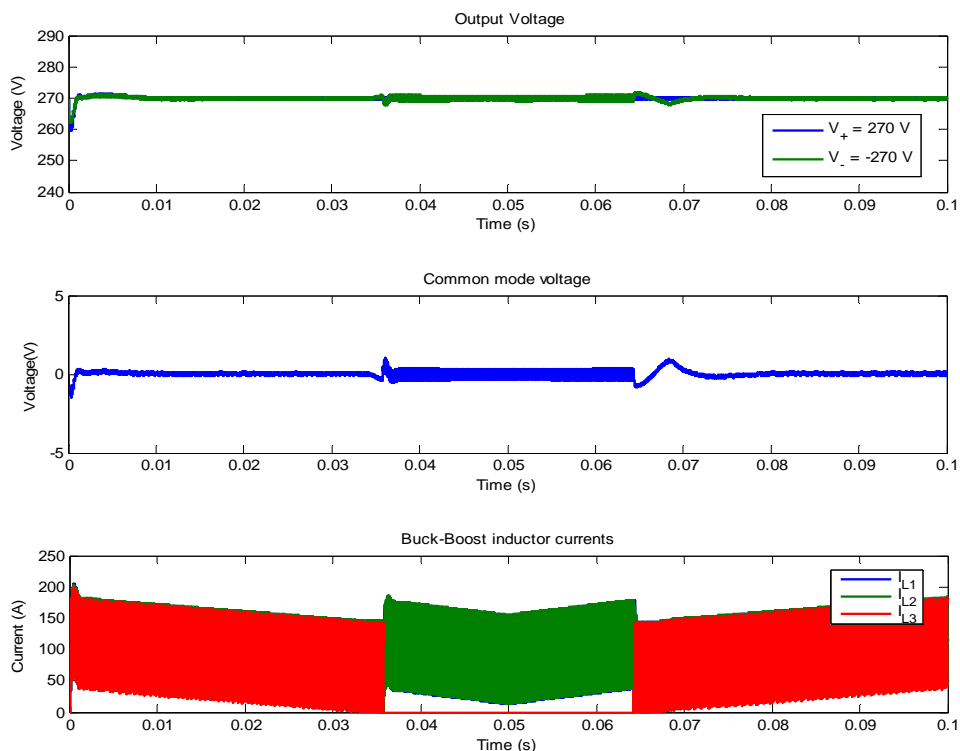


**Figure III. 62: Time evolution of common mode and output voltages (SLOPE load profile) and inductor currents of the “Buck-boost converter part”.**

As expected, the common mode voltage ripple in steady state increased after the branch switching-off. Nevertheless, during the transients for the branch switching-on and branch switching-off, the common mode voltage presents a dynamic response that did not exist with the power converters with one and two branches. **Even if the common mode voltage evolution due to the branch switching-off and switching-on effect does not seem to reach really important values, it would be interesting for future works to determine theoretically the common mode overvoltage caused by the branch switching-off technique.**

### III.3.6.5 Conclusions about the common mode voltage study

Comparing the behaviors of the analyzed three power converters (Figure III. 63) for the common mode voltage, it is possible to obtain the following conclusions:

- The proposed generic control laws permit to obtain a similar output voltage behavior for each power converter, but not identical. Nevertheless, for the studied cases, the common mode voltage is inferior to 1% of the global DC bus voltage.
- Interleaving technique will reduce the common mode voltage if the power converter operates in the continuous mode (A and B subplots Figure III. 63). Nevertheless, if one branch has to be switched off in order to avoid operating in the discontinuous mode, the transient for the common mode voltage will increase and the common mode voltage in steady state will also increase (C subplot in Figure III. 63).



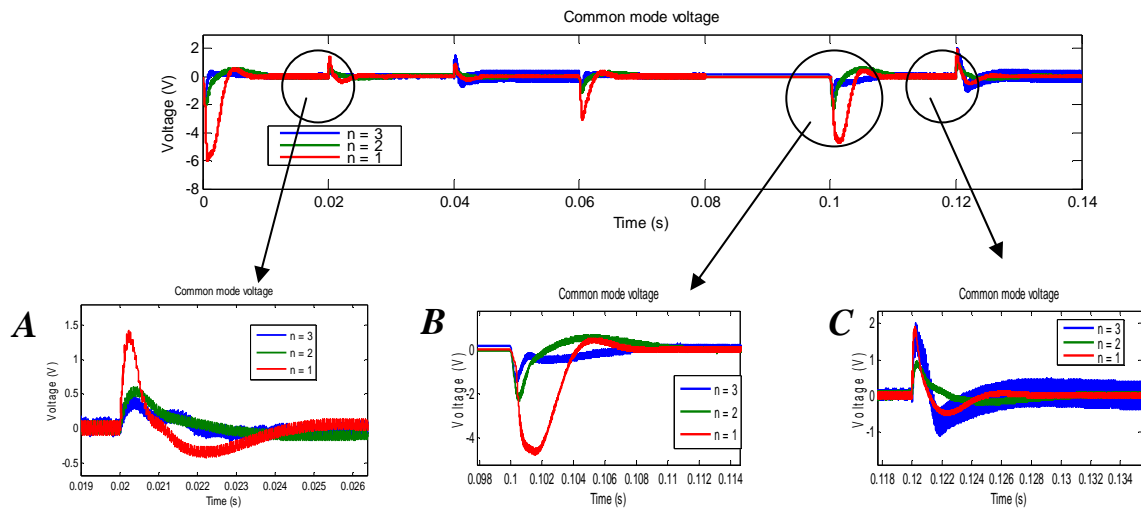


**Figure III. 63: Evolution of the common mode voltage according to the parallel branch number (STEP load profile).**

Similar conclusions can be drawn for the SLOPE load profile (Figure III. 64). Nevertheless, in this case, if one branch has to be switched off or switched on, a common mode voltage transient can be created when the parallel branch number increases. Nevertheless, the transitory common mode overvoltage seems to stay in tolerated margins. **This is one of the identified drawbacks to the branch switching-off technique.**

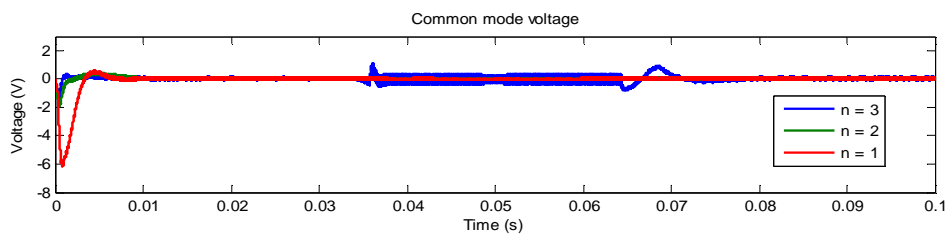


**Figure III. 64: Evolution of the common mode voltage according to the parallel branch number (SLOPE load profile).**

## III.4 Power converter efficiency and weight study

In order to evaluate the performances of the proposed power converters, a study about their efficiencies and weights will be achieved in the next paragraphs.

### III.4.1 Models of the losses within a power converter

The considered losses are the losses generated by the silicon switches and the passive components (capacitors and inductors).

The efficiency of a power converter will be calculated as follows:

$$\eta = \frac{P_{input} - \sum losses}{P_{input}} \quad \text{E III.65}$$

Our objective in this part only is to give an idea to the reader of our methodology to **estimate** losses. No calculation details are given.

#### IGBT conduction losses.

Only IGBT are considered in our study (they naturally corresponds to the silicon switches T in the different schemes of the proposed power converters). The IGBT conduction losses are calculated as in [Ralliers], [Turpin]:

$$W_{IGBT\ cond} = V_{ceo} \langle I_{IGBT} \rangle + r_{IGBT} I_{IGBT\ rms} \quad \text{E III.66}$$

The mean and the rms current values can be easily determined thanks to expressions in §Appendix I. The IGBT characteristics ( $V_{ceo}$  and  $r_{IGBT}$ ) are obtained from the datasheets as it is illustrated in Figure III. 65

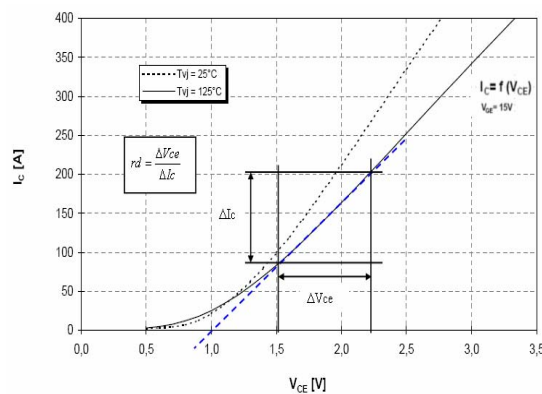


Figure III. 65: IGBT characteristics.

#### IGBT switching losses.

The IGBT switching losses are calculated as in [Ralliers], [Turpin]:

$$W_{IGBT\ switch} = f_s (E_{on} + E_{off}) \tag{E III.67}$$

The most of the silicon switch makers proposes in their datasheets an estimate of the lost energy during the switching phases ( $E_{on}$  and  $E_{off}$ ). Silicon switch makers usually give dissipated energy in function of the commutated current as shown in Figure III. 66. It is possible to obtain a polynomial law that models the curves in Figure III. 66.

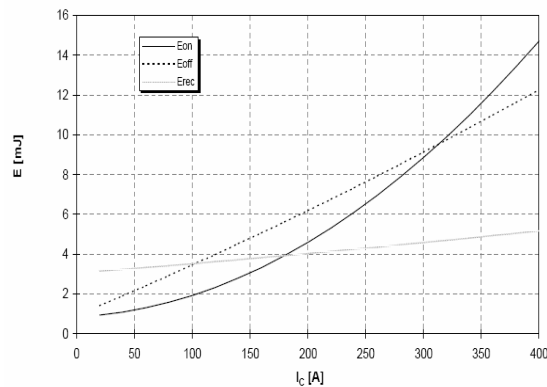


**Figure III. 66: IGBT dissipated energy during switching phases.**

Energy values are generally given for specific test conditions. The previous expression has thus to be modified:

$$W_{IGBT\ switch} = f_s (E_{on}(I_{IGBT\ on}) + E_{off}(I_{IGBT\ off})) \frac{V_{switch}}{V_{test}} \tag{E III.68}$$

**Diode conduction losses.**

The diode conduction losses can be calculated in a similar way to the IGBT conduction losses:

$$W_{d\ cond} = V_{ceo} \langle I_d \rangle + r_d I_{d\ rms} \tag{E III.69}$$

The diode parameters have to be extracted from the diode datasheets. We here chose to use the diode which is coupled with the IGBT by manufacturers in the case (Be careful! “Case” means “packaging of the switch” in this sentence).

**Diode switching losses.**

The diode switching losses are calculated in a similar way to the IGBT switching losses:

$$W_{IGBT\ switch} = f_s E_{rev}(I_{Diode\ off}) \frac{V_{Diode}}{V_{test}} \tag{E III.70}$$

From Figure III. 66 the dissipated recovery energy can be estimated in test conditions. As in the previous case, the loss expression has to be multiplied by a  $\frac{V_{Diode}}{V_{test}}$  coefficient in order to calculate the losses in other switching conditions..

### Diode and IGBT leakage losses.

These losses, which appear when the component is supposed be not conducting, are due the imperfections. These losses are a priori weak. Leakage currents can be obtained from the datasheets.

$$W_{leakage\ IGBT} = V_T \cdot I_{leakage\ IGBT} \quad \text{E III.71}$$

$$W_{leakage\ diode} = V_D \cdot I_{leakage\ diode} \quad \text{E III.72}$$

### Inductor losses

A detailed method to design an inductor is proposed in §Appendix IV. The design method provides all the data, such as core volume and winding equivalent resistor, needed for losses estimation.

### Iron losses.

Core losses (or iron losses) are energy losses that occur in electrical transformers and inductors using magnetic cores. The losses are due to a variety of mechanisms related to the fluctuating magnetic field, such as eddy currents and hysteretic phenomena. Most of the energy is released as heat, although some may appear as sound ("hum"). Core losses do not include the losses due to the electrical resistance in the conductors of the windings.

The usual way to estimate inductor core losses is to use the charts supplied by magnetic core makers (Figure III. 67). These charts usually give maximal induction and switching frequency function and provide the volumetric loss estimation. Thus, in order to obtain an estimate of the total iron losses, the total core volume should be multiplied by the obtained value.

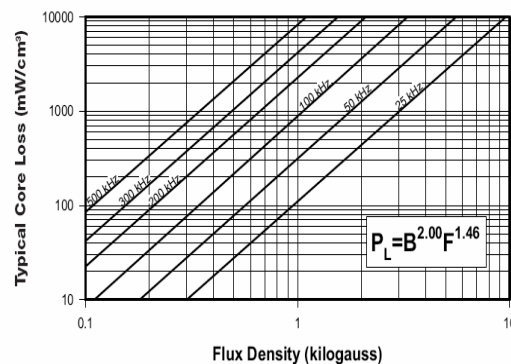


Figure III. 67: Example of iron loss chart given by magnetic core makers .

### **Copper losses.**

The copper losses are often used to explain the heat produced by electrical currents in the windings of inductors of transformers, or other electrical devices. In addition of the well-known conduction losses, the copper losses can also result from induced currents in adjacent components.

The expression of the copper losses is given in E III.73:

$$W_{Lcopper} = R_{winding} I_{Lrms}^2 \quad \text{E III.73}$$

### **Capacitors losses**

The capacitor losses will be here estimated thanks to the equivalent resistance, which is usually available in the datasheets. The expression of the capacitor losses is given in E III.74:

$$W_C = R_C I_{Crms}^2 \quad \text{E III.74}$$

## **III.4.2 Weight model**

Due to the studied transportation application, it is mandatory to estimate the power converter weight. Estimating the weight of the power converters is not an easy task. There are many components whose weight is difficult to estimate. Therefore, the proposed model does not pretend to be an exact calculation. It has to be seen just as an estimation tool that will evaluate the weight of power converters in the same conditions. The model was proposed by Jean-Philippe Besnard, engineer with THALES AES, member of the CELINA project.

### **Inductor weight model**

The estimated inductor weight is the addition of iron core and copper weights. The iron core weight can be obtained directly from the core datasheets. The copper weight can be easily calculated by just multiplying the total copper length by the wire section and by the copper density.

### **Silicon switches model**

The estimated weight of the silicon switches is easily calculated by multiplying the total number of IGBT-diodes cases by the weight of a single case obtained from the datasheets.

### **Heat sink weight model**

First of all, the heat sink thermal resistance  $R_{th\ h}$  that dissipates all the silicon losses must be calculated. This calculation is based on the thermal model presented in Figure III. 68

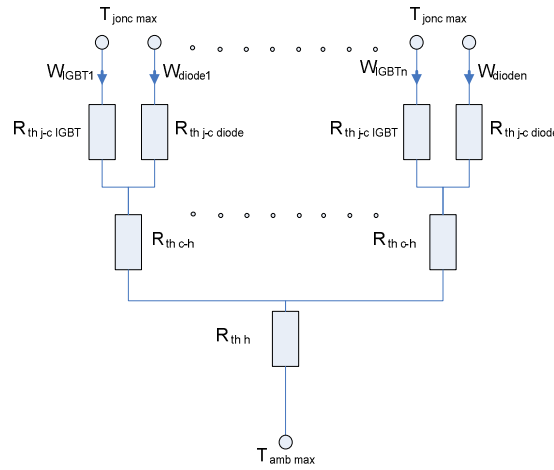


**Figure III. 68: Heat sink thermal model.**

The thermal resistance can be calculated thanks to the following expression:

$$R_{th h} = \frac{T_h - T_{amb}}{\sum_{n=1}^n (W_{IGBT n} + W_{diode n})} \tag{E III.75}$$

with:

$$T_h = T_c - (W_{IGBT n} + W_{diode n}) R_{th c-h} \tag{E III.76}$$

and:

$$T_c = \max[(W_{IGBT n} R_{th j-c IGBT}), (W_{diode n} R_{th j-c diode})] \tag{E III.77}$$

According to Jean-Philippe Besnard’s estimations, the weight of a heat sink ventilated with a 6 m/s air flow follows the fitted law with the thermal resistance:

$$Weight_{hs} = 0.7178 \left( \frac{R_{th}}{0.226} \right)^{-1.445} \tag{E III.78}$$

### Bus Bar weight

According to Jean-Philippe Besnard’s estimation, the bus bar weight can be estimated as follows:

$$Weight_{bus bar} = \frac{1.33}{6} n_{//IGBT} n_{//branches} \tag{E III.79}$$

### Capacitor weight

The capacitor weight can be obtained from the datasheets.

### Converter total weight

The converter total weight is the addition of all the calculated weights multiplied by 1.35. This factor is based on the experience of Jean-Philippe Besnard: it takes into account the concrete implementation and packaging.

$$Weight_{CVS} = 1.35 \cdot (Weight_{hs} + Weight_{busbar} + Weight_L + Weight_C + Weight_{sw}) \quad \text{E III.80}$$

### III.4.3 Library of components for power converters

All the models of losses depend on the components characteristics. Thus a library of components was generated based on the datasheets of the concerned component manufacturers.

The chosen silicon switches are the BSM family from EUPEC [EUPEC]. According to EUPEC datasheets, this family belongs to a Low Loss IGBT technology. In this family, two different voltage ranges were chosen: 1200V and 600V. Maximal voltage imposed to the silicon switches in the Boost converter will be 270V: a 600V switch seems a correct choice. Nevertheless, the Buck and Buck-Boost converters will have to withstand bigger voltages: the 1200V range seems to be well suited.

Both 600V and 1200V IGBT families can withstand currents between 50A and 300A, depending on the chosen switch. The maximal current through the silicon switch determines the current switch. The chosen switch, for security reasons, must be able to withstand twice the maximal expected current. If it is not possible to find a switch with these characteristics, several switches will be placed in parallel in order to reach twice the sizing current value.

The selected magnetic cores are the Kool Mu E-cores from MAGNETICS [Magnetics]. This core family is made of a ferrous alloy powder, which offers low losses at elevated temperature. Kool Mu E-cores have a distributed air-gap which makes them ideally suited for power converter inductors, Flyback transformers, and power factor correction. Furthermore Kool Mu E-cores are competitively priced compared to gapped ferrite E-cores, and their distributed air-gap eliminate air-gap loss problems associated with ferrites. Kool Mu E-cores have significantly lower losses and substantially better thermal properties compared to powder iron E-cores.

### III.4.4 Discussion about the sizing of interleaved power converters

The number of interleaved branches and the switching frequency of the silicon switches are important parameters that will fix the efficiency and weight of the power converter. On the one hand, important switching frequencies will make increase switching losses and inductor losses. On the other

hand, inductances will be smaller and this may be favorable in terms of weight and volume. Something similar happens with the number of interleaved branches: the stored energy is reduced with the number of interleaved branches, but the current ripple is increased at the same time, and thus the current RMS value (present in all expressions of losses).

In order to obtain an optimized power converter and to evaluate the sensibility of weight and efficiency to both parameters, a sweeping for the switching frequency and the number of parallel branches is proposed. Efficiency and weight results are presented in Figure III. 69 and in Figure III. 70. The assumptions are the following: the minimal fuel cell voltage value is 70V and the nominal power is 20 kW. Our reflections will thus be illustrated with the classical Boost converter topology Figure III. 24.

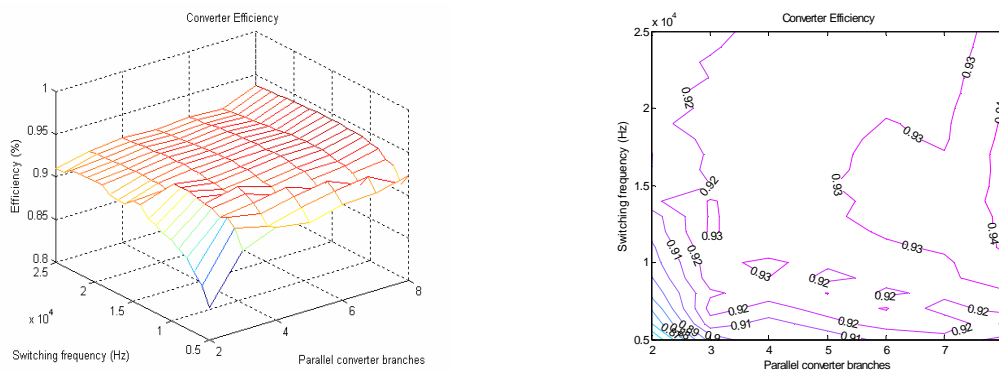


Figure III. 69: Power converter efficiency surface.

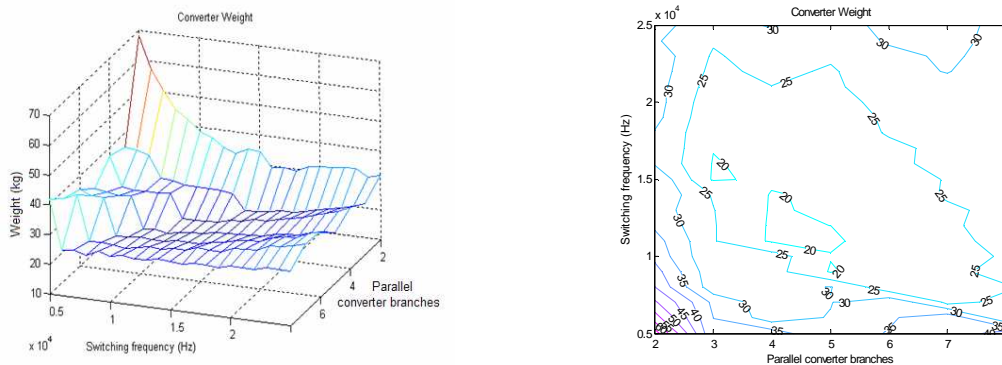


Figure III. 70: Power converter weight surface.

Analyzing results from Figure III. 69 and Figure III. 70, it is possible to conclude that:

- Interleaved power converters with a branch number lower than 3 and a switching frequency lower than 8 kHz and higher than 20 kHz are not optimized in terms of efficiency and weight.



- Interleaved converters with a higher branches number of 6 do not present the best weight ratio.

Thus, the chosen switching frequency for these Boost converter requirements could be between 10 kHz and 20 kHz.

Furthermore, it seems that 4-5 interleaved branches is a good compromise between the interleaving advantages and the implementation difficulty and the cost of the power converter (the implementation difficulty and the cost increase with the number of interleaved branches: sensors, control circuits...). According to THALES AES, a bigger number of interleaved branches will excessively complicate the conception of the power converter.

Nevertheless, the choices of the switching frequency and the number of interleaved branches will remain arbitrary choices because it is not the same quantity which optimizes the power converter in terms of weight and efficiency.

The selected range of frequencies (10kHz - 20kHz) and the number of interleaved branches (4 branches) lead to the following loss and weight distributions presented in Figure III. 71 and Figure III. 72.

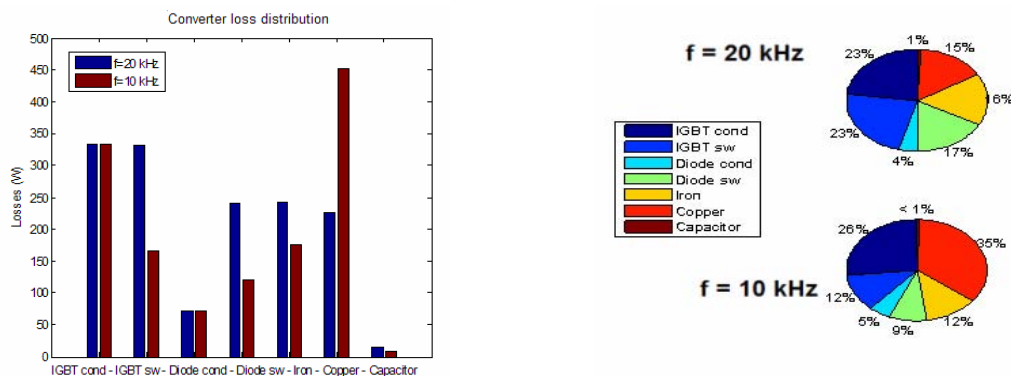


Figure III. 71: Converter loss distribution according to switching frequency (n = 4, 20kW, 70V).

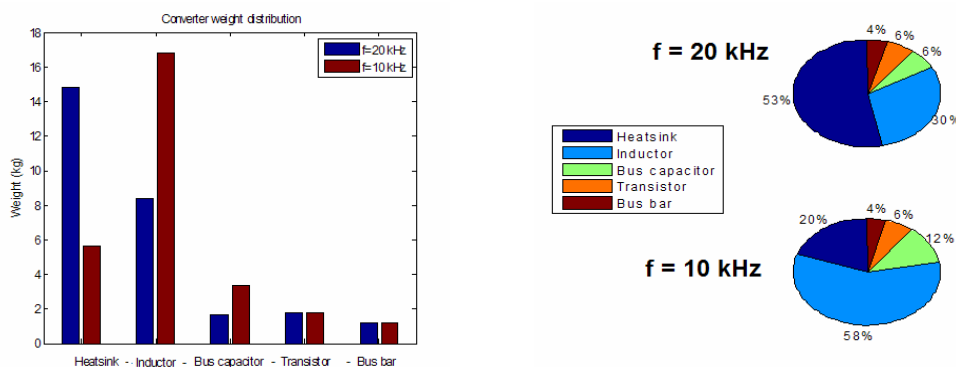
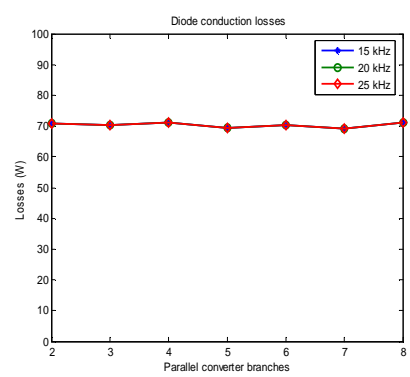
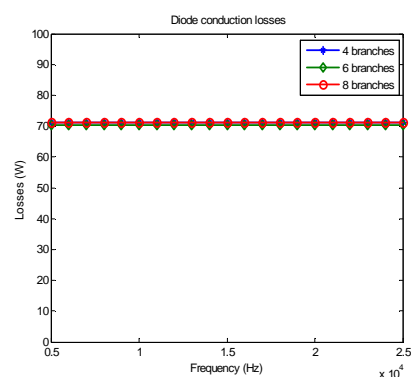
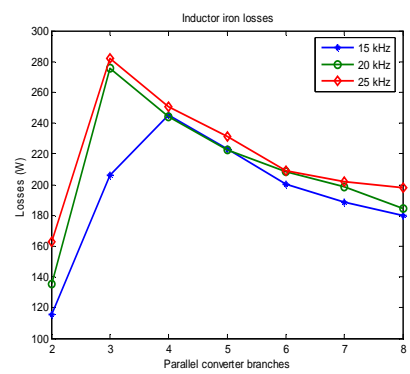
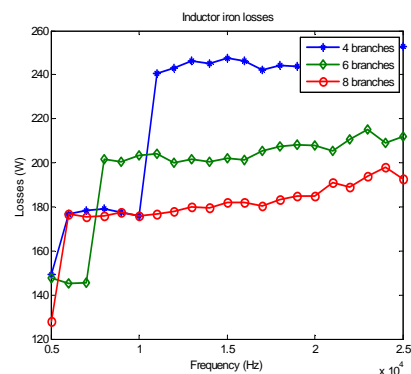
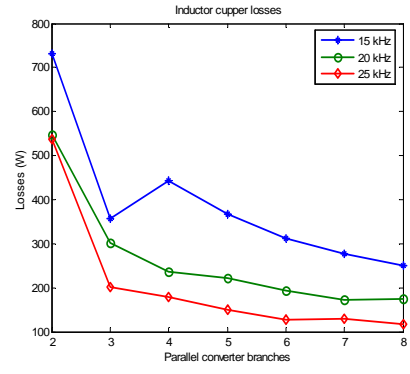
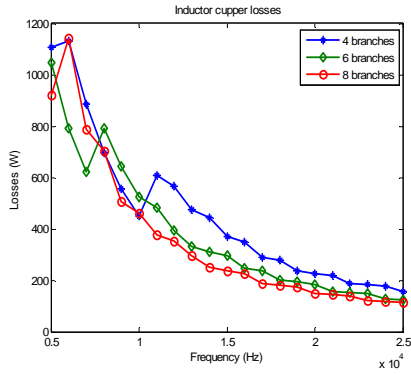
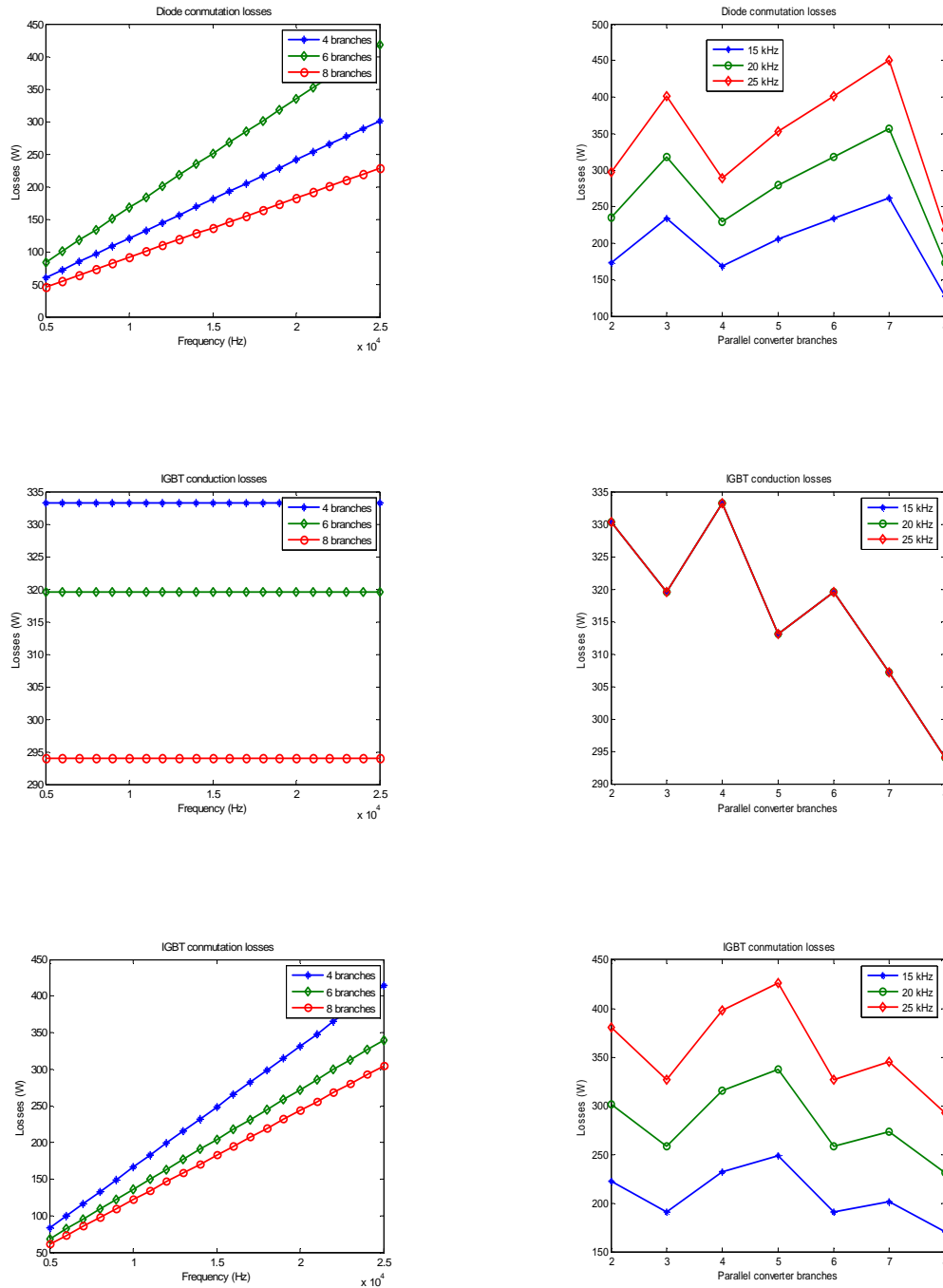


Figure III. 72: Converter weight distribution according to switching frequency (n = 4, 20kW, 70V).

Thanks to the sweeping achieved for both parameters (number of interleaved branches and switching frequency), it is possible to observe the different evolutions of the modeled losses of the power converter. Some of them are shown in Figure III. 73.





**Figure III. 73: Evolution of the different power converter losses with the number of interleaved branches and the switching frequency.**

Some conclusions after the analysis of Figure III. 73 can be achieved.

The rise of the switching frequency will generally make increase switching losses and iron losses, and decrease copper losses and will not affect conduction losses. The inductor losses (iron and copper) present a big discontinuity around 8 – 12 kHz due to the change of the iron core range.

The number of interleaved branches will generally reduce inductor losses. On the other hand, the effect of the number of interleaved branches on the silicon switches seems much more difficult to determine. Indeed, the number of interleaved branches will make vary the current flow through the silicon switches. This will make change the current range of silicon switches. Thus, in this case, the evolution of losses becomes a discrete problem depending on the library of silicon switches.

However, the power converter sizing will strongly depend on the power converter requirements. The same number of interleaved branches will not be the optimized number at any power range. In order to prove this affirmation, the evolutions of global losses and the estimated weight have been plotted in Figure III. 74 and Figure III. 75 for several output powers and for different numbers of interleaved branches. The chosen frequency was 15 kHz.

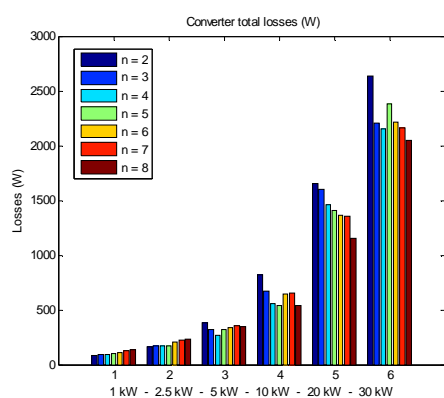


**Figure III. 74: Loss evolution according to the output power and the number of interleaved branches ( $f_s=15\text{kHz}$ ).**

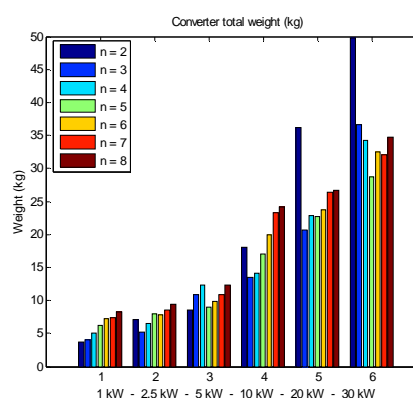


**Figure III. 75: Weight evolution according to the output power and the number of interleaved branches ( $f_s=15\text{kHz}$ ).**

Anyway, as already said, the choice of an optimized number of interleaved branches is an arbitrary choice. Nevertheless, looking at Figure III. 74 and Figure III. 75, **a number of 3 or 4 interleaved branches seems to be an adequate choice for power requirements below 20 kW.** This number presents a good compromise between the power converter efficiency and the power converter weight. **For 20 kW or higher power requirements, a number of 5 or 6 interleaved branches seems to be the best compromise between the converter efficiency and the converter weight.** Indeed, higher branch number leads to better efficiency, but nevertheless, the power converter is penalized in terms of weight.

Nevertheless, the choice of an adequate switching frequency and an adequate number of interleaved branches remains a complex problem, that depends on the specific mission requirements. **In Chapter IV, the global system optimization problem is fully detailed, and obviously the converter optimization is treated.**

### III.4.5 Branch switching-off technique effect on the power converter efficiency

In previous paragraphs, optimized numbers of interleaved branches and switching frequencies have been determined considering the weight and the efficiency of the power converter for a large power range but for the minimal input voltage.

In § III.2.3, it has been explained that interleaved power converters risk to reach easily the discontinuous mode, and thus, to meet problems with the power converter control. In order to solve these problems, a branch switching-off technique was proposed. In Figure III. 76, it is shown the number of active branches in function of the input voltage and the load power for a Boost power converter. This method seems to solve the power converter control, but nevertheless, the effect of the proposed technique on the power converter efficiency has not been determined yet.

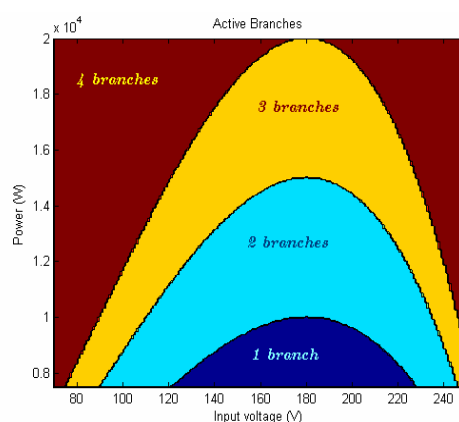


**Figure III. 76: Chart of the active branches according to the input voltage and the load power for a 4-branch 20kW Boost power converter.**

For the study of this effect on the efficiency of interleaved power converters, all losses and efficiencies will be calculated for all the possible operation points for the 4 power converters with 4 interleaved branches: the 4-branch Boost converter, the 4-branch Buck converter, the 4-branch Buck-Boost converter, the 4-branch non-reverser Buck-Boost voltage.

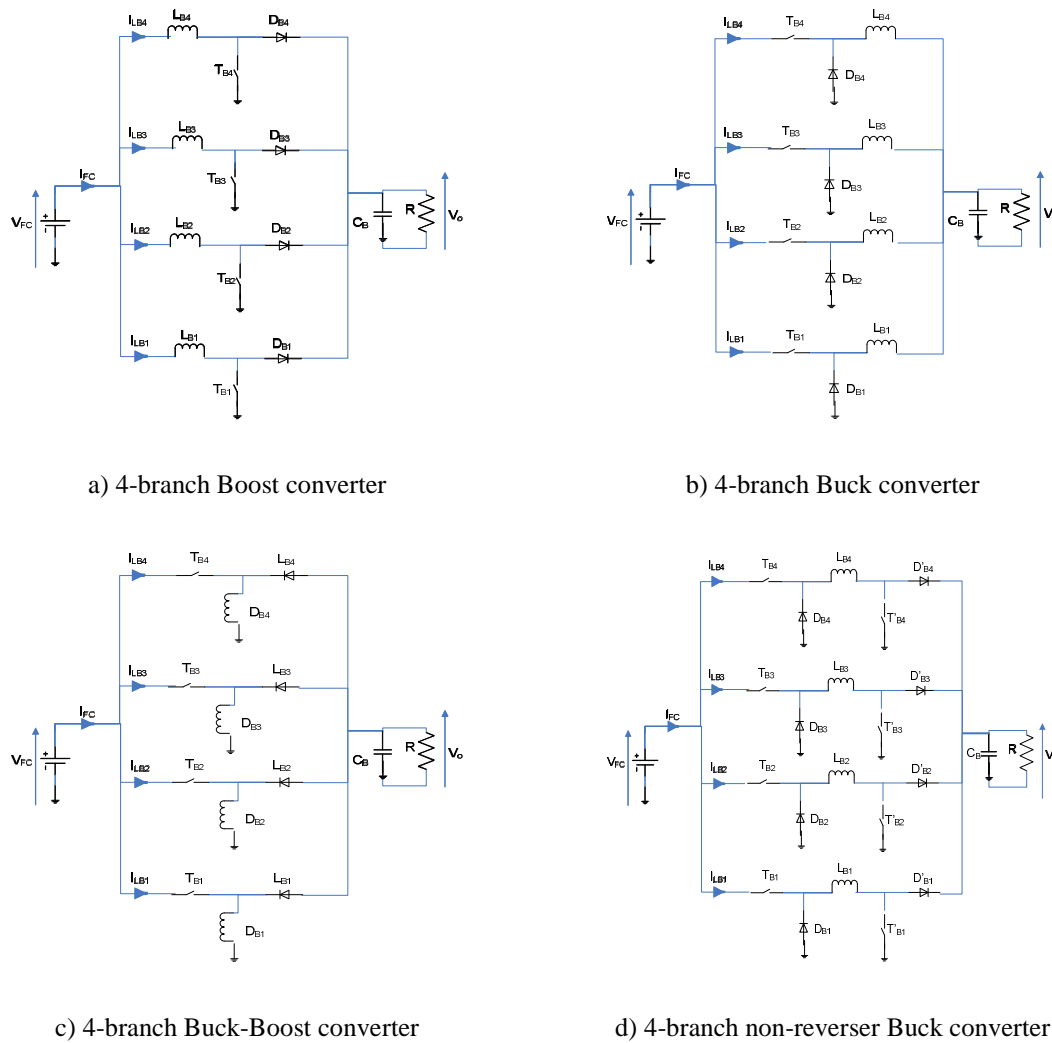


Figure III. 77: Evaluated 4-branch power converters.

The assumptions for these four evaluated power converters:

- The switching frequency is fixed: 20kHz
- The load power range will be swept from 500W to 20kW.

**Note to the reader:** Be careful with all the following figures because the order for the axes is not always the same one. Sometimes (particularly for the “input voltage” axis), the axis scale is graduated with decreasing values whereas with increasing values in most cases. All these choices are justified by the will to offer the most readable 3-D view.

III.4.5.1 Effect on a 4-branch BOOST converter (Figure III. 77- a)

The calculations of the power converter efficiency for load power and input voltage sweepings are plotted in the 3-D surface shown in Figure III. 78. The input voltage range is swept from 70V to 250V.

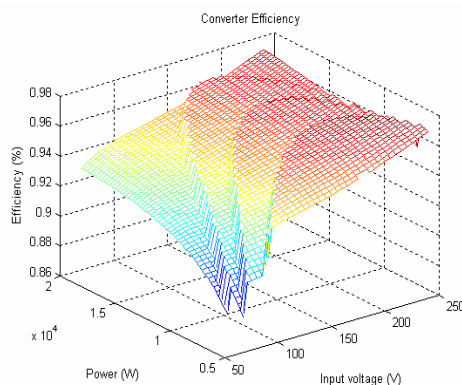


**Figure III. 78: Power converter efficiency according to the load power and the input voltage (4-branch Boost converter).**

Looking at Figure III. 78, it is possible to observe “traces” or “steps” due to the branch switching-off technique on the converter efficiency surface. Four small “steps” (for better appreciation, see the red part of the surface) can be counted on the efficiency surface. Each “step” is caused by a branch switching-off. Notice the similarity of the “steps” with the four areas shown in Figure III. 76. Thus, **the branch switching-off technique does not damage the converter efficiency. Furthermore, this technique will lightly improve** (because it is a positive “step”) **the converter efficiency.** In the following lines, all surfaces of the different estimated losses within the power converter are plotted in order to better analyze and understand the branch switching-off technique effect on the power converter efficiency.

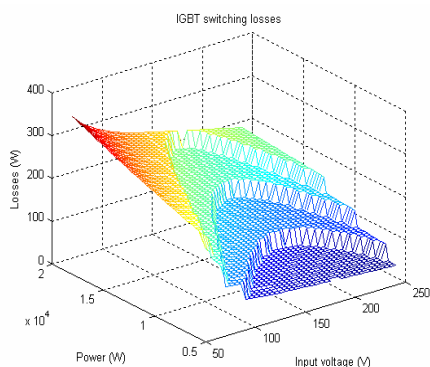


**Figure III. 79: IGBT switching losses according to the load power and the input voltage (4-branch Boost converter).**

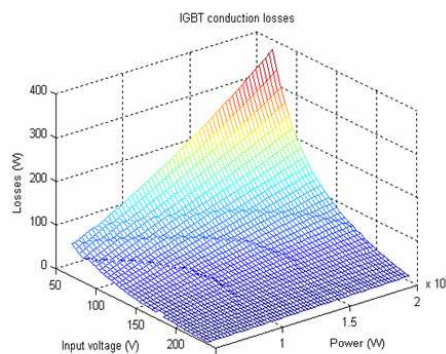


**Figure III. 80: IGBT conduction losses according to the load power and the input voltage (4-branch Boost converter).**

Figure III. 79 and Figure III. 80 show the surfaces of the IGBT switching and conduction losses according to the load power and the input voltage. The branch switching-off technique seems to be advantageous for the IGBT switching losses. After a branch switching-off, IGBT switching losses are considerably reduced. In the other hand, IGBT conduction losses are lightly increased after a branch switching-off.

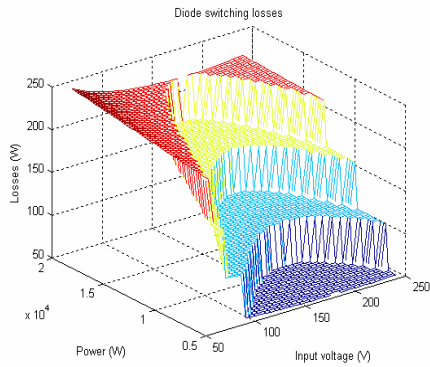


**Figure III. 81: Diode switching losses according to the load power and the input voltage (4-branch Boost converter).**

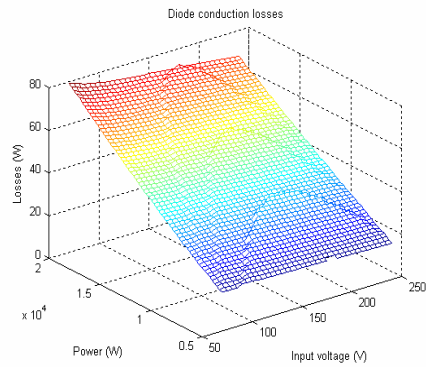


**Figure III. 82: Diode conduction losses according to the load power and the input voltage (4-branch Boost converter).**

The same conclusions can be obtained concerning the diode losses (Figure III. 81 and Figure III. 82). Switching losses will decrease when an branch is switched-off and conducting losses will increase. Nevertheless, it seems that the positive effect on the switching losses is much more important than the negative effect on the conduction losses.

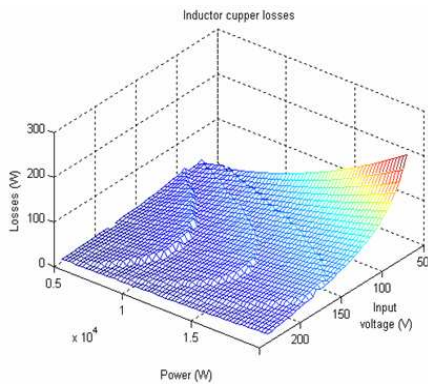


**Figure III. 83: Inductor copper losses according to the load power and the input voltage (4-branch Boost converter).**

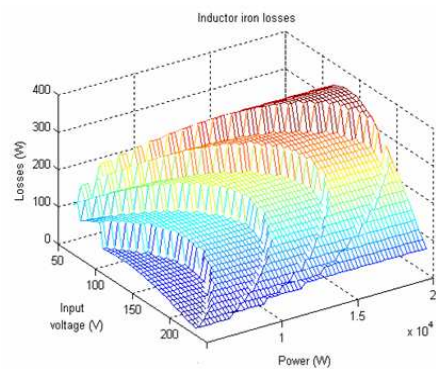


**Figure III. 84: Inductor iron losses according to the load power and the input voltage (4-branch Boost converter).**

Inductor copper losses will also increase if the number of active branches decreases. Nevertheless inductor iron losses present apparently a really significant variation with the number of active interleaved branches. This is easy to explain because iron losses depend mainly on the switching frequency  $f_s$  the current ripple  $\Delta i$  and the number of interleaved branches  $n$  (§III.4.1). As  $f_s$  and  $\Delta i$  do not depend on the number of active branches or load power, iron losses must decrease if a branch is switched-off. It should be also noticed that iron losses are the only losses that do not reach their maximal value at the minimal input voltage. According to Figure III. 11, the maximal current ripple is obtained with a duty cycle equal to 0.5. Thus, the maximal value of iron losses will be obtained at 135V or which is the same with a 0.5 duty cycle.



**Conclusion:** all the RMS values of the different currents will increase more and less lightly if the number of active branches decreases. Nevertheless the IGBT and diode switching losses and the inductor iron losses will considerably decrease if the number of active branches decreases. Therefore, all extra losses created by the branch switching-off technique will be more and less compensated and even it seems that is possible to improve the converter efficiency.

### III.4.5.2 Effect on a 4-branch Buck converter (Figure III. 77- b)

Similarly to the Boost converter case, the calculations of the power converter efficiency for load power and input voltage sweepings are plotted in the 3-D surface shown in Figure III. 85. The input voltage range is swept from 320V to 400V.

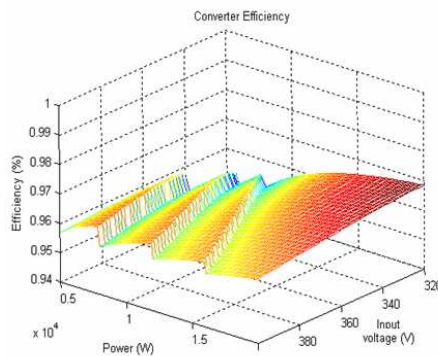


**Figure III. 85: Power converter efficiency according to the load power and the input voltage (4-branch Buck converter).**

As in the Boost converter case, the branch switching-off technique seems to have a positive influence on the converter efficiency. Nevertheless, the efficiency decreases with high input voltage. This can be explained with a finer look at the evolution of the different losses.

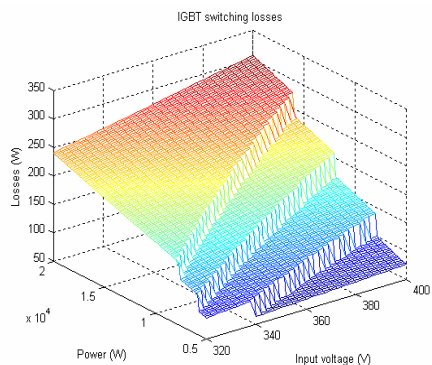


**Figure III. 86: IGBT switching losses according to the load power and the input voltage (4-branch Buck converter).**

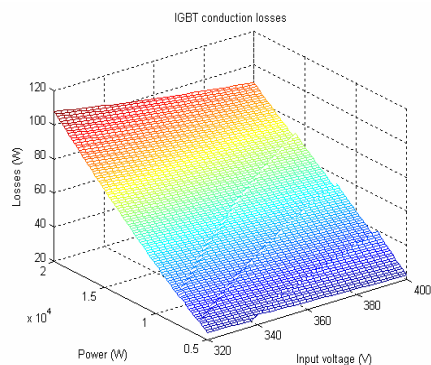


**Figure III. 87: IGBT conduction losses according to the load power and the input voltage (4-branch Buck converter).**

IGBT switching losses also decrease if a branch is switched-off. Furthermore and contrarily to the Boost converter case, IGBT switching losses increase with the input voltage because the switching voltage is equal to the input voltage. For the conduction losses, the branch switching-off technique effect do not seem to be very important: the conduction losses will lightly increase. Let us recall that the conduction losses decrease with the rise of the input voltage because the currents flowing through the silicon switches have lower RMS values and mean values.

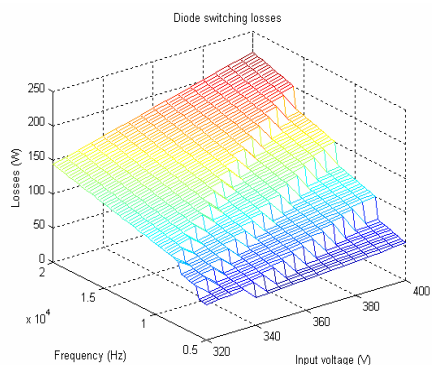


**Figure III. 88: Diode switching losses according to the load power and the input voltage (4-branch Buck converter).**

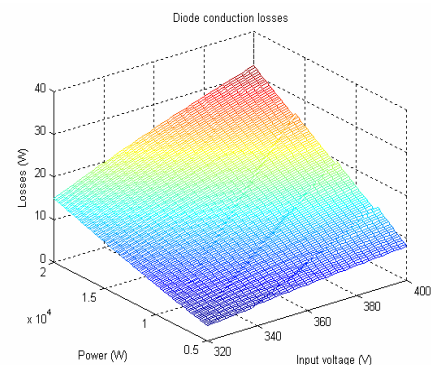


**Figure III. 89: Diode conduction losses according to the load power and the input voltage (4-branch Buck converter).**

The branch switching-off technique effect on the diode losses is not significant. Diode conduction losses, contrarily to the IGBT conduction losses, increase with the input voltage decrease because the RMS values and mean values of currents increase (they are dependent of the duty cycle).

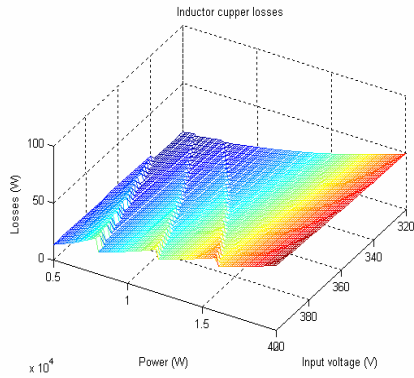


**Figure III. 90: Inductor copper losses according to the load power and the input voltage (4-branch Buck converter).**

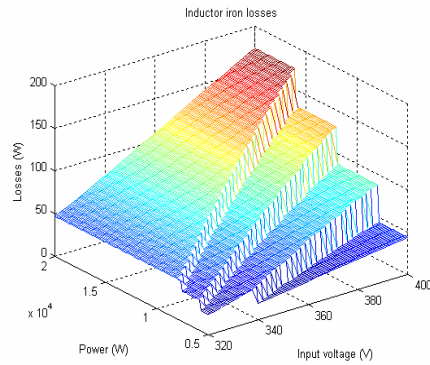


**Figure III. 91: Inductor iron losses according to the load power and the input voltage (4-branch Buck converter).**

Inductor copper losses will lightly increase if the number of active interleaved branches decreases. Nevertheless, inductor iron losses present apparently a really significant variation with the number of active interleaved branches. The explanation is similar to the Boost converter case. Indeed iron losses do not depend on load power. Thus, if the number of branches decreases, losses must decrease. Furthermore losses increase with the input voltage because the current ripple  $\Delta i$  increases with this voltage.

Conclusion: the results obtained for the 4-branch Buck converter are quite similar to the ones obtained for the 4-branch Boost converter. The branch switching-off technique seems to be favorable in terms of global efficiency. Nevertheless, it appears that **in order to obtain a performing converter, it is interesting to design a fuel cell that supplies a voltage close to 270V.**

**III.4.5.3 Effect on a 4-branch Buck-Boost converter (Figure III. 77- c)**

Similarly to the Boost converter case, the calculations of the power converter efficiency for load power and input voltage sweepings are plotted in the 3-D surface shown in Figure III. 92. The input voltage range is swept from 70V to 250V.

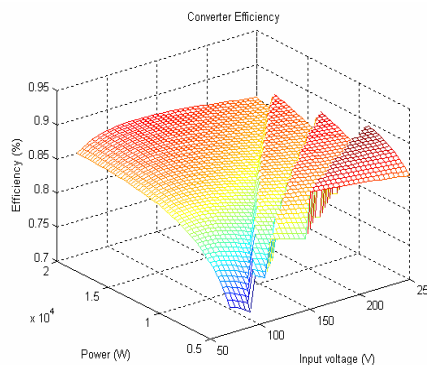


**Figure III. 92: Power converter efficiency according to the load power and the input (4-branch Buck-Boost converter).**

As in the Boost converter case, the branch switching-off technique seems to have a positive influence on the converter efficiency. Nevertheless, the efficiency is much lower than in the Boost converter case. This can be easily explained because the currents that flow through the silicon switches and the passive elements are much more important than in the Boost converter case; and thus the efficiency will be highly deteriorated.

In the next figures, it is possible to observe the evolution of the different losses for all the possible operating points. Conclusions similar to the Boost converter and Buck converter cases can be drawn.

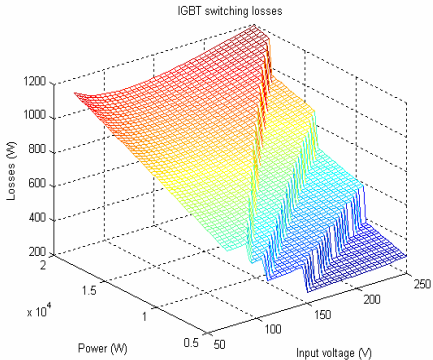


**Figure III. 93: IGBT switching losses according to the load power and the input voltage (4-branch Buck-Boost converter).**

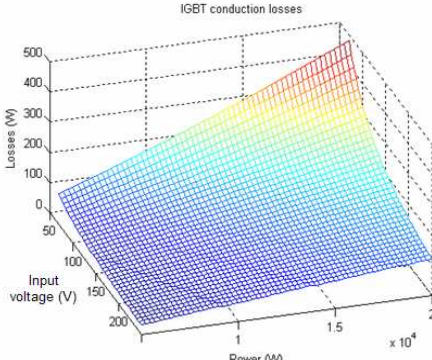


**Figure III. 94: IGBT conduction losses according to the load power and the input voltage (4-branch Buck-Boost converter).**

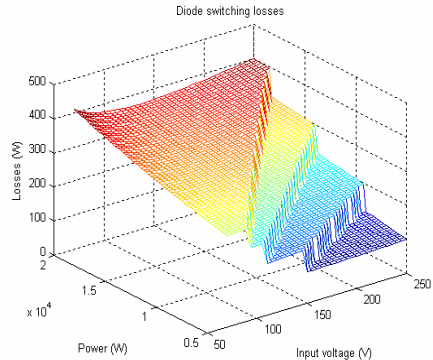


**Figure III. 95: Diode switching losses according to the load power and the input voltage (4-branch Buck-Boost converter).**

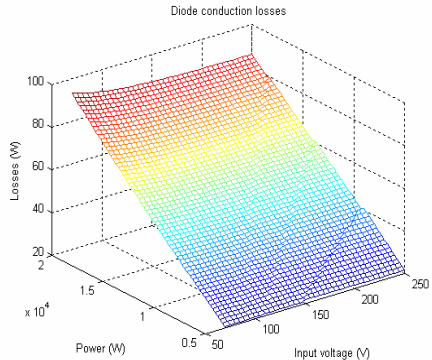


**Figure III. 96: Diode conduction losses according to the load power and the input voltage (4-branch Buck-Boost converter).**

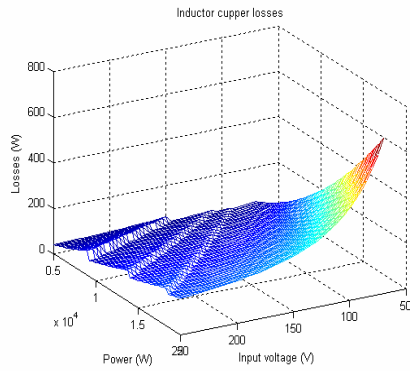


**Figure III. 97: Inductor copper losses according to the load power and the input voltage (4-branch Buck-Boost converter).**

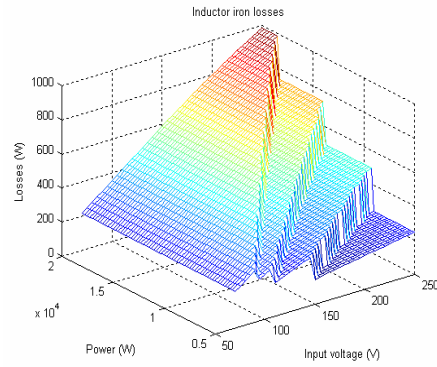


**Figure III. 98: Inductor iron losses according to the load power and the input voltage (4-branch Buck-Boost converter).**

#### III.4.5.4 Effect on a non-reverser 4-branch Buck-Boost converter (Figure III. 77 - c)

Similarly to the Boost converter case, the calculations of the power converter efficiency for load power and input voltage sweepings are plotted in the 3-D surface shown in Figure III. 99. The input voltage range is swept from 70V to 400V.

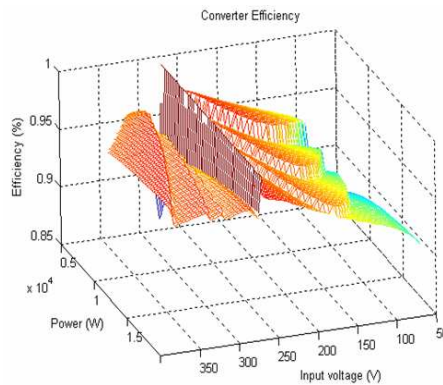


**Figure III. 99: Power converter efficiency according to the load power and the input voltage (4-branch non-reverser Buck-Boost converter).**

As expected, the generated efficiency surface is a mix between the Boost converter and the Buck converter surfaces. It is also important to observe a maximum efficiency point corresponding to a 270V input voltage. Indeed, for this input voltage, the converter is in a freewheel operating mode, and thus, there are no switching and inductor iron losses.

**As in all previous cases, the branch switching-off technique improves the power converter efficiency.** The evolution of the different losses can be observed in the following figures..



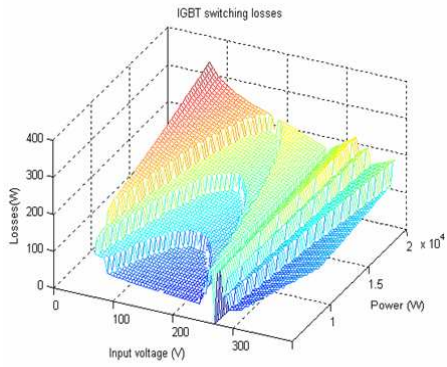


**Figure III. 100: IGBT switching losses according to the load power and the input voltage (4-branch non-reverser Buck-Boost converter).**

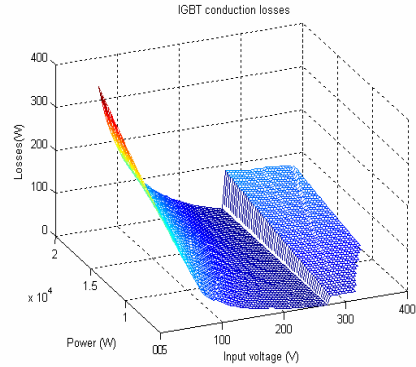


**Figure III. 101: IGBT conduction losses according to the load power and the input voltage (4-branch non-reverser Buck-Boost converter).**

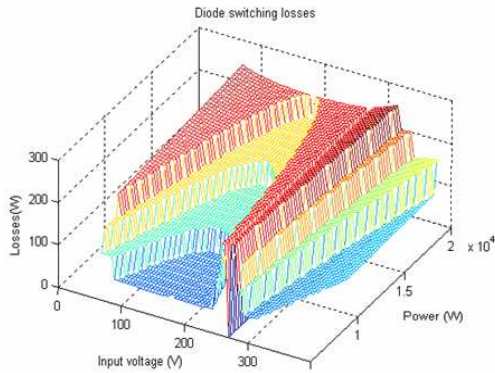


**Figure III. 102: Diode switching losses according to the load power and the input voltage (4-branch non-reverser Buck-Boost converter).**

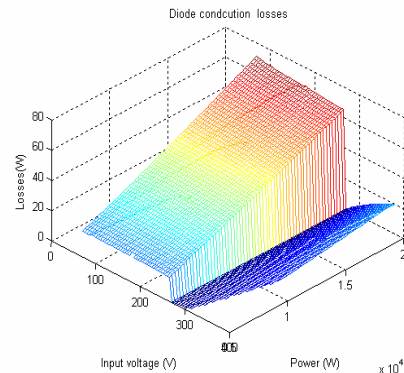


**Figure III. 103: Diode conduction losses according to the load power and the input voltage (4-branch non-reverser Buck-Boost converter).**

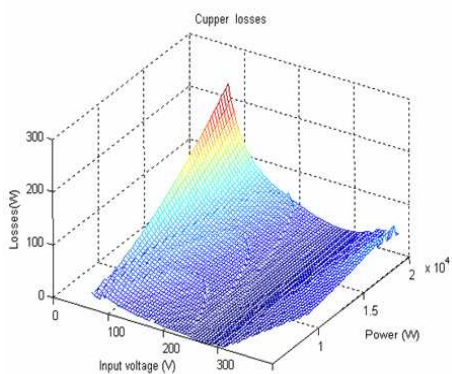


**Figure III. 104: Inductor copper losses according to the load power and the input voltage (4-branch non-reverser Buck-Boost converter).**

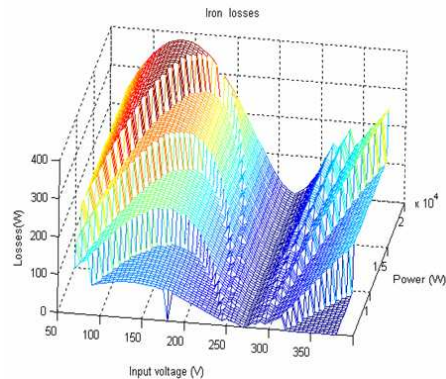


**Figure III. 105: Inductor iron losses according to the load power and the input voltage (4-branch non-reverser Buck-Boost converter).**

### III.4.6 Evaluation of non insulated power converter topologies with interleaved branches for the AIRBUS requirements

#### III.4.6.1 Power converter topologies proposed for this evaluation.

According to the output voltage delivered by the fuel cell (data not fixed by the requirements) (Figure III. 2), three different topologies of power converters are proposed to carry out the Airbus requirements. All these topologies are based on the parallel association of two elementary power converters (which can be themselves achieved by interleaved parallel branches!):

- One power converter (Boost, Buck or Non-reverser Buck-Boost depending on the input voltage) makes the +270V.
- One Buck-Boost converter makes the -270V.

Our objective here is to give global tendencies for these three proposed topologies, not to design each topology. Therefore, the three power converter topologies will be compared in terms of weight and efficiency **for a given example**.

Airbus requirements fix the mean load power approximately at 40kW (plus ultracapacitor branch losses). Due to the structure of the proposed power converters, the load power will be equally shared between the two elementary power converters. Therefore, each power converter will treat approximately 20 kW plus half of the ultracapacitor branch losses (if it is the case) as maximal power.

For each proposed topology, the efficiency will be equal to:

$$\eta = \frac{1}{2}(\eta_a + \eta_b) \quad \text{E III.81}$$

with  $\eta_a$  and  $\eta_b$  the efficiencies of the two elementary power converters (which can be themselves achieved by interleaved parallel branches!) associated in parallel in the topology.

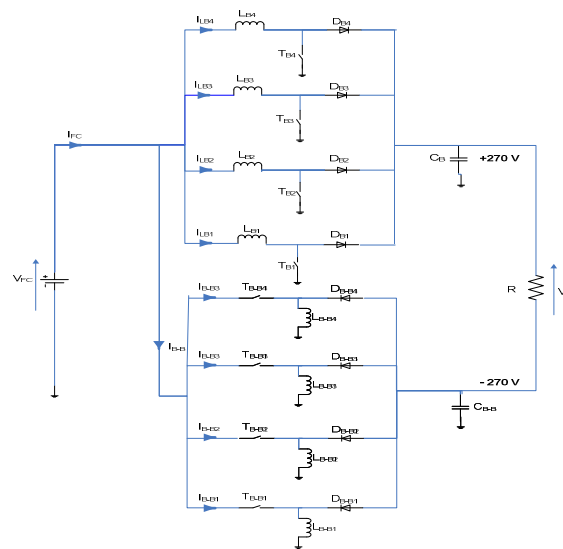
The study achieved in § III.4.4 proved the importance of a correct choices of the number of the interleaved parallel branches and of the switching frequency of the silicon switches. These choices are not independent, and will depend on the global system conditions: particularly the power that flows through the power converter that, itself, will depend on the chosen fuel cell size. **This sizing problem will be detailed in the next chapter IV. Thus, for the following evaluations, arbitrary number of interleaved branches and switching frequency were chosen (not optimized!):** the chosen branch interleaved number is 4 and the chosen switching frequency is 20kHz.

In the previous part § III.4.5, we studied the influence of the branch switching-off technique on the parallel association of elementary power converters (Boost converter, Buck converter, Buck-Boost

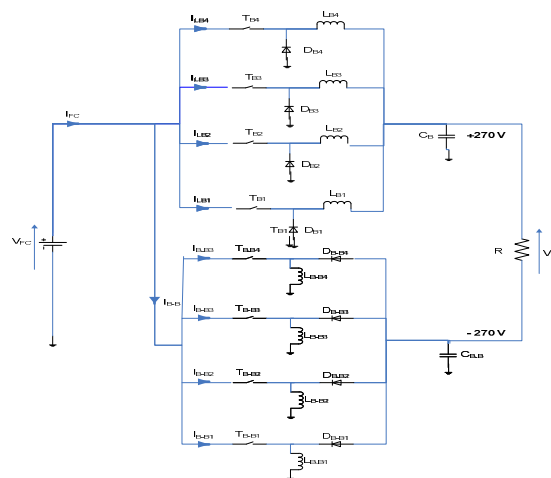
converter, Non-reverser Buck-Boost converter). In each case, four branches of elementary power converters were interleaved.

In the following part, these 4-branch power converters are now associated “two by two” in parallel in order to deliver the  $\pm 270\text{V}$  DC bus required by AIRBUS:

- 4-branch Boost converter with 4-branch Buck-Boost converter: this association will be called “**Boost topology**” in the following (Figure III. 106-a).
- 4-branch Buck converter with 4-branch Buck-Boost converter: this association will be called “**Buck topology**” in the following (Figure III. 106-b).
- 4-branch non-reverser Buck-Boost converter with 4-branch Buck-Boost converter: this association will be called “**Buck-Boost topology**” in the following (Figure III. 106-c).

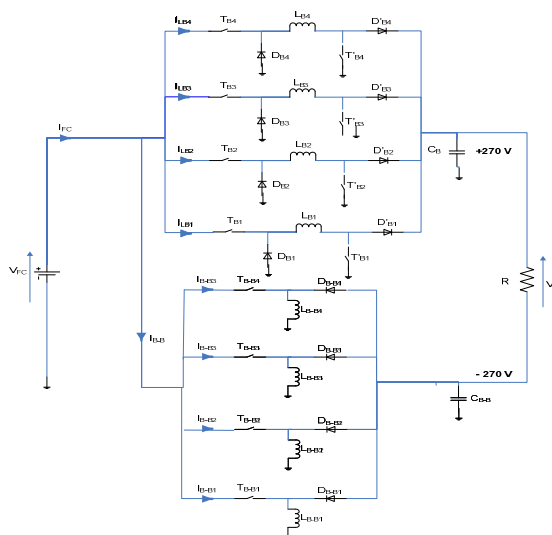


a) Boost topology



b) Buck topology





c) Buck-Boost topology

Figure III. 106: Evaluated power converters for AIRBUS requirements.

**Note to the reader:** As in the previous part, be careful with all the following figures because the order for the axes is not always the same one. Sometimes (particularly for the “input voltage” axis), the axis scale is graduated with decreasing values whereas with increasing values in most cases. All these choices are justified by the will to offer the most readable 3-D view.

### III.4.6.2 Evaluation of the Boost topology for the AIRBUS requirement.

The evaluated scheme is drawn in Figure III. 106 a. This topology is well adapted if the voltage supplied by the fuel cell is inferior to 270V. The efficiency surfaces were calculated for an input voltage variation between 70V and 270V.

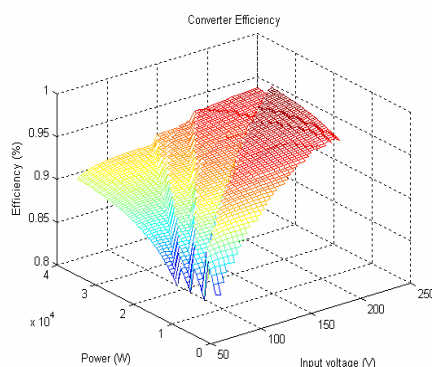
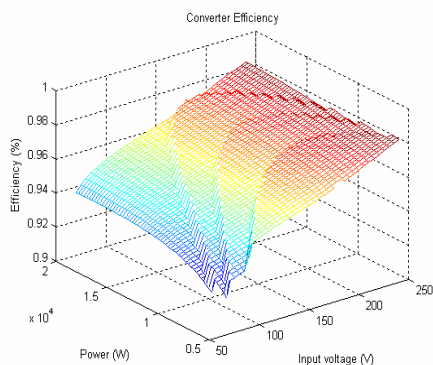


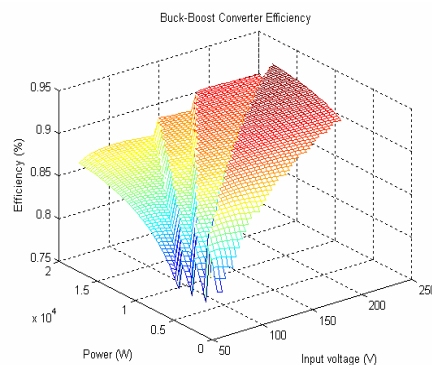
Figure III. 107: Boost topology efficiency surface according to the load power and the input voltage.

Figure III. 107 shows the efficiency surface for the Boost topology for the AIRBUS requirement. On this surface, it is possible to distinguish the “steps” produced by the branch switching-off technique. In order to better analyze the global Boost topology efficiency, the efficiency surfaces of

the “4-branch Boost part” and of the “4-branch Buck-Boost part” are plotted in Figure III. 108 and in Figure III. 109.



**Figure III. 108: Efficiency surface of the “4-branch Boost part” according to the load power and the input voltage.**



**Figure III. 109: Efficiency surface of the “4-branch Buck-Boost part” according to the load power and the input voltage.**

The “4-branch Buck-Boost part” presents a worse efficiency surface. This result is logical, because the “Buck-Boost part” will have to handle a higher current than the “Boost part” for identical powers. The losses being strongly dependent on current values, high current values will create higher losses and worse efficiencies.

The branch switching-off technique effects are observable on both efficiency surfaces: both surfaces present light “steps”. Nevertheless the effect is positive: the “steps” in the efficiency are indeed always positive. But both surfaces do not present the same kind of “steps” because the discontinuous conduction modes are different for each converter part. In Figure III. 110 and Figure III. 111, the chart of the active branches is given for both converter parts.

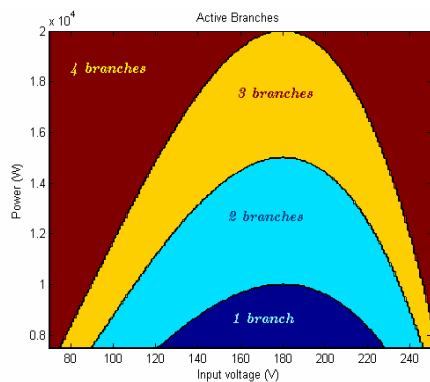


**Figure III. 110: Chart of the active branches according to the input voltage and the load power for the “4-branch Boost part”.**

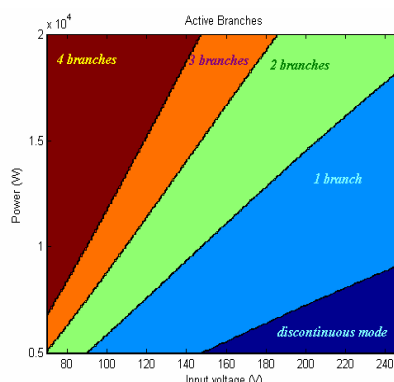


**Figure III. 111: Chart of the active branches according to the input voltage and the load power for the “4-branch Buck-Boost part”.**

Figure III. 112 and Figure III. 113 respectively show the distribution of the losses and the weight distribution for each part of the Boost topology. The losses were evaluated at the maximal power and the minimal input voltage (40kW and 70V).

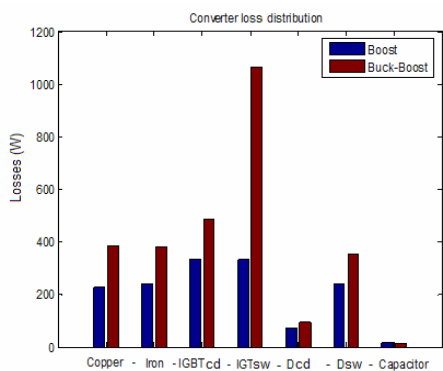


**Figure III. 112: Loss distribution according to the part of the global Boost topology (40kW ; 70V).**

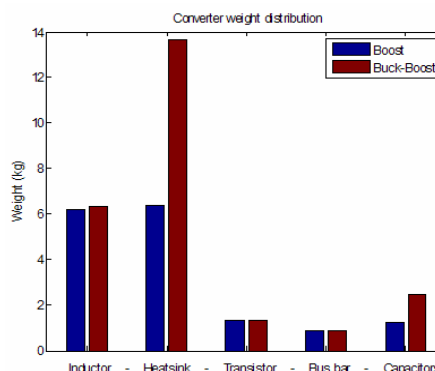


**Figure III. 113: Weight distribution according to the part of the global Boost topology.**

As predicted, losses in the “4-branch Buck-Boost part” are more important than in the “4-branch Boost part”. Thus, the weight “Buck-Boost part” will be higher than the weight of the “Boost part”. The great difference between both parts concerns the switching losses. This is due to the different switched voltages by the silicon switches. Indeed, for the “Boost part”, they will switch with a maximum voltage of 270V (= the output voltage). On the other hand, for the “Buck-Boost part”, the silicon switches will switch with a voltage equal to the sum of the input voltage and the output voltage (almost 600 V if the start-up phase is considered). 1200V IGBTs must be used instead 600V IGBTs for the “Boost part”. The 1200V IGBTs have higher switching losses than 600V IGBTs which are faster.

Finally, the summary of evaluated performances for an input voltage of 70V (the worst case!) is given by the following table:

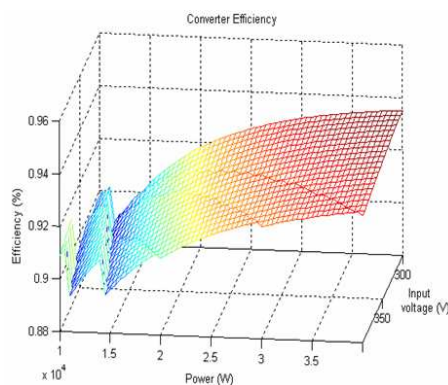
<b>Power</b>	40 kW	<b>Minimal input voltage</b>	70 V
<b>Global Efficiency</b>	89.3 %	<b>Global weight</b>	54.9 kg
<b>Boost part efficiency</b>	93.2 %	<b>Boost part weight</b>	21.6 kg
<b>Buck-Boost part efficiency</b>	85.7 %	<b>Buck-Boost part weight</b>	33.2 kg

**Table III. 2: Worst case of Boost topology sizing for the AIRBUS requirements.**

### III.4.6.3 Evaluation of the Buck topology for the AIRBUS requirement.

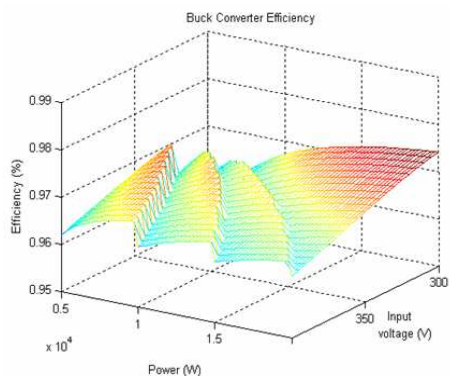
The evaluated scheme is drawn in Figure III. 106 b). This topology is well adapted if the voltage supplied by the fuel cell is superior to 270V. In this illustration, the efficiency surfaces were calculated for an input voltage variation between 300V and 400V..

Figure III. 114 shows the efficiency surface for the Buck topology for the AIRBUS requirement.. The ‘steps’ created by the branch switching-off technique are always positive improving the power converter efficiency. In order to better analyze the global Boost topology efficiency, the efficiency surfaces of the “4-branch Buck part” and of the “4-branch Buck-Boost part” are plotted in Figure III. 115 and in Figure III. 116.



**Figure III. 114: Buck topology efficiency surface according to the load power and the input voltage.**

Identically to the previous case, the “Buck-Boost part” presents a worse efficiency surface than the “Buck part”. The reasons are similar to the previous case.



**Figure III. 115: Efficiency surface of the “4-branch Buck part” according to the load power and the input voltage.**

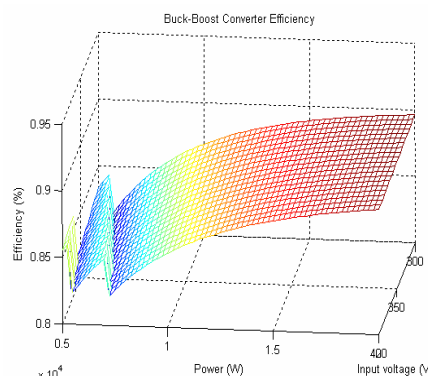


**Figure III. 116: Efficiency surface of the “4-branch Buck-Boost part” according to the load power and the input voltage.**

Due to the branch switching-off technique, both surfaces present ‘efficiency steps’, nevertheless the effect is positive because these ‘steps’ are always positive. The effect is much more aggressive than previously for the ‘Buck-Boost part’. Nevertheless, the effect of the branch switching-off technique always improves the global efficiency.

Both surfaces do not present the same kind of ‘steps’ because of different discontinuous conduction modes (Figure III. 117 and Figure III. 118).

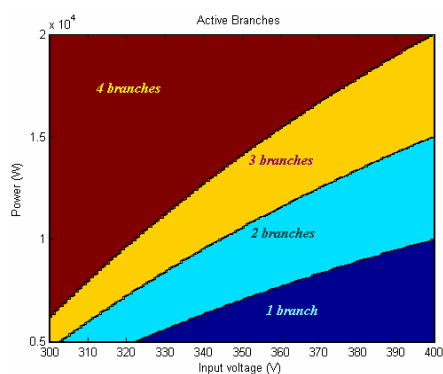


**Figure III. 117: Chart of the active branches according to the input voltage and the load power for the “4-branch Buck part”..**

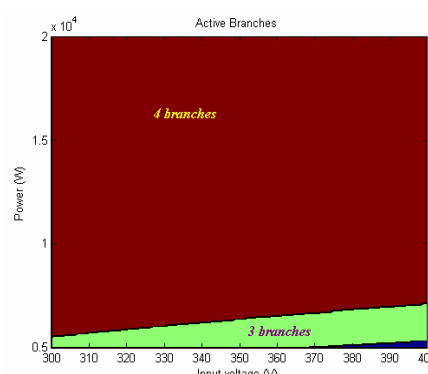


**Figure III. 118: Chart of the active branches according to the input voltage and the load power for the “4-branch Buck-Boost part”..**

Figure III. 119 and Figure III. 120 respectively show the distribution of the losses and the weight distribution for each part of the Buck topology. The losses were evaluated at the maximal power and the minimal input voltage (40 kW and 300V).

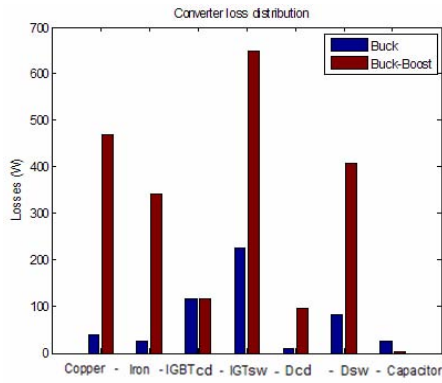


Figure III. 119: Loss distribution according to the part of the global Boost topology (40kW ; 300V).

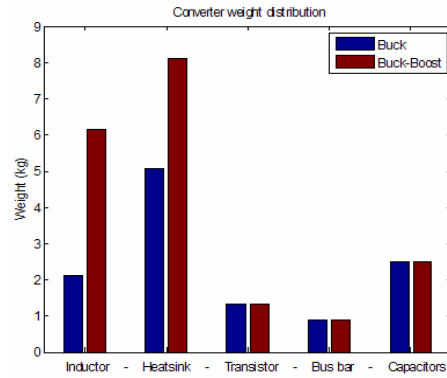


Figure III. 120: Weight distribution according to the part of the global Boost topology.

As in the previous case, losses in the “4-branch Buck-Boost part” are more important than in the “4-branch Buck part”.. It should be noticed the great efficiency obtained by the “Buck part”. Thus, the “Buck-Boost part” weight will be higher than the “Boost part” weight.

Finally, the summary of evaluated performances for an input voltage of 300V (the worst case!) is given by the following table:

<b>Power</b>	40 kW	<b>Minimal input voltage</b>	300 V
<b>Global Efficiency</b>	93.51 %	<b>Global weight</b>	41.5 kg
<b>Buck part efficiency</b>	97.40 %	<b>Buck part weight</b>	16.0 kg
<b>Buck-Boost part efficiency</b>	89.61 %	<b>Buck-Boost part weight</b>	25.5 kg

Table III. 3: Worst case of Buck topology sizing for the AIRBUS requirements.

### III.4.6.4 Evaluation of the Buck-Boost topology for the AIRBUS requirement.

The evaluated scheme is drawn in Figure III. 106 c). This topology is well adapted if the voltage supplied by the fuel cell varies between lower and higher voltage values than 270V. In this illustration, the efficiency surfaces were calculated for an input voltage variation between 70V and 370V.

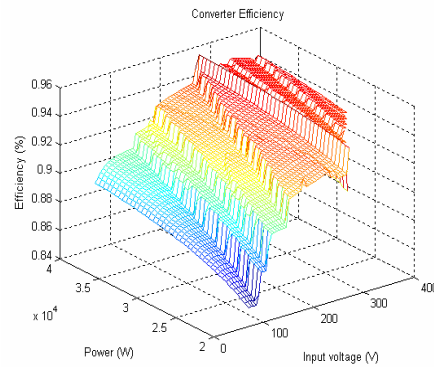


**Figure III. 121: Buck-Boost topology efficiency surface according to the load power and the input voltage.**

It should be noticed that this Buck-Boost topology could operate in all the identified areas in §III.1. Nevertheless, the topology is composed of a higher number of silicon switches than both previous topologies; that necessarily leads to worse efficiencies.

Figure III. 122 and Figure III. 123 show the efficiency surfaces of the “4-branch non-reverser Buck-Boost part” and of the “4-branch Buck-Boost part”.

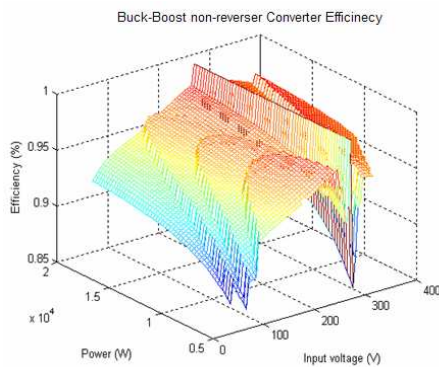


**Figure III. 122: Efficiency surface of the “4-branch non-reverser Buck-Boost part” according to the load power and the input voltage.**

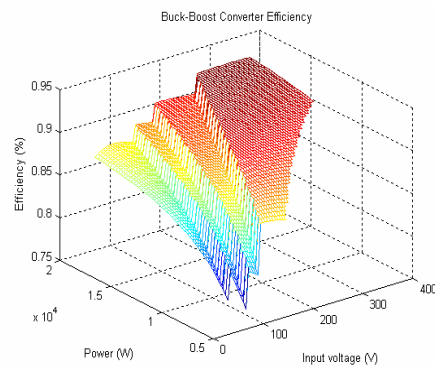


**Figure III. 123: Efficiency surface of the “4-branch Buck-Boost part” according to the load power and the input voltage.**

For better comprehension of the efficiency surfaces, the charts of active branches are plotted in Figure III. 124 and in Figure III. 125

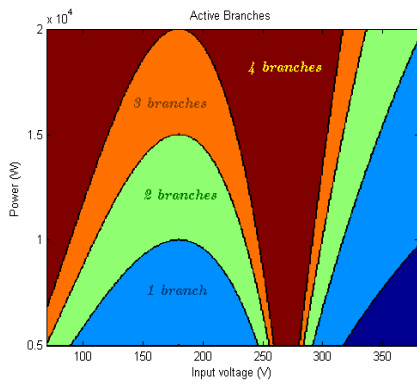


**Figure III. 124: Chart of the active branches according to the input voltage and the load power for the “4-branch non-reverser Buck-Boost part”.**

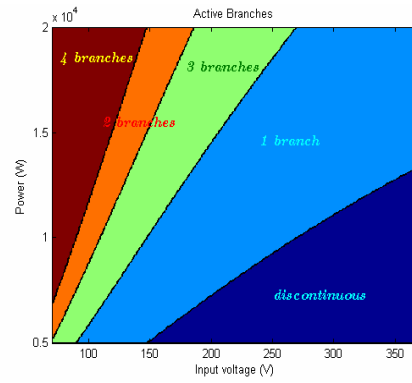


**Figure III. 125: Chart of the active branches according to the input voltage and the load power for the “4-branch Buck-Boost part”..**

Figure III. 126 and Figure III. 127 respectively show the distribution of the losses and the weight distribution for each part of the Buck-Boost topology. The losses were evaluated at the maximal power and the minimal input voltage (40 kW and 70V).

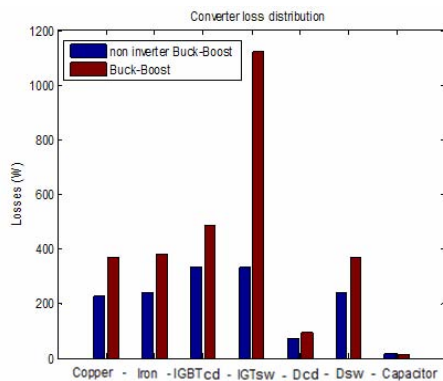


**Figure III. 126: Loss distribution according to the part of the global Boost topology (40kW ; 70V).**

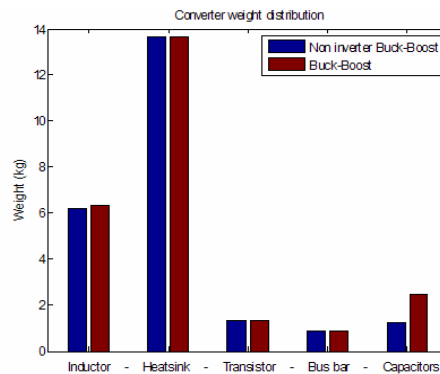


**Figure III. 127: Weight distribution according to the part of the global Boost topology.**

Evaluation results are similar to the Boost topology case, however the “non-reverser Buck-Boost part” results are lightly worse than the “Boost part” (in the Boost topology) due to the bigger number of silicon switches.

Finally, the summary of evaluated performances for an input voltage of 70V (the worst case!) is given by the following table:



<b>Power</b>	40 kW	<b>Minimal input voltage</b>	70 V
<b>Global Efficiency</b>	90.05 %	<b>Global weight</b>	64.7 kg
<b>Non inverter Buck-Boost efficiency</b>	91.32 %	<b>Non reverser Buck-Boost weight</b>	31.46 kg
<b>Buck-Boost efficiency</b>	88.79 %	<b>Buck-Boost weight</b>	33.28 kg

**Table III. 4: Worst case of Buck-Boost topology sizing for the AIRBUS requirements.**

## III.5 Conclusion of chapter III

In this chapter the design of a power converter that accomplish the Airbus DC electrical network requirements was presented. That means to obtain a  $\pm 270\text{V}$  DC bus starting from just one fuel cell stack. Therefore, two possible solutions were considered: insulated converters and non insulated converters.

Due to the important power that must be held by the converter, an interleaving technique was presented as the best option in order to achieve good power converter efficiency and good weight ratio. Nevertheless, this technique present one main drawback. Indeed, the inductor value reduction can easily lead the power converter to operate in the discontinuous mode. This fact makes more difficult the control of the power converter.

In order to solve this problem a branch switching off technique was proposed. The idea consists in **switching off** some branches in order to avoid reaching the discontinuous mode. The impact of this technique in the power converter control and in the global converter efficiency was also evaluated.

Concerning the power converter sizing two design variables must be determined: the switching frequency and the number of interleaved branches. Indeed, these two variables determines the power converter weight and efficiency. Nevertheless, we consider that it is most interesting to size the power converter considering all the system couplings and/or the power converter interaction with the fuel cell and the ultracapacitor systems. This can be easily explained because our main goal is to minimize the global system weight and gas consumption (and not only the power converter weight!). Therefore, in next chapter a global system optimization tool will be implemented, including obviously the power converter models developed in this chapter.



## *Chapter IV :*

# **Optimization study. Architecture comparisons**

---

**D**ue to the transportation application of the CELINA project, the designed fuel cell system and its associated electrical network should be lightweight, should present high efficiency and the volume should be reduced as much as possible. In the previous chapters, it was explained that in order to size the fuel cell system, some sizing criteria must be arbitrarily chosen. These criteria will determine the global system mass, volume and efficiency. The main difficulty to determine the sizing criteria that lead to an optimized sizing resides in the system complexity and in the couplings existing between each subsystem. Indeed, a fuel cell that operates at high current densities will be smaller in terms of mass and volume compared to one that operates with low current densities. Nevertheless, the high current density fuel cell will consume more hydrogen than the one that operates with low current densities. Thus, the global system that operates with a “small” fuel cell can be heavier than the one that operates with a “large” fuel cell, because the hydrogen mass is lower in the last case. **The system couplings make the global system design a difficult issue.** Furthermore, the number of optimized sizing criteria (design variables) is important in the CELINA project: an optimized configuration for the system cannot be achieved only using, *a priori*, a sweeping of parameters.

**The development of an optimization tool, that will make it possible to compare the three retained architectures, seems necessary in our case.**

Another difficulty in the CELINA project is that the system should be optimized in terms of mass, volume and energy efficiency. Generally, lightweight systems present small volumes. It seems pertinent to affirm that optimizing the system in terms of mass is equivalent to optimizing the system in terms of volume. However, best efficiency systems are generally oversized, and therefore they are not optimized in terms of mass. This involves that mass and efficiency are conflicting sizing objectives: **a multi-objective optimization problem should be solved.**

Two different strategies could be applied in order to solve this problem:

- Using standard one-objective optimization algorithms. That means optimizing the system in terms of mass and efficiency independently. Then, both ideal solutions can be found and some intermediate compromises can be investigated by combining the different objectives into a global quality function (typically with the “goal attainment method” [Rao] for instance). The main advantage of this strategy resides in its simplicity (i.e. standard optimization algorithms with one-objective formulation can be used) but its drawback is related to the objective scalarization necessary to aggregate all objectives into the global quality function.
- Using a **multi-objective optimization algorithm** that permits to obtain the global Pareto-optimal front (§IV.1.2). This approach leads to a collection of non-dominated solutions. Furthermore, it is possible to obtain some useful information about the evolution of the design variables through the Pareto front that helps to better understand couplings between design variables, constraints and objectives. On the other hand, the algorithm implementation is much more complex and computation costs can become huge.

**For the CELINA project, the second strategy was chosen.** This strategy was already successfully applied for the design of a small wind turbine system [Abdelli], of an electrical vehicle [Régnier] [Tounsi], electrical drives [Kone] [Wurtz], and photovoltaic panels [Siegneurbieux]. Some researchers defend that this optimization approach is a useful tool to design the electrical engineering systems [Sareni].

## IV.1 Multi-objective optimization

### IV.1.1 Optimization algorithms

According to the optimum point research operation, the optimization methods can be classified in two different classes.

#### IV.1.1.1 Deterministic methods

Given a particular input (initial exploration point and/or initial control parameters values), these methods always produce the same path, covering in the same way to the same optimum. The search for the optimum point always behaves predictably. This family can be divided into two subfamilies.

##### □ *Gradient search methods*

The optimum research is oriented thanks to the calculation of the partial derivatives of the objective function. These strategies permit to detect easily the closest optimum. The steepest descent, Newton or quasi-Newton and Levenberg-Marquardt methods belong to this family [**Rao**].

The main drawbacks of these methods reside in the following points:

- The partial derivatives of the objective function need to be computed.
- Local convergence is only guaranteed: in the case of multinodal problems, these methods tend to localize a local optimum. In order to ensure the global convergence, the designer has to perform several optimizations with different initial points.
- These methods can be applied only to continuous problems. They are not suitable for problems with discrete parameters.

However, gradient search optimization methods present two main advantages. If an exact expression of the partial derivatives is available, these methods converge easily and quickly [**Wurtz**]. Furthermore, in most cases, exact convergence criteria can be used to stop the search of an optimal point.

##### □ *Geometric or heuristic Methods*

These methods only use the objective function values. They explore the search space by making consecutive tests and trying to find the best directions. Similarly to gradient search techniques, convergence in geometric methods is local, but robustness is better if the objective function is noised or discrete. The main drawback of these methods is the computation cost. Hooke and Jeeves [**Hooke**], Nelder- Mead, Rosenbrock [**Rosenbrock**] and Powell [**Powell**] are geometrical methods.

### IV.1.1.2 Stochastic methods

Stochastic methods are based on random exploration of the search space thanks to probabilistic transition rules. Thus, for different optimization problems with the same initial conditions, stochastic methods will not cover exactly the space solutions in order to converge to the same optimum in each optimization run. Genetic algorithms and Simulated Annealing are the most popular stochastic optimization methods

#### □ Genetic algorithms

Genetic algorithms are stochastic optimization methods inspired by natural evolution and genetics. They operate with a collection of candidate solutions (i.e. the population of individuals), randomly initialized in the search space. A fitness score (i.e. the objective function in the one-objective case) measures the individual adaptation in relation to their environment. For each algorithm iteration (i.e. each generation), the population evolves thank to Darwinian and genetic operators, typically selection, crossover, mutation and replacement. Commonly the algorithms terminate when either a maximum number of generations has been produced or a satisfactory fitness level has been reached for the population.

The main advantages of genetic algorithms are:

- They can be applied to all kind of optimization problems (discrete, continuous or mixed variable problems)
- Only the objective function has to be calculated (partial derivatives are not required)
- Discontinuities of the objective function do not affect the global convergence.

### IV.1.2 Pareto-optimal front

Multi-objective optimization seeks to simultaneously minimize  $n$  objectives where each of them is a function of a vector  $\mathbf{X}$  of  $m$  parameters (*decision variables* or *design variables*). These parameters may also be subject to  $k$  inequality constraints, so that the optimization problem may be expressed as:

$$\begin{array}{ll} \text{Minimize} & f(\mathbf{X}) = (f_1(\mathbf{X}), f_2(\mathbf{X}), \dots, f_n(\mathbf{X})) \\ \text{subject to} & g_i(\mathbf{X}) \leq 0 \quad \text{for } i = 1 \dots k \end{array} \quad \mathbf{E IV. 1}$$

For this kind of problem, objectives typically conflict with each other. Thus, in most cases, it is impossible to obtain the global minimum at the same point for all objectives. Therefore, the problem has no single optimal solution but a set of efficient solutions representing the best objective trade-offs. These solutions consist of all design variable vectors for which the corresponding objective vectors cannot be improved in any dimension without disimprovement in another. They are known as Pareto-optimal solutions in reference to the famous economist [**Pareto**]. Mathematically, Pareto-optimality

can be expressed in terms of Pareto dominance. Consider two vectors  $\mathbf{X}$  and  $\mathbf{Y}$  from the design variable space. Then,  $\mathbf{X}$  is said to dominate  $\mathbf{Y}$  if and only if:

$$\begin{aligned} &\forall i = 1..n \quad f_i(\mathbf{X}) \leq f_i(\mathbf{Y}) \\ &\text{and } \exists j \in 1..n \Rightarrow f_j(\mathbf{X}) < f_j(\mathbf{Y}) \end{aligned} \tag{E IV. 2}$$

All design variable vectors which are not dominated by any other vector of a given set are called *non-dominated* regarding this set. The design variable vectors that are non-dominated over the entire search space are Pareto-optimal solutions and constitute the *Pareto-optimal front*. We illustrate in Figure IV. 1, the Pareto-dominance of any solution  $\mathbf{X}$  relative to a given solution  $\mathbf{Y}$  in the objective space, for a two dimensional case ( $n=2$ ).

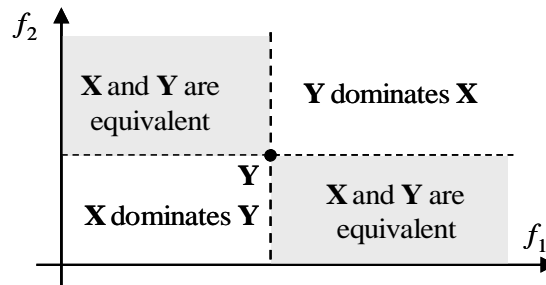


Figure IV. 1: Pareto-dominance – Two-objective minimization.

### IV.1.3 Multi-objective Genetic Algorithms

Since the mid-1990s, there has been a growing interest in solving multi-objective problems by Genetic Algorithms. Extensive research in this field has been carried out because of the GA capacity to approximate the set of optimal trade-offs in a single run by investigating multiple solutions in parallel. More than 2000 papers related to this topic are referenced in the Evolutionary Multi-Objective Optimization (EMOO) website [EMOO]. A classification of Multi-Objective Genetic Algorithms (MOGA) is given in Figure IV. 2. MOGA approaches can be divided into two groups according to whether they exploit or not the concept of Pareto dominance. Most efficient algorithms are Elitist MOGAs associated with niching and clustering methods.

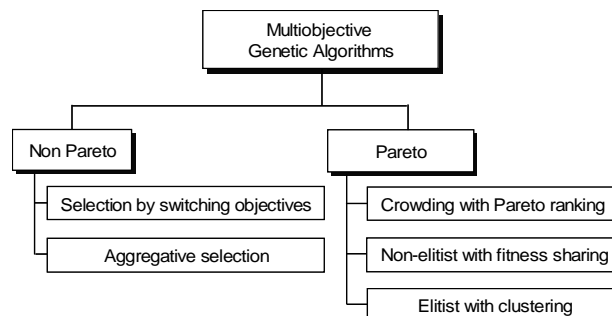


Figure IV. 2: MOGA classification.



Elitist MOGAs use an external population, namely *archive*, which preserves non-dominated individuals in the population. In these algorithms, a fitness assignment procedure is generally used to assess the individual adaptation as a function of their Pareto-dominance. At each generation, individuals (*parents*) selected from the archive (and/or from the population) are crossed and mutated to create new individuals (*children*). The population of children and the archive are merged to assess the non-dominated set of the next generation. If the number of non-dominated individuals is higher than the size of the archive, a *clustering* method is used to preserve most representative solutions and eliminate others in order to keep a constant archive size. Note that a niching procedure is used in the selection process when competing individuals have a similar fitness or a similar Pareto ranking. The skeleton of an Elitist MOGA is given in Figure IV. 3

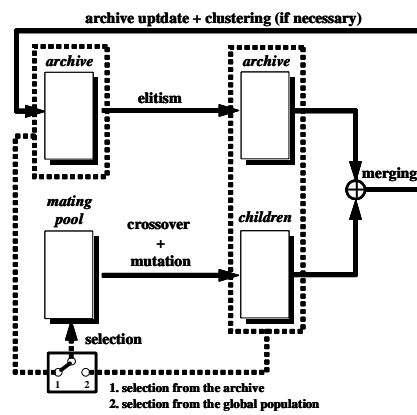


Figure IV. 3: Structure of an Elitist MOGA (one step generation).

The characteristics of the most popular algorithms of this class are summarized in Table 1.

POPULAR ELITIST MOGAS			
	FITNESS ASSIGNMENT	Niching Scheme	Clustering
PAES	None	Based on a grid in the objective space	Random elimination of non-dominated individuals belonging to the most populated region of the grid
PESA	Pareto ranking tournaments		
SPEA	Strength	Through fitness assignment	Based on distances between individuals in the population
SPEA2			
NSGA-II	None Pareto ranking tournaments	Density estimation ( <i>I</i> -distance)	Based on <i>I</i> -distance

Table IV. 1: Popular Elitist MOGAs.

#### IV.1.4 Description of the NSGA-II

We specifically present the second version of the *Non-dominated Sorting Genetic Algorithm* (NSGA-II) which has been used to show the interest of MOGAs. NSGA-II is based on the principles previously given. It determines all successive fronts in the population (the best front corresponding to the non-dominated set). Moreover, a crowding distance called *I*-distance estimates the density of

solutions surrounding each individual on a given front. The computation of the I-distance is given by the following pseudocode:

```

For each individual belonging to a front  $F$  of size  $l = |F|$ 
Set  $I(i)_{distance} = 0$ 
For each objective  $n$ 
Sort individual of the front  $F$  using the  $n$ th objective value
Set  $I(1)_{distance} = I(l-1)_{distance} = \infty$ 
For  $i=1$  to  $(l-1)$ 

$$I(i)_{distance} = I(i)_{distance} + \frac{f_n(i+1) - f_n(i-1)}{f_n(l) - f_n(1)}$$

    
```

where  $f_n(i)$  denotes the  $n$ -th objective relative to the  $i$ -th individual of the front  $F$ . Note that implicit scalarization of the objectives is carried out by normalizing the  $I$ -distance with the maximum objective deviation. An example of  $I$ -distance computation is illustrated in Figure IV. 4 for a two objective problem.

The  $I$ -distance density estimator index is then used in the selection and the clustering procedures:

- in a tournament, if individuals belong to the same front, the selected one has the greater  $I$ -distance.

- at the end of a generation, individuals of the global population (created children and archive elements of the current generation) are sorted in relation to their Pareto rank (i.e. the front they belong to, the first front being composed of non-dominated individuals). Then individuals of each front are resorted according their  $I$ -distance by giving preference to individuals of greater  $I$ -distance (extreme solutions of the front and isolated individuals). Finally, the new archive is obtained by truncation from this widened population considering the previous sorts. It should be noted that one particularity of the NSGA-II resides in the fact that the archive is diversified since it can contain non-dominated individuals as well as individuals of the successive dominated fronts. Finally, we will implement the NSGA-II with the self-adaptive recombination scheme described in [Sareni] to increase its robustness.

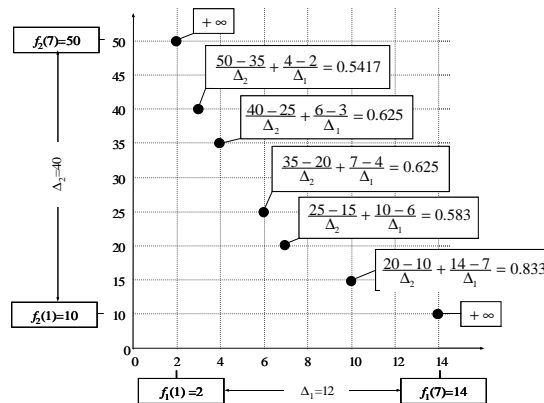


Figure IV. 4: Example of I-distance computations.

### IV.1.5 Design constraint handling in MOGAs

Some specificities of the real world problems require the adaptation of standard MOGAs to take all design constraints into account. Contrary to mathematical problems, constraints cannot be simultaneously evaluated but have to be sequentially computed. For instance, it is obvious that it is not possible to determine constraints and objectives related to a given system if one of its elements is itself non-feasible. Consequently, for each problem, a constraint graph can be established characterizing the couplings and the sequence of the design constraints in the system model. A constraint graph example is given in Figure IV. 5 as an illustration. Note that the constraint graph can be decomposed into different levels to facilitate its analysis. Only constraints belonging to the same level can be computed in parallel. Note that objectives are also subject to this representation and can figure in the constraint graph.

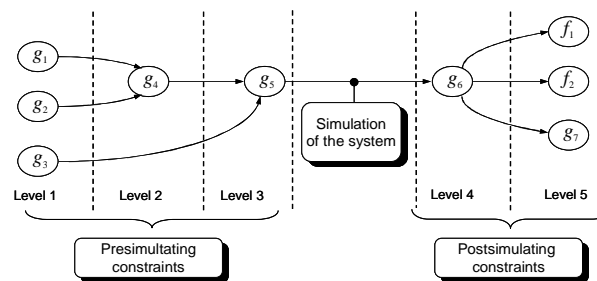


Figure IV. 5: Illustration of the constraint graph concept.

In the example of Figure IV. 5, it can be seen that the objectives are computable if the constraints  $g_1$  to  $g_6$  are fulfilled, the last constraint being assessable in parallel. The higher the number of levels in the graph, the more difficult the problem. Furthermore, in real world problems, constraints can be divided into two groups according to whether their determination is done before or after the system simulation (main cost in CPU time). On the one hand, pre-simulating constraints are mainly “local” relative to specific elements of the system or to their association in the system. On the other hand, post-simulating constraints are essentially “global” concerning the whole system.

As underlined before, the sequential computation of the constraints increases the difficulty of the optimization problem. Violated constraints act as a barrier with regard to the optimization algorithm which is in addition “blind” towards non-computable constraints of the higher levels. In practice, when a constraint  $g(\mathbf{X})$  cannot be computable (because it depends on another violated constraint at a lower level in the graph), we chose to assign for its value the maximum penalty (death penalty) i.e.  $g(\mathbf{X}) = +\infty$ . To take into account the design constraints in MOGAs, the Pareto-dominance rule can be modified as follows:

- If two individuals are non-feasible, the Pareto-dominance relative to these individuals is applied in the constraint space.

- If two individuals are feasible, the Pareto-dominance relative to these individuals is applied in the objective space.

- If one individual is feasible and the other non-feasible, the feasible individual dominates the non-feasible individual.

In this manner, Pareto ranking tournaments between individuals include the constraint minimization as well as the objective minimization. Note in the case of the NSGA-II, for non-feasible individuals belonging to a given front in the constraint space, the computation of the  $I$ -distance density estimator is carried out in relation to all constraints. In this way, niching will occur in the two different spaces (i.e. constraint and objective spaces) and diversity will be preserved to avoid premature convergence.

## IV.2 The Optimization problem

The Non-dominated Sorting Genetic Algorithm (NSGA-II) [Deb] with self-adaptive recombination [Sareni2] was in order to find the optimized sizing of the three proposed electrical architectures. In the following lines, the optimization problem of the architecture with two parallel power converters is formulated. The optimization problems of the two other architectures have a similar formulation, but they are not developed here due to space considerations.

### IV.2.1 The design objectives

Two conflicting sizing objectives have to be optimized: the global system mass should be minimized and the system efficiency should be maximized.

Nevertheless, and in order to facilitate the problem formulation, the hydrogen consumption will replace the system efficiency. Indeed, the system hydrogen consumption is proportional to the system efficiency. High efficiency system will reduce hydrogen consumption and vice versa. The hydrogen consumption is given by:

$$n_{H_2} = \frac{N}{2F} \int_0^t I_{FC} \cdot dt \quad \text{E IV. 3}$$

Thus the first optimization objective  $F_1$  that must be integrated is the **hydrogen consumption**:

$$F_1(X) = \langle n_{H_2} \rangle \quad \text{E IV. 4}$$

The hydrogen consumption is calculated after submitting the system to the Airbus load profile presented in Figure IV. 44. According to Airbus requirements, that is the most constraining mission.

The second optimization objective  $F_2$  is the **total system mass**. The fuel cell auxiliaries' mass was not considered. The system total mass is given by:

$$F_2(X) = \langle M_{FC} + M_{UC} + M_{CVS_{FC}} + M_{CVS_{SC}} + M_{H_2} \rangle \quad \text{E IV. 5}$$

The masses are obtained as follows:

*Fuel cell*: from the fuel cell mass model in § I.4.1.4 [Davies]

*Ultracapacitor*: from the ultracapacitor datasheet [Maxwell] (§ Appendix II)

*Power converter*: from the power converter mass model in § III.4

*Stored hydrogen*: The hydrogen storage capability is fixed to 5% in mass. This means that in order to store 5kg of  $H_2$ , a 100kg tank is needed. This information is

obtained from [Air Liquide]. Air Liquide studied the optimum board hydrogen pressure in a transportation application in the European integrated project (EIHP2). Figure IV. 6 shows the best results achieved in this project.

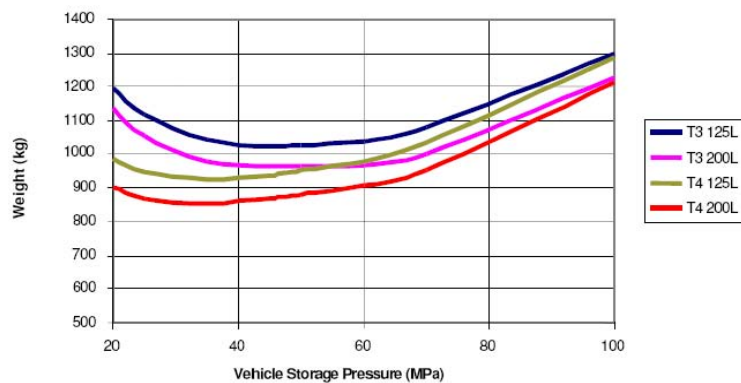


Figure IV. 6: Estimated System Masses To Store 40Kg Hydrogen At 20-100MPa. Source: Air Liquide

## IV.2.2 The design variables

As explained in the previous chapters, some arbitrary sizing criteria determine the system size, and consequently the system efficiency. These criteria will receive the name of “design variables” in the optimization problem in order to respect the usual optimization vocabulary. These design variables are:

### *Power sharing*

The chosen power sharing strategy will, “roughly speaking”, determine the load power distribution between the fuel cell and the ultracapacitor pack. As the frequential power sharing strategy is chosen, the cut-off frequency  $f$  determines the power sharing between both sources.

### *Fuel cell*

The fuel cell mass is given by the fuel cell surface and the cell number. The stack surface is determined thanks to the maximal admitted fuel cell current density  $J_{FC\ max}$  given by the fuel cell makers. The cell number is given by the minimal voltage  $V_{FC\ min}$  that must be guaranteed during the whole mission.  $V_{FC\ min}$  and  $J_{FC\ max}$  are the design variables related to the fuel cell stack.

### *Ultracapacitors*

The number of elementary ultracapacitor cells is given by the maximal voltage value  $V_{UC\ max}$  and the maximal authorized discharge ratio. In this case, due to efficiency reasons [Barrade], the discharge ratio is limited up to 50 % of the authorized maximal voltage. Furthermore, the ultracapacitor internal losses and the voltage-current response are conditioned by the chosen ultracapacitor technology. Therefore, an ultracapacitor library was implemented in the model. This library consists in 6 different ultracapacitors (§ Appendix II).

### ***Energy management loop***

In the chapter II, it was explained that the energy management loop is necessary for the system correct operation. This loop compensates for the ultracapacitor internal losses, and depending on the chosen loop values, determines the storage device size. Thus the voltage reference  $V_{ref}$  and the gain  $G$  are design variables related to the energy management loop.

The voltage reference depends on the ultracapacitor maximal voltage  $V_{UCmax}$ . In order to avoid this dependence, the voltage reference is transformed into a reference gain  $K_{Vref}$  that multiplied by the ultracapacitor maximal voltage gives the voltage reference. Obviously this gain must be lower than one. The  $K_{Vref}$  expression is given by:

$$V_{UC\ ref} = K_{Vref} V_{UC\ max} \quad \text{E IV. 6}$$

### ***Power converters***

The power converter efficiency and mass are directly linked with the voltage supplied by the concerned input source, the switching frequency  $f_s$ , and the number of parallel elementary branches  $n_b$ . The architecture with the two parallel power converters presents two different power converters whose powers are not identical. Thus, it was decided that there are two design variables for the parallel elementary branches: one related to the fuel cell converter  $n_b\ FC$  and another one related to the ultracapacitor power converter  $n_b\ UC$ . On the other hand, it was decided, in order to reduce the number of design variables, to set the same switching frequency for both converters.

Table IV. 2 summarizes all the design variables, and gives the evolution range for each variable. These values were established after some preliminary system simulations.

<b>Design variables</b>	<b>Type</b>	<b>Range</b>
Fuel cell minimal voltage	Continuous	$50 \leq V_{FC\ min} \leq 400$ [V]
Fuel cell current density	Continuous	$0.1 \leq J_{FC\ max} \leq 0.8$ [ $A/cm^2$ ]
Filtering frequency	Continuous	$0.001 \leq f \leq 1$ [Hz]
Ultracapacitor maximal voltage	Continuous	$50 \leq V_{UC\ max} \leq 400$ [V]
Ultracapacitor technology	Discrete	Library [1.....6]
Energy management loop gain	Continuous	$0.1 \leq G \leq 5$
Energy management loop reference voltage	Continuous	$0.75 \leq K_{Vref} \leq 1$
Interleaved converter branches FC	Discrete	$2 \leq n_b\ FC \leq 8$
Interleaved converter branches UC	Discrete	$2 \leq n_b\ UC \leq 8$
Switching frequency	Continuous	$8.000 \leq f_s \leq 25.000$ [Hz]

**Table IV. 2: Design variable for architectures with two parallel power converters.**

### IV.2.3 The system constraints

In order to ensure the system feasibility, some technological constraints should be fulfilled.

#### *Fuel cell constraints*

Due to structural reasons and gas distribution problems, it is not possible to stack in series any number of elementary cells. Indeed, nowadays the technological limit seems to be around 300 elementary cells [Hydrogenics][Ballard]. It is depending on fuel cell technology and still evolving. Due to the futuristic frame of the CELINA project, and assuming a technological evolution during the next years, this limit is extended up to 400 cells. Thus, if  $N$  is the number of elementary cells stacked in series, this constraint could be formulated as follows:

$$g_1 = N - 400 \leq 0 \quad \text{E IV. 7}$$

The fuel cell surface sets a similar problem. Indeed, the limitation is linked to current density and temperature uniformity, and also to structural limitation with mechanical pressing systems. Thus, and projecting the study in a futuristic case, the fuel cell stack surface is limited to 2500 cm<sup>2</sup>. The fuel cell surface constraint could be defined as follows:

$$g_2 = S - 2500 \leq 0 \quad \text{E IV. 8}$$

#### *Power converter constraints*

The power converters are formed by silicon switches (semiconductors), capacitors and inductors. Therefore, libraries of inductor cores and silicon switches were implemented in the model. In some cases, it is possible that there are no available silicon switches or cores in the model library. Thus, the MatLab sizing file (§ IV.2.5) automatically sends an error message and the solution is not valid. Therefore, there is no need to formulate any constraint in the optimization problem.



### IV.2.4 Complete optimization problem formulation

The problem could be formulated as follows:

$$\text{Find a group of solutions } X^* = \begin{Bmatrix} V_{FC \min} \\ J_{FC \max} \\ f \\ V_{UC \max} \\ UC \\ G \\ K_{V_{ref}} \\ n_b_{FC} \\ n_b_{UC} \\ f_s \end{Bmatrix}$$

that guarantees the simultaneous minimization of

$$F = \left\{ \begin{array}{l} F_1(X) = \langle n_{H_2} \rangle \\ F_2(X) = \langle M_{FC} + M_{UC} + M_{CVS_{FC}} + M_{CVS_{SC}} + M_{H_2} \rangle \end{array} \right\}$$

under the constraints

$$g_1 = N - 400 \leq 0 \text{ and } g_2 = S - 2500 \leq 0.$$

### IV.2.5 Optimization process

The global optimization process, including the NSGA-II optimization algorithm, the system sizing iterative method and the system model, is presented in Figure IV. 7.

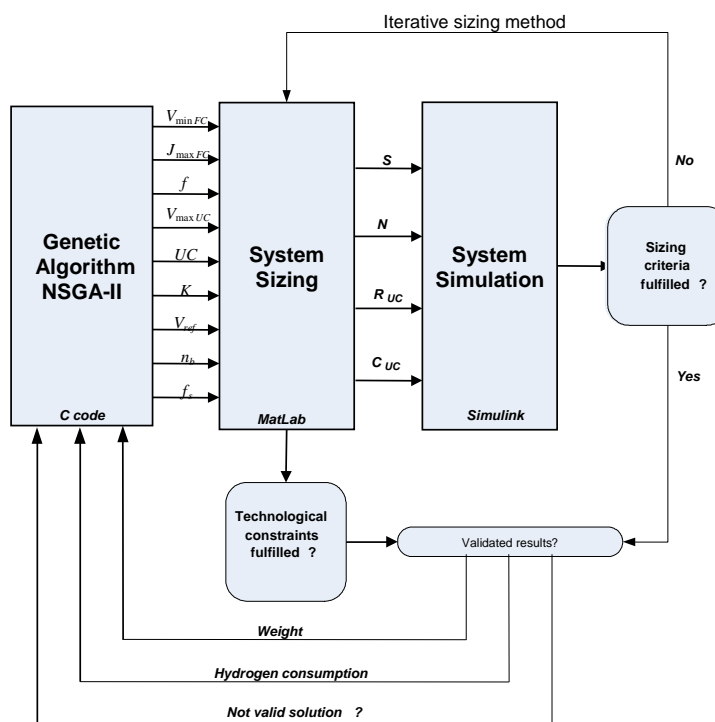


Figure IV. 7: Optimization tool schema.

The next step is to set the NSGA-II control parameters. The aim is to ensure the optimization convergence, and to obtain enough diversified solutions in the Pareto front. A population size of 40 seems an adequate population number permitting to have enough diversified results. Then, the generation number that assures the optimization convergence must now be determined.

A large generation number (800 generations) optimization is launched. Figure IV. 15 and Figure IV. 16 present the evolution of the total system mass and the hydrogen consumption (the objective functions) according to the generation number. These figures show that the objective functions reach the optimized state of evolution after 270 generations. Therefore, the system NSGA-II generations number can be fixed around this value.

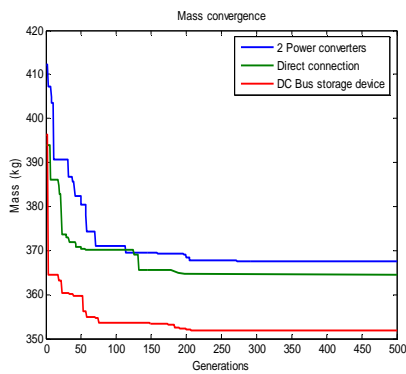


Figure IV. 8: Mass convergence.

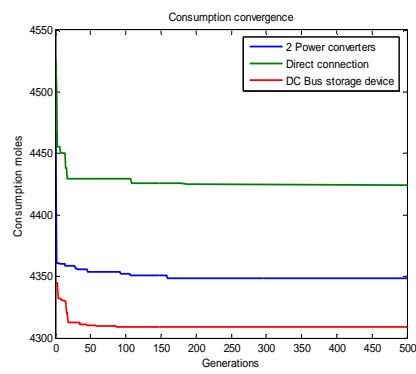


Figure IV. 9: Consumption convergence.

The NSGA-II control parameters are summarized in Table IV. 3.

<b>Population size</b>	$N_{ind}=40$
Generation number	$N_{gene}=280$
Run number	5
Mutation rate	1/variable number
X-gene crossover rate	5%

Table IV. 3: NSGA-II parameters.

## IV.3 Optimization results

### IV.3.1 Architecture comparison

The three proposed architectures in the chapter II are compared in the next lines. The three architectures are submitted to the power profile in Figure IV. 44, and then, the global system mass and hydrogen consumption can be estimated. The NSGA-II optimization algorithm permits to obtain the optimized Pareto charts shown in Figure IV. 10.

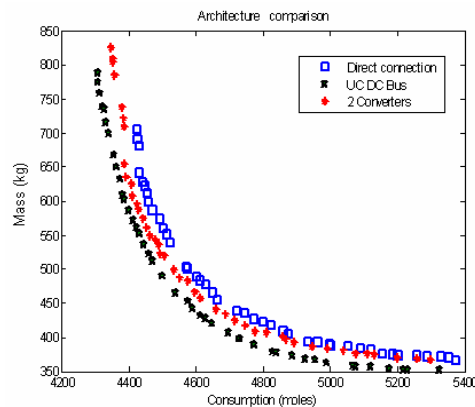


Figure IV. 10: Pareto plot of the three retained architecture.

We can observe in Figure IV. 10. that the architecture with the storage device connected to the DC bus presents the best Pareto plot among all the proposed architectures. Indeed, this architecture (green stars) “dominates” the other architectures. The architecture with two parallel power converters is itself better than to the direct connection architecture. This last architecture presents the worst H<sub>2</sub> consumption-mass ratio between the three architectures.

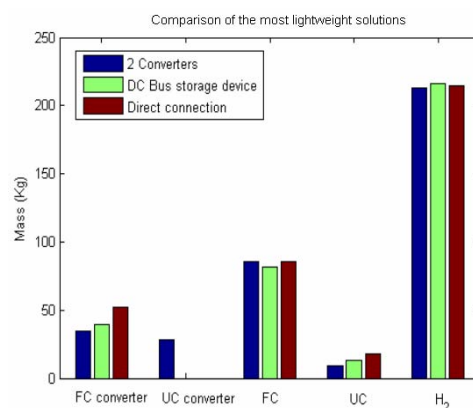


Figure IV. 11: Mass comparison of the most lightweight solutions.

Figure IV. 11 helps to better understand the mass distribution in every architecture. This figure shows the mass distribution for three solutions (each one is the most lightweight solution of architecture). It is interesting to notice that the stored hydrogen mass and the fuel cell mass are, more

or less, similar in the three architectures. The power converter and the ultracapacitor pack masses explain the main difference between the three architectures.

The architecture with the storage device connected to the DC bus does not present a heavy power converter. Indeed, even if the ultracapacitor size is not optimized, this architecture gives the best H<sub>2</sub> consumption-mass compromise. Let us underline that the UC discharge margin (or the DC bus variation) was limited to 30V. If the margin were more restrictive, the storage device could be highly heavier (§II.4.).

The architecture with two parallel converters presents the best ultracapacitors use. But the need of two power converters increases the global system mass and makes the solution less competitive.

Finally, the direct connection architecture, even if only one power converter is used, presents the worst performances. The power converter is heavier because all the load power must transit through the converter. Furthermore, the ultracapacitor pack use is not optimized leading to a heavy ultracapacitor pack.

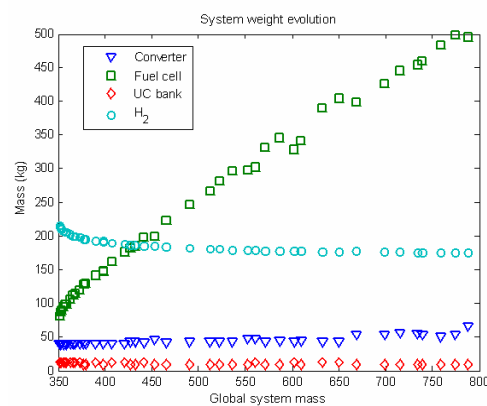


**Figure IV. 12: System mass evolution along the Pareto front. (architecture with the storage device connected to the DC bus).**

Figure IV. 12 shows the mass distribution evolutions along the Pareto front. This evolution is similar for the three architectures. Thus, just only the results for the architecture with the storage device connected to the DC bus are drawn in Figure IV. 12. The fuel cell mass increases along the Pareto plot. Indeed, “large” fuel cells stacks lead to better efficiencies, and as a consequence, lower hydrogen consumptions. On the other hand, the stored hydrogen mass obviously decreases along the Pareto plot (the hydrogen consumption decreases). The storage device mass remains more or less constant through the Pareto plot. Finally, the power converter mass increases slightly.

### IV.3.2 Evolution of the design variables along the Pareto plot

In the next lines, the evolution of the design variables along the Pareto plot is now analyzed. The aim is to find the similarities in the system conception between all the proposed architectures.

Furthermore, the evolution of the design variables helps to better understand the design of a fuel cell system.

**This study is based on the steady-state. The start-up phase is not considered.**

### IV.3.2.1 The architecture with the storage device connected to the DC bus

The operation modes of the optimized solutions are shown in Figure IV. 13. Almost all the solutions operate in Boost mode. Indeed, the fuel cell voltage never exceeds 270V during the whole mission.

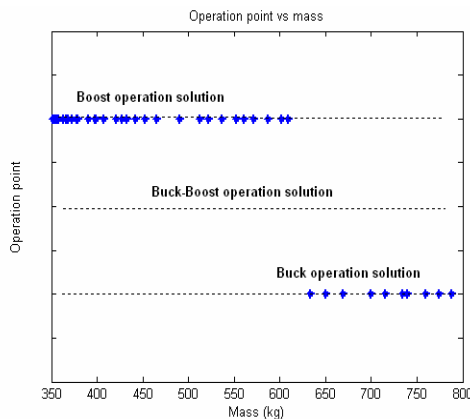


**Figure IV. 13: Operation mode results according to the system global mass.**

According to Figure IV. 14, the optimized power sharing cut-off frequencies seem to be placed between 0.1 and 0.5 Hz (note that the logarithmic scale is used in this figure). Thus, if there are no important fuel cell dynamics limitations, there is no reason to filter as much as possible the load power.

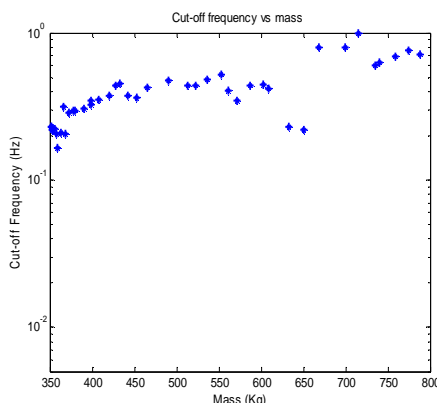


**Figure IV. 14: Cut-off frequency vs system mass.**

The evolutions of the fuel cell design variables are shown in Figure IV. 15 and Figure IV. 16. All the Boost operation solutions (the solutions that minimize the mass) suggest a minimal voltage point around 240V. That means that the fuel cell voltage evolution during the mission only varies of 30V (from 270V to 240V). It is remarkable that all the optimized solutions are tuned to this value.

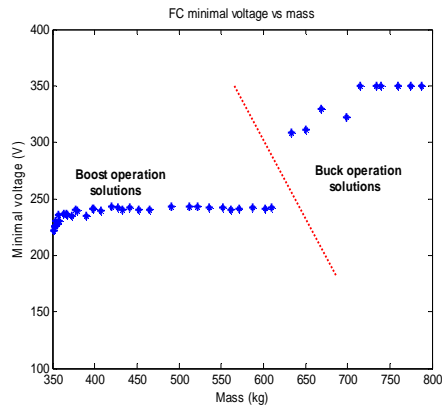


**Figure IV. 15: FC minimal voltage vs system mass.**

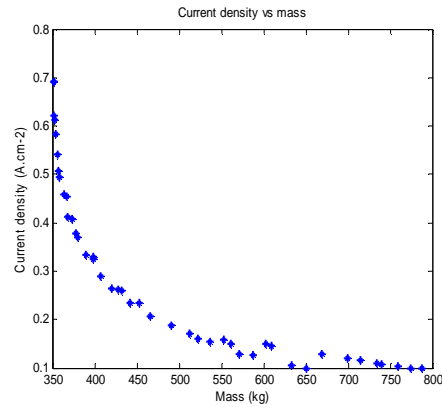


**Figure IV. 16: FC maximal current density vs system mass.**

The evolution of the maximal current density is proposed in Figure IV. 16. As expected, high current densities lead to smaller fuel cells and generally to smaller systems. Nevertheless, one important fact should be noticed. The higher fuel cell current density limitation is  $0.8 \text{ A/cm}^2$ . Looking carefully at Figure IV. 16, it can be seen that there are no solutions with this current density (the higher optimized fuel cell current density does not reach  $0.7 \text{ A/cm}^2$ ). This can be easily explained because, according to optimization results, if the fuel cell would operate at  $0.8 \text{ A/cm}^2$ , the losses and the hydrogen consumption would increase, and therefore the stored  $\text{H}_2$  mass would increase too. Thus, even if the fuel cell stack mass is reduced, the global system mass can become higher than the same system operating with a  $0.7 \text{ A/cm}^2$  current density. This will be farther explained in section § IV.4.

The design variables related to the system energy management are plotted in Figure IV. 17 and Figure IV. 18. It seems that the voltage reference could be fixed to 525V, which is exactly the medium point between the two accepted discharge margins. It is more difficult to obtain some conclusions with the corrector gain, but it seems that for the Boost operation solutions, values from 0.1 to 0.5 could be a good option.

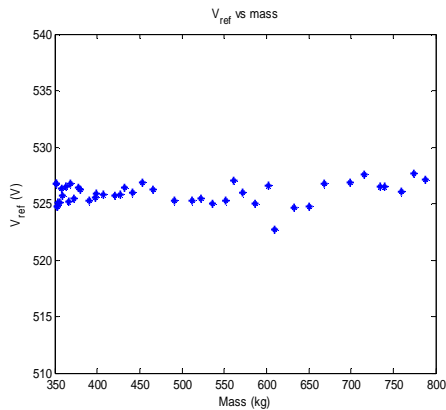


**Figure IV. 17: UC voltage reference vs system mass.**

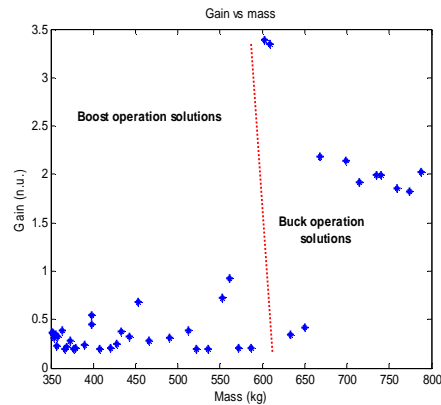


**Figure IV. 18: Energy management loop Gain vs system mass.**

In Figure IV. 19, it is possible to find the results obtained in § III.4.4 where 5 to 6 branches seemed to be an optimized branch number in terms of mass for a power of 30 kW (Figure III. 74). Nevertheless, if it is desired to increase the power converter efficiency (or in other words, to reduce the hydrogen consumption), the branch number can be increased. But the power converter cost could be affected with the rise of the power converter mass.

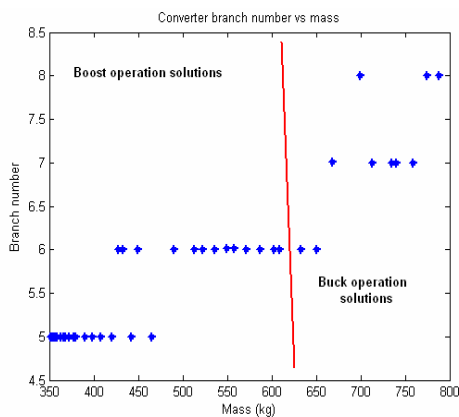


**Figure IV. 19: Converter parallel branch number vs system mass.**

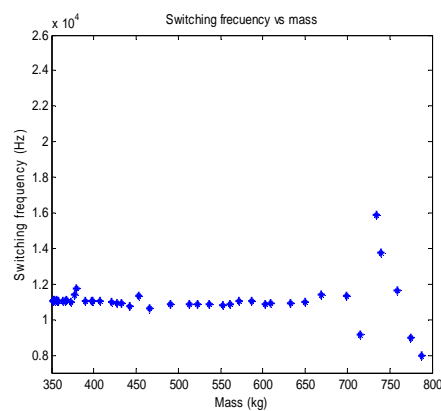


**Figure IV. 20: Switching frequency vs system mass.**

Looking at Figure IV. 20, a switching frequency of 11 kHz should be chosen.

The ultracapacitor choice seems to be clarified with Figure IV. 21. Indeed, the ultracapacitor technology lightweight but with small capacities is the most suitable option according to Figure IV. 21. while heavier ultracapacitors with higher capacities are not present in the optimized solutions group.

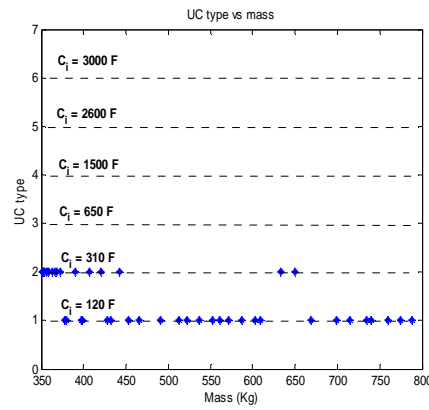


Figure IV. 21: UC type vs system mass.

### IV.3.2.2 The direct connection architecture

The same approach, applied to the direct connection architecture, is developed in the following lines.

In Figure IV. 22, the optimized solutions along the Pareto front present some similarities with the previous architecture results. The H2 consumption optimized solutions are mostly Buck operating mode solutions. The mass ‘intermediately optimized’ solutions operate in Boost mode. The main difference is that the most lightweight solutions are Buck-Boost mode solutions. Nevertheless, these Buck-Boost solutions are really close to Boost operation mode solutions: the Buck-boost operation mode is just due to a few volts.

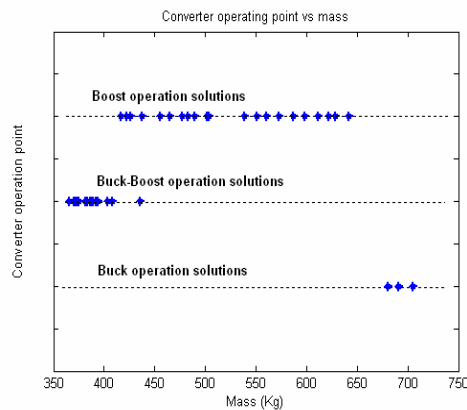
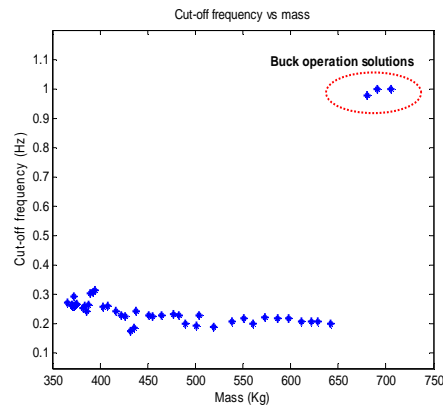


Figure IV. 22: Operation point results according to the system global mass.

According to Figure IV. 23, the optimized power sharing cut-off frequencies seem to be placed between 0.2 and 0.3 Hz. Thus, the same conclusions as in the previous architecture can be applied.





**Figure IV. 23: Cut-off frequency vs system mass.**

The evolution of the fuel cell minimal voltage design variable shows, as observable in Figure IV. 24, that the mass optimized solutions converge around 250V. The buck case solutions are obviously over 250V. Concerning the current density, a similar evolution to the previous architecture can be observed in Figure IV. 25. It should be noticed, that again, in this case too, there are no solutions over 0.7 A/cm<sup>2</sup>. This also can be explained with the same approach as the previous architecture. Nevertheless, this topic will be further developed in § IV.4.

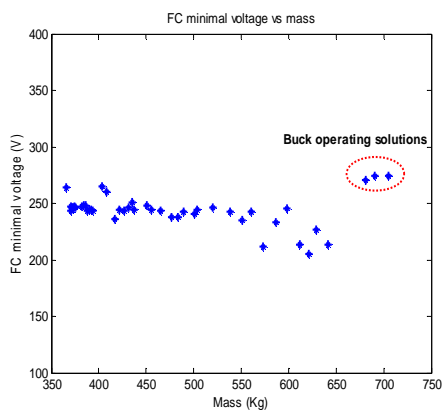


**Figure IV. 24: FC minimal voltage vs system mass.**

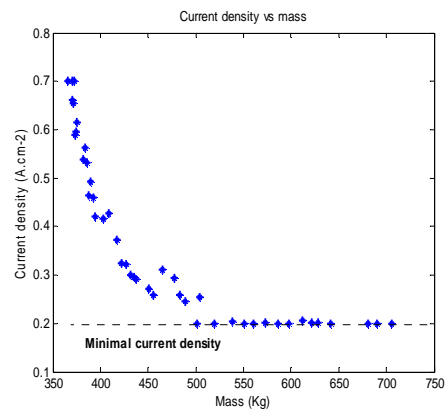


**Figure IV. 25: FC maximal current density vs system mass.**

The evolution of the power converter design variables are plotted in Figure IV. 26 and in Figure IV. 27. The branch number evolution seems to correspond to the converter sizing results achieved in the chapter III. Nevertheless, in this case, there are no solutions with 5 branches. This is due to the fact that, in the direct connection architecture, all the whole load power (over 70kW) transits through the power converter, and not only the 50 kW power as in the previous case. Thus, it seems coherent that if the handled power rises, the branch number should also be increased. Finally, it is not possible to find a tendency in the Buck operation solutions.

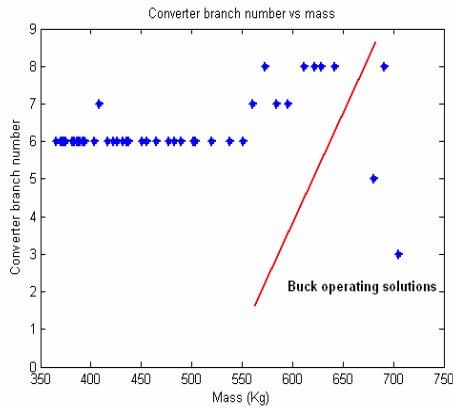


**Figure IV. 26: Converter parallel branch number vs system mass.**

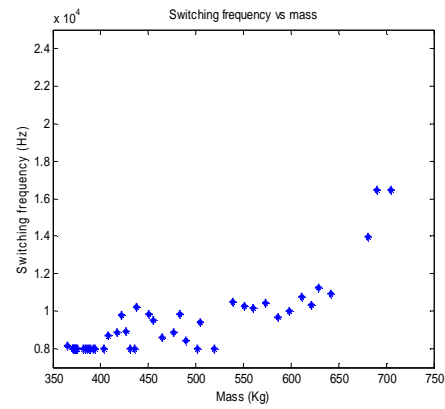


**Figure IV. 27: Switching frequency vs system mass.**

Concerning the power converter switching frequency, it seems that it should be set between 8 and 10 kHz. This result shows that, it is not convenient to operate with high switching frequencies, even if high frequencies lead to the inductor mass reduction.

Finally, the choice of the ultracapacitor technology seems to follow the same tendencies as for the previous architecture. Indeed, the ultracapacitor technologies lightweight but with small capacities are the most suitable option once again. Heavy and high elementary capacity ultracapacitors are just present in the Buck operation optimized solutions.

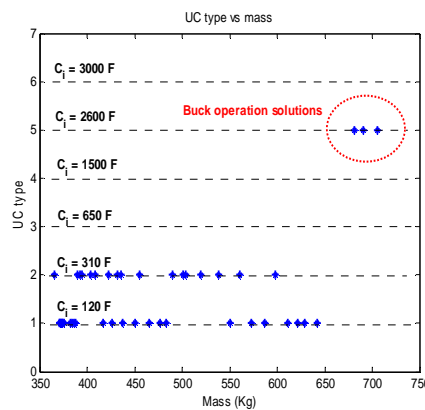


**Figure IV. 28: UC type vs system mass.**

### IV.3.2.3 The architecture with two parallel power converters

In this architecture, two power converters are used. The operation mode of each power converter must be identified. Figure IV. 29 and Figure IV. 30 show the optimization results for both converters.

For the fuel cell converter, the same tendencies found for the two previous architectures can be constated (Figure IV. 29). The most lightweight solutions are Boost operation solutions (Figure IV. 29). On the other hand, some Buck operation solutions are found among the less hydrogen

consumption solutions. There are no Buck-Boost solutions. Nevertheless, for the UC power converter, there are only Boost operation solutions (Figure IV. 30).

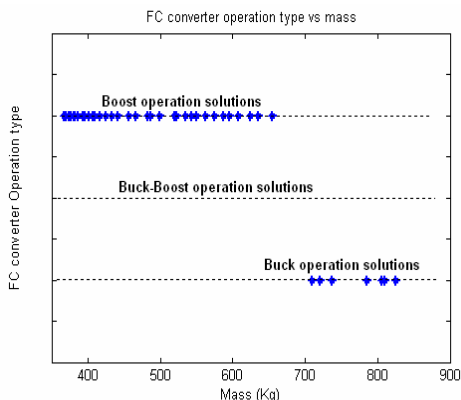


**Figure IV. 29: FC operation point results according to the system global mass.**

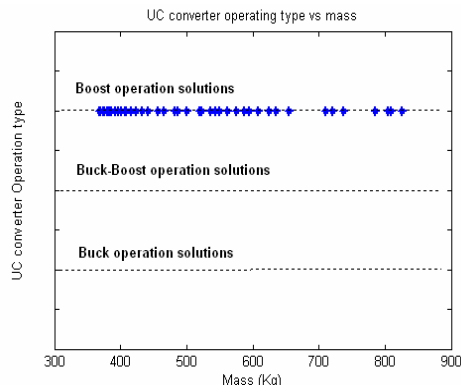


**Figure IV. 30: UC operation point results according to the system global mass.**

The power shating cut-off frequency results (Figure IV. 31) are not so well defined as in the two previous architectures. Indeed, it seems that the most lightweight solutions are grouped around 0.1 Hz values. Nevertheless, solutions are more dispersed than in the two previous architectures. Less hydrogen consumption solutions are grouped around a cut-off frequency of 1 Hz.

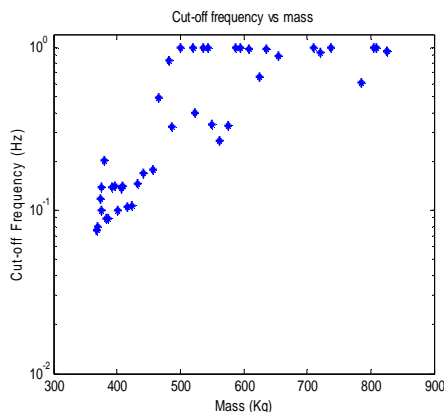


**Figure IV. 31: Cut-off frequency vs system mass.**

As it can be observed in Figure IV. 32, the fuel cell minimal voltage for an optimal mass is fixed once again around 250V. On the other hand, the less hydrogen consumption solutions are grouped within margins between 300 and 350V..

The fuel cell maximal current density varies similarly to the two previous architectures along the Pareto plot. Nevertheless, in this case, the maximal current density is just slightly over 0.55 A/cm<sup>2</sup>, as observable in Figure IV. 33.

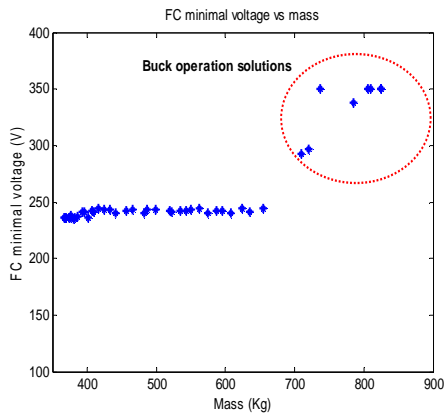


**Figure IV. 32: FC minimal voltage vs system mass.**

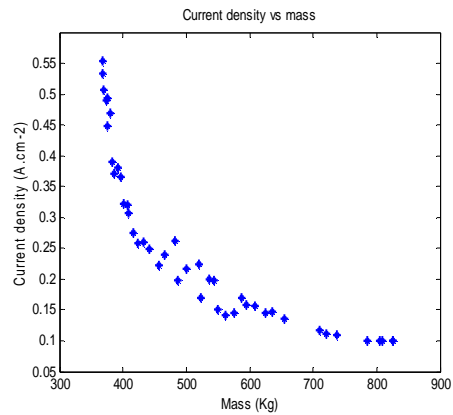


**Figure IV. 33: FC maximal current density vs system mass.**

In this architecture, the maximal ultracapacitor pack voltage is a design variable. The evolution of the maximal ultracapacitor pack voltage along the Pareto plot is plotted in Figure IV. 34. In all cases, the maximal voltage value never exceeds 270V, or in other words, the DC bus voltage. The main optimized solutions are grouped between 200 and 270V.

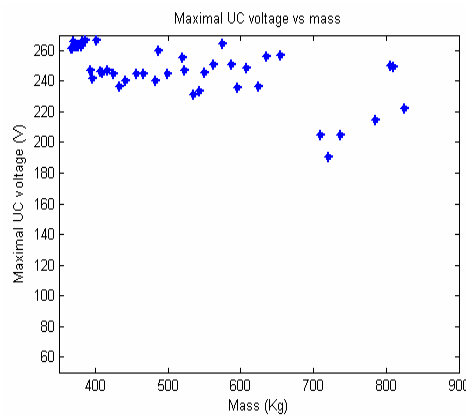


**Figure IV. 34: UC maximal voltage vs system mass**

Concerning the design variables related to the energy management strategy, it is quite difficult to obtain clear conclusions due to the results dispersion. According to Figure IV. 35, the energy management voltage reference must cover between 0.8 and 0.9 times the maximal ultracapacitor pack voltage.

The energy management loop gain is very dispersed along the Pareto plot. Nevertheless, the evolution is quite similar to the solutions in Figure IV. 31. Thus, it is possible to wonder if there is a coupling between the system cut-off frequency and the energy management strategy design variables. This question will be answered in § IV.3.3.

The fact that the energy management loop design variables are so dispersed shows the difficulty to tune correctly the control loop. This fact was already noticed in §II.2.3.1.

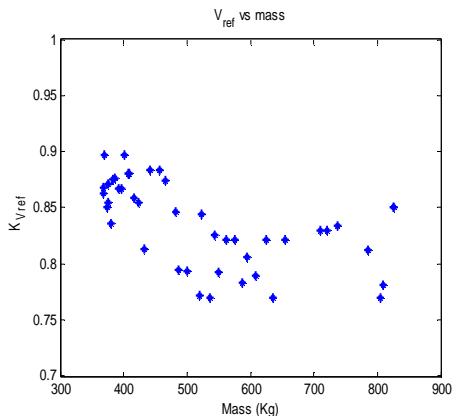


**Figure IV. 35: Voltage reference vs system mass.**

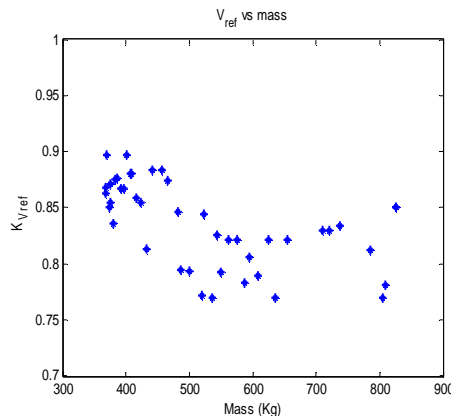


**Figure IV. 36: Gain vs system mass.**

The same switching frequency was fixed for both power converters. In this case, the optimized switching frequency also covers 8 to 10 kHz. Once again, the optimization results show that it is not interesting to operate with high frequencies.

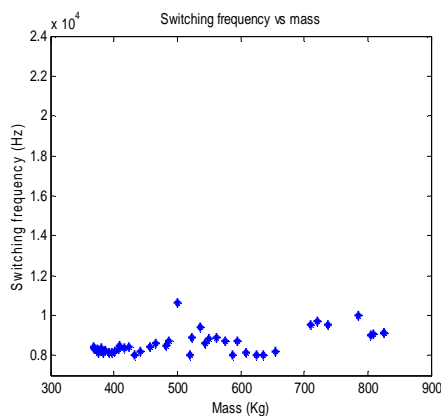


**Figure IV. 37: Switching frequency vs system mass.**

The evolution of the fuel cell converter branch number is drawn in Figure IV. 38. Similar results to the architecture with the storage device connected to the DC bus are found. This is not strange, because, more or less, the same amount of power transits through the fuel cell power converter.

Nevertheless, the optimized branch number is equal to 4 for the UC power converter. This can be easily explained because the power absorbed by the ultracapacitor power converter is lower than in the case of the fuel cell power converter (around 35 kW).

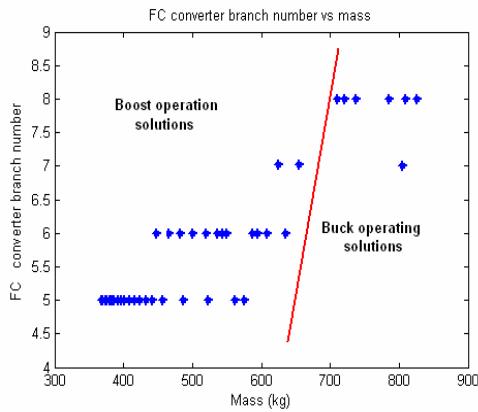


**Figure IV. 38: FC Converter parallel branch number vs system mass.**

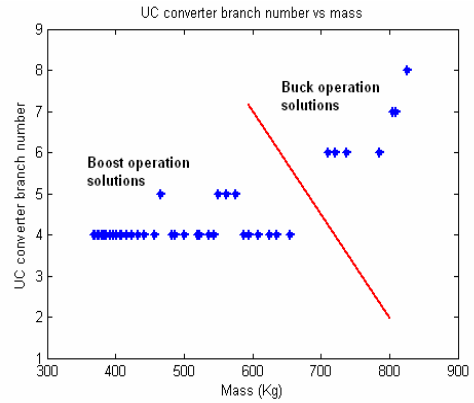


**Figure IV. 39: UC converter parallel branch number vs system mass.**

Finally, the choice of the ultracapacitor technology is unanimous for all the solutions. Indeed, the ultracapacitor technology lightweight but with a small capacity of 120F is the chosen one, even for the Buck optimized solutions.

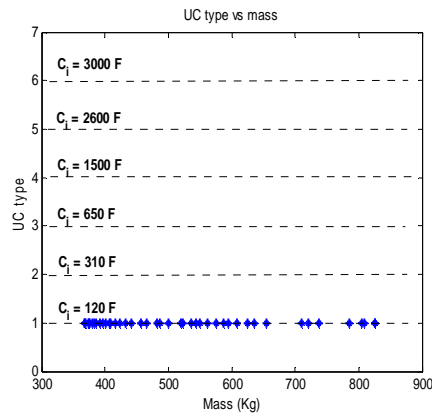


**Figure IV. 40: UC type vs system mass.**

### IV.3.3 System couplings

One of the main difficulties in the system design is to identify couplings between design variables, constraints and objectives in case of a complex multi-physical model. The knowledge of these interactions is valuable with regard to the system behaviour understanding. We can use the following method proposed in [Regnier]:

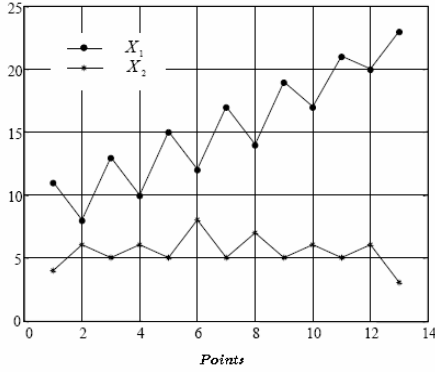


**Figure IV. 41: Evolution example of two coupled design variables  $X_1$  and  $X_2$ .**

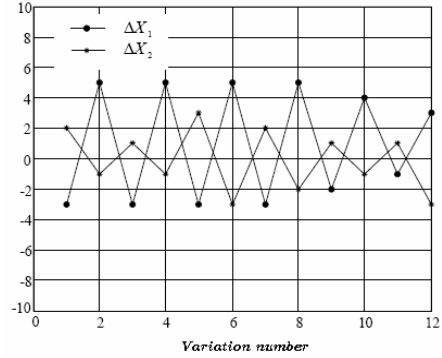


**Figure IV. 42: Corresponding variations of the coupled design variables  $X_1$  and  $X_2$ .**

We propose to use a correlation coefficient in order to evaluate quantitatively the influence of couplings. Let us consider for example two coupled design variables  $X_1$  and  $X_2$  (Figure IV. 41); the correlation coefficient between the corresponding variations of these variables  $\Delta X_1$  and  $\Delta X_2$  (Figure IV. 42) is defined by E IV.9. [Papoulis]

$$\begin{aligned} \text{cor}(\Delta X_1, \Delta X_2) &= \text{cov}(\Delta X_1, \Delta X_2) / \sigma_{\Delta X_1} \sigma_{\Delta X_2} \quad \text{with} \\ \Delta X_1 &= X_{1(i+1)} - X_{1(i)} \\ \Delta X_2 &= X_{2(i+1)} - X_{2(i)} \\ \text{and} \quad i &= 1, \dots, N - 1 \end{aligned} \tag{E IV. 9}$$

Where  $N$  denotes the number of considered points,  $\sigma_{\Delta X_i}$  the standard deviation of  $\Delta X_i$ , and  $\text{cov}(\Delta X_1, \Delta X_2)$  the covariance between  $\Delta X_1$  and  $\Delta X_2$ . Nevertheless, let us note that this coefficient has no signification with the discrete design variables. In the example of Figure IV. 42, the correlation coefficient equals to -1 which signifies that each variation of  $X_1$  is always related to an inverse variation of  $X_2$ . Therefore these two variables are strongly coupled.

The correlation coefficient interpretation is explained in Table IV. 4

$ \text{cor}(\Delta X_1, \Delta X_2)  < 0.2$	Inexistent coupling
$ \text{cor}(\Delta X_1, \Delta X_2)  = 0.2 \text{ to } 0.4$	Very low coupling
$ \text{cor}(\Delta X_1, \Delta X_2)  = 0.4 \text{ to } 0.6$	Not enough value to obtain a conclusion
$ \text{cor}(\Delta X_1, \Delta X_2)  = 0.6 \text{ to } 0.8$	Existent coupling
$ \text{cor}(\Delta X_1, \Delta X_2)  = 0.8$	Strong coupling

**Table IV. 4: Interpretation of the correlation coefficient.**

The identifying technique of system couplings is applied to the architecture with the two parallel power converters. Indeed, in § IV.3.2.3, similar evolutions along the Pareto-optimal front were found between the power sharing cut-off frequency and the design variables of the energy management loop

( $G$  and  $K_{Vref}$ ). The correlation coefficient between the power sharing cut-off frequency and other design variables are presented in Figure IV. 43.

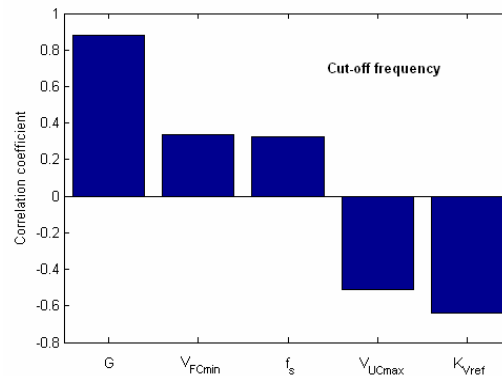


**Figure IV. 43: Case of the architecture with two parallel converters. Correlation coefficient between the cut-off frequency  $f$  and other design variables.**

Figure IV. 43 shows that a strong coupling exists between the energy management loop gain  $G$  and the power sharing cut-off frequency  $f$ . On the other hand, the coupling with the ultracapacitor voltage reference  $K_{Vref}$  is less important. There is no significant coupling between the cut-off frequency and the other design variables  $V_{FCmin}$ ,  $f_s$  and  $V_{UCmax}$ .

#### IV.3.4 Conclusions

Figure IV. 10 shows that the architecture with the storage device connected directly to the DC bus is the best architecture in terms of mass and hydrogen consumption. Nevertheless, for the CELINA project requirements, some interesting conclusions were obtained thanks to the variable evolutions along the Pareto plot. These conclusions seem to be common to all the architectures, if the designer's aim is to minimize the global system mass:

- Optimized architectures in terms of mass do not need to filter extremely the load power. Power sharing cut-off frequencies between 0.1Hz and 0.4Hz seem a good compromise.
- All the architectures converge towards 240V for the fuel cell minimal voltage value.
- Even if the most lightweight fuel cells are obtained with a maximal fuel cell current density of  $0.8A/cm^2$ , lower current densities were obtained for all the optimized systems. This leads to save hydrogen and to obtain a more lightweight global system.
- It is difficult to obtain tendencies about the design variables related to the energy management. This shows the difficulty to tune correctly the energy management control loop.
- The switching frequency should not be very high. Optimized switching frequencies vary between 8kHz and 11kHz.



- The technological choice for the ultracapacitors converges towards the small and lightweight 120F ultracapacitors.

## IV.4 Influence of the mission duration

In the previous section, it was shown that there were no solutions operating with current densities close to  $0.8 \text{ A/cm}^2$ . *A priori*, fuel cells operating at  $0.8 \text{ A/cm}^2$  increase fuel cell stack losses and hydrogen consumption. Thus, the extra hydrogen that must be stored to provide these losses becomes heavier than a fuel cell that operates at  $0.7 \text{ A/cm}^2$ . In the following lines, this assumption will be proved with an application example.

Two optimizations were performed with the architecture with the storage device connected to the DC bus. The only difference between these two optimizations is the mission duration. Both power profiles are plotted in Figure IV. 44 and Figure IV. 45. Both profiles present the same aircraft landing approach, but the 40 kW constant consumption duration is 3,5 hours in the first case and 14,5 hours in the second case. The landing approach is composed of a succession of power profiles like in Figure I. 3. **Even if this example is not very realistic for an aeronautical application, it illustrates the importance of the fuel cell operation point in transportation applications, for which the hydrogen tank must be boarded.**

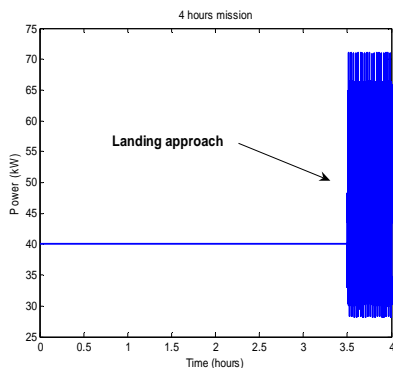


Figure IV. 44: 4 hours mission profile.

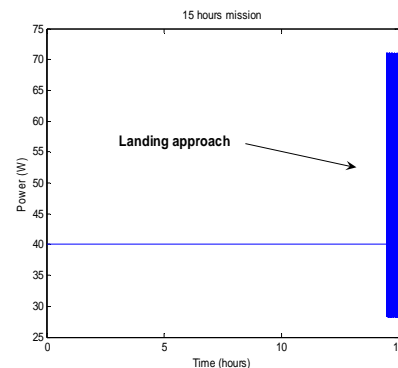


Figure IV. 45: 15 hours mission power profile

Figure IV. 46 and Figure IV. 47 give the Pareto plots of the two systems. Both of them seem to converge correctly. However, it is difficult to compare them because of the big difference between their masses.

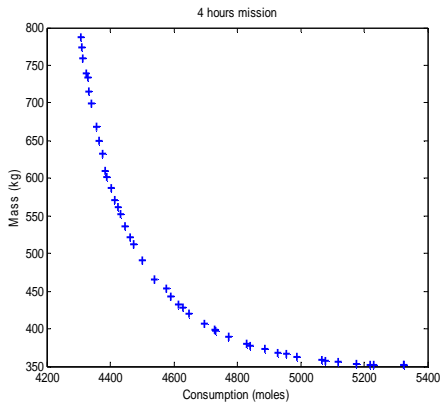


Figure IV. 46: Pareto plot for a 4 hours mission.

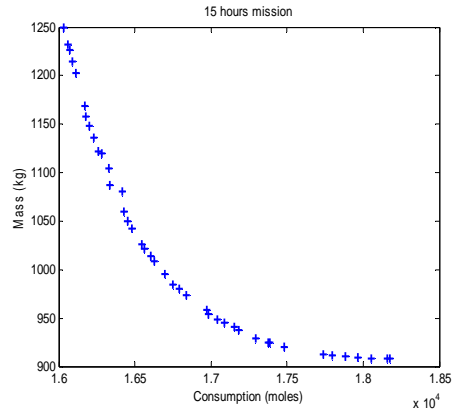


Figure IV. 47: Pareto plot for a 15 hours mission.

The sizing results for the most lightweight solutions in both cases are presented in Table IV. 5. It should be noticed that the fuel cell sizing is different. Indeed, the fuel cell surface for the 4 hours mission is smaller compared to the fuel cell surface for the 15 hours mission.

4 hours mission	15 hours mission
Surface = 442.6 cm <sup>2</sup>	Surface = 712.4 cm <sup>2</sup>
Stacked cells in series = 381	Stacked cells in series = 350
Minimal voltage = 221.7 V	Minimal voltage = 242 V
Maximal current density = 0.69 A/cm <sup>2</sup>	Maximal current density = 0.38 A/cm <sup>2</sup>

Table IV. 5: System sizing results for two missions of different durations.

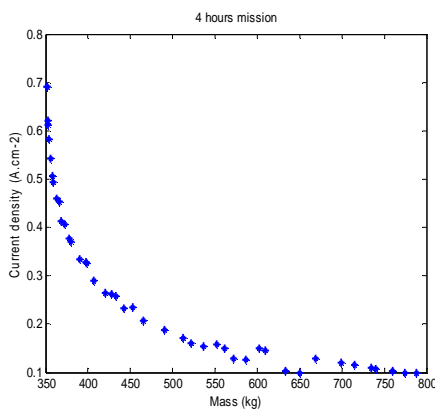


Figure IV. 48: FC current density vs system mass.

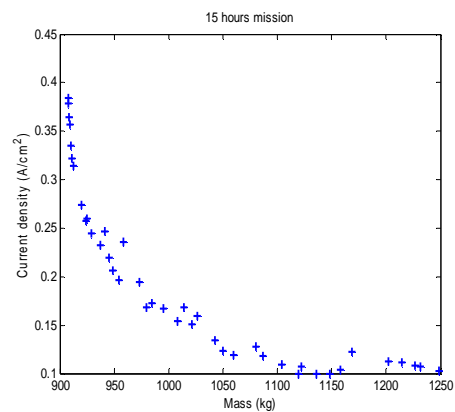
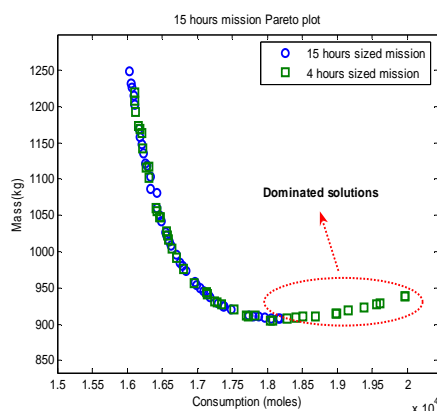


Figure IV. 49: FC current density vs system mass.

Figure IV. 48 and Figure IV. 49 give more useful information. Indeed, it is quite interesting to observe that, for the 15 hours mission, the maximal fuel cell current density is limited to less than 0.4A/cm<sup>2</sup>. This proves that in this case, it is more interesting to operate with low current densities in order to reduce losses and not to increase the amount of boarded hydrogen.

Moreover, we can wonder whether the system optimized for the 4 hours mission would be an optimized system if it is submitted to the 15 hours mission. Therefore, let us submit the solutions sized for the 4 hours mission to a load profile of 15 hours.



**Figure IV. 50: 15 hours mission. Behavior of the solutions optimized for the 4 hours mission.**

Figure IV. 50 present the distribution of the solutions in the mass- H<sub>2</sub>consumption plan for the two different sizings. In the case of the solutions optimized for the 15 hours mission, the plotted solutions form a Pareto plot because there are no dominated solutions. Nevertheless, in the other case, the green square solutions in the red circle are dominated. This means that these solutions present a worse mass- H<sub>2</sub> consumption ratio, and they do not belong to the Pareto front. It should be noticed that the dominated solutions operate at high fuel cell current densities (between 0.5 and 0.7 A/cm<sup>2</sup>). Thus, this explains why the solutions optimized for the 15 hours mission do not consider current densities over 0.4 A/cm<sup>2</sup>.

The two solutions sized in Table IV. 5 lead to the following global system mass and hydrogen consumption.

<b>15 hours mission</b>	
<b>system sized for 4 hours mission</b>	<b>system sized for 15 hours mission</b>
System mass = 939 kg	System mass = 904 kg
Consumption = 19843 moles	Consumption = 18177 moles

**Table IV. 6: System mass and hydrogen consumption results.**

Figure IV. 51 proposes the mass distribution for the two solutions sized in Table IV. 5 submitted to a 15 hours power profile. It can be observed that the 15-hours-sized fuel cell is heavier than the 4-hours-sized fuel cell. Nevertheless, the hydrogen mass is higher in the 4-hours-sized case and thus, the global mass is higher.

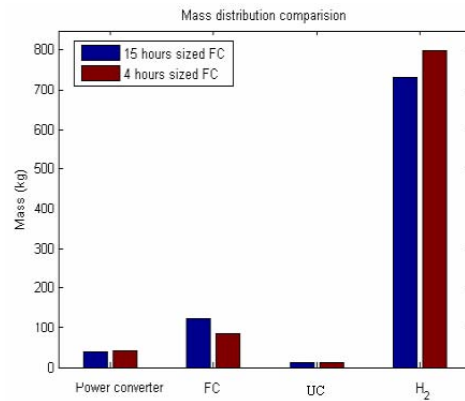


**Figure IV. 51: Mass distribution. (15 hours mission)**

This section shows the importance of the fuel cell operation point on the amount of boarded hydrogen in transport applications. Indeed, the fuel cell size (or in other words, the maximal fuel cell current density  $J_{max}$ ) is a compromise between the fuel cell mass and the gas consumption. Thus, **this proves that it is not always pertinent to size a fuel cell for a classical operation point of 0.7V and 0.6A/cm<sup>2</sup>.**

## IV.5 Evolution of ultracapacitor pack and fuel cell voltages along the Pareto plot

### IV.5.1 Evolution of the ultracapacitor pack voltage

In the first and second chapters, it was explained that, if the aim of the system designer is to reduce the ultracapacitor pack, the ultracapacitors should use the entire authorized discharge margin. Indeed, an ultracapacitor pack with low capacitance leads to a more lightweight system. This can be easily explained because the number of elementary cells that must be stacked in series or parallel is proportional to the pack capacitance. Therefore, it seems that, *a priori*, the system designer always should try to use the entire authorized discharge margin for the ultracapacitors.

The aim of this paragraph is to validate this tendency and verify the ultracapacitor pack voltage time evolution with all the Pareto front optimal solutions. Therefore, three Pareto plot solutions for the architecture with two parallel converters are further analyzed.

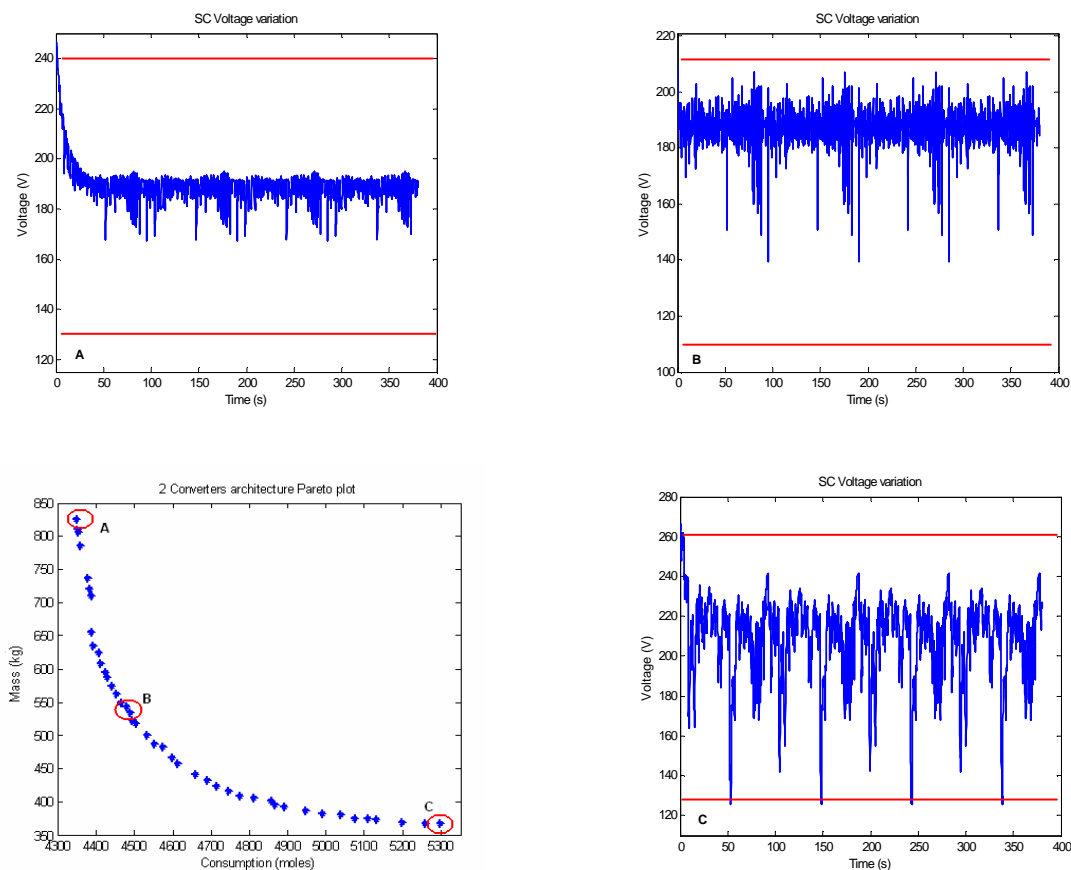


**Figure IV. 52: UC voltage time evolutions for three Pareto plot optimal solutions. (architecture with two parallel converters)**

As it can be observed in Figure IV. 52, the most lightweight solution (solution C) presents a really good use of the authorized voltage margins. The ultracapacitor pack voltage varies over almost all the authorized margin.

Nevertheless, solutions A and B offer a really bad use of the ultracapacitor discharge capacity. Indeed, in these cases, the ultracapacitor voltage time evolution is completely different from the solution C: the voltage does not use completely the authorized margins. That does not mean that the optimization process failed. The optimization algorithm chose large ultracapacitor packs in order to reduce losses. This illustrates that, in terms of efficiency and hydrogen consumption, there is no interest to use the entire authorized discharge margin.

### IV.5.2 Evolution of the fuel cell voltage

In a similar way as for the ultracapacitor pack, it is possible to analyze the fuel cell stack use. The same three optimized solutions are analyzed (Figure IV. 53).

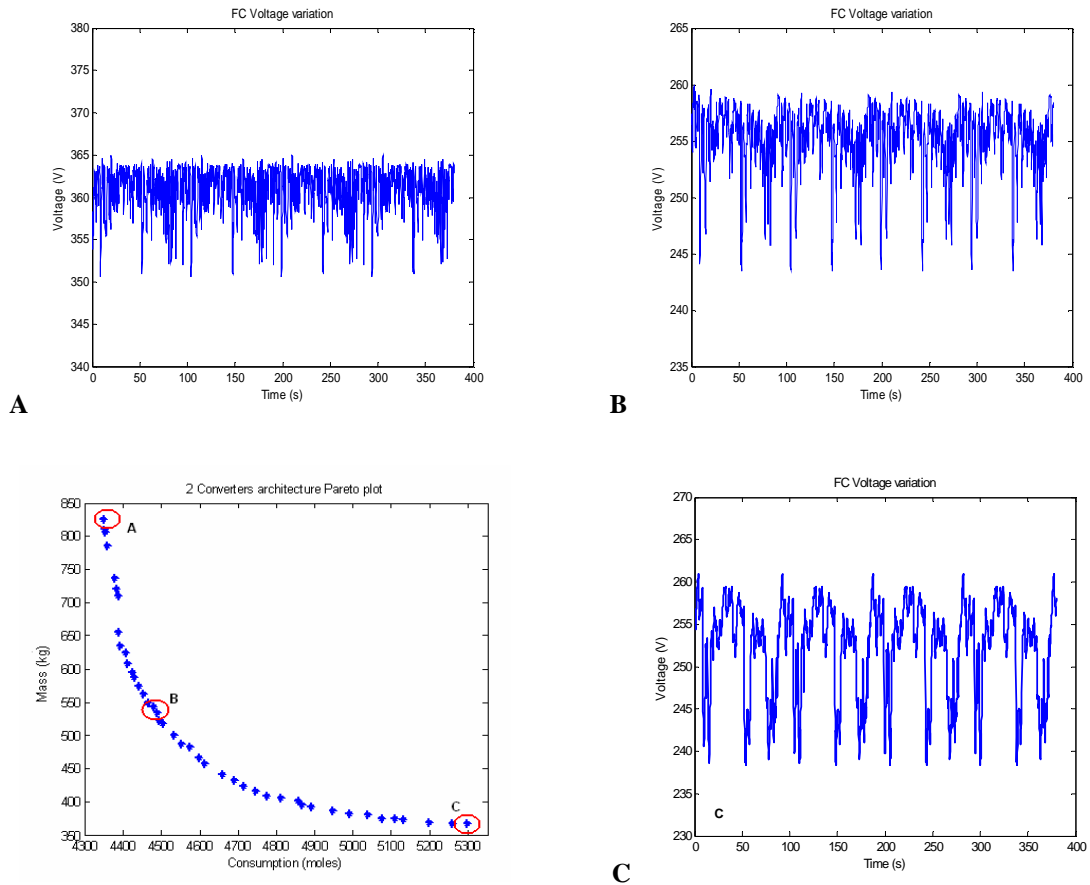


**Figure IV. 53: Fuel cell voltage time evolutions for three Pareto plot optimal solutions. (architecture with two parallel converters) .**

Similarly to the ultracapacitor case, with the most lightweight solutions, the fuel cell voltage presents a higher voltage variation. The solution C voltage varies of 20V during the mission. The solution B voltage variation is 15V, and finally the optimized solution in terms of hydrogen consumption presents a voltage variation of just 10V.

This fact can be easily explained because the optimized solutions in terms of hydrogen consumption are composed of large surface fuel cell stacks. Thus, and as it was explained in § I.4.1.6, large surface fuel cell stacks present smaller equivalent resistor, and therefore, their polarization curve (V (I) curve) is more similar to a perfect voltage source.

## IV.6 Comparison between air-pressurized and pure oxygen fuel cells

Unfortunately the CELINA consortium could not provide us precise data concerning pure oxygen and pure hydrogen fuel cells. Thus, the following assumptions were done:

- The auxiliaries consumption is estimated as 5 % of the fuel cell supplied power.
- No air compressor is boarded.
- The hydrogen and the oxygen bottles are boarded
- The fuel cell electrical performances are improved in 10 % compared to pure H<sub>2</sub> – Air fuel cells (see Figure IV. 54 and Figure IV. 55).

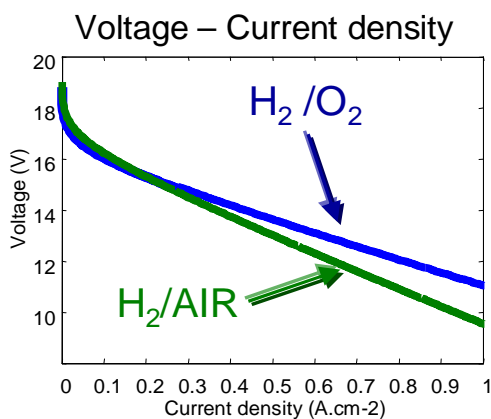


Figure IV. 54: Air – pure O<sub>2</sub> fuel cells comparison.

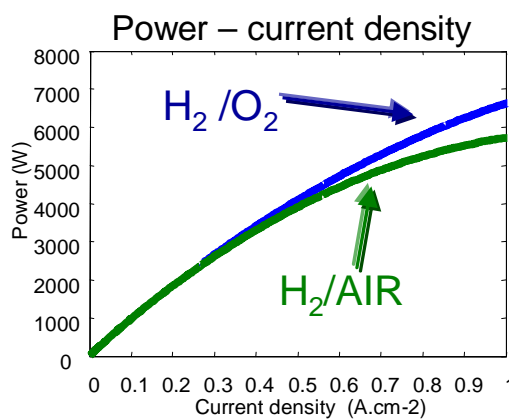


Figure IV. 55: Air – pure O<sub>2</sub> fuel cells comparison.

### IV.6.1 Oxygen bottle mass estimation

The oxygen bottles mass is estimated according to Air Liquide data. The retained reference bottle is bottle n° 829 from the SCI website [SCI]. The mass distribution of this bottle is:

- Bottle pressure : 234 bar
- Water volume : 31.14 l
- Cylinder mass: 15.65 kg
- Stored oxygen mass: 10.11 kg
- Other devices: 4 kg

$$\text{Mass ratio: } \frac{10.11}{10.11 + 15.65 + 4} = 0.34$$

### IV.6.2 Optimization results

Figure IV. 56 shows the Pareto plot of the retained architectures. In this case the architecture with the storage device connected to the DC bus seems once again to be the best option.

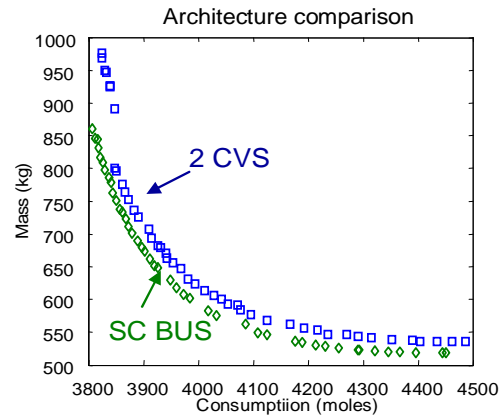


Figure IV. 56: Architectures Pareto plot.

Nevertheless, in this case the system mass is higher than 500 kg. This mass value is huge compared to the pure hydrogen – Air fuel cells (350 kg, see Figure IV. 10).

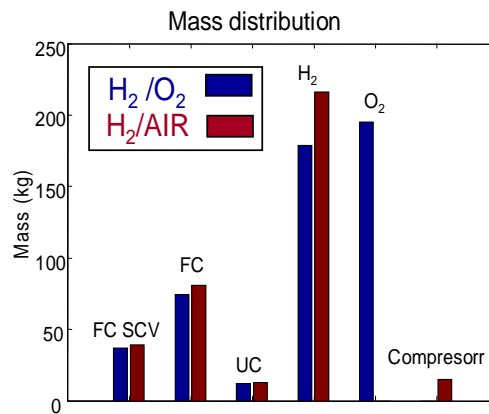


Figure IV. 57: Mass distribution comparison.

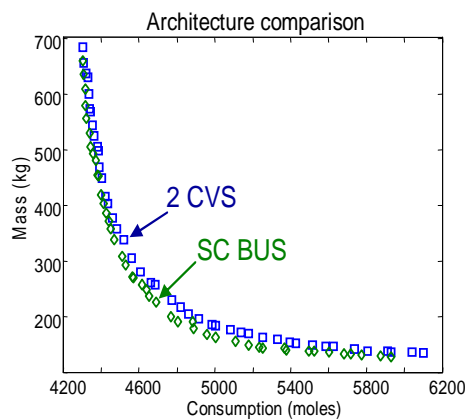
Figure IV. 57 presents the mass distribution of the most lightweight solutions in the pure oxygen and air cases. It can be observed that even if the fuel cell mass is reduced and the air compressor mass is saved, the global system mass is highly increased due to the boarded oxygen bottles. Thus, it can be concluded that **the pure hydrogen pure oxygen fuel cell technology is not competitive compared to the pure hydrogen – air fuel cell technology for this application.**



## IV.7 Comparison between pure hydrogen and reformat fuel cells.

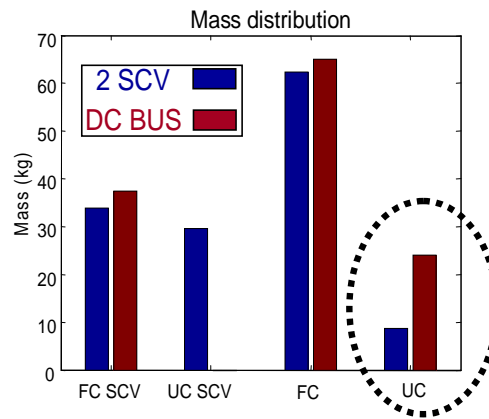
The main difference between the pure hydrogen and the reformat case is that the fuel cell system response is slower in the reformat case. This is due to higher response time of the kerosene reformer compared to the air compressor.

At this moment, we have no precise data concerning the response time of a kerosene reformer. Thus, in order to obtain some conclusions, we assumed that the kerosene reformer response time is around 25 seconds which can be judge too futurist. Nevertheless, this approach will permit us to obtain some conclusions thanks to the optimization tool. The air compressor response time was fixed to 1 second.



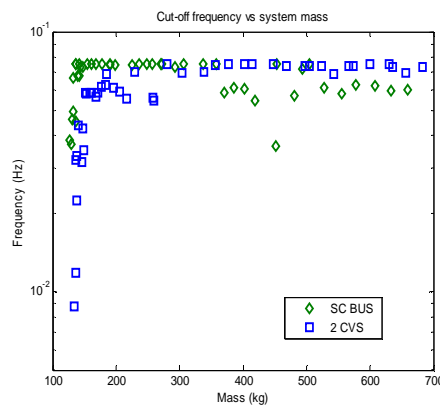
**Figure IV. 58: Architecture Pareto plot.**

Figure IV. 58 shows the Pareto plot of the storage device connected to the DC bus architecture and the Pareto plot of the two parallel power converter architecture. In this case, and comparing to Figure IV. 10, it is possible to observe that the two Pareto plot are more and less similar. In other words, in this case these two architectures seem to achieve the same mass-hydrogen consumption performances (Remark: in this optimization results the reformer mass was not considered).



**Figure IV. 59: Mass distribution comparison.**

Figure IV. 59 shows the mass distribution for both architectures. Comparing Figure IV. 59 mass distribution to the one obtained in the pure hydrogen case (Figure IV. 11), it is possible to observe that ultracapacitors mass has strongly increased. This can be easily explained because the storage device connected to the DC bus architecture does not optimize the ultracapacitor use, and this lead to heavier ultracapacitor banks. This statement can be proved looking to Figure IV. 60



**Figure IV. 60: Cut-off frequency evolution through the Pareto plot.**

According to these results, **the statement is that the storage device connected to the DC bus architecture declines its mass-consumption performances with the system response time. In other words, slower response time systems lead to higher mass-consumption ratios.**

**Finally, it is is not possible to compare the pure hydrogen and the reformat hydrogen case because at this step we do not know the kerosene reformer mass estimation.**

## IV.8 Conclusion of the chapter IV

In this chapter, a system optimization tool was developed. This tool can help the designer to choose among the proposed architectures if the choice is done ‘just’ considering the mass, volume and efficiency criteria.

As the optimization problem clearly is a multi-objective problem, we proposed to determinate the Pareto-optimal solutions. The Pareto plots moreover make it possible to obtain useful information about the design variables evolution.

For that purpose, the NSGA-II was used to perform multiple runs with the aim of obtaining Pareto-optimal results.

These results show that the architecture with the storage device directly connected to DC bus seems to be the best one in terms of mass and hydrogen consumption. This is due to the small size of the power converter. Indeed, this architecture presents just one power converter, and furthermore, this power converter handles only, roughly speaking, the mean load power.

The architecture with two parallel power converters seems to be the second choice. In this case two power converters are used. This is sure penalizing in terms of mass and hydrogen consumption. Nevertheless, the ultracapacitor power converter permits a deeper ultracapacitor discharge. Thus, this architecture presents the lowest storage device mass.

Finally, the architecture with a direct connection (hybridization) between the fuel cell and the storage device seems to be the worst alternative. Indeed, even if only one power converter is needed, the power converter mass is important because it should handle the whole load power (about 70kW). Furthermore, the main disadvantage of this architecture is the bad use of the ultracapacitors. Therefore, this architecture presents the highest storage device mass.

Nevertheless, even if the three architectures do not lead to the same global mass and hydrogen consumption, it is possible to obtain some common characteristics for the three architectures by looking at the design variables evolution along the Pareto plots. Indeed, the design variable evolution seems to be more or less the same for all the architectures. This gives interesting results, like the optimized cut-off frequency, the fuel cell minimal voltage value, the ultracapacitor technology, the power converter switching frequency...

A very interesting result is that the most lightweight systems do not operate with the maximal permitted fuel cell current density ( $0.8 \text{ A/cm}^2$ ). Indeed, even if the most lightweight fuel cells operate with high current densities, the optimization results show no solutions that operate with such high values. This is a consequence of the better conversion efficiency of fuel cells at low current densities, high current densities leading to important losses, and thus, higher hydrogen consumptions. Therefore,

the hydrogen mass rises, and thus, the global system mass become higher. It was illustrated with the comparison of the same architectures but sized for different mission durations. A longer mission leads to lower current densities in order to avoid an oversizing due to the hydrogen storage. The high current density solutions clearly become dominated by the lower current solutions.

As a final conclusion, it can be said that the optimization tool is very useful to help to make a choice between architectures. But it is not only a decision tool. The information provided by the optimization tool can be really useful to improve the knowledge and understanding of the global system behaviour.



# General conclusion and perspectives

This work deals with the conception of an electrical network based on a fuel cell stack and an associated storage device. Thanks to a “system approach”, the study of the possible electrical architectures, the global system sizing, the energy management, the DC-DC power converter design and the system optimization were achieved and explained along the pages of this report.

In the first chapter, the European Union hydrogen and fuel cell research axes were presented. These axes are: hydrogen production and distribution, hydrogen storage, fuel cell basic research, stationary and portable applications and transportation applications. The European project CELINA, framework of this PhD thesis, is in keeping with several of these axes. The aim of the CELINA project is indeed to study the potentialities of fuel cells in aeronautical applications, especially for the emergency electrical network.

“Generic sizing methods” for the fuel cell stack and the ultracapacitor pack were afterwards presented. They are called “generic sizing methods” because these methods do not take into account the system coupling. They can only be applied if the source is directly connected to a load, and if there is no other interaction with another source. Nevertheless, these methods are necessary to size the global system. Batteries were not considered in this PhD work, because internal Airbus studies proved that ultracapacitors are better adapted to the Airbus requirements of the emergency electrical network.

These sizing methods all operate starting from power profiles to satisfy. Starting from a given load power profile, several methods were proposed to share this load power profile between each electrical source of the system (fuel cell and ultracapacitor pack). The frequential power sharing method was selected for the project. It could nevertheless be interesting to evaluate the other proposed power sharing methods in future works.

The possible electrical architectures for the emergency electrical network were then developed along the second chapter. The aim was to reduce as much as possible the number of power converters due to mass and efficiency reasons, but always by respecting the electrical network requirements. After a preliminary study, three electrical architectures appeared as good candidates. These three architectures were: the *architecture with two parallel converters*, the *architecture with a direct connection between the fuel cell and the ultracapacitor pack* and finally the *architecture with the storage device directly connected to the DC bus*.

The *architecture with two parallel converters* presents two degrees of freedom that permit a good use of the ultracapacitor discharge capacity. Nevertheless, this architecture needs an extra energy

management loop in order to compensate for the system losses. Without this extra energy management loop, the storage device abnormally discharges by supplying the system losses and the system must be probably stopped. Two different energy management strategies can be adopted:

- The *storage device voltage reference method* can be applied to all the storage devices whose voltages are good images of their states of charge. This method consists in compensating indirectly the system losses by forcing a continuous recharge of the storage device thanks to a regulator (the storage device voltage must always tend towards its reference). The main advantage of this method is its simplicity. Nevertheless, tuning correctly the corrector parameters and the voltage reference is not easy.
- The *estimator method* consists in estimating the system losses starting from models. The difficulty is to have valid models especially for the storage device. The main disadvantage of this method is its complexity and the computation cost. This method has never been proposed before, and an experimental validation is recommended for future works.

The *architecture with a direct connection between the fuel cell and the ultracapacitor pack* is an original architecture that can self-manage the energy exchanges within the system. In other words, there is no need to implement an energy management control loop. Nevertheless, not all the desired power sharing between the fuel cell and the ultracapacitor pack can be achieved. The filtering of the load power achieved by this direct association is indeed equivalent to the filtering of a first order low-pass filter. In this architecture, the different losses within the system do not act similarly. Indeed, the power converter losses can be considered as an extra load, and they can be added to the mission load power profile. In the other hand, the ultracapacitor internal losses can be seen as a source of harmonic perturbation. The fuel cell cannot be completely protected against the fast current steps in this association. This effect can be limited if the equivalent resistor of the ultracapacitor pack is much smaller than the equivalent resistor of the fuel cell.

The *architecture with the storage device directly connected to the DC bus* presents similarities with the *architecture with two parallel converters*. This architecture also needs an energy management loop that avoids the fully discharge of the ultracapacitor pack. Furthermore, this architecture presents the disadvantage that the DC bus voltage cannot be controlled. Indeed, a voltage variation margin must be allowed in order to make it possible the charge and discharge of the ultracapacitor pack. In the other hand, this architecture presents just one converter that must handle only with the mean load power. Thus, it is expected to obtain good efficiencies and lightweight systems.

There is one point common to all the architectures. If the generic sizing methods are directly applied to size the electrical devices, the system will not respect the sizing criteria. The reasons are that the initial power sharing did not take into account the system couplings, the system losses, the

energy management loops...Thus, an iterative sizing method, identical for all the architectures, was proposed.

The third chapter presented the conception and the design of the different DC-DC power converters that must be implemented in the proposed electrical architectures. The Airbus requirements impose a  $\pm 270\text{V}$  electrical network. Furthermore, the system energy source is limited to just one fuel cell stack. In all cases, the negative pole of the fuel cell stack must be connected to the aircraft ground. This last requirement was essential to select solutions. Two solutions were proposed:

- Classical insulated power converters based on the push-pull topology and implementing high frequency transformers.
- Original parallel associations of elementary non-insulated DC-DC power converters. The principle consists in associating a DC-DC power converter (Boost or Buck or non-reverser Buck-Boost depending on the voltage of the input source) that creates the  $+270\text{V}$  DC pole with a Buck-Boost power converter that creates the  $-270\text{V}$  pole.

Only the second solution was studied in this report, the first one being evaluated by another partner (THALES AES) involved in the CELINA project. The three possible combinations for this second solution were deeply analysed in terms of design and performances.

Due to the considered high powers, each DC-DC power converter has to be concretely composed of several branches connected in parallel and interleaved in order to obtain satisfactory efficiencies and masses. The first idea is rather to split the required power through several parallelized “little” power converters with high efficiencies than to handle it with one “big” power converter with a low efficiency. The second idea is to take advantage of this parallelization of branches to reduce the masses of components thanks to the interleaving technique. Indeed, the interleaving technique makes it possible to release the constraint in terms of ripple current for each parallelized branch while guarantying the required current ripple in the input source (especially for the fuel cell). This technique indeed offers an active filtering for the input current which is the sum of the currents of all the parallelized branches. The current ripple being reduced in each branch, the branch inductance can be strongly reduced and consequently the mass of the power converter.

Nevertheless, this strategy of parallelization can easily lead to an operation in discontinuous conduction mode. Indeed, if the inductance is reduced, the area of operation in discontinuous conduction mode will be large and can be reached easily if the load power decreases. In this case, the control of the power converter can become a complex issue. To remove this drawback, an original control strategy for interleaved power converters was proposed: the *branch switching-off technique*. The principle of this technique is to avoid having conditions that lead to an operation in the



discontinuous conduction mode. So, one branch is switched off each time the load power decreases and leads the power converter into the area of the discontinuous conduction mode. The same amount of power is then shared by a reduced number of branches rejecting the limit of operation in continuous conduction mode for the remaining branches. Even if the simulation results did not raise any problem, an experimental validation is recommended for future works.

The principles of operation for the power converters being developed, a deep study of the proposed non-insulated power converters was achieved in terms of efficiency and mass. It was proved that the *branch switching-off technique* improves the power converter efficiency. Nevertheless, the proposed power converters do not present an excellent mass-efficiency ratio. This is mainly due to the bad mass-efficiency ratio of the “Buck-Boost part” involved in the proposed association.

The fourth and last chapter dealt with the global system optimization. As transportation applications are aimed in the CELINA project, the mass, volume and efficiency become crucial sizing objectives.

Different solutions were previously considered for the electrical architectures, the power converters and the energy management strategies. The aim of this global system optimization clearly is to compare and classify all the possibilities in order to choose the best one in terms of mass and efficiency. All the previously developed models to calculate the different masses and efficiencies for the fuel cell, the ultracapacitors and the power converters were naturally used.

The system being complex (a lot of continuous and discrete variables and multiple objectives), the use of advanced optimization techniques was decided. So a genetic algorithm was implemented.

More or less outstanding results were achieved by the optimizer.

The *architecture with the storage device directly connected to the DC bus* appears to be the best architecture in terms of mass and efficiency. This architecture presents a lightweight power converter which only handles the mean load power.

The *architecture with two parallel converters* seems the second best option. If this architecture logically leads to the most lightweight ultracapacitor pack, the implementation of two parallel power converters is prejudicial for the global system mass.

Finally, the *architecture with a direct connection between the fuel cell and the ultracapacitor pack* does not seem to be a good option in this study. A heavy power converter that must handle the whole load power and a bad use of the ultracapacitor pack make this architecture not adapted compared to the others.

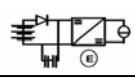






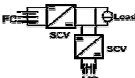






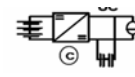






As widely illustrated along the chapter, the optimization tool appears to be not only a decision tool, but also a tool for understanding and analysis. Here are some main lessons drawn from the optimization results.

. First interesting results are the quantified tendencies for the numerous system parameters difficult to fix *a priori*: the optimal power sharing cut-off frequency, the optimal minimal fuel cell voltage, the optimal technology for the ultracapacitor pack, the optimal switching frequency for power converter...

Even if the three architectures do not lead to the same global mass and hydrogen consumption, the evolution of the design variables along the Pareto front seems to be more or less the same for all the architectures. Some particularities exist but the tendencies are similar.

One of the most surprising results is that the most lightweight systems do not operate with the maximal current density permitted for the fuel cell (0.8 A/cm<sup>2</sup> in our case). Indeed, for a given power, a fuel cell operating at 0.8 A/cm<sup>2</sup> is for sure the most lightweight possible fuel cell stack. This optimization result can be explained because high current densities lead to high losses, and thus, to high hydrogen consumptions increasing the global system mass. In order to prove this hypothesis, the same architecture was sized for two mission durations. The longer mission leads to fuel cells operating with lower current densities in order to avoid an overweight due to the hydrogen storage. Both differently sized solutions were furthermore simulated for an identical long mission. Clearly, in this case, the solutions with fuel cells operating with low current densities (but with better efficiencies) are better than the ones operating with high current densities.

Nevertheless, the final choice is not only based on mass-consumption criteria. The next table summarizes the main advantages and the main drawbacks of each architecture.

		Mass-consumption	DC bus control	UC use	Power electronics	Filtering capacity	Reliability
	CD						
	2 CVS						
	SC BUS						

As perspectives for this work, a robustness study of the optimization tool is highly desired. Indeed, the system sizing is based on the mission power profile, and therefore, the impact of perturbation on the power profile should be studied. Furthermore, the robustness of the model face to modelling errors should also be evaluated and the auxiliaries and kerosene reformer models should be integrated in the global model

The next step for future projects should be the experimental validation of the proposed system. The experimental prototype will allow to validate the proposed power converters and the proposed energy management strategies.

Finally a mass estimation of the kerosene reformer seems mandatory in order to compare and choose between the pure hydrogen and reformat hydrogen cases.

# Bibliography

- [Abdelli] A. Abdelli, “*Optimisation multicritère d’une chaîne éolienne passive*”, thèse INP Toulouse, 2007.
- [Abdelli2] A. Abdelli, B. Sareni, X. Roboam “*Optimization of a Small Passive Wind Turbine Generator with Multiobjective Genetic Algorithms*” OIPE 2006.
- [Air Liquide] Air Liquide, “*Identification of the optimum on-board storage pressure for gaseous hydrogen city buses*”, European integrated hydrogen project EIHP2 Report, March 2004.
- [Astier] S. Astier, “*Des machines à aimants permanents aux systèmes énergétiques autonomes. Systémique, électricité et développement durable*”, HDR INP-ENSEEIH, 2003.
- [Babu] C. S. Babu, M. Veerachary, “*Predictive controller for interleaved boost*” converter Industrial Electronics, 2005. ISIE 2005. Proceedings of the IEEE International Symposium on Volume 2, 20-23 June 2005 Page(s):577 – 581 vol. 2
- [Ballard] <http://www.ballard.com/>
- [Barrade] P. Barrade, A. Rufer, “*Current capability and power density of supercapacitors: considerations on energy efficiency*”, EPE 2003: European Conference on Power Electronics and Applications, 2-4 September, Toulouse, France.
- [Barrade2] P. Barrade, D. Hotellier, A. Rufer, “*Apport des Supercondensateurs dans le transport terrestre : une meilleure gestion de l’énergie*”, Colloque Transport Terrestre Électrique, 25 April, Belfort, France.
- [Belachemi] F. Belachemi, “*Modélisation et caractérisation des supercondensateurs à couche double électrique utilisés en électronique de puissance*”, Thèse Institut National Polytechnique de Lorraine, 2001.
- [Bianchi] N. Bianchi, F. Dughiero, “*Optimal design techniques applied to transverse flux induction heating systems*”, IEEE Trans. On Mag., vol. 31, n°3, p. 1992-1995,

May 1995.

- [Bilanovic]** F. Bilanovic, O. Music and A. Sabanovic, “*Buck converter regulator operating in sliding mode*”, Proceedings of 1983 PCI, pp. 331-340
- [Brett]** A. M. Brett, “*Interleaved conversion techniques for high density power supplies*”, Massachusetts Institute of Technology, May 1992.
- [Büchi]** F.N. Büchi, A. Delfino, P. Dietrich, S.A. Freunberger, R. Kötz, et al. “*Electrical Drivetrain Concept with Fuel Cell System and Supercapacitor Results of the “HY-LIGHT®”-vehicle*”. VDI Tagung Innovative Fahrzeugantriebe, Nov. 9./10. 2006, Dresden,
- [Burke]** K. A. Burke, “*High energy density regenerative fuel cell systems for terrestrial applications*”, in Aerospace and Electronic Systems Magazine, IEEE Publication Date: Dec 1999
- [Calderon]** G. Calderon-Lopez, A. J. Forsyth, D. R. Nuttall, “*Design and Performance Evaluation of a 10-kW Interleaved Boost Converter for a Fuel Cell Electric Vehicle*” Power Electronics and Motion Control Conference, 2006. IPEMC '06. CES/IEEE 5<sup>th</sup> International Volume 2, 14-16 Aug. 2006 Page(s):1 – 5
- [Candusso]** D. Candusso, “*Hybridatioin du groupe électrogène à pile à combustible pour l'alimentation d'un vehicule électrique*”, Thèse INP Grenoble, LEG, 2002.
- [Chang]** C. Chang, M. A. Knights, “*Interleaving technique in distributed power conversion systems*”, IEEE Transactions on Circuits and Systems I, vol 42, No 5, May 1995, pp. 245-251
- [Chapoulie]** P. Chapoulie, S. Astier, “*Modelling of an electric vehicle including ultracapacitors with SABER*”, conference EVS'98, Bruxelles, Belgium, September 1998.
- [Christen]** T. Christen, M. W. Carlen, “*Theory of Ragone plots*”, Journal of power sources 91, 2001.
- [Colson]** J. F. Colson, “*Modélisation de l'état de charge des batteries de véhicules électriques*”, Travail fin d'étude, univerité de Liège, Faculté des Sciences Appliquées, 1998.

- [Costan]** V. Costan “*Convertisseurs parallèles entrelacés : étude des pertes fer dans le transformateur inter-cellules*”, thèse INP Toulouse, 2007.
- [Dang Bang]** V. Dang Bang “*Conception d’une interface d’électronique de puissance pour la Pile à combustible*”, Thèse de doctorat, 2007, UJF.
- [Davies]** D. P. Davies, P. L. Adcock, “*Lightweight, high power density fuel cell stack*”, DTI sustainable energy programmes contract rapport. Advances power sources Ltd, 2002.
- [Dagget]** D. L. Daggett, S. Eelman, “*Fuel cell for commercial aircraft*”, AIAA/ICAS International Air and Space Symposium and Exposition: The Next 100 Year, 14-17 July 2003, Dayton, Ohio
- [Destraz]** B. Destraz, P. Barrade, A. Rufer, “*A new interleaved multi-channel DC/DC converter specially dedicated to low voltage, high current applications*”, PCIM 2006 : International Conference on Power Electronics, Intelligent Motion and Power Quality, 30 May-1 June, Nuremberg, Germany.
- [Destraz2]** B. Destraz, P. Barrade, A. Rufer, “*A new solution for increasing the efficiency of an electric scooter with supercapacitors through a novel, interleaved multi-channel DC/DC converter*”, EM 05 : 6th International Symposium on Advanced Electromechanical Motion Systems, 27-28 September, Lausanne, Switzerland.
- [Dicks]** Dicks A., Larminie J., “*Fuel Cell Systems Explained*” , Wiley International Edition, 2000
- [Do]** D. V. Do, C. Forguez, G. Friedrich, “*Observateur d’état de charge de batterie NIMH*”, Conférence EF 2007, ENSEEIHT, Toulouse 5-6 Septembre 2007
- [DOW]** CELINA, “*Description Of Work*”, CELINA Project. Confidential document.
- [Drolia]** A. Drolia, P. Jose, N Mohan, “*An approach to connect ultracapacitor to fuel cell powered electric vehicle and emulating fuel cell electrical characteristic using switched mode converter*”, in Industrial Electronics Society, IECON '03, vol 1 pp 897-901, 2003.

- [EU] European Union, Directorate-General for Research Sustainable Energy systems, “*European Fuel Cell and Hydrogen Projects*”, in [http://ec.europa.eu/research/energy/pdf/hydrogen\\_synopses\\_en.pdf](http://ec.europa.eu/research/energy/pdf/hydrogen_synopses_en.pdf)
- [EMOO] the Evolutionary MultiObjective Optimization (EMOO) website <http://www.lania.mx/~ccoello/EMOO/>
- [EERE] US Department of Energy. Energy Efficiency and Renewable Energy (EERE) <http://www.eere.energy.gov/>
- [Ferrieux] J. P. Ferrieux, F. Forest, “*Alimentation à découpage, Convertisseur à résonance*”, 3<sup>ème</sup> édition, Dunond, 1999.
- [Flumian] D. Flumian, “*Création d’un réseau alternatif local à partir d’une pile à combustible associée à un onduleur survolteur*”, thèse CNAM, Avril 2003.
- [Friend] M. Friend, D. Daggett, “*Fuel cell demonstrator airplane*”, AIAA/ICAS International Air and Space Symposium and Exposition: The Next 100 Year, 14-17 July 2003, Dayton, Ohio
- [García] M. García Arregui, C. Turpin, S. Astier, “*Direct connection between a fuel cell and ultracapacitors*”, Clean Electrical Power Conference, Capri, May 2007.
- [García2] M. García Arregui, C. Turpin, S. Astier, “*Groupe électrogène pour aéronef à pile à combustible hybridée par supercondensateurs*”, Conférence EF 2007, ENSEEIHT, Toulouse 5-6 Septembre 2007
- [Giral] R. Giral Castellón, “*Síntesis de estructuras multiplicadoras de tensión basadas en células convertidoras continua-continua de tipo conmutado*”. Tesis de la Universitat Politècnica de Catalunya, 2005.
- [Giral2] R. Giral, L. Martínez-Salamero, R. Leyva, Y. Maixé, “*Sliding-Mode Control of Interleaved Boost Converters*”, in IEEE Transactions on Circuits and Systems, Vol 47, No 9, September 2000
- [Hooke] R. Hooke, T. A. Jeeves, “*Direct search solution of numerical and statistical problems*”, 1961, JACM 8, 212-229.
- [Hydrogenics] <http://hydrogenics.com/>

- [Kim] Kim et al. , “*Modelling of PEMFC performance with an empirical equation*”, Journal of the Electrochemical Society 142 (1995) 2670
- [Kone] A.D. Kone, “*Contribution à la conception des actionneurs électriques par formulation en terme d’optimisation* ”, Thèse de doctorat, 1993, INPT
- [Lachaize] J. Lachaize, “*Etude des stratégies et des structures de commande pour le pilotage des systèmes énergétiques à pile à combustible destinés à la traction*”, Thèse INP Toulouse, 2004.
- [Lai] J.-S Lai,. “*A high-performance V6 converter for fuel cell power conditioning system*”, Vehicle Power and Propulsion, 2005 IEEE Conference 7-9 Sept. 2005 Page(s):7 pp.
- [Langlois] O. Langlois, “*Conception d’un réseau de secours électrique pour l’aéronautique*”, Thèse de l’INP Toulouse, juin 2006
- [Langlois2] O. Langlois, E. Foch, X. Roboam, H. Piquet, “*De l’avion plus électrique à l’avion tout électrique : état de l’art et prospective sur les réseaux de bord* ”, Journées 2004 de la section électrotechnique du club EEA, 10-11 Mars, Cergy-Pontoise.
- [Lee] P. W. Lee, Y. Lee, D. K. W. Cheng, X. Liu, “*Steady-State Analysis of an Interleaved Boost Converter with Coupled Inductors*”, in IEEE Transactions on Industrial Electronics, Vol 47, No. 4, August 2000.
- [Lefevre] G. Lefevre, “*Conception de convertisseurs statiques pour l’utilisation de la pile à combustible* ”, Thèse de doctorat, 2004, UJF.
- [Li] W. Li, X. He, “*ZVT interleaved boost converters for high-efficiency, high step-up DC-DC conversion Electric Power Applications*”, IET Volume 1, Issue 2, March 2007 Page(s):284 - 290
- [Magnetics] <http://www.mag-inc.com/>
- [Markel] T. Markel, A. Pesaran, M. Zolot, S. Sprik, H. Tatara, T. Duong, “*Energy Storage Fuel Cell Vehicle analysis*”, in EVS 21 Monaco, 2 -6 april 2005.
- [Maxwell] <http://www.maxwell.com/>



- [Nergard]** T. A. Nergaard, J. F. Ferrell, L. G. Leslie, and J.-S. Lai, “*Design considerations for a 48v fuel cell to split phase inverter system with ultracapacitor storage*”, in Proceedings of Power Electronics Specialists Conference’, vol. 4, pp. 2007-2012, 2002.
- [Olm]** J. M. Olm, “*Asymptotic tracking with DC-to-DC bilinear power converters*”, Tesi doctoral Universitat Politècnica de Catalunya, 2003.
- [Pareto]** V. Pareto, “*Cours d'Economie Politique*”, Rouge, Lausanne, Suisse, 1896.
- [Papoulis]** A Papoulis, S. Unnikrishna Pillai, “*Probably, Random variables and stochastic processes*”, 4th ed., McGraw-Hill, New york, NY.
- [Powell]** M. J. D. Powell, “*An iterative method for finding stationary values of a function of several variables*”, 1962, Comp. J. 5, 147-151.
- [Raël]** S. Raël, “*Composant nouveaux pour le stockage et la génération d'énergie électrique : modélisation électrique, caractérisation, et mise en œuvre*”, HDR INP Lorraine, 2005
- [Raissi]** T. Raissi, “*Current technology of fuel cell systems*”, Energy Conversion Engineering Conference, 1997. IECEC-97. Proceedings of the 32ndIntersociety Volume 3, 27 July-1 Aug. 1997 Page(s):1953 - 1957 vol.3
- [Ralliers]** O. Ralliers, “*Dimensionnement et évaluation énergétique de convertisseurs dérivés du Boost pour la conversion très basse tension fort courant*”, thèse CNAM, Juillet, 2005.
- [Rao]** S.S. Rao, “*Engineering Optimization – Theory and practice*”, WileyInterscience Publication (3rd edition), New York, 1996
- [Ren]** .Yuan Ren; Guang-Yi Cao; Xin-Jian Zhu; “*Predictive control of proton exchange membrane fuel cell (PEMFC) based on support vector regression machine*”, in Machine Learning and Cybernetics, 2005. Proceedings of 2005 International Conference on Volume 7, 18-21 Aug. 2005 Page(s):4028 - 4031 Vol. 7
- [Regnier]** J. Regnier, “*Conception des systèmes hétérogènes en génie électrique par*

*optimisation évolutionnaire multicritères*”, thèse INP Toulouse, 2003.

- [Roasto]** I. Roasto, T. Lehtla, T. Moller, A. Rosin, “*Control of Ultracapacitors Energy Exchange*” 12th International Power Electronics and Motion Control Conference Aug. 2006 Page(s):1401 – 1406.
- [Rosenbrock]** H. H. Rosenbrock, “*An automatic method for finding the greatest or least value of a function*”, 1960 Comp. J. 3, 175-184.
- [Rufer]** A. Rufer, P. Barrade, D. Hotellier, “*Power-Electronic Interface for a Supercapacitor-Based Energy-Storage Substation in DC-Transportation Networks*”, EPE Journal, Volume: 14, No: 4, November 2004, Pages: 43-49.
- [Santi]** E. Santi, D. Franzoni, A. Monti, D. Patterson, F. Ponci and N. Barry, *A Fuel cell based domestic uninterruptible power supply*, in Proceedings of Applied Power Electronics Conference and Exposition, vol. 1, pp 605-613, 2002.
- [Saïssset]** R. Saïssset, C. Turpin, S. Astier, J.M. Blaquiere, “*Electricity Generation Starting From A Fuel Cell Hybridised With A Storage Device*”, IEEE VPP04, Paris, October 2004.
- [Sanchis]** P. Sanchis; “*Sistemas de conversión para energía solar fotovoltaica: topologías, técnicas de control e interacción con la red eléctrica*” Tesis Universidad Pública de Navarra, 2002.
- [Sanchis2]** P. Sanchis, A. Ursua, E. Gubia and L. Marroyo, “*Boost DC–AC Inverter: A New Control Strategy*”, IEEE transactions on power electronics, Vol 20, No 2, March 2005
- [Sareni]** B. Sareni, J Regnier, X Roboam, “*Integrated Optimal Design of Heterogeneous Electrical Energetic Systems using Multiobjective Genetic Algorithms*”, IREE, Oct 2001.
- [Sareni2]** B. Sareni, “*Conception simultanée par Optimisation des Systèmes D’énergie Electrique* ” HDR INP Toulouse, 2006
- [Schenck]** M. Schenck, K. Stanton, and J. S. Lai, “*Fuel Cell and Power Conditioning*

*System Interactions*,” Proc. of IEEE Applied Power Electronics Conference, Austin, TX, March 2005, pp. 114 – 120.

- [SCI] [http://www.scicomposites.com/aviation\\_cylinders.html](http://www.scicomposites.com/aviation_cylinders.html)
- [Siegneurbieux] J. Siegneurbieux, Y. Thiaux, B. Multon, B. A. Hamid, “*Optimisation sur cycle de vie de systèmes photovoltaïques autonomes. Influence des profils de consommation*”, Conférence EF 2007, ENSEEIHT, Toulouse 5-6 Septembre 2007
- [Sickel] Sickel, R.; Vettors, D.; Mehlich, H.; Bodach, M.; Bocklisch, T.; Lutz, J.; “*Modular converter for fuel cell systems with buffer storage*” Power Electronics and Applications, 2005 European Conference on 11-14 Sept. 2005 Page(s):9 pp.
- [Shoyama] Shoyama, M.; Harada, K, “*Zero-voltage-switched push-pull DC-DC converter*” Power Electronics Specialists Conference, 1991. PESC '91 Record., 22nd Annual IEEE 24-27 June 1991 Page(s):223 – 229
- [Turpin] C. Turpin, “*Développement, caractérisation des pertes et amélioration de la sûreté de fonctionnement d’un onduleur multicellulaire à commutation douce (ARCP)*”, Thèse INP Toulouse, 2001.
- [Wang] Jin Wang; Peng, F.Z.; Anderson, J.; Joseph, A.; Buffenbarger, R.; “*Low cost fuel cell converter system for residential power generation*”, in Power Electronics, IEEE Transactions on Volume 19, Issue 5, Sept. 2004 Page(s):1315 - 1322
- [Wei] H. Wei, A. Ionovici, D. Sutanto “*A simple zero-voltage-switching boost converter*” in Southeastcon '98. Proceedings. IEEE 24-26 April 1998
- [Wetzel] Wetzel, H.; Frohleke, N.; Bocker, J.; Ide, P.; Kunze, J.,” *Fuel cell inverter system with integrated auxiliary supply*”, in Power Electronics and Applications, 2005 European Conference on 11-14 Sept. 2005 Page(s):10 pp.
- [Wurtz] F. Wurtz, “*Une nouvelle approche pour la conception sous contraintes de machines électriques*”, Thèse de doctorat, mai 1996, INPG.
- [Yao] G. Yao, A. Chen, X. He, “*Soft Switching Circuit for Interleaved Boost*

*Converters*” Power Electronics, IEEE Transactions on Volume 22, Issue 1, Jan. 2007 Page(s):80 – 86

- [Zubieta]** L. Zubieta, R. Bonert, “*Characterization of double-layer capacitors for power electronics applications*”, IEEE january/february 2000, Transactions on industry applications, vol. 36.
- [Zugasti]** H. Zugassti, “*Hybridation directe d’une pile à combustible et d’une batterie d’accumulateurs*”, Rapport de stage de Master Recherche, Collaboration LAPLACE/HELION, Septembre 2007.



## **Appendix**

---



# Appendix I: Classical power converters sizing.

## Boost

Transfer Function	
Transfer Function (continuous mode)	$\frac{V_o}{V_i} = \frac{1}{1-\alpha}$
Transfer Function (discontinuous mode)	$\frac{V_o}{V_i} = 1 + \frac{\alpha^2 V_e}{2L f_s I_s}$
Inductor	
Current ripple	$\Delta I_L = \frac{\alpha V_i}{L f_s}$
Inductor value ( $\alpha \rightarrow 1$ )	$L = \frac{\alpha V_i}{\Delta I_{L \max} f_s}$
Maximal inductor voltage value ( $\alpha \rightarrow 1$ )	$V_{L \max} =  V_i - V_o $
Rms inductor current value	$I_{L \text{ rms}} = \sqrt{I_o^2 + \frac{\Delta I_{\max}^2}{12}}$
Capacitor	
Voltage ripple	$\Delta V_{C \max} = \frac{\alpha V_i}{(1-\alpha) R C f_s}$
Capacitor value	$C = \frac{\alpha V_i}{(1-\alpha) R \Delta V_{C \max} f_s}$
Maximal capacitor voltage value ( $\alpha \rightarrow 1$ )	$V_C = V_o$
Rms capacitor current value	$I_{C \text{ rms}} = I_o \sqrt{\frac{\alpha}{1-\alpha}}$
Switch	
Switch maximal voltage	$V_{T \max} = V_o$
Switch maximal current	$I_{T \max} = I_i + \frac{\Delta I_{\max}}{2}$
Mean current	$\langle I_T \rangle = \alpha I_i$
Rms current	$I_{T \text{ rms}} = \sqrt{\alpha I_i^2 + \frac{\Delta I_{\max}^2}{12}}$
Diode	
Diode maximal voltage	$V_{D \max} = V_o$
Diode maximal current	$I_{D \max} = I_i + \frac{\Delta I_{\max}}{2}$
Mean current	$\langle I_D \rangle = (1-\alpha) I_o$
Rms current	$I_{D \text{ rms}} = \sqrt{(1-\alpha) I_i^2 + \frac{\Delta I_{\max}^2}{12}}$



## Buck

Transfer Function	
Transfer Function (continuous mode)	$\frac{V_o}{V_i} = \alpha$
Transfer Function (discontinuous mode)	$\frac{V_o}{V_i} = \frac{1}{1 + \frac{2Lf_s I_o}{\alpha^2 V_e}}$
Inductor	
Maximal current ripple	$\Delta I_{L \max} = \frac{V_i}{4Lf_s}$
Inductor value	$L = \frac{V_i}{4\Delta I_{L \max} f_s}$
Maximal inductor voltage value ( $\alpha \rightarrow 1$ )	$V_{L \max} =  V_i - V_o $
Rms inductor current value	$I_{L \text{ rms}} = \sqrt{I_o^2 + \frac{\Delta I_{\max}^2}{12}}$
Capacitor	
Maximal voltage ripple	$\Delta V_{C \max} = \frac{V_i}{32LCf_s}$
Capacitor value	$C = \frac{V_i}{32L\Delta V_{C \max} f_s}$
Maximal capacitor voltage value ( $\alpha \rightarrow 1$ )	$V_C = V_o$
Rms capacitor current value	$I_{C \text{ rms}} = I_o \sqrt{\frac{\alpha}{1-\alpha}}$
Switch	
Switch maximal voltage	$V_{T \max} = V_i$
Switch maximal current	$I_{T \max} = I_o + \frac{\Delta I_{\max}}{2}$
Mean current	$\langle I_T \rangle = \alpha I_o$
Rms current	$I_{T \text{ rms}} = \sqrt{\alpha I_o^2 + \frac{\Delta I_{\max}^2}{12}}$
Diode	
Diode maximal voltage	$V_{D \max} = V_i$
Diode maximal current	$I_{D \max} = I_o + \frac{\Delta I_{\max}}{2}$
Mean current	$\langle I_D \rangle = (1-\alpha)I_o$
Rms current	$I_{D \text{ rms}} = \sqrt{(1-\alpha)I_o^2 + \frac{\Delta I_{\max}^2}{12}}$

## Buck-Boost

Transfer Function	
Transfer Function (continuous mode)	$\frac{V_o}{V_i} = \frac{\alpha}{1-\alpha}$
Transfer Function (discontinuous mode)	$\frac{V_o}{V_i} = \frac{\alpha^2 V_i}{2L f_s I_o}$
Inductor	
Current ripple ( $\alpha \rightarrow 1$ )	$\Delta I_L = \frac{\alpha V_i}{L f_s}$
Inductor value ( $\alpha \rightarrow 1$ )	$L = \frac{\alpha V_i}{\Delta I_{L \max} f_s}$
Maximal inductor voltage value ( $\alpha \rightarrow 1$ )	$V_{L \max} = \max(V_i, V_o)$
Rms inductor current value	$I_{L \text{ rms}} = \sqrt{I_L^2 + \frac{\Delta I_{\max}^2}{12}}$
Capacitor	
Voltage ripple ( $\alpha \rightarrow 1$ )	$\Delta V_{C \max} = \frac{\alpha^2 V_i}{(1-\alpha) R C f_s}$
Capacitor value ( $\alpha \rightarrow 1$ )	$C = \frac{\alpha^2 V_i}{(1-\alpha) R \Delta V_{C \max} f_s}$
Maximal capacitor voltage value ( $\alpha \rightarrow 1$ )	$V_C = V_o$
Rms capacitor current value	$I_{C \text{ rms}} = I_o \sqrt{\frac{\alpha}{1-\alpha}}$
Switch	
Switch maximal voltage	$V_{T \max} = V_i$
Switch maximal current	$I_{T \max} = I_L + \frac{\Delta I_{\max}}{2}$
Mean current	$\langle I_T \rangle = \alpha I_L$
Rms current	$I_{T \text{ rms}} = \sqrt{\alpha I_L^2 + \frac{\Delta I_{\max}^2}{12}}$
Diode	
Diode maximal voltage	$V_{D \max} = V_i$
Diode maximal current	$I_{D \max} = I_L + \frac{\Delta I_{\max}}{2}$
Mean current	$\langle I_D \rangle = (1-\alpha) I_L$
Rms current	$I_{D \text{ rms}} = \sqrt{(1-\alpha) I_L^2 + \frac{\Delta I_{\max}^2}{12}}$



## Appendix II: Supercapacitors library.

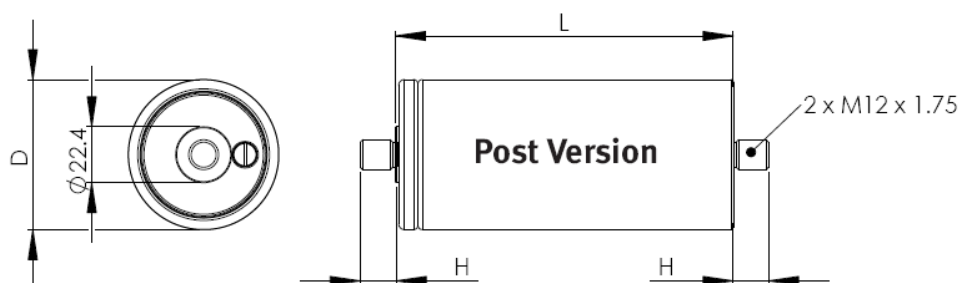
The chosen supercapacitors are from Maxwell ([www.maxwell.com/ultracapacitors/index.asp](http://www.maxwell.com/ultracapacitors/index.asp)). Between the wide ranges of Maxwell's supercapacitors, the BCAPxxxx E270 and the BCAPxxxx P250 families were retained. The mechanical and physical properties of the chosen supercapacitors are shown in the following lines.

### MC Energy Product Specifications:

Part Number	Capacitance (F)	ESR, DC (mohm)	ESR, 1kHz (mohm)	Ic (mA)
BCAP0650 E270	650	1.15	0.80	1.5
BCAP1200 E270	1200	0.79	0.56	2.7
BCAP1500 E270	1500	0.63	0.43	3.0
BCAP2000 E270	2000	0.46	0.35	4.2
BCAP3000 E270	3000	0.37	0.30	5.2

### MC Energy Product Properties:

Maxwell Part No.	Rth (C/W)	Isc (A)	E <sub>max</sub> (Wh/kg)	P <sub>max</sub> (W/kg)	Pd (W/kg)
BCAP0650 E270	6.5	3500	3.29	11,300	3,800
BCAP1200 E270	5.3	3750	4.05	10,800	3,600
BCAP1500 E270	4.5	3900	4.75	13,200	4,300
BCAP2000 E270	3.8	4300	5.06	13,000	4,700
BCAP3000 E270	3.2	4800	5.52	11,000	4,200



Part Number	Vol (l)	Mass (kg)	Size (mm)		
			L	H	D
BCAP0650 E270 T04	0.211	0.20	51.5	14.0	60.0
BCAP1200 E270 T04	0.294	0.30	74.0	14.0	60.0
BCAP1500 E270 T04	0.325	0.32	85.0	14.0	60.0
BCAP2000 E270 T04	0.373	0.40	102.0	14.0	60.0
BCAP3000 E270 T04	0.475	0.55	138.0	14.0	60.0

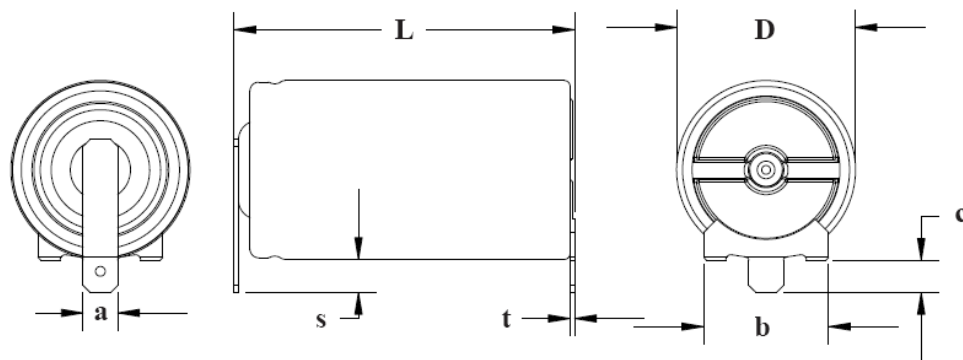
Figure A. 1: BCAPxxxx E270 supercapacitor family mechanical and physical characteristics.

## BC Power Product Specifications:

Part Number	Capacitance (F)	ESR, DC (mohm)	ESR, 1kHz (mohm)	Ic (mA)
BCAP0120 P250	120	5.00	2.50	0.15
BCAP0310 P250	310	2.20	1.00	0.45

## BC Power Product Properties:

Maxwell Part No.	Rth (C/W)	Isc (A)	Emax (Wh/kg)	Pmax (W/kg)	Pd (W/kg)
BCAP0120 P250	15.0	500	3.59	21,500	5,100
BCAP0310 P250	10.9	1500	4.48	26,000	5,600



Part Number	Vol (l)	Mass (g)	Size (mm)						
			L	D	a	b	c	s	t
BCAP0120 P250	.027	29.0	51	26	4.75	16.0	5.9	6.9	0.5
BCAP0310 P250	.053	60.0	62	33	6.40	22.9	5.9	6.9	0.8

Figure A. 2: BCAPxxx P250 supercapacitor family mechanical and physical characteristics.

## Appendix III: IGBT and diode library.

The chosen IGBT and diodes are from EUPEC ([www.infineon.com/cms/en/product/index.html](http://www.infineon.com/cms/en/product/index.html)).

Depending on the chosen converter topology, different voltage ranges will be needed. Thus, two different libraries were implemented.

The first library groups all the switches whose maximal withstood voltage is 600 Volts. Thus, the family BSMxxGB60DLC from EUPEC is proposed. In the CELINA project proposed power converter, these switches can be used in the classical Boost converter. In this case the switch maximal voltage is around 270 volts. Some characteristics of these switches are shown in Table A. 1.

$I_{\max}$ (A)	$R_t$ ( $\Omega$ )	$V_t$ (V)	$R_d$ ( $\Omega$ )	$V_d$ (V)	$R_{th\ j-t}$ (K/W)	$R_{th\ j-d}$ (K/W)	$R_{th\ j-b}$ (K/W)
50	0.022	1.1	0.0075	0.85	0.44	0.8	0.03
75	0.015	1.1	0.004	0.85	0.35	0.66	0.03
100	0.010	1.1	0.003	0.85	0.28	0.5	0.03
150	0.008	1.1	0.002	0.85	0.21	0.4	0.02
200	0.006	1.1	0.0015	0.85	0.17	0.19	0.02
300	0.004	1.1	0.001	0.85	0.10	0.21	0.01

**Table A. 1 : 600 volts switches characteristics.**

In the case of the Buck and Buck-Boost converters, the voltage value that the switches must withstand is higher and can reach in some cases values up to 600 volts. Therefore, the BSMxxGB120DLC from EUPEC is proposed in this case. These switches can withstand voltages up to 1200 volts. Some characteristics of these switches are shown in Table A. 2

$I_{\max}$ (A)	$R_t$ ( $\Omega$ )	$V_t$ (V)	$R_d$ ( $\Omega$ )	$V_d$ (V)	$R_{th\ j-t}$ (K/W)	$R_{th\ j-d}$ (K/W)	$R_{th\ j-b}$ (K/W)
50	0.022	1.3	0.0125	1.05	0.27	0.6	0.05
75	0.0143	1.3	0.0083	1.05	0.18	0.5	0.05
100	0.011	1.3	0.0067	1.05	0.16	0.3	0.01
150	0.0075	1.3	0.005	1.05	0.1	0.25	0.01
200	0.0055	1.3	0.0037	1.05	0.08	0.18	0.01
300	0.0037	1.3	0.0023	1.05	0.05	0.125	0.01

**Table A. 2: 1200 volts switches characteristics.**



## Appendix IV: Inductor cores library and sizing procedure.

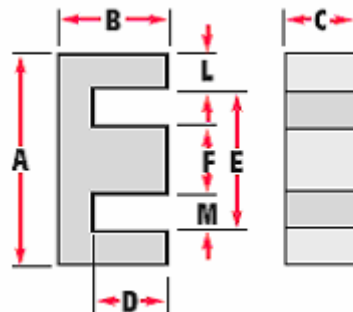
The chosen cores are Kool M $\mu$  E Cores from Magnetics ([www.mag-inc.com](http://www.mag-inc.com)). This choice has been done according the advice of Jean Philippe Besnard, engineer with Thales and also involves in the CELINA project. The sizing procedure has been established according with the information available in Magnetics website.

Kool M $\mu$  E Cores have a distributed air gap which makes them ideally suited for switching regulator inductors, flyback transformers, and power factor correction (PFC) inductors. The 10,500 gauss saturation level of Kool M $\mu$  provides a higher energy storage capability than can be obtained with gapped ferrite E cores, resulting in smaller core size. Kool M $\mu$  E cores are competitively priced against gapped ferrite E cores and their distributed air gap eliminates gap loss problems associated with ferrites. Kool M $\mu$  E cores have significantly lower losses and substantially better thermal properties when compared to powdered iron E cores.

	MPP	High Flux	Kool M $\mu$
<b>Permeability</b>	14-550	14-160	26-125
<b>Core Loss</b>	Lowest	Moderate	Low
<b>Perm vs. DC Bias</b>	Better	Best	Good
<b>Saturation (<math>B_{sat}</math>)</b>	7.5 Kilogauss	15 Kilogauss	10.5 Kilogauss
<b>Nickel Content</b>	80%	50%	0%
<b>Relative Cost</b>	High	Medium	Low

Table A. 3: Powder cores comparison.

The available Kool M $\mu$  E cores and its mechanical and physical characteristics are presented in next page





PART NO.		A	B	C	D (mils.)	E (mils.)	F	L (no. of turns)	M (mils.)
00K1207E (EF 12.6)	in (mm)	.500±.010 (12.70)	.252±.004 (6.40)	.140±.006 (3.56)	0.178 (4.42)	0.35 (8.89)	.140±.005 (3.56)	0.07 (1.78)	0.104 (2.64)
00K1808E (EI-187)	in (mm)	.760±.012 (19.30)	.319±.007 (8.10)	.188±.006 (4.78)	0.218 (5.54)	0.548 (13.90)	.188±.005 (4.78)	0.094 (2.39)	0.183 (4.65)
00K2510E (E-2425)	in (mm)	1.000±.015 (25.40)	.375±.007 (9.53)	.250±.004 (6.53)	0.245 (6.22)	0.74 (18.80)	.250±.005 (6.22)	0.125 (3.17)	0.246 (6.25)
00K3007E (DIN 30/7)	in (mm)	1.185±.018 (30.10)	.591±.009 (15.01)	.278±.006 (7.06)	0.376 (9.70)	0.768 (19.50)	.274±.008 (6.96)	0.201 (5.11)	0.254 (6.46)
00K3515E (EI-375)	in (mm)	1.360±.020 (34.54)	.557±.009 (14.10)	.368±.007 (9.35)	0.378 (9.65)	0.995 (25.30)	.367±.008 (9.32)	0.175 (4.45)	0.31 (7.87)
00K4017E (EE 42/11)	in (mm)	1.687±.025 (42.80)	.830±.013 (21.10)	.424±.010 (10.80)	0.587 (15.00)	1.195 (30.40)	.468±.010 (11.90)	0.234 (5.95)	0.365 (9.27)
00K4020E (DIN 42/15)	in (mm)	1.687±.025 (42.80)	.830±.013 (21.10)	.608±.010 (15.40)	0.587 (15.00)	1.195 (30.40)	.468±.010 (11.90)	0.234 (5.95)	0.365 (9.27)
00K4022E (DIN 42/20)	in (mm)	1.687±.025 (42.80)	.830±.013 (21.10)	.788±.010 (20.00)	0.587 (15.00)	1.195 (30.40)	.468±.010 (11.90)	0.234 (5.95)	0.365 (9.27)
00K4317E (EI-21)	in (mm)	1.609±.024 (40.90)	.650±.011 (16.50)	.493±.007 (12.50)	0.409 (10.40)	1.115 (28.30)	.493±.008 (12.50)	0.238 (6.00)	0.31 (7.90)
00K5528E (DIN 55/21)	in (mm)	2.16±.032 (54.90)	1.085±.016 (27.60)	.812±.015 (20.60)	0.729 (18.50)	1.476 (37.50)	.660±.015 (16.80)	0.33 (8.38)	0.405 (10.30)
00K5530E (DIN 55/25)	in (mm)	2.16±.032 (54.90)	1.085±.016 (27.60)	.969±.015 (24.61)	0.729 (18.50)	1.476 (37.50)	.660±.015 (16.80)	0.33 (8.38)	0.405 (10.30)
00K6527E (Metric E65)	in (mm)	2.563±.050 (65.10)	1.279±.150 (32.50)	1.063±.016 (27.00)	.874 (22.20)	1.740 (44.20)	.775±.012 (19.70)	.394 (10.00)	.476 (12.10)
00K7228E (F11)	in (mm)	2.850±.043 (72.39)	1.100±.020 (27.94)	.750±.015 (19.05)	0.699 (17.78)	2.072 (52.63)	.750±.015 (19.05)	0.375 (9.52)	0.665 (16.89)
00K8020E (Metric E80)	in (mm)	3.150±.047 (80.01)	1.500±.025 (38.10)	.780±.015 (19.81)	1.103 (28.14)	2.334 (59.28)	.780±.015 (19.81)	0.39 (9.91)	0.78 (19.81)

PART NO.	A <sub>L</sub> mH/1000 TURNS±0%				Path Length l <sub>p</sub> (cm)	Cross Section A <sub>c</sub> (cm <sup>2</sup> )	Volume V <sub>0</sub> (cm <sup>3</sup> )
	26p	40p	60p	90p			
00K1207E***	-	-	-	-	2.96	0.130	0.385
00K1808E***	26	35	48	69	4.01	0.228	0.914
00K2510E***	39	52	70	100	4.85	0.385	1.87
00K3007E***	33	46	71	92	6.56	0.601	3.94
00K3515E***	56	75	102	146	6.94	0.840	5.83
00K4017E***	56	76	105	151	9.84	1.28	12.6
00K4020E***	80	108	150	217	9.84	1.83	18.0
00K4022E***	104	140	194	281	9.84	2.37	23.3
00K4317E***	88	119	163	234	7.75	1.52	11.8
00K5528E***	116	157	219	NA	12.3	3.50	43.1
00K5530E***	138	187	261	NA	12.3	4.17	51.4
00K6527E***	-	-	-	NA	14.7	5.40	79.4
00K7228E***	-	-	-	NA	13.7	3.68	50.3
00K8020E***	103	145	190	NA	18.5	3.89	72.1

\*\*\* Add material code to part number, e.g., for 60p the complete part number is 00K1808E060

**Table A. 4: Kool Mμ E cores mechanical and physical characteristics.**

The sizing procedure could be described as follows:

Only two parameters of the design application must be known: inductance required with dc bias and the dc current. Use the following procedure to determine the core size and number of turns.

1. Compute the product of  $LI^2$  where: L = inductance required with dc bias (millihenrys) I = DC current (amperes)

2. Locate the  $LI^2$  value on the Core Selector Chart (Figure A. 3). Follow this coordinate to the intersection with the first core size that lies above the diagonal permeability line. (Small core sizes are at the bottom; large core sizes are at the top.) This is the smallest core size that can be used.

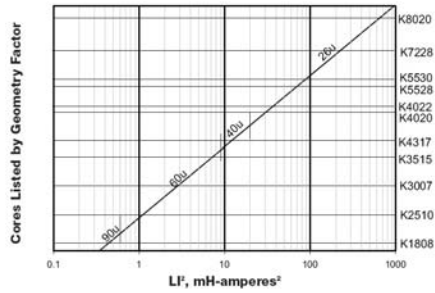


**Figure A. 3: Core selection chart.**

3. The permeability line is sectioned into standard available core permeabilities. Selecting the permeability indicated will yield the smallest core that can be used. Lower or higher permeabilities can be used, but the resulting core size will be larger.

4. Inductance, core size, and permeability are now known. Calculate the number of turns by using the following procedure:

(a) The nominal inductance ( $AL$  in  $mH / 1000$  turns) for the core is obtained from the core data sheet. Determine the minimum nominal inductance by using the worst case negative tolerance (-8%, -12%, or -15%, depending on the core size). With this information, calculate the number of turns needed to obtain the required inductance.

(b) Calculate the bias in oersteds from:  $H = 0.4\pi NI/le$

(c) From the Permeability vs. DC Bias curves (Figure A. 4), determine the rolloff in per unit of initial permeability ( $\mu_{pu}$ ) for the previously calculated bias level.

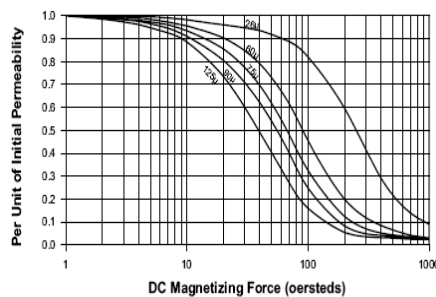


**Figure A. 4: Permeability vs. DC Bias curves .**

(d) Increase the number of turns by dividing the initial number of turns (from step 4a) by the per unit value of initial permeability. This will yield an inductance close to the required value. A final adjustment of turns may be necessary if a specific inductance is required.

5. Choose the correct wire size using the Wire Table (Table A. 5). Duty cycles below 100% allow smaller wire sizes and lower winding factors, but do not allow smaller core sizes.

AWG Wire Size	Resistance $\Omega$ /meter ( $\times .305 = \Omega$ /ft)	Wire O.D. (cm) Heavy Build	Wire Area		Current Capacity, Amps (listed by columns of amps/sq.cm.)			
			Circ. mths	sq. cm ( $\times 0.001$ )	200	400	600	800
8	.00207	.334	18,000	91.2	16.5	33.0	49.5	66.0
9	.00259	.298	14,350	72.7	13.1	26.2	39.3	52.4
10	.00328	.267	11,500	58.2	10.4	20.8	31.2	41.6
11	.00413	.238	9,160	46.4	8.23	16.4	24.6	32.8
12	.00522	.213	7,310	37.0	6.53	13.1	19.6	26.1
13	.00656	.1902	5,850	29.6	5.18	10.4	15.5	20.8
14	.00827	.1714	4,680	23.7	4.11	8.22	12.3	16.4
15	.01043	.1529	3,760	19.1	3.26	6.52	9.78	13.0
16	.01319	.1369	3,000	15.2	2.58	5.16	7.74	10.3
17	.01657	.1224	2,420	12.2	2.05	4.10	6.15	8.20
18	.0210	.1095	1,940	9.83	1.62	3.25	4.88	6.50
19	.0264	.0980	1,560	7.91	1.29	2.58	3.87	5.16
20	.0332	.0879	1,250	6.34	1.02	2.05	3.08	4.10
21	.0420	.0785	1,000	5.07	.812	1.63	2.44	3.25
22	.0531	.0701	810	4.11	.640	1.28	1.92	2.56
23	.0666	.0632	650	3.29	.511	1.02	1.53	2.04
24	.0843	.0566	525	2.66	.404	.808	1.21	1.62
25	.1063	.0505	425	2.15	.320	.641	.962	1.28
26	.1345	.0452	340	1.72	.253	.506	.759	1.01
27	.1686	.0409	270	1.37	.202	.403	.604	.806
28	.214	.0366	220	1.11	.159	.318	.477	.636
29	.266	.0330	180	.912	.128	.255	.382	.510
30	.341	.0295	144	.730	.100	.200	.300	.400
31	.430	.0267	117	.593	.0792	.158	.237	.316
32	.531	.0241	96.0	.487	.0640	.128	.192	.256
33	.676	.0216	77.4	.392	.0504	.101	.152	.202
34	.856	.01905	60.8	.308	.0397	.0794	.119	.159
35	1.086	.01702	49.0	.248	.0314	.0627	.0940	.125
36	1.362	.01524	39.7	.201	.0250	.0500	.0750	.100
37	1.680	.01397	32.5	.165	.0203	.0405	.0608	.0810
38	2.13	.01245	26.0	.132	.0160	.0320	.0480	.0640
39	2.78	.01092	20.2	.102	.0123	.0245	.0368	.0490
40	3.51	.00965	16.0	.081	.00961	.0192	.0288	.0384
41	4.33	.00864	13.0	.066	.00785	.0157	.0236	.0314
42	5.45	.00762	10.2	.052	.00625	.0125	.0188	.0250
43	7.02	.00686	8.40	.043	.00484	.00968	.0145	.0194
44	8.50	.00635	7.30	.037	.00400	.00800	.0120	.0160
45	10.99	.00546	5.30	.027	.00309	.00618	.00927	.0124
46	13.81	.00498	4.40	.022	.00248	.00496	.00744	.00992
47	17.36	.00452	3.60	.018	.00194	.00388	.00582	.00776
48	22.1	.00394	2.90	.015	.00175	.00350	.00525	.00700
49	27.6	.00353	2.25	.011	.00150	.00300	.00450	.00600

Table A. 5: Wire table.

6. The core chosen will have an inductance equal to or greater than that required when biased with the specified dc current. The resulting winding factor will be between 25% and 45%.

## Appendix V : Résumé these en langue française.

Ces travaux s'inscrivent dans le cadre du projet européen CELINA (fuel CEL application In a New configured Aircraft). Ce projet, porté par deux industriels européens, à savoir AIRBUS et DASSAULT AVIATION, est une étude théorique (pas de démonstrateur) sur les potentialités des piles à combustible dans les applications aéronautiques. Malgré une étude qui se veut être la plus générique possible, la principale application étudiée dans le projet est le réseau électrique de secours qui est utilisé ultimement quand la génération principale électrique (dépendante des réacteurs) est perdue (situation très critique !). Il s'agit notamment de voir si la pile à combustible pourrait remplacer avantageusement l'éolienne mise en œuvre actuellement. Environ vingt entreprises et laboratoires de recherches universitaires sont impliqués dans CELINA qui a démarré le 1<sup>er</sup> janvier 2004.

Le profil de puissance typique à satisfaire lors de la mission de secours est présenté sur la figure 1.

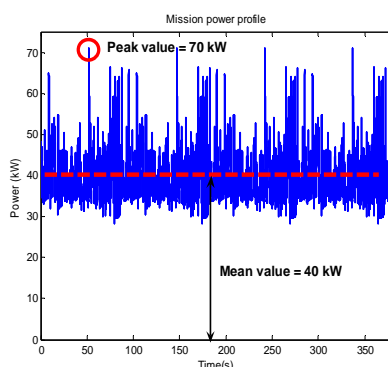


Figure 1 : Profil de puissance de la mission à satisfaire. Source Airbus France.

Ce profil est très « chahuté » (manœuvres de pilotage essentiellement) et fait apparaître de nombreux pics de puissance brefs et de valeurs quasiment doubles de celle de la puissance moyenne mise en jeu sur la mission. Afin de ne pas surdimensionner en puissance la pile à combustible (coûteux économiquement et d'un point de vue massique), il semble judicieux d'hybrider la pile à combustible avec un élément de stockage. L'objectif d'une telle association, dans une vision simplifiée, est que la pile à combustible fournisse la puissance moyenne et l'élément de stockage toute la puissance fluctuante.

Outre l'aspect surdimensionnement, un autre aspect peut justifier une réflexion sur ce type d'hybridation : le temps de réponse des piles à combustible alimentées par hydrogène et oxygène de l'air ambiant qui peut s'avérer limité à cause du temps de réponse des auxiliaires, notamment le compresseur d'air. Ainsi, certains pics de puissance rapides ne pourraient être satisfaits.

Cette thèse traite donc de la conception d'un réseau électrique architecturé autour d'une pile à combustible et d'un élément de stockage pour réaliser la fonction « groupe électrogène de secours »

d'un avion. Le challenge à relever est ambitieux et schématisé sur la figure 2. Il s'agit :

- de définir et d'étudier les architectures électriques possibles pour connecter un groupe électrogène à pile à combustible à un réseau électrique d'avion.
- de concevoir les convertisseurs statiques DC-DC permettant d'obtenir le réseau  $\pm 270V$  requis par AIRBUS.
- de réaliser une optimisation complète du groupe électrogène au moins en termes de masse, de volume et de rendement.

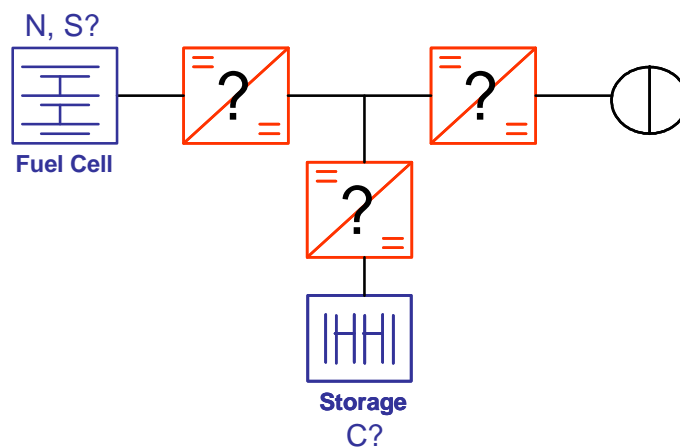


**Figure 2 : Challenge à relever pour la conception de l'architecture électrique du projet CELINA.**

Le manuscrit est composé de quatre chapitres qui vont être succinctement résumés :

- Chapitre I : Cadre du projet européen CELINA et méthodes génériques de dimensionnement.
- Chapitre II : Etude des architectures électriques
- Chapitre III : Conception des convertisseurs statiques
- Chapitre IV : Etude de l'optimisation du système. Comparaisons des architectures.

## **CHAPITRE I : Cadre du projet européen CELINA et méthodes génériques de dimensionnement**

Les axes de recherches autour de l'hydrogène et des piles à combustible de l'Union Européenne sont tout d'abord présentés : production et distribution d'hydrogène, recherches fondamentales sur les piles à combustible, applications stationnaires, portables et transports. Le projet européen CELINA, cadre de cette thèse, s'inscrit pleinement dans plusieurs de ces axes.

Toutes les méthodes de dimensionnement décrites dans la suite du chapitre partent de la connaissance du profil de puissance à satisfaire, tout au long de la mission, pour le composant

concerné. Le profil fourni par le cahier des charges est celui que le système dans sa globalité doit satisfaire. Il s'agit donc, dans le cas d'une hybridation de deux sources électriques, d'être capable de définir pour chacune de ces sources le profil de puissance à satisfaire partant du profil global. Plusieurs solutions sont proposées dans le manuscrit, mais une solution a été retenue : le partage de puissance par une approche fréquentielle. A noter qu'il serait intéressant dans de futurs travaux d'évaluer les autres solutions proposées.

Cette méthode (figure 3) consiste à appliquer la transformée de Fourier au profil de puissance global requis. Une répartition spectrale de la puissance est alors obtenue. L'étape suivante consiste à définir une fréquence de filtrage (ou fréquence de coupure) qui fixera le domaine fréquentiel pour chacune des deux sources. L'idée directrice étant que la pile à combustible gère la composante continue de la puissance et les harmoniques basses fréquences et l'élément de stockage le restant du spectre. Les harmoniques étant répartis, il est alors possible, par une transformée inverse de Fourier ( $FFT^{-1}$ ) d'obtenir les profils de puissance temporels pour chacune des deux sources.

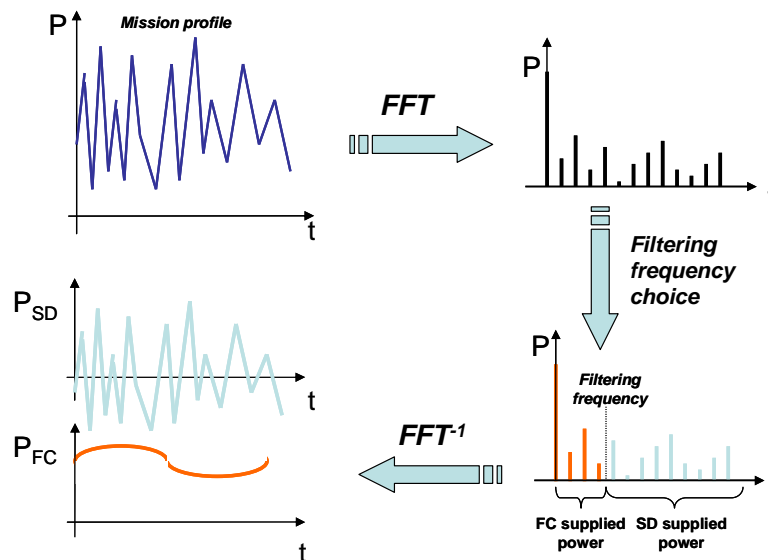


**Figure 3 : Partage de la puissance partant d'une analyse fréquentielle (FFT) du profil de puissance de la mission globale.**

La suite du chapitre est ensuite consacrée à la description de « méthodes génériques de dimensionnement » d'un stack pile à combustible et d'un pack de supercondensateurs. Ces méthodes de dimensionnement sont appelées « génériques » car elles ne prennent pas en compte les couplages qui peuvent exister au sein d'un système. Elles ne peuvent être appliquées que si la source est connectée directement à la charge et si aucune réaction avec une autre source n'existe. Les interactions sont traitées dans la suite. Notons que les batteries ne sont pas considérées dans ces travaux car des études internes menées chez AIRBUS ont prouvé que les supercondensateurs sont mieux adaptés au cahier des charges du réseau électrique de secours.

De façon simplifiée, un stack pile à combustible est défini quand son nombre  $N$  de cellules empilés en série et la surface  $S$  de chacune des cellules sont définis. La méthode suppose que le profil de puissance à satisfaire pour la pile à combustible a été défini. Le dimensionnement d'une pile à combustible est proposé sur la figure 4.

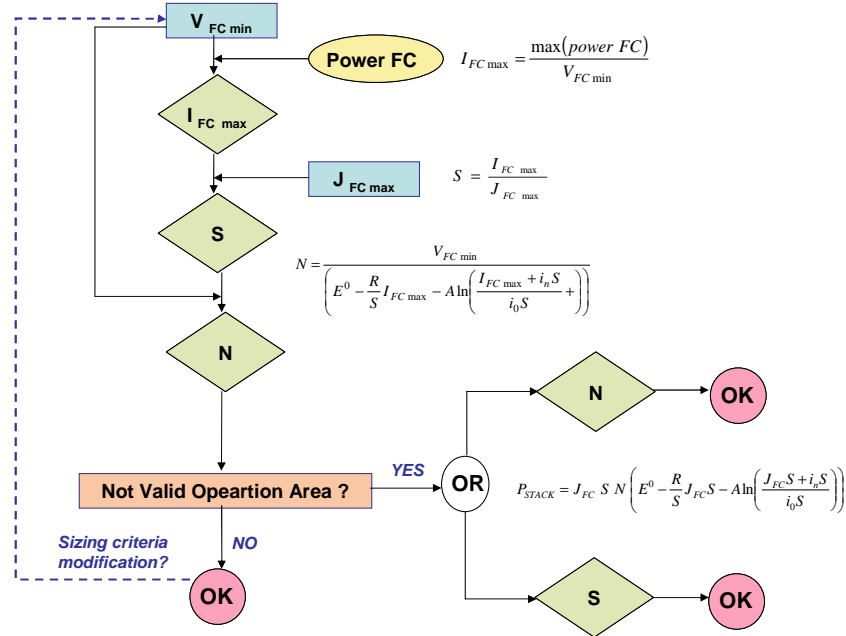


Figure 4 : Méthode de dimensionnement proposé pour la pile à combustible.

Le principe de dimensionnement proposé consiste à garantir une tension minimale  $V_{FCmin}$  délivrée par la pile à combustible, sur toute la mission, de façon à toujours placer le convertisseur statique en aval dans de bonnes conditions de fonctionnement. Il s'agit en outre de ne jamais dépasser la densité de courant maximale  $J_{FCmax}$  prescrite par le fabricant de piles à combustible. Une courbe statique tension-courant de référence est nécessaire : elle doit être fournie également par le fabricant de piles à combustible.

Concernant le pack de supercondensateurs, il s'agit de définir sa capacité faradique  $C$  et sa tension de précharge initiale. Une nouvelle fois, la méthode suppose que le profil de puissance à satisfaire pour le pack de supercondensateurs a été défini (exemple sur la figure 5). Ce profil de puissance est intégré pour obtenir les variations maximales positive et négative au cours de la mission. A partir d'un cahier des charges donnant la tension maximale  $V_{UCmax}$  du pack de supercondensateurs et la profondeur de décharge  $d$  tolérée, et des contraintes énergétiques maximales identifiées pour la mission, il est alors possible de dimensionner entièrement le pack de supercondensateurs. Une fois ce premier dimensionnement effectué, il s'agit d'effectuer un choix technologique pour réaliser le pack qui sera composé de branches en série (tenir la tension maximale requise) et de branches en parallèle (délivrer le courant maximal requis). La prise en compte des pertes dans les supercondensateurs, jusque là négligées, est finalement discutée et réalisée.

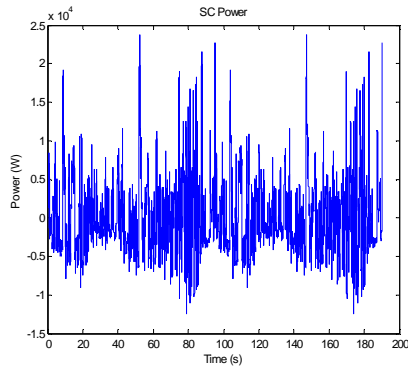


Figure 5 : Exemple de profil de puissance à satisfaire pour le pack de supercondensateurs.

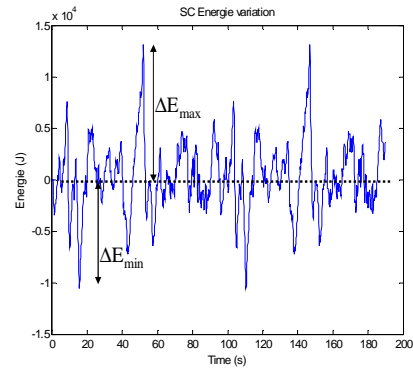


Figure 6 : Variation de l'énergie dans le pack de supercondensateurs au cours de la mission.

## **Chapitre II : Etude des architectures électriques**

Les méthodologies générales de dimensionnement ayant été proposées et décrites dans le chapitre I, nous nous intéressons dans ce chapitre aux différentes architectures électriques possibles pour le groupe électrogène de secours partant de la figure 1.

Si l'on cherche à minimiser la masse, le volume et à maximiser le rendement, il semble logique de réduire le nombre de convertisseurs statiques, mais il faut veiller à satisfaire les critères électriques par le cahier des charges. Ainsi, après une étude préliminaire de toutes les solutions possibles, trois architectures candidates sont retenues :

- « SOLUTION D » : l'architecture avec deux convertisseurs statiques (un par source) connectés parallèlement sur le bus continu  $\pm 270V$  (figure 7).
- « SOLUTION E » : l'architecture avec une connexion directe entre la pile à combustible et le composant de stockage suivi d'un convertisseur de connexion au bus continu  $\pm 270V$  (figure 10).
- « SOLUTION F » : l'architecture avec un convertisseur associée à la pile à combustible et le composant de stockage directement connecté au bus continu  $\pm 270V$  (figure 11).

Considérons ces trois architectures les unes après les autres en décrivant leurs caractéristiques.

**« SOLUTION D » : l'architecture avec deux convertisseurs statiques (un par source) connectés parallèlement sur le bus continu  $\pm 270V$  (figure 7) :**



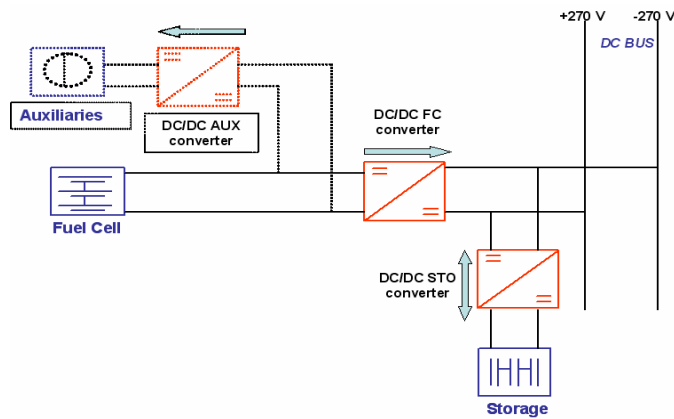


**Figure 7 : Architecture avec deux convertisseurs. Solution D.**

La solution D possède deux degrés de liberté permis par les deux convertisseurs. Le convertisseur associé aux supercondensateurs en permet une bonne utilisation en terme de profondeur de décharge.

Cependant le prix à payer pour disposer de ces deux degrés de liberté est l'obligation de développer une gestion énergétique permettant de compenser les pertes du système. Effectivement, sans la mise en place de cette gestion énergétique, le composant de stockage se décharge anormalement en fournissant les pertes du système conduisant probablement à l'arrêt du système.

Le principe de base de la gestion énergétique consiste à contraindre la pile à combustible à compenser les pertes du système. Deux stratégies sont envisagées :

- La méthode dite de la « tension de référence du composant de stockage » (figure 8) qui peut être appliquée à tout composant de stockage dans la tension est une bonne image de son état de charge. Cette méthode consiste à compenser indirectement les pertes du système en forçant une recharge permanente (et a priori plutôt lente) du composant de stockage grâce à un régulateur : la tension aux bornes du composant de stockage doit toujours tendre vers sa référence. Le principal avantage de cette méthode est la simplicité. Néanmoins, le dimensionnement du régulateur et de la tension de référence n'est pas très facile.
- La méthode dite de l' « estimateur des pertes » (figure 9) qui consiste à estimer les pertes du système à partir de modèles prédictifs. La difficulté majeure est naturellement de disposer de modèles prédictifs valides particulièrement pour le composant de stockage. En outre, le principal inconvénient de cette méthode est sa complexité et le temps de calcul requis. Cette méthode a été fort peu étudiée à notre connaissance ; une validation expérimentale est donc recommandée pour le futur.

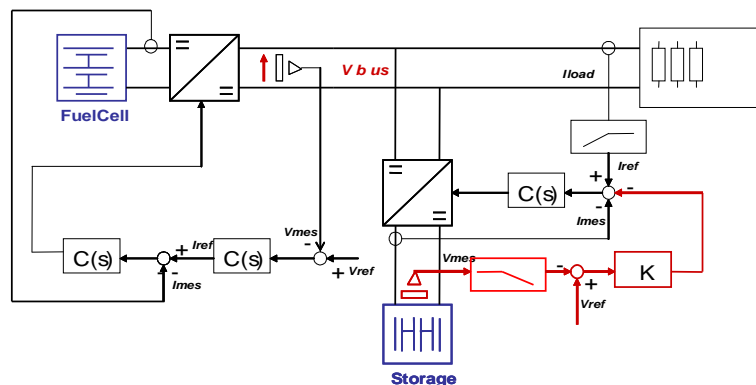


Figure 8 : Boucle de compensation indirecte des pertes du système basée sur le maintien de la tension aux bornes des supercondensateurs à une tension de référence souhaitée.

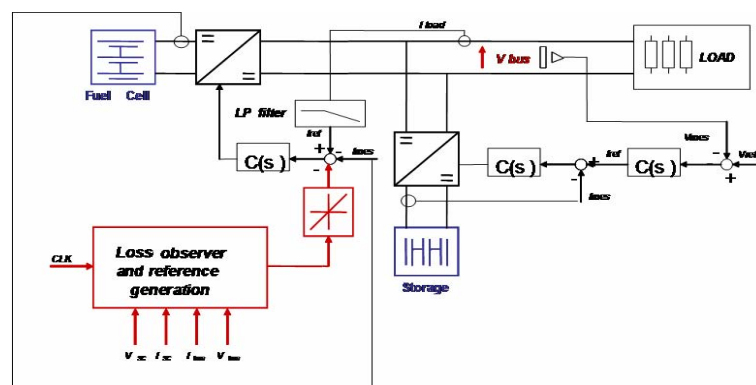


Figure 9 : Boucle de compensation directe des pertes basée sur une estimateur des pertes.

« SOLUTION E » : l'architecture avec une connexion directe entre la pile à combustible et le composant de stockage suivi d'un convertisseur de connexion au bus continu  $\pm 270V$  (figure 10) :

Cette architecture est une architecture originale qui gère intrinsèquement les échanges énergétiques au sein du système. Aucune stratégie de gestion énergétique ne doit être implantée.

Néanmoins, il est démontré que le partage de puissance souhaité entre les deux sources ne peut être que partiellement mis en œuvre. En effet, nous démontrons que cette association directe se comporte comme un filtre passe-bas du premier ordre vis-à-vis de la puissance demandée par la charge. En d'autres termes, c'est le meilleur filtrage de la puissance requise par la charge qu'il est possible d'offrir pour la pile à combustible dans ce type de connexion directe.

Si nous nous intéressons aux pertes au sein du système, il est possible de constater qu'elles ont un impact différent suivant leur nature. Les pertes au sein du convertisseur peuvent être vues « simplement » comme une puissance additionnelle au profil de mission que doit satisfaire la pile à combustible. Les pertes internes du composant de stockage, quant à elles, peuvent être assimilées à

une source de perturbations harmoniques pour la pile à combustible. La pile à combustible ne peut être ainsi complètement protégée contre des variations rapides de courant dans une telle association directe. Cet effet peut être limité si la résistance électrique équivalente des supercondensateurs est beaucoup plus petite que la résistance électrique équivalente de la pile à combustible.

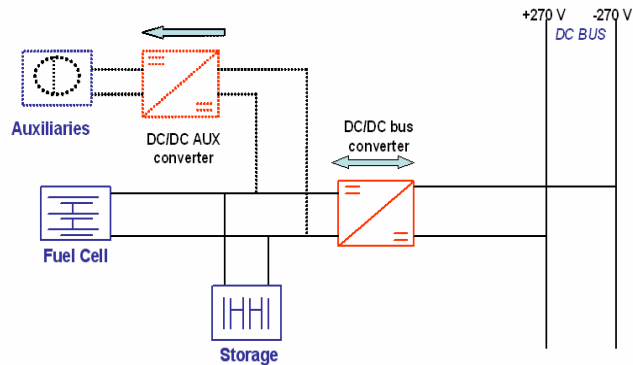


**Figure 10 : Architecture avec un convertisseur. Couplage direct des deux sources électriques. Solution F.**

« *SOLUTION F* » : l'architecture avec un convertisseur associée à la pile à combustible et le composant de stockage directement connecté au bus continu  $\pm 270V$  (figure 11) :

Cette architecture présente des similitudes avec la solution D. Elle requiert également l'implantation d'une gestion énergétique pour éviter la décharge complète des supercondensateurs due à leurs pertes internes.

En outre, cette architecture ne permet pas le contrôle du bus continu  $\pm 270V$  qui est imposé par le composant de stockage et donc nécessairement variable. En effet, le composant de stockage étant imparfait, une marge de variation de tension du bus continu doit être impérativement autorisée pour permettre la charge et la recharge des supercondensateurs.

Le principal avantage de cette architecture est de ne présenter qu'un seul convertisseur traitant « seulement » la puissance moyenne requise par la charge. Cela doit permettre de conduire à de bons rendements et à un système léger.

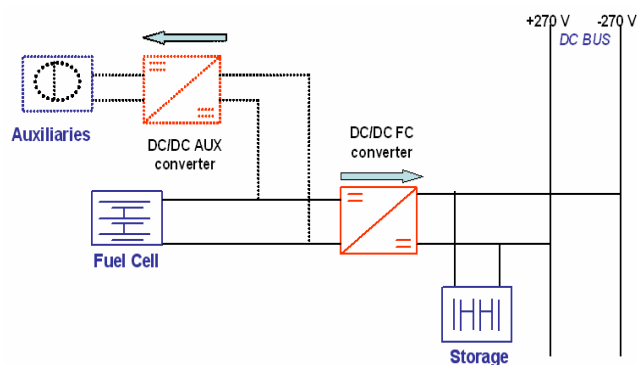


**Figure 11 : Architecture avec un convertisseur. Composant de stockage directement connecté au bus continu. Solution E**

Après avoir détaillé les trois architectures précédentes, les auteurs reviennent sur le dimensionnement du système.

Un point commun est mis en évidence pour toutes les architectures en terme de dimensionnement : si les méthodologies génériques de dimensionnement (chapitre I) sont directement appliquées pour dimensionner la pile à combustible et les supercondensateurs, le système dimensionné ne pourra respecter les critères de dimensionnement requis. L'explication est le partage initial de la puissance requise par la charge entre la pile à combustible et le composant de stockage ne prend en compte les couplages au sein du système, les différentes pertes du système, la stratégie de gestion énergétique...

Pour résoudre cette importante difficulté, les auteurs proposent une méthode de dimensionnement itérative, identique pour toutes les architectures. Elle est schématisée sur la figure 12. L'idée est de modifier de façon itérative les profils de puissance exigés pour les deux sources tant que les critères de dimensionnement ne sont pas satisfaits en relançant des simulations du système global avec les dimensionnements réajustés des composants en incluant un maximum d'aspects comme les pertes et la stratégie de gestion énergétique.

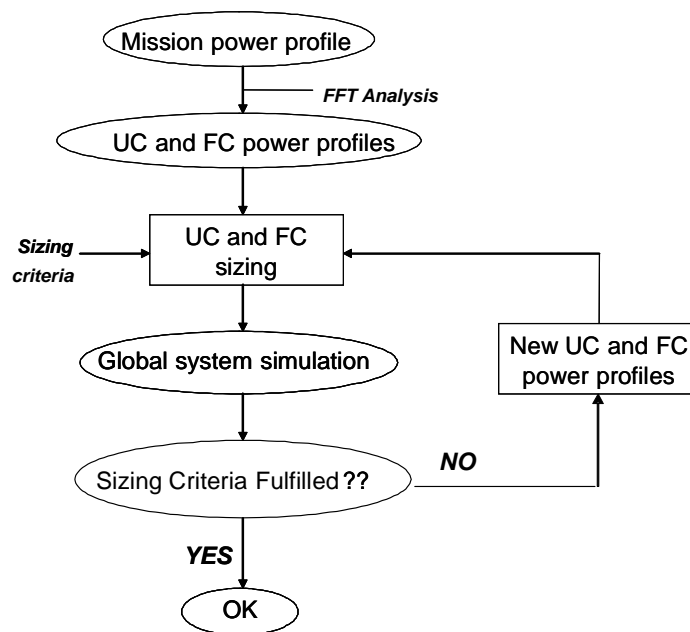


Figure 12 : Méthode itérative de dimensionnement proposée.

### Chapitre III : Conception des convertisseurs statiques

Airbus impose le cahier des charges suivant : un bus continu de  $\pm 270V$  à partir d'une seule pile à combustible, la borne négative de la pile devant être reliée à la carcasse de l'avion qui constitue la masse électrique. Ce cahier des charges impose clairement le développement de topologies de

convertisseurs continu-continu spécifiques. C'est justement l'objet de ce troisième chapitre.

Tout convertisseur associé à la pile à combustible ne requiert pas d'être réversible en courant. En revanche, tout convertisseur associé seul à l'élément de stockage doit être réversible en courant (cas de la solution D).

Deux solutions de conversion statique sont proposées :

- **De « classiques » convertisseurs statiques isolés** basés sur la topologie de type push-pull mettant en œuvre des transformateurs hautes fréquences. Un exemple est proposé sur la figure 13. Outre leur complexité, il n'est pas aisé de rendre réversible en courant ces structures.

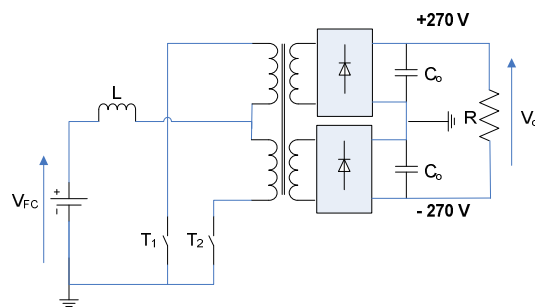


**Figure 13 : Push-pull alimenté en courant proposé pour satisfaire le cahier des charges AIRBUS.**

- **Des associations originales de convertisseurs continu-continu élémentaires.** Le principe consiste à associer un convertisseur continu-continu (de type boost, buck ou buck-boost non inverseur en fonction de la gamme de tension délivrée par la pile à combustible) qui crée le pôle continu +270V avec un convertisseur de type buck-boost qui crée le pôle continu -270V. Les associations série imposant un double traitement de la moitié de la puissance, les associations parallèles s'imposent pour garantir des rendements satisfaisants. Un exemple d'association parallèle est proposé sur la figure 14. L'avantage de ces structures élémentaires est qu'elles peuvent être rendues réversibles aisément.

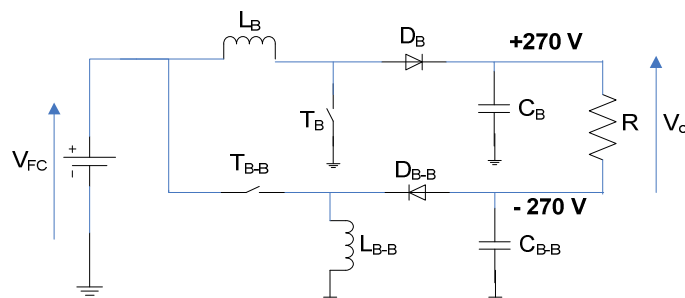


**Figure 14 : Topologie globalement « boost » ±270V. Association parallèle.**

Seule la seconde solution a été étudiée dans ce travail de thèse, la première ayant été évaluée (dans sa version non réversible) par un autre partenaire (THALES AES) impliqué dans le projet CELINA.

Les trois combinaisons possibles pour créer le pôle continu +270V sont analysées en profondeur en termes de dimensionnement et de performances.

Au regard des puissances à traiter (de l'ordre de 40kW pour la puissance moyenne à fournir pour la pile à combustible), chaque convertisseur créant un pôle sera concrètement composé par plusieurs branches identiques en parallèle et entrelacés afin d'offrir des rendements et des masses satisfaisants.

La première idée consiste ainsi à fractionner la puissance  $P$  à traiter en parallélisant  $N$  convertisseurs identiques traitant chacun une puissance réduite de  $P/N$ . Ces « petits » convertisseurs parallélisés offrent clairement un rendement plus élevé comparé à la solution avec un seul « gros » convertisseur traitant toute la puissance  $P$ .

La seconde idée est de tirer avantage de cette parallélisation de « petits » convertisseurs pour réduire la masse des composants grâce à la technique d'entrelacement des commandes. En effet, cette technique d'entrelacement permet de relâcher la contrainte de dimensionnement en termes d'ondulation de courant pour chacun des convertisseurs parallélisés tout en garantissant l'ondulation de courant requise pour la source d'entrée (spécialement pour la pile à combustible). Cette technique d'entrelacement des commandes conduit effectivement à un filtrage actif du courant dans la source d'entrée qui est la somme de tous les courants des convertisseurs parallélisés. L'ondulation de courant pouvant ainsi être réduite dans chaque branche, l'inductance concernée peut être fortement réduite et par conséquent sa masse et celle du convertisseur.

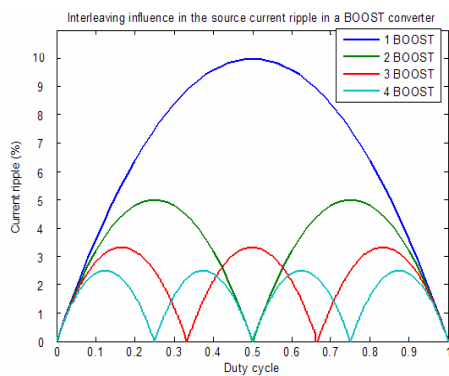


**Figure 15 : Ondulation de courant dans la pile à combustible en fonction du rapport cyclique et du nombre  $N$  de branches entrelacées.**

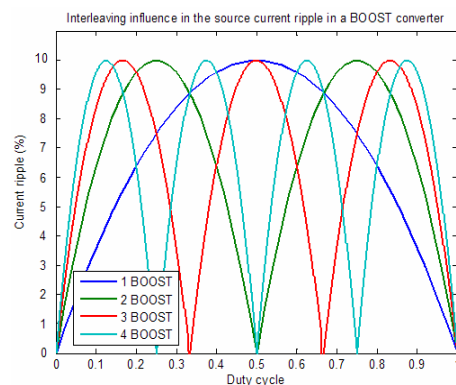


**Figure 16 : Ondulation de courant dans la pile à combustible en fonction du rapport cyclique et du nombre  $N$  de branches entrelacées en supposant une inductance variable avec  $N$ .**

Néanmoins, cette stratégie de parallélisation peut facilement conduire à un fonctionnement en conduction discontinue. En effet, si la valeur de l'inductance est réduite, la zone de fonctionnement en conduction discontinue est accrue et peut être facilement atteinte si le niveau de puissance requis par la charge décroît. Si cette zone est atteinte, le contrôle du convertisseur statique peut devenir délicat.

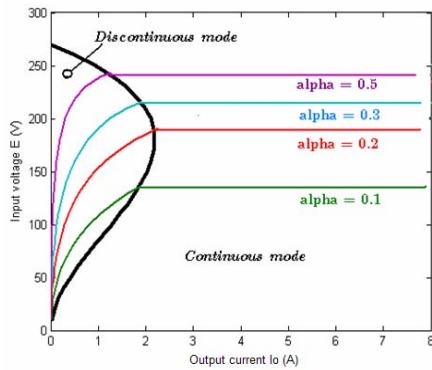


**Figure 17 : Frontière entre les modes de conduction continue et discontinue.**

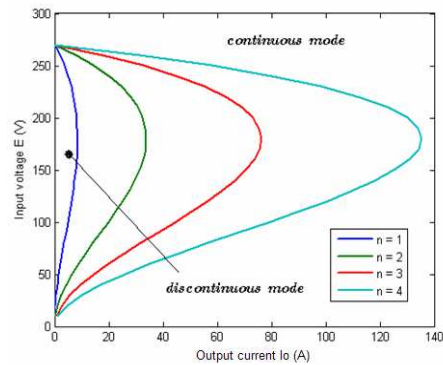


**Figure 18: Evolution de la frontière entre les modes de conduction continue et discontinue avec le nombre de branches entrelacées.**

Pour éliminer (ou réduire fortement) cet inconvénient qui peut être très marqué si la plage de fonctionnement varie fortement, une stratégie originale de contrôle des convertisseurs a été proposée : la technique dite « d'extinction de branches ». Le principe de cette technique consiste à éviter d'être dans des conditions conduisant à un fonctionnement en conduction discontinue. Ainsi, une branche est éteinte chaque fois que la puissance requise par la charge décroît et conduit le convertisseur dans la zone de conduction discontinue. La puissance exigée est alors partagée en un nombre réduit de branches repoussant la limite de fonctionnement en conduction discontinue pour les branches restantes. Même si cette technique donne de très bons résultats en simulation (figures 19 à 21), une validation est recommandée dans les travaux futurs.

La suite du chapitre III est ensuite consacrée à une étude très approfondie des rendements et des masses des solutions non isolées proposées. Un exemple est donné sur les figures 22 et 23. Il est prouvé quantitativement que la technique d'extinction de branches améliore significativement le rendement du convertisseur. Les convertisseurs proposés ne présentent pas au final un excellent rapport masse/rendement ; cela s'explique principalement par le plus faible rendement de la partie « buck-boost », réalisant le pôle -270V.

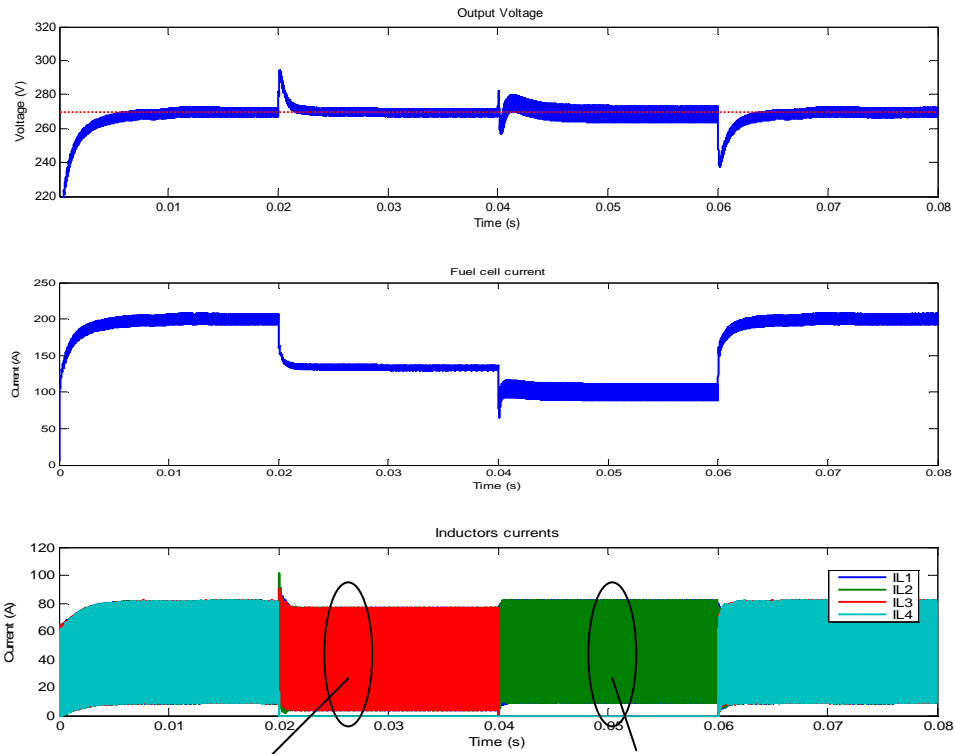


Figure 19 : Simulation de la technique d'extinction de branches.

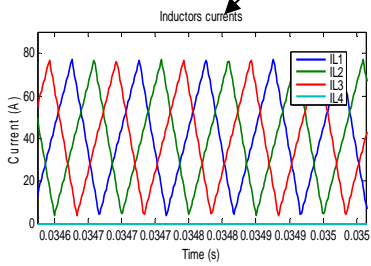


Figure 20 : Extinction d'une branche.

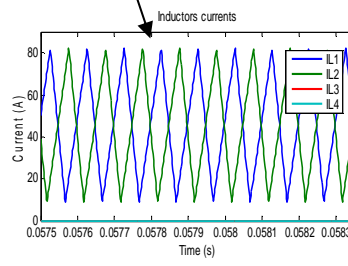


Figure 21 : Extinction de deux branches.

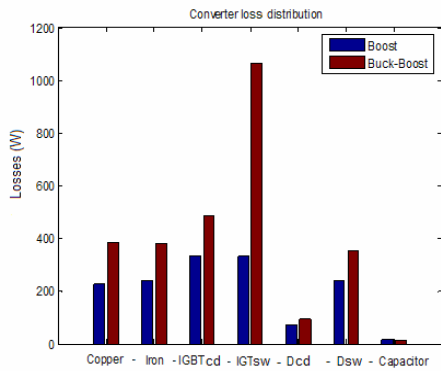


Figure 22 : Distribution des pertes au sein topologie globalement Boost (40kW ; 70V).

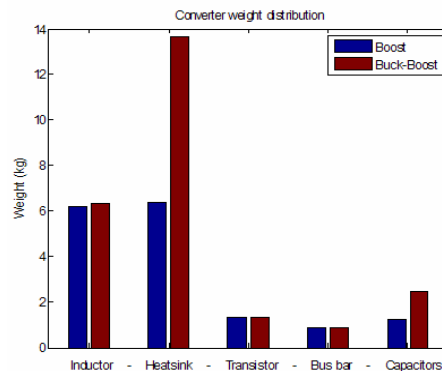


Figure 23 : Distribution de la masse au sein topologie globalement Boost.



## Chapitre IV : Etude de l'optimisation du système. Comparaisons des architectures.

Ce quatrième et dernier chapitre traite de l'épineux problème de l'optimisation du système global. Le groupe électrogène développé étant destiné à être embarqué dans un avion, cette optimisation vise la minimisation de sa masse et de son volume et la maximisation de son rendement. Dans cette étude, la masse et le volume sont considérés comme évoluant dans le même sens, étant liés par la masse volumique.

Dans les chapitres précédents, trois architectures électriques, des topologies de convertisseurs et des stratégies de gestion énergétique ont été proposées et étudiées. L'optimisation du système global doit permettre de comparer et classer toutes les possibilités offertes dans le but final de sélectionner la meilleure solution en termes de masse et rendement. Tous les modèles précédemment développés pour calculer les masses et rendements des différents composants (pile à combustible, supercondensateurs, convertisseurs statiques) sont ici pleinement exploités.

Le système étant complexe (nombreuses variables continues et discrètes et multicritère d'optimisation), le recours à des techniques d'optimisation avancées s'est rapidement imposé. Ainsi, un algorithme génétique a été implémenté. L'architecture de l'outil d'optimisation développé est proposé sur la figure 24.

De nombreuses optimisations ont été réalisées. Globalement, les résultats sont plus ou moins surprenants.

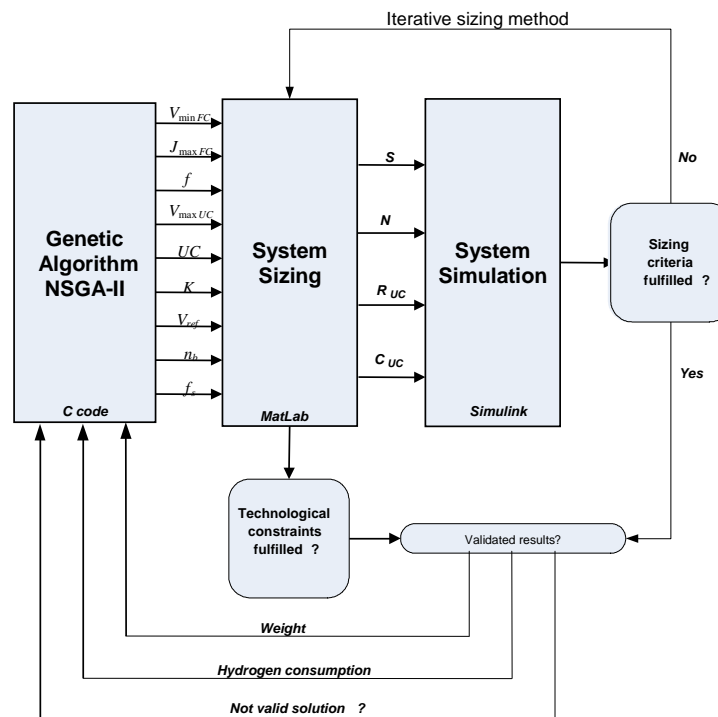
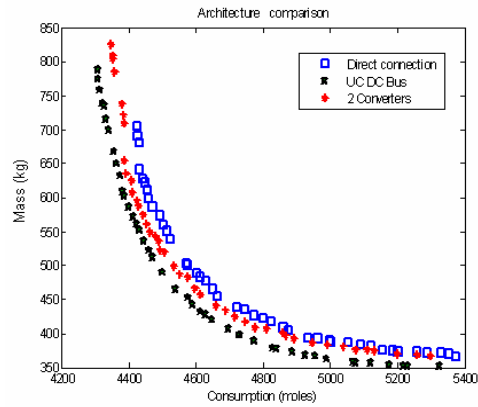


Figure 24 : Schéma de l'outil d'optimisation développé.



**Figure 25 : Front de Pareto pour les trois architectures électriques retenues.**

L'architecture avec le stockage directement connecté au bus continu (solution F) apparaît être la meilleure en termes de masse et de rendement (figure 25). Cette architecture offre un convertisseur léger qui ne traite que la puissance moyenne.

L'architecture avec deux convertisseurs (solution D) semble être la meilleure seconde option. Si cette architecture conduit logiquement au pack de supercondensateurs le plus léger, le recours à deux convertisseurs est préjudiciable en termes de masse pour le système global comparativement à la solution précédente.

Enfin, l'architecture avec connexion directe de la pile à combustible et des supercondensateurs ne semble pas être une bonne option pour notre cahier des charges. Un convertisseur lourd qui doit traiter toute la puissance requise pendant la mission et une mauvaise utilisation des supercondensateurs rendent cette architecture non adaptée comparée aux deux autres.

Tout au long du chapitre, l'outil d'optimisation apparaît, au travers des nombreuses illustrations, ne pas être seulement un outil d'aide à la décision, mais également un outil de compréhension et d'analyse. Nous avons pu en effet tirer plusieurs enseignements des résultats d'optimisation. En voici les principaux.

Les premiers résultats intéressants sont les tendances chiffrées pour les nombreux paramètres difficiles à fixer a priori : la fréquence optimale de coupure pour la répartition de la puissance entre les deux sources, la tension minimale de la pile à combustible au dessous de laquelle il ne faut pas descendre (figure 26), la densité maximale de courant optimale pour la pile à combustible (figure 27), le choix de la technologies pour les supercondensateurs, la fréquence optimale de commutation pour les convertisseurs statiques...

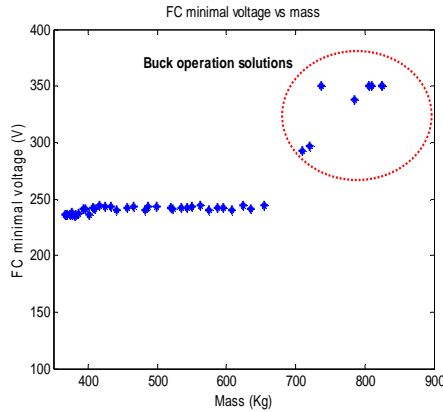


**Figure 26 : Tension minimale de la pile à combustible en fonction de la masse du système.**

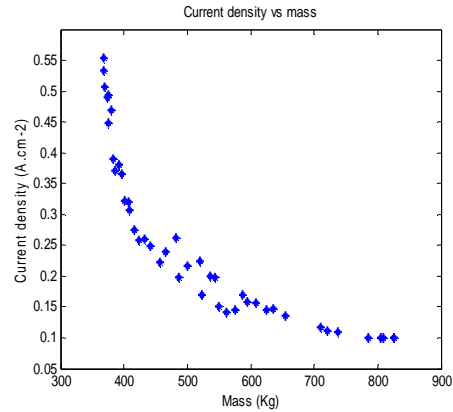


**Figure 27 : Densité de courant maximale de la pile à combustible en fonction de la masse du système.**

Même si les trois architectures ne conduisent pas à la même masse globale et la même consommation d'hydrogène, l'évolution des variables de dimensionnement le long du front de Pareto semble plus ou moins la même pour toutes les architectures. Quelques particularités existent, mais les tendances sont bien les mêmes.

Un des plus surprenants résultats (figure 27) est que les systèmes les plus légers ne mettent pas en oeuvre une pile à combustible fonctionnant à la densité de courant maximale autorisée pour l'optimisation à savoir  $0.8 \text{ A/cm}^2$  dans notre cas. Pourtant, pour une puissance donnée, une pile fonctionnant à  $0.8 \text{ A/cm}^2$  est clairement la pile à combustible la plus légère possible dans cette optimisation. Ce résultat d'optimisation s'explique cependant par le fait que de hautes densités de courant conduisent à des pertes élevées, et donc, à des consommations d'hydrogène plus élevées augmentant alors la masse globale du système.

Pour prouver cette hypothèse, la même architecture a été dimensionnée pour deux missions de durées différentes (4 heures et 15 heures). La mission la plus longue conduit à des piles à combustible fonctionnant à de faibles densités de courant, mais à des rendements élevés, pour éviter un surpoids dû au stockage d'une plus grande quantité d'hydrogène.

De plus, les solutions dimensionnées pour des missions différentes (longues et courtes) ont été comparées pour une mission identique de longue durée (15 heures). Dans ce cas, les solutions avec les piles fonctionnant à de faibles densités de courant, mais à des rendements élevés, sont clairement préférables à des piles fonctionnant à de fortes densités de courant.

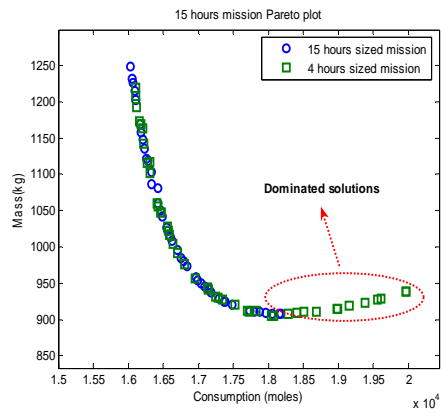


**Figure 28 : Comportement des solutions optimisées pour une mission de 4 heures dans le cadre d'une mission de 15 heures.**





